Experimental and Computational Characterization of the Anterior Cruciate Ligament:

Challenges and Considerations for Soft Tissue Biomechanics

by

Kaitlyn Flora Mallett

A dissertation submitted in partial fulfillment
of the requirements for the degree of
Doctor of Philosophy
(Mechanical Engineering)
in the University of Michigan
2017

Doctoral Committee:

Professor Ellen M. Arruda, Chair
Professor James A. Ashton-Miller
Professor Alan S. Wineman
Professor Edward M. Wojtys

Kaitlyn F. Mallett

kmallett@umich.edu

ORCID iD: 0000-0001-8673-7860

Dedication

To my parents, grandparents, and ancestors.

Thank you.

Acknowledgements

I'd like to thank my advisor, Ellen M. Arruda, for all your guidance, support and time. I've learned so much from you, and have greatly enjoyed and benefitted from our time together. Thank you for inspiring me to fundamentally understand mechanics and to champion its understanding the biomechanics community.

Thank you to Professor Alan Wineman, Professor James Ashton-Miller, and Dr. Edward Wojtys for your advice and support for this dissertation. It has been a pleasure and an honor to learn from you and work with you.

I'd like to thank all of the current and former members of the Mechanics of Materials laboratory during my time at UM: Jinjin, Keqin, Tyler, Lixiang, Zhouzhou, Ben, Callan, Marie, Ryan, Haolu, Cameron, Vasu, Aleesa, Stoyna, Kyubum, Adam, Zhe, Jared, Jason, Michael, Yue, Alan, Marissa, Will, Maya, Michelle, Hai, Fanbo, James, Dandan, Isha, and Kisik. Thank you so much for all your support and discussions on research. Thank you to Jinjin for pioneering my particular project and providing a fantastic foundation for my work. Ben, thanks for keeping me sane on computational work, I learned so much from you. Vasu, thanks for all your time and assistance on biomechanics testing. Joyce (Yue), thank you for all the conversations on DIC, patterning, experimental setup design and computational work. Your insight has been invaluable and I so appreciate all the time and energy you've spent figuring things out with me and on my behalf. Thank you to the Facilities people: Matt Navarre and Charlie Weger for all the support during the lab move, and to Marv Cressey for teaching me to flourish in the machine shop. I'd also like to thank the undergrads I've had the privilege to work: Casey, Keith, Kip, Fabian, Antonia, and Rebecca. Thank you for being so understanding and hardworking, and for inspiring me to work harder. I'm grateful to my undergraduate advisor Professor Alan Argento and Dr. Wonsuk Kim, you piqued my interest in biomechanics and inspired me to pursue an advanced degree. Thank you to my church family at H2O and core group members, especially Nathinee, Akima and Nancy and Lianette for creating such a welcoming environment for core groups. I'd also like to thank my fellow RMFers Johanna, Anna, Esmeralda, Mauro, Karlo, and Aresha for making the first months at UM so memorable. Thank you to all the friends that have made life fun and it easier to get through the difficult times. Sona, Gyeong Jin, Shinuo, Yuqing, Biqiao, Shuna, Nathinee, Deema, Xin, Adaleena, Lu, I have so enjoyed our times together chatting, studying together, hanging out and eating fantastic food.

I'd like to thank my family and friends: the Martins, Watermans, Navarros, Katherine Vinson, Lydia Cleaver and Glenn Galler. Thank you to the Samahas (Auntie Kholoud, Mr. Mufeed, Hiba, Wlaa, Alaa, Abdallah and Ahmad) for always supporting me and being proud of me. Thank you to the Carters (Auntie Renee, Uncle Mike, Brittany, Bethany, Rachel, Michael, Chris and Reed) for being true family to me, and for always having a place for me in your warm and welcoming home. To my bawsy best friend Joyce, you've been such a blessing to me, thank you for the hours and hours of conversation, commiseration, and tough love.

To my siblings Alyssa, Mariah, Jared, Jordan and Tessa, thank you for supporting and believing in me and making me feel so loved and encouraged. Alyssa, our conversations have helped me so much in figuring things out, thanks for sharing everything from life struggles to pets. Mariah, thank you for always being happy to see me and for being a steadfast friend and sister, I so admire your work ethic and caring nature. Jared, I’ve loved talking with you about the struggles of being a student, especially in grad school, thanks for being a fantastic listener and encouraging me so much with your down-to-earth advice. Jordan, I have learned so much from you, thank you for always thinking of me and encouraging me, I so look forward to the time we spend together. Tessa, my longest roomie, thanks for lovingly putting up with my shenanigans for so long, always including me in the happenings of your life, and listening to me. To my parents Lamont and Kathy, there is no way I would be where I am without all the sacrifice and love you have poured into my life. Thank you Daddy for being the best teacher I have ever had, I am so proud to be a mechanical engineer like you. Mommy, you are my first best friend, thank you for the countless hours talking about life and my struggles during this process, and for always being my loudest cheerleader.

Finally, to my Heavenly Father and Lord Jesus Christ, all the glory and honor is Yours for this degree and time in my life. Thank you for providing me such a profound experience, putting people in my life to learn from and live life with, and allowing me to appreciate the love of so many.

Table of Contents

List of Figures

List of Tables

Chapter 1: Introduction

1.1 Introduction

The anterior cruciate ligament (ACL) is one of four major ligaments in the knee, playing a critical role in stabilizing the joint during daily loading activities. The other three stabilizing ligaments are the posterior cruciate ligament (PCL), the medial collateral ligament (MCL), and the lateral collateral ligament (LCL). The location of the ACL within the joint renders it highly susceptible to injury, often precipitating catastrophic long-term joint outcomes [2]. Tears of the ACL in sporting activities are relatively frequent, with the native tissue demonstrating a limited ability to repair itself. Currently the highest incidence of initial ACL injury is in females in the 14-17 year old age group (18-21 for males); this is also the population with the current greatest rate of increase in ACL injuries [3]. The sex-based disparity in sports related ACL injury rates is also well documented, with females suffering these injuries between 2-7 times more frequently than their male counterparts [4].

Full tears of the ligament tissue require a complete surgical replacement if a return to moderate physical activities is desired. The ideal replacement for a torn ACL would restore native anatomy and function to the knee. Mounting evidence, however, suggests current strategies, typically using a patellar tendon or hamstrings tendon graft, substantially alter the biomechanics of the joint. This altered mechanical profile is posited to promote a hazardous mismatch between joint and underlying articular cartilage mechanics [5,6] driving an increased risk of early onset osteoarthritis [7,8]. While mechanical factors governing this debilitative progression remain unclear, structural and mechanical inconsistencies between the graft tissue and native ACL are thought to play important roles [9–11]. Instabilities could be developed over time through a graft tissue that is more lax than the native tissue [12,13], arising either through loosening [14,15], mechanical degradation [16,17], or possibly a combination of both. Limited additional sources for native graft tissue exist but tissue-engineering approaches may one day offer a solution [18–20].

With ACL injury carrying significant short- and long-term morbidities, accurate characterization of the tissue's structural and mechanical properties seems paramount for two key reasons. First, it provides critical baseline information for elucidating and ultimately countering the mechanism/s of ACL injury. Second, it affords a platform for designing a more appropriate graft replacement that can essentially restore and maintain pre-injury joint function and control. With these facts in mind, this review examines the current level of understanding pertaining to ACL structure and mechanics. In doing so, it highlights what is considered to be critical knowledge gaps compromising the success of current ligament injury risk screening and prevention and reconstructive methods. It additionally proposes future methods and technologies that could plausibly fill these gaps. Through such steps, enhanced short and longer term joint health and general life quality may ultimately be possible.

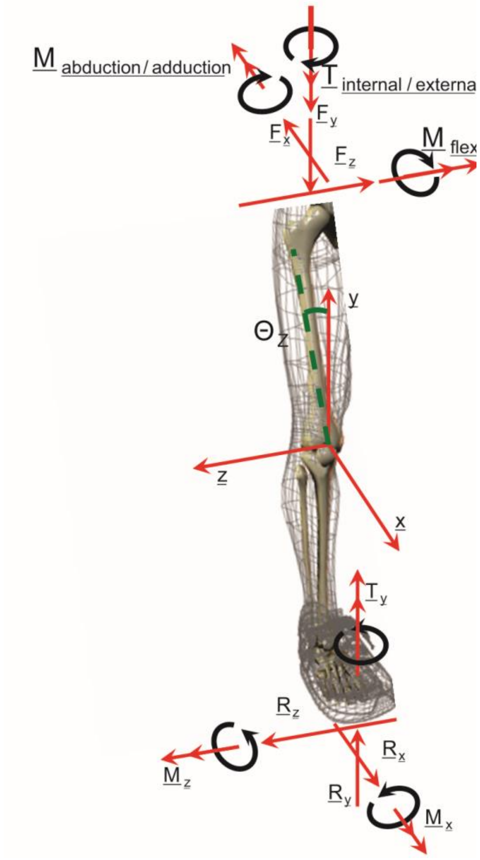

Figure 1.1: External forces and moments acting on the human leg. [1]

Chapter 1 is organized as follows. In **Section 1.2** forces, moments, and motions relevant to the knee joint and referred to within this review are defined. This is followed by a discussion on of ACL structure in **Section 1.3**. Next, ACL mechanics are discussed, first in terms of function during knee motions (**Section 1.4**) and then at the level of the tissue biomechanics (**Section 1.5**). Mechanics comparisons between native ACL and common replacement grafts (**Section 1.6**), the use of animal models in understanding the ACL response (**Section 1.7**), and computational models (**Section 1.8**), are discussed in subsequent sections, with conclusions in **Section 1.9**.

1.1 A knee biomechanics primer

The ACL is most frequently injured during dynamic landing tasks that typically incorporate rapid deceleration and an equally rapid direction change [4]. The external forces and moments that drive these high-risk maneuvers are illustrated acting at the foot and hip in **Figure 1.1**. The ground reaction forces are shown acting in the positive sense. Upper and lower leg weights and the accelerations that balance these forces are not shown. All six degrees of freedom exist in the knee [21–24]. Knee motion can be described as movement in relation to the three mutually perpendicular principle axes: the tibial shaft axis (y-axis), the femoral epicondylar axis (z-axis), and the anterior-posterior axis (x-axis) [21,24]. The three associated body planes are xy – saggital, yz – coronal and xz – transverse. Typically, translations along these respective axes are defined as proximal-distal, lateral-medial and anterior-posterior where all three translation pairs list the positively directed motion first. Knee flexion/extension is rotation about the z-axis. The knee flexion angle, θ_Z, is measured from the y-axis; θ_Z = 0 is full extension. Knee abduction or adduction bends about the x-axis. The abduction/adduction rotation moment as illustrated would result in an abducted knee, also known clinically as a valgus deformation. Adduction or varus deformation is the result of bending about the x-axis in the opposite sense shown. The twisting moment (torque) about the y-axis in the sense illustrated in **Figure 1.1** results in external tibial rotation of the proximal end of the tibia (near the knee) with respect to its distal end (near the foot) [21,23–26]. Excessive anterior tibial shear load [27] or knee abduction motions and/or loads [28,29] have typically been posited to play a critical role in the resultant injury mechanism. Consensus continues to grow, however, that injury arises through more complex combined 3D joint biomechanical maneuvers, which necessarily incorporates internal tibial rotation [30–32].

1.2 Structure of the ACL

Characterization of ACL mechanical properties in physiologically relevant positions is impeded by difficulties associated with finding fully unloaded configurations that coincide with physiologically relevant ones. The complexities in the shape, structure, and orientation of the ACL all contribute to this challenge. The ACL originates on the posterior aspect of the medial surface of the lateral femoral condyle, with the attachment observed to be oval in shape and covering an area of approximately 2 cm^2 [33–38]. The ligament courses anteriorly, medially, and distally from the femur to the tibia, spiraling laterally (counter-clockwise in the right knee, clockwise in the left) as it does so. It then fans out, inserting over a broad flattened hourglass shaped region of approximately 3 cm^2 between and slightly anterior to the tibial spines [36,38,39]. The tibial attachment is also substantially wider and stronger than the femoral one in adults [40]. Harner et al. 1999 [41], digitizing ACL attachments in three dimensions, found both ACL insertions to be relatively planar, with the femoral attachment being more circular than the larger, more oval shaped tibial attachment. At the tibial insertion, the ligament passes beneath the transverse meniscal ligament. It is believed that some fibers of the ACL may blend with the anterior attachment of the lateral meniscus [42]. The clinical significance of this blending, however, has not been established. Cross-sectional area varies along the length of the ligament, with the smallest value evident in the mid-substance [38,41]. This geometric phenomenon has long been postulated to serve to minimize stress concentrations that may arise on the ligament-bone interface [41,43–45]. It may also explain why the majority of adult ACL injuries occur within the proximal third of the tissue mid-substance [4]. Conversely, ACL injuries in skeletally immature individuals arise primarily through tibial avulsions [46]. The adult ACL also demonstrates sex-dimorphic size characteristics, with the male ligament tending to be longer, wider, and thicker [34,36,38,40].

The ACL possesses two functionally discrete bundles demonstrating similarly divergent spatial/mechanical properties - the anteromedial bundle (AM) and the posterolateral bundle (PL) [33,34,36,38,40,47–50]. Anatomically, the bundles have been previously reported to wrap about each other as they extend between insertions and vary in length, with the AM reported to be significantly longer [49,51,52]. The twist of the AM around the PL increases with flexion angle. At the respective insertion sites, each bundle component is reported to occupy approximately 50% of the attachment area, with this separation being relatively consistent between individuals [50,53]. The AM inserts posteriorly and superiorly at the femur and medially at the tibia, while the PL inserts anteriorly and inferiorly into the femur and laterally into the tibia [53]. Functional delineation of the these bundles arises through their observed reciprocal tensioning pattern during passive flexion-extension of the knee joint, with the longer AM (29 mm – 35 mm) observed to be more taut in flexion and the PL (18 mm- 26 mm) in extension [23,33,39,42,47,53–56]. Others have posited the ligament comprises more bundles [53,57–59]. However, it is unlikely that these supposed anatomical distinctions are functionally discrete. There is evidence of a series of near isometric bands that runs along the length of the ACL, being taut at all flexion angles [33,56,60]. Precise understanding of the mechanical relevance of such fibers, however, remains unclear. Methods to elucidate this and other features of the deformation and failure response of the ACL have been developed by the experimental mechanics community, and their application to ACL mechanics has lagged behind.

The ACL is clearly geometrically complex. It is structurally unique among the ligaments and tendons of the body. Commonly utilized replacement graft tissues, therefore, such as the patellar tendon (PT) and the semitendinosus tendon alone or in conjunction with the gracilis tendon - often referred to clinically as the hamstring tendon(s) (HT), may not successfully replicate this structure. A double-bundle geometry is achieved if the HT graft is comprised of both the semitendinosus and gracilis tendons, which may more effectively replicate native ACL structure. Of course, restoring ACL structure is secondary to recapturing the pre-injury biomechanics of the knee. The argument can be made, however, for the need to similarly match the structural uniqueness of the ACL in order to achieve native function over the entire range of knee motion. Mechanical properties of the native and graft tissues and structural properties of normal and reconstructed (ACLr) knees are both important to the question of whether biomechanics have been altered in the ACLr knee [5,61,62]. This outcome is particularly important considering modified joint mechanics post-surgery are posited to incur debilitative mismatches between the joint contact profile and underlying articular cartilage mechanics [10,63]. With this fact in mind, a detailed description of the ACL's role in controlling and/or limiting explicit joint motions is critical to optimizing the ligament reconstruction process, both in terms of graft design and fixation. If ACL-constrained motions can be accurately quantified, then it is feasible that graft tissues can be mechanically optimized to replicate these motions, independent of structural consistencies.

1.3 Native ACL function

Many methods exist for experimentally characterizing either the response of the ACL as the entire knee joint or limb is articulated, or the tissue level properties of the ACL itself. The former type of testing assesses the functional performance of the ACL structure while measuring *in situ* forces and displacements, often in clinically relevant loading situations [64]. As the ACL is often not the only tissue deforming in the knee joint in these types of experiments, however, the applied loads on the ACL itself cannot be determined. ACL strains and strain rates during these structural tests may be measured via various contact or non-contact methods, which, in some instances may require the removal of other soft tissues. Care must be taken here as the ACL is often not undergoing a well-defined strain state and the strains are not necessarily uniform, although both assumptions have oftentimes been made [49,51,52,65]. Structural tests provide clinically relevant information about ACL failure conditions, and can be extremely useful when coupled with a computational framework to validate constitutive models of the ACL alone or as part of larger knee structure. Historically however, these experiments often failed to report geometric data such as the length and cross-sectional area of the ACL [66–69]. Such omissions obfuscate attempts to compare results from one structural experiment to another and to develop geometrically relevant simulation models. The majority of experiments characterizing ACL behaviors have focused on its role in stabilizing the knee joint, rather than on its mechanical properties. With successful reconstruction of the ACL injured knee requiring a graft that can successfully replicate the ligament’s functional role, this bias is intuitive. Extensive research efforts, for example, have been undertaken to define the ACL’s role in restraining 3D knee motions and to thus understand the types of movements that place it at risk for rupture.

1.3.1 The role of the ACL in knee translation

The role of the ACL in restraining anterior tibial translation (ATT) has been the most thoroughly investigated and thus the most clearly defined [24,55,70–76]. There is general consensus that the ACL is the primary restraint to ATT under application of an anterior force [70,73,77]. Through the nature of its attachments, the ACL is oriented primarily in the sagittal plane [34,40]. Anterior translation of the tibia therefore, necessarily moves the attachments further apart, causing fibers to become taut and restrain the motion. There is no other passive knee joint structure that has an equally ideal orientation to restrict anterior tibial motion. As a result, a sagittal plane loading mechanism has long been viewed to drive the resultant ACL injury mechanism [27,78].

Noyes et al. 1976 sequentially sectioned knee joint structures to determine their relative contributions to restraining knee motion and reported that for 5 mm of ATT with the knee in 30° flexion, the ACL carried 87% of the load [77]. Piziali et al. 1980 similarly examined the contribution of the ACL to restraining anterior loads (500 – 600 N) in cadaveric knees, reporting similar results (73% and 87%) [76]. Both Fukubayashi et al. 1982 and Markolf et al. 1976 found that isolated removal of the ACL produced more than twice the amount of anterior tibial displacement measured prior to sectioning

[72,73]. Butler and associates 1980, reported similar findings, but noted that the degree of displacement measured depended on the order of ligament cutting, reflecting the often complex ligament interactions that act to restrain knee motion [70]. Marans et al. 1989, using an externally fixed 6-degree of freedom electrogoniometer, observed significant increases in *in vivo* ATT as a result of ACL deficiency. Despite agreement with cadaveric observations, the accuracy with which translations of such small magnitudes can be accurately measured *in vivo* should be questioned [79–84]. Regardless, the ACL's role as a primary restraint in the sagittal plane is well established.

The role of the ACL in controlling medial-lateral tibial movement has been afforded far less attention. Early investigations, such as those conducted by Brantigan and Voshel 1941, claimed that medial-lateral knee translation was prevented purely by contact between the articulating bones of the joint [85]. Piziali et al. 1980, however, demonstrated that large medial loads (660 – 690 N) applied to the tibia stretch the ACL, while laterally applied loads are restrained primarily by the PCL and LCL [76]. Marans et al. 1989 found that ACL deficiency did not affect medial-lateral tibial translations *in vivo* during walking [25]. The ability to accurately measure knee joint translations externally, however, has been called into question by some of these investigators themselves [25]. Regardless, with the ACL injury mechanism increasingly posited to manifest by a combined 3D loading mechanism [30–32], accurately defining the ACL's role in constraining/controlling medial-lateral knee motions remains critical.

1.3.2 The role of the ACL in knee rotation

The exact role of the ACL in controlling/limiting axial tibial rotation appears to be unclear, with descriptions of its function ranging from almost non-existent, to one of extreme importance. Lane et al. 1994, attempting to simulate vertical stance in fresh human cadaveric knee joints, reported that the ACL had a limited effect in controlling tibial rotation, with rotational instability not a major factor after isolated ACL sectioning [86]. Reuben and associates 1989 observed similar results *in vitro*, with ACL sectioning producing anterior but not rotational instabilities [87]. Others however, viewed the ACL as a fine-tuning mechanism, guiding and controlling tibial rotations under external load application. Fukubayashi et al. 1982 for example, observed significant changes in tibial rotation patterns in ACL sectioned cadavers under anterior-posterior loading (100 N to 125 N) [72]. Anderson and Dyhre-Poulson 1997 similarly found that sectioning the ACL produced significant increases in axial rotation magnitudes under externally applied (6 N-m to 14 N-m) internal-external tibial torques [88].

In the past, the ACL has been viewed to play a secondary role in restraining internal tibial rotation, acting in conjunction with medial and lateral compartmental structures [73,89–93]. Lipke et al. 1981 for example, applied compressive and torsional loads to cadaveric knees and observed increased internal tibial rotation with isolated ACL sectioning, which became significantly greater with additional sectioning of the LCL and posterolateral corner structures (fibular (lateral) collateral ligament, popliteus tendon, and popliteofibular ligament) [89]. Wroble and associates 1993, similarly found that removal of these same structures increased resultant cadaveric knee external tibial rotation and abduction magnitudes in both flexed and extended postures [94].

Discrepancies in the precise rotation response (internal versus external) likely stemmed from concomitant differences in the overarching load application protocols. However, more recently Wojtys et al. 2016 discussed relative ACL strains under a dynamic jump landing. This study found that internal tibial rotation, combined with a knee flexion moment and knee impulsive compression, as well as large trans-knee forces, manifested the largest relative ACL strains [95]. This study points to a more critical role played by internal tibial rotation on ACL strains; especially in worst-case scenarios for dynamic pivot jump landings. Beaulieu et al. 2013 investigated the effect of constraining internal femoral rotation during dynamic loading in a study of male and female knees. While sex was not found to be a significant factor in the prediction of ACL failure, knees with constrained ranges of motion had a chance of failure 8.3 times that of unconstrained knees [96].

The ACL's role in restraining knee adduction-abduction rotations has similarly been viewed as secondary [58,73,93,94,97,98]. Both Grood et al. (1981, 1988) and Markolf et al. 1976 for example, found the ACL to be a secondary restraint to knee abduction - adduction with the knee in full knee extension [73]. Hollis and associates 1991 additionally observed increases in ACL length under abduction load application with increased knee flexion angle [58]. Direct comparison among these investigations is confounded, however, by differences in the applied joint constraints. This has likely also contributed to discrepancies regarding the ACL's role in knee rotational control, since variations in pre-test joint constraint will necessarily impact the resultant load-induced movement response. Examining the ligament response with the knee unconstrained to move freely in response to the external load application (Hollis et al. 1991), for example, eliminates the concern of unknown constraint forces and moments. It does, however, necessarily require accurate 6 DoF kinematic measures. Understanding precisely how knee motion impacts resultant ACL response under well-defined load states appears critical. With this in mind, the next section explores the effects of joint constraints on resultant ACL function in more detail below.

1.3.3 Effects of constraints on ACL function

As noted, a key factor compromising successful comparison of observed *in vitro* ACL responses to external load states is the degree to which knee motion is constrained during the test protocol [23,24,99,100]. Restrictions or constraints placed on the joint can have a significant impact on the amount of movement possible for each of the remaining unconstrained degrees of freedom [55,99,101,102]. Such constraints, while assisting in determining the ACL's role in controlling explicit joint motions, have limited relevance to *in vivo* joint motions and resultant passive tissue behaviors. Takai et al. 1993 found that with all but one DoF constrained, the ACL provided 82% - 90% of the total anterior restraint between 0°- 90° knee flexion. When the test was replicated for an unconstrained (5 DoF) joint condition, however, the ACL only provided 74% - 83% of the anterior restraint [55]. Inoue et al. 1987 similarly found that limiting knee motion to three degrees of freedom (varus-valgus, proximal-distal and medial-lateral) resulted in the MCL being the major restraint to knee abduction. When five degrees of freedom were allowed however, abduction was restrained primarily by the ACL. Specifically, sectioning the ACL for the unconstrained case produced a 123% increase in knee abduction compared to the ACL-intact state [99]. The coupled anterior tibial displacement and internal tibial rotation presenting with valgus rotation (i.e. pivot shift) [24,103], likely alters the relative ACL attachment locations, its resultant orientation and its instantaneous axis of rotation [57] such that it becomes taut in abduction. Such outcomes highlight the likely critical need to not only replicate the native ACL's structural and mechanical properties during the reconstruction process, but also its position and orientation. Further, data necessary to successfully drive this process should be obtained under conditions when overarching knee motions remain unconstrained, more effectively reflecting the joint and resultant ligament response.

Multiple degree of freedom testing apparatus involving combined robotics technology and universal force sensors have been successfully developed with the above goal in mind [101,102,104–106]. Using this same approach, *in situ* ACL loads in combined low magnitude 3D load states have also been quantified [64,107,108]. By enabling predetermined motion pathways to be replicated with high precision, such efforts have been vital in understanding ACL load responses to clinically relevant knee displacements. By adopting the superposition principle, these methods rely on relative bone positions being identical before and after ACL sectioning [106]. Superposition holds for linear viscoelastic materials [109], but if any of the loaded soft tissue components of the knee are viscoelastically non-linear, the superposition assumption breaks down. Moreover, for more dynamic high impact loading conditions, increased stiffness in the viscoelastic joint structures due to higher load rates may render such calculations more sensitive to joint position errors. Thus, while this approach may be accurate for quasi-static or low (e.g. clinical) load rate scenarios [64,107], accuracy will be compromised under more dynamic states consistent with injury causing events.

1.3.4 Dynamic knee loading models

To address the above concerns, recent efforts have assessed ACL mechanical behaviors under more realistic dynamic movement scenarios. As noted, relations between 3D knee mechanics and resultant ACL loading have been examined extensively *in vitro* under relatively low, clinically relevant load states [106,107,110,111]. Such models can present with similar benefit, however, when assessing specific injury scenarios [78], which is not feasible for *in vivo* human experimentation. This information is not only critical to elucidating injury causality, but also significantly enhances prevention efforts that rely on reducing impact-induced ACL strain magnitudes [112]. Cadaveric models have recently been used with this direct intent, where ACL responses under isolated [78], combined [112], and impact-induced external loads [113,114] have been examined, providing some of the highest ACL strain rate data available (~5/s, or equivalently, 500%/s). Comprehensive methods capable of simulating 3D knee joint dynamics associated with high-risk single limb impacts represent the current state of the art in this area [114]. With these models, the effects of specific muscle activation strategies [115], 3D joint load combinations [31,116], and joint geometric configurations [117,118] on ACL strains and resultant injury risk have been explored. Other, equally complex models have begun to emerge, providing important new insights into the destructive versus protective role of overarching muscle activation strategies synonymous with high-risk movements [119,120]. Few of these models, however, induce actual injuries [121], failing to capture the necessary joint load magnitudes and associated ligament strain rates necessary to compromise tissue integrity. Enhanced determination of ACL mechanics in response to more extreme knee joint and ligament loading scenarios thus seems critical to elucidating ACL injury mechanisms. This may be equally critical for determining optimal replacement tissues moving forward. Further, the recent suggestion of a tissue fatiguing-induced injury mechanism [121], whereby multiple sub-failure loads may ultimately contribute to tissue compromise, appears novel and worthy of further exploration, particularly within similar experimental frameworks.

There is growing consensus that the ACL injury mechanism is multifactorial, arising through a combination of morphologic, mechanical, strength, and neuromuscular factors [30]. While cadaveric modeling efforts have contributed greatly to our evolving understanding of knee and associated ACL loading behaviors in naturalistic settings, their ability to truly characterize the *in vivo* 3D joint neuromechanical response is limited. Further, associated ACL force/strain estimates are typically derived from sensors attached directly to isolated portions of the ligament, which cannot obtain a zero strain state and fail to adequately capture both the true nature of the strain state and the heterogeneous 3D ligament response. To address these concerns, computational models have recently been developed to quantify knee joint and/or resultant ACL loading during complex and highly dynamic movement scenarios [122–125]. Models of this type enable explicit load outcomes to be examined in detail, during normal and injury causing events, while controlling all aspects of the overarching neuromuscular control pattern [122]. Recent surrogate modeling methods extend this concept, coupling forward dynamic and structurally relevant tissue deformation models [126] and could be highly beneficial in our understanding of the complex 3D ACL and graft replacement tissue mechanical response. Computational model success, however, is often compromised by an inability to validate predicted responses against the true *in vivo* state [30]. Recent experimental advances with the potential for characterizing ACL loading during highly dynamic movement tasks *in vivo* [127–130] may assist in this process.

1.4 Biomechanical properties of the native ACL

Characterization of the biomechanical properties of the ACL requires isolating the ACL as the only load-bearing structure spanning the femur and tibia, and designing gripping and loading geometries that provide well-characterized deformation states. With such an approach the stresses, strains, and strain rates acting on the ACL may be experimentally collected in a straightforward manner and used to determine underlying material properties. Obtaining well-characterized load and displacement boundary conditions in soft tissue structures is often quite challenging, and it is also imperative that the tissue is tested from an initially unloaded configuration. Additional assumptions of linearity vs. non-linearity, elasticity vs. viscoelasticity, homogeneity vs. heterogeneity, and isotropy vs. anisotropy must be experimentally probed in order to completely characterize the tissue response. Moreover, anisotropic tissues such as the ACL usually require characterization in more than one strain state, e.g. uniaxial tension and shear, but the geometric realities of the ACL limit the accessible strain states. These critical factors should be considered when interpreting previous efforts (below) attempting to characterize ACL material properties under a variety of explicit loading conditions.

1.4.1 Elastic properties of the ACL

The response of the ACL to axial deformation is non-linear. Elastic properties of the ACL are often measured by deforming the tissue at constant displacement rate or constant strain rate until failure, noting the load and displacement at failure, converting the raw load vs. displacement data to stress and strain, and reporting properties such as the tangent modulus at a given strain level, the ultimate (peak) strength, and the failure strain. As a viscoelastic tissue, these properties are directly sensitive to the applied strain rate and thus comparisons among studies require reporting of strain rates of loading. In particular the tangent modulus will increase with increased strain rate, whereas the failure strain will decrease.

Essentially it is strain that determines the risk of ligament injury [48,131,132] and hence, this parameter has been central to investigations examining potential ACL injury mechanisms. There has been a great deal of work investigating the ultimate strain or strain to failure of the ACL under uniaxial tensile loads [49,71,77,133–135]. However, there is a paucity of tensile data providing the critical strain magnitudes at strain rates associated with ACL injury risk; typical test methods used are limited to strain rates of about 1/s whereas injury rates may exceed 4/s [114]. This limitation is typically governed by the inherent difficulty in developing a testing apparatus that can quantify mechanical behaviors at physiologic strain rates. Further, dynamic load simulators that can replicate such conditions [31,32] are necessarily unable to examine strain responses in a repeatable and systematic fashion. Future efforts into examining ACL mechanical properties at higher, more naturalistic loading rates, thus appear well justified.

The results stemming from the existing research, while providing significant insights into the non-linear ACL strain response, are far from conclusive. Noyes and Grood 1976 reported ACL failure strains at a strain rate of 1.0/s in old (48 - 86 years) and young (16 - 26 years) human femur-ACL-tibia complex (FATC) specimens of 0.485 ± 0.119 and 0.602 ± 0.068 respectively [77]. Chandrashekar et al. also using FATC specimens, reported ACL failure strains of 0.30 ± 0.06 for males and 0.27 ± 0.08 for females at 1.0/s [134]. Kennedy et al. 1976 reported strain values at damage onset of 0.23 ± 0.02 at low (2 mm/s) and 0.28 ± 0.03 at high (8 mm/s) displacement rates [135]. Given an approximate ACL length of 34 mm [34], these displacement rates correspond to strain rates on the order of 0.06/s and 0.25/s, respectively. In the Kennedy et al. study, the testing device was clamped directly to ligamentous tissue making direct comparison between it and the other studies difficult. It has been reported, for example, that gripping any collagenous tissue can produce premature failure in the fibers and/or slippage in the grips, resulting in either a lower (failure) or higher (slippage) strain response [71]. In work that followed Noyes and Grood 1976, Noyes et al. reported failure strains for several soft tissues using two displacement measurements – the grip-to-grip displacement and the direct tissue level displacements (the latter via the application of fiduciary markers on the tissues) and showed that grip-to-grip measurements exceeded actual tissue level strains by more than a factor of two [136]. Testing the bone-ligament-bone complex also presents complications however, as ligament length is not always easy to define and the strains along the specimen are not uniform under tension, especially at the ligament-bone interface [132,137]. In particular it has been shown previously that ACL bundle femoral insertion location has a significant effect on strain measurement [59,138,139]. Some authors have taken this into consideration, conducting bone-ligament-bone tests in a series of relative orientations [59,140–142]. This approach has not yet been used to determine ultimate strains in the ACL however.

Table 1.1: Mechanical properties of native human ACL and common replacement graft tissues: patellar tendon (PT) and hamstrings tendon (HT). [1]

Authors	Strain Rate (/s)	Failure Strain	Initial Modulus (MPa)	Tangent Modulus (MPa)	Tensile Strength (MPa)	Notes
Chandrashekar et al.	1.0	0.30 ± 0.06	-	128 ± 35	-	ACL, male
		0.27 ± 0.08	-	99 ± 50	-	ACL, female
Hashemi et al, Chandrashekar et al.	1.0	0.18 ± 0.03	103 ± 64	479 ± 141	-	PT, male
		0.18 ± 0.04	140 ± 75	490 ± 131	-	PT, female
Donahue et al.	0.02	0.088	-	904	66	HT, without co sexes

In addition to failure strain, other ACL elastic properties of interest are its tensile strength and tangent modulus, the latter computed as the terminal slope of the nominal stress (load divided by initial cross-sectional area) vs. nominal strain (change in length between two points divided by initial separation) response curve. Here again, the results are not conclusive. Noyes and co-workers for example reported the tensile strength of the ACL at 1/s as 38 ± 9 MPa whereas Chandrashekar et al. also at 1/s, found 26 ± 10 MPa for males and 23 ± 9 MPa for females [77,134,136]. Noyes and co-workers did not report tangent moduli but did provide data from which values of 110 ± 15 MPa (young) and 62 ± 7 (old) may be calculated (geometric stiffness, 182 ± 56 kN/m; length, 26.9 ± 1.5 mm; cross-sectional area, 44.4 ± 10.0 mm^2 (young), 129 ± 39 kN/m; length, 27.5 ± 2.8 mm; cross-sectional area, 57.5 ± 16.2 mm^2 (old) [136]. Chandrashekar et al. found tangent moduli of 128 ± 35 MPa for males and 99 ± 50 MPa for females (see **Table 1.1)** [134].

The tangent modulus depends on strain and is therefore sensitive to discrepancies associated with the method of strain measurement and uncertainties in strain determination as discussed above. The tangent modulus at a given strain level is also sensitive to the strain rate of loading in the viscoelastic ACL. Thus it is imperative that the community adopts e.g. optical tracking methods for accurately determining and reporting tissue level strains and strain

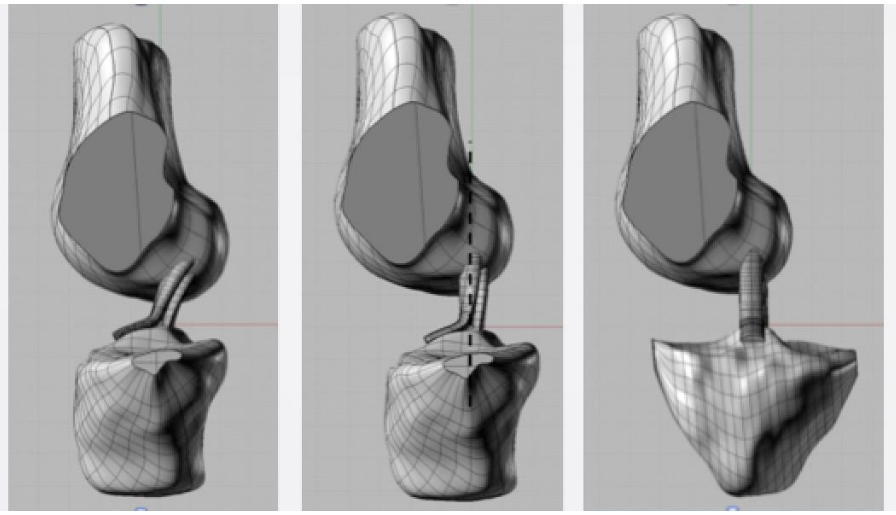

Figure 1.2: For uniaxial ACL loading, the fully extended knee in the anatomical position (**left**) undergoes a posterior and lateral translation of the tibia relative to the femur (**center**) followed by a 90° internal rotation of the tibia (**right**) [65]**.** [1]

rates that do not carry the inherent inaccuracies associated with grip-to-grip measurements.

1.4.2 Elastic properties of the ACL bundles

As discussed earlier, it is not possible to untwist and align the intact ACL from femur to tibia. Nor is the anatomical orientation conducive to material property determination. **Figure 1.2** illustrates a sequence of motions of the tibia relative to the femur applied to orient the ACL uniaxially. At full knee extension the tibia is posteriorly and laterally translated (**Figure 1.2, left** to **1.2, center**) then internally rotated approximately 90° to untwist the bundles (**Figure 1.2, center** to **1.2, right**).

Although the two bundles of the ACL are aligned with the load axis of a test apparatus in this orientation, owing to their mismatched lengths, there is no flexion or abduction/adduction angle at which both bundles are in unloaded and unslackened configurations. Butler et al.

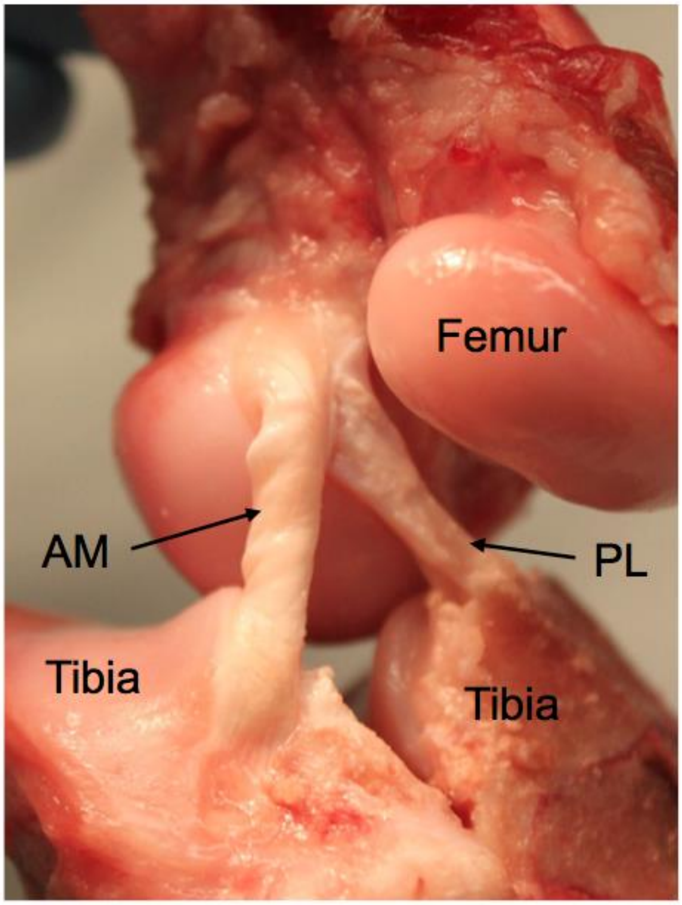

Figure 1.3: AM separated from the PL via a transection of the tibia at their natural separation.

recognized this when separating the ACL into bundles at the femoral insertion [49,51,133]. In each knee specimen they preserved only one of the bundles for testing. Butler et al. 1992 separated ACLs from seven young (21-30 years) human donors into three discrete bundles (with nomenclature of anteromedial (AMB), anterolateral (ALB) and posterolateral (PLB)), and reported varying maximum strain values for each. At a strain rate of 1.0/s, the AMB resisted the greatest elongation prior to disruption, failing at 0.191 ± 0.028. The ALB and the PLB failed at 0.161 ± 0.039 and 0.152 ± 0.052 respectively. The bundle divisions adopted by Butler et al. 1992 do not correspond to those that have been commonly defined, however this is one of the few works that has studied the mechanical properties of the individual bundles as opposed to the entire ACL [48,50,53]. Other investigators similarly separated the ACL, albeit into two bundles, in these instances removing either the AMB or the PLB, for functional testing of the remaining bundle [53,106,107,143–145]. Understanding the mechanical response of the ACL bundles goes beyond reporting strains and stresses at failure. The entire response curve to imposed deformation is needed to describe and fully characterize the non-linear viscoelastic response. Ma 2012 demonstrated that the AM and PL may be separated by cutting the tibia along the plane that intersects the delineation between the AM and PL tibial insertions

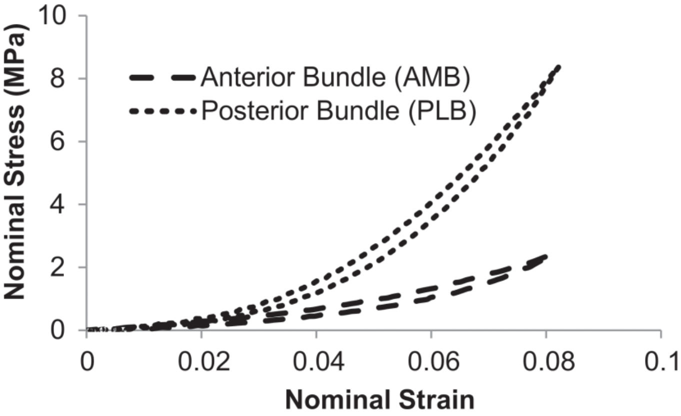

Figure 1.4: Load-unload responses of ovine AM and PL. This is representative data from a study of bundles from 6 ovine knees. [1]

[65]. With both bundles attached at the femoral insertion, the AM was retracted for PL testing and then the PL retracted for AM testing of both bundles from the same knee. **Figure 1.3** illustrates the separated bundles prior to individual uniaxial tension loading. The bundles were tested via load-unload, and not strained to failure, to elucidate viscous effects. Typical results from 6 ovine knees are shown in **Figure 1.4**. The data are plotted as nominal stress vs. nominal strain. The data in **Figure 1.4** illustrate heterogeneity in the mechanical properties of the two bundles, non-linearity of the response with an initial toe region” and the small, but important viscous effects manifest as the difference between the loading and unloading paths. The terminal slope of the loading path is the tangent modulus. It is from this maximum slope of the stress vs. strain response curve at a strain of 0.07 that the tangent modulus of each bundle is determined as 105 ± 67 MPa for the AM and 210 ± 58 MPa for the PL. Such isolated testing of the individual AM and PL reveals that the differences in the mechanical responses of these two ACL structures extend beyond strain to failure, as the stress vs. strain response curves diverge at small strains. It is clear from the literature examining the ACL bundles individually that treating the ACL as a homogeneous material with uniform mechanical properties in analytical and computational models is inaccurate. Moreover the ability to design replacement tissue requires more than end point measures (e.g. strength) but knowledge of the entire response path to failure. As will be seen in the next section, characterization of the viscous response has also historically lacked the reporting of critical data.

1.4.3 Viscoelastic properties of the ACL

As a viscoelastic structure, the ACL demonstrates specific properties that significantly influence its role in stabilizing the knee against daily, often high-rate loading phenomena. Accurate characterization of these properties is particularly important in designing graft replacement tissues, since compromised stabilization in reconstructed joints is most evident for dynamic scenarios in which viscoelastic behaviors prevail [5]. Limitations of tissue availability and specimen-to-specimen variability have generally motivated investigators to maximize the number of characterization experiments conducted on one specimen. The goal in most instances, therefore, has been to probe the entire physiologically relevant viscoelastic strain range with each loading excursion, without damaging the tissue. This can be problematic in viscoelastic materials; care must be taken to insure each subsequent test is not influenced by the past history of loading, i.e. linearity of response must be maintained, and the tissue must fully relax after each load excursion before the next is applied [109]. Usual practice is to randomize the order in which the suite of tests is conducted for each specimen to minimize biased results in the event of non-linear effects. Beynnon et al. found the AM bundle of the ACL strains up to 0.05 in a variety of weightbearing and non-weightbearing knee flexion and extension activities [146–149]. This peak magnitude, being consistent with that measured *in vivo* for landing maneuvers [127], is well below that reported necessary to compromise tissue integrity [51,71]. **Figure 1.4** demonstrates that at a strain of 0.05 the response curves of the ACL bundles are well within their toe regions. If this strain level is assumed to be the approximate limit of the normal physiological response, it might therefore be expected that the viscoelastic response probed within this range will be highly non-linear.

The viscoelastic properties of the ACL have been quantified by investigating either its strain rate dependent response to uniaxial loading or its uniaxial stress relaxation and/or creep responses. Data on human tissue are extremely limited; therefore some of what is presented below to illustrate viscoelastic phenomena is derived from studies utilizing animal models or other human connective tissue structures.

Stress relaxation

Stress relaxation tests are ideally conducted by deforming the tissue as rapidly as possible to a pre-determined strain level, holding the deformation constant, and monitoring the time dependent stress response until it ceases to evolve. Kwan et al. 1993 investigated the viscoelastic properties of the AM bundle of porcine ACL by straining specimens to a strain of 0.05 at a strain rate of 0.03/s and holding it at that strain level for 3,600 s [145]. They found a reduction in stress of 50% between the peak and minimum values. In addition, the stress relaxation was not linear with logarithmic time, indicating it was not describable by a single exponential relaxation function [109]. The peak stress and final stress values were not reported, making it difficult to compare with other studies. Yamamoto et al. 1999 studied the mechanical properties of bulk rabbit patellar tendon and individual collagen fascicles [150]. They performed stress relaxation experiments by deforming to a strain of 0.02 at a strain rate of 0.02/s and holding at constant strain for 350 seconds. The resulting initial stress of approximately 7 MPa also relaxed by about 50% over the time interval tested. Other investigators have sought to compare the stress relaxation responses of various tissues by deforming to pre-determined stress levels. For example, Johnson et al. 1994 studied the viscoelastic nature of the patellar tendon in young (29-50) and old (64-93) populations [151]. They strained the tissues in each instance to initial stresses of 1 and 4 MPa, and held the strain constant for 900 seconds. Tendons from the older population stress relaxed to 50% of the initial value, whereas the younger tendon group stress relaxed to 55% of the initial value [151].

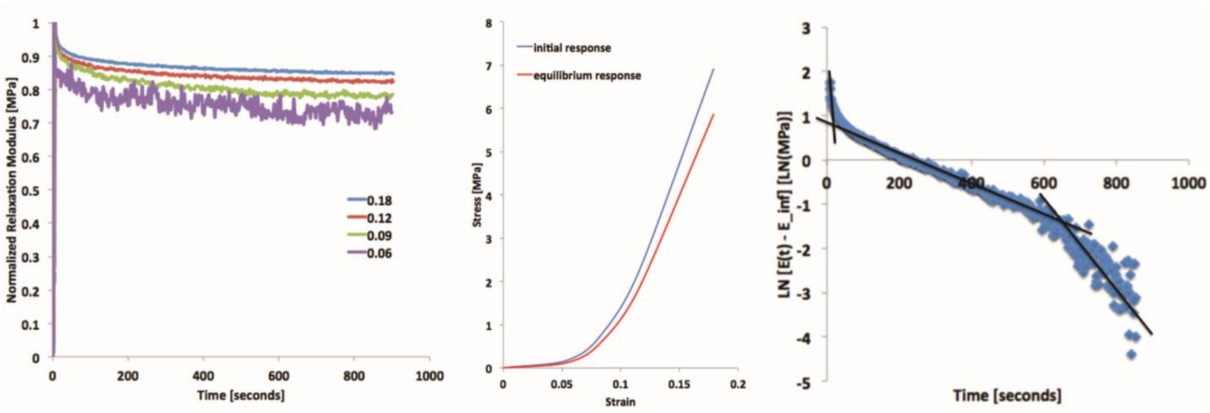

Figure 1.5: Viscoelastic response of a human AM. Non-linear stress relaxation experiments from various initial strain levels (**left**). The initial and equilibrium (elastic) responses from the initial and final stress vs. strain pairs in the stress relaxation experiments (**center**). Relaxation modulus function at 0.18 strain plotted on a logarithmic scale to demonstrate its three distinct relaxation regions (**right**) [65]. [1]

The majority of studies in the literature report the initial and final stress levels, but not the entire stress relaxation response curves. The latter are important for characterizing the viscoelastic response of the ACL and for developing accurate analytical models that can be incorporated into simulation tools of ACL and entire knee mechanics. An example of the data required appears in **Figure 1.5** for the AM of a human knee. When isolated from the PL and tested under uniaxial stress relaxation conditions the AM exhibits non-linear stress relaxation as evidenced by the lack of superposition of the normalized relaxation modulus function response – the time dependent stress response divided by the constant strain input – for various initial strain levels (**Figure 1.5, left**). Additionally, substantial nonlinearity is manifest in the equilibrium elastic response, determined from the endpoints of the stress relaxation response functions for each initial stress – strain pair (**Figure 1.5, center**). The initial loading response of the AM at 0.025/s, which is also highly non-linear, is also represented in **Figure 1.5 (center)**. **Figure 1.5 (right)** demonstrates that the AM stress relaxation response at an initial strain of 0.18 contains three characteristic relaxation times. Previously, Ma 2012 examined the stress relaxation response of the AM and PL of sheep and similarly found the AM to be non-linear in both its elastic and viscous responses whereas the PL was elastically non-linear but linearly viscous [65]. Moreover the sheep bundles each had two characteristic relaxation times, in contrast to the human bundles.

The relaxation response of the data in **Figure 1.5 (right)** may be represented as follows,

$$E_R(t) = E_{inf} + E_1 e^{\left(\frac{-t}{\tau_1}\right)} + E_2 e^{\left(\frac{-t}{\tau_2}\right)} + E_3 e^{\left(\frac{-t}{\tau_3}\right)} \quad (1)$$

where E_{inf} is the equilibrium modulus and the exponential terms contain the characteristic moduli (E_i, i=1,2,3) and characteristic times (τ_i, i=1,2,3). At times $t \gg \tau_1, \tau_2$ the pair τ_3, E_3 may be found from

$$ln\left(E_R(t) - E_{inf}\right) \cong lnE_3 - \frac{t}{\tau_3} \quad (2)$$

using the slope and intercept of the best line fit through the data in **Figure 1.5 (right)** at long times. Once these parameters are determined, the other parameters may be found in pairs by assuming $\tau_3 \gg t \gg \tau_1$ to find τ_2 and E_2, followed by assuming $t \ll \tau_2, \tau_3$ to find τ_1 and E_1.

Reporting only the initial and final stress levels is insufficient for characterizing the viscous response. Very little data exist in the literature to support or refute the results in **Figure 1.5** and therefore there is no acceptance of whether the ACL bundles are linear viscoelastic structures, what their equilibrium stress vs. strain response functions are, and how many viscoelastic parameters are needed to characterize them. An improved understanding of the detailed viscoelastic response of the ACL is important in developing modeling tools that can be predictive of ACL mechanics, and, as will be discussed in the next paragraph, in reconciling creep vs. stress relaxation responses.

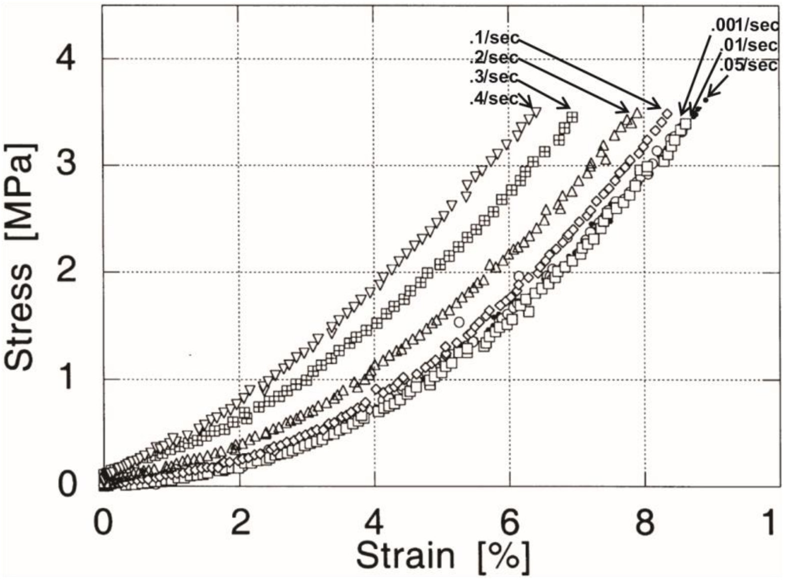

Figure 1.6: The strain rate dependent uniaxial loading response of bovine ACL, adapted from Pioletti et al. 1999 [153]. [1]

Creep

Creep tests monitor the time dependent deformation response to a fixed stress level. Creep data for the ACL are less prevalent in the literature than stress relaxation data. One study that examined both creep and stress relaxation is due to Thornton et al. 1997, which examined creep and stress relaxation in the same tissue, in this case rabbit MCL [152]. Creep and stress relaxation specimens were both initially loaded to 14 MPa. The stress (load) was held constant in creep, and the displacement (strain) in stress relaxation, for 1,200 seconds. Thornton et al. found a 14% decrease in stress over the relaxation period and a 65% increase in strain during creep over the same amount of time, highlighting the non-linearity that results in differences between the characteristic creep and stress relaxation times. Again, very little creep data exist that would allow one to determine if the response is linear or non-linear, to e.g. model the response such that the creep response could be predicted from the stress relaxation response, and to design replacement ACL materials and structures that replicate the native viscous response. The data needed are the entire response curves in creep, not just the beginning and ending strain levels.

Strain rate dependent response

The lack of data characterizing human (or animal) ACL tissue at strain rates commensurate with injury risk is a critical problem. According to the data in Withrow et al. 2006, conditions during non-contact ACL injury exceed strains of approximately 0.05 at strain rates of 4/s [114]. Studies detailing the effect of strain rate on ACL mechanical properties are helpful, although as mentioned previously, such data in the literature often test the same tissue over multiple rates, therefore they rarely contain failure strain information. In one comprehensive examination of rate effects, Pioletti et al. 1999 investigated bovine ACL over a broad range of strain rates (0.001, 0.01, 0.05, 0.10, 0.20, 0.30, and 0.40/s) up to 300 N load [153]. They found that the stress response to a strain of 0.04 (4%) increased by a factor of three from the lowest to highest strain rates. The data in **Figure 1.6**, adapted from Pioletti et al. 1999, demonstrate the strain rate effect over the entirety of the strain region examined. Although none of these tests was taken to failure it is evident from the trend that the failure strain decreases markedly with strain rate, highlighting the need for more information on the strain to failure response of the ACL at the high strain rates associated with injury, strain rates that are at least an order of magnitude higher than the highest strain rate response shown in **Figure 1.6**. Methods to control the strain rates of loading beyond about 1/s are rare, however impact and blast loading experiments in which the strain rate history of the loading is collected during testing would significantly reduce the knowledge gap in failure strengths and strains at high strain rates.

1.4.4 Effects of pre-conditioning

Experiments on ligaments often incorporate a pre-conditioning phase prior to actual data collection [70,71]. Pre-conditioning is the application of cyclic loading and unloading during which the response curve of a viscoelastic material softens and eventually stabilizes. **Figure 1.7** illustrates the initial loading-unloading excursion (red) and the stabilized (pre-conditioned) response (blue) of a hypothetical viscoelastic tissue that undergoes softening during pre-conditioning. The black dashed line indicates the equilibrium response achieved if the tissue were to be loaded at a strain rate that is not only slower than the strain rate used to pre-condition, but also much slower than any relaxation rate associated with the tissue. Softening experienced during pre-conditioning without damage is the result of accumulated effects of the previous history of loading when the strain rate is on the order of the relaxation processes occurring within [109]. For this reason pre-conditioning probes the long-term or equilibrium (elastic) response of the material, and does so at a strain rate that is faster than the equilibrium response strain rate, rather than the response of the tissue to the strain rate actually used during pre-conditioning and data collection. The practice of pre-conditioning is not universal in ACL experiments [154–158], contributing to discrepancies among various studies.

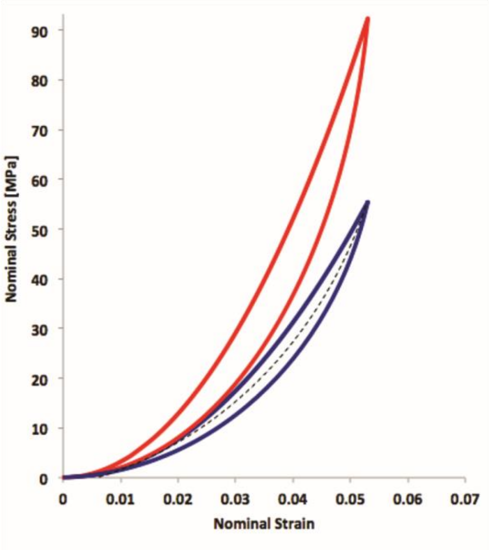

Figure 1.7: The initial (red) and stress-softened via pre-conditioning (blue) load-unload response of a hypothetical viscoelastic tissue. The equilibrium response of this tissue is illustrated by the black dashed line. [1]

1.4.5 Effects of sex

Sex-based differences in ACL injury rates are well established, with females suffering sports related injuries 2-7 times more frequently than males in comparable sports [4,159] (males demonstrate higher frequencies of ACL injuries overall). This disparity rises to 10/1 for women vs. men in military training [160–165]. While neuromuscular factors are commonly viewed to drive this disparity [166–168], explicit ACL structural and/or mechanical indices may play an equally important role. Sex differences exist in a number of inherently non-modifiable ACL factors. Females have ACLs of smaller length, cross-sectional area and volume [169–172]. Even after accounting for these relative size differences, female ACLs demonstrate structural and mechanical characteristics that make them inherently different from male ACLs. Chandrashekar et al. 2005, for example, found that female cadaveric ACLs possess significantly lower load at failure (1266 ± 527 N), stiffness (199 ± 88 N/mm) and modulus of elasticity (99 ± 50 MPa) magnitudes compared to male ACLs (1818 ± 699 N, 308 ± 89 N/mm, 128 ± 35 MPa) [170]. The two structural characteristics (failure load and stiffness) may be attributable to differences in female vs. male ACL size. The modulus of elasticity is independent of size; therefore female vs. male differences in moduli reflect differences in material constitution. Sex-dimorphic ligament ultrastructure, particularly fibril number and size, are posited to govern these structural and mechanical differences. Hashemi et al. 2008, found that female ACLs possessed lower fibril concentrations and lower percent area occupied by collagen fibrils compared to male ACLs [173]. Furthermore for the female ACL, stiffness and modulus of elasticity were strongly associated with fibril concentration. For the male ACL, load to failure and ultimate strength were associated with the percentage of ligament area occupied by collagen fibrils. It is unclear and counterintuitive as to why the female presents with structural and mechanical properties that seemingly increase its risk of injury. These differences are often posited to be driven developmentally by the increased presence of sex-specific hormones, which may promote a more lax female ACL [174,175]. Joint function is dictated by multiple structural, mechanical, geometric, strength and neuromuscular factors [4,176]. With this in mind, it is unclear whether tissues used to reconstruct the ruptured ligament should similarly demonstrate sex-specific structural and mechanical characteristics. Chandrashekar et al. 2008 has shown that the PT graft, at least within its non-linear loading range, elicits sex-specific mechanics that are somewhat consistent with that seen for the ACL [177]. The PT, however, is still significantly stiffer geometrically and mechanically than the native ACL regardless of sex, suggesting that neither will adequately promote pre-injury joint motion patterns.

1.4.6 Effects of joint geometry

The knee joint presents as a combination of complex geometries [178,179] that drive an equally complex joint mechanical response [30]. Being largely non-modifiable, these factors are typically ignored in ACL injury risk screening and prevention models [4,167]. Many of these factors, however, are strong predictors of ACL injury, suggesting their consideration is well warranted. This consideration should also be extended to the reconstructive process, where as noted the goal is to restore native ACL knee motions. While not influencing ACL mechanics explicitly, knee joint geometric factors can impact the resultant ligament loading response and its potential to be high risk, either directly or indirectly. A smaller, less round (“A-shaped”) and narrower notch [180,181], for example, demonstrating clear prospective [182] and retrospective [180] injury links, is posited to promote injury via either indirect or direct mechanisms. The first (indirect) mechanism is that a smaller notch corresponds to a smaller ACL that will fail at lower load magnitudes irrespective of any size dependent material properties [172,183,184]. With a smaller notch suggested more common in women than in men [185,186], and females possessing a comparatively smaller [186] and potentially weaker ACL

[118,134,170], this indirect mechanism seems possible. Considering ACL ultrastructure demonstrates significant sex-based divergence [173], however, and relations between sex and notch size are inconclusive [186–189], additional mechanisms may similarly prevail. A second and equally plausible (direct) mechanism, for example, is that a smaller notch promotes ACL injury directly via excessive impingement on a comparatively large ligament [180,190,191], particularly under combined transverse and axial loading [192–194]. The existence of a boney ridge in the anteromedial aspect of an already smaller notch may further exacerbate high-risk ACL impingement loading under similar load states [195]. The underlying rationale for these “notch-driven” injury mechanisms suggests either is viable. It is worth noting, however, that a larger ligament will possess greater comparative load carrying capability [170,173], and may thus be capable of withstanding greater impingement-induced loading when housed within a small notch. Conversely, a smaller and weaker ligament will undergo far less impingement-induced loading when housed within a comparatively large notch. Considering these possibilities, in conjunction with the fact that ACL injury presents for a wide variety of femoral notch-ACL volume combinations [196,197], it appears injury may arise via more complex scenarios.

Several key tibial plateau indices are also directly linked to sex-based ACL injury risk. Individuals previously suffering an ACL injury, for example, particularly females [198,199], demonstrate larger lateral posterior tibial slope angles compared to healthy controls. The combination of a large lateral slope and a shallow medial tibial plateau depth of concavity is viewed to promote an even greater risk of ACL injury in females

[200]. Specifically, a larger lateral slope anteriorly shifts the tibiofemoral contact point under impact-induced compressive loading [61]. In this position, the anterior shear component of the resultant joint reaction force is similarly larger, increasing anterior tibial motions [117,200,201] and ACL strains [37,110]. A shallow medial plateau depth of concavity additionally fails to restrain or catch these large and often rapidly occurring anterior motions, precipitating even greater ligament deformation [200]. Large inter-joint differences between lateral and medial posterior tibial slope angles in females are also posited to elicit high-risk out of plane knee motions with the propensity to injure the ACL [201]. Bojicic et al. 2017 recently found that increases of 1° of posterior tibial slope and lateral middle cartilage slope increased the chances of ACL injury by 12% and 13% respectively [202].

Considering the above findings, understanding the roles that explicit knee geometric factors play in the resultant joint mechanical profile appears critical, both to elucidating injury mechanisms and enhancing ACL reconstructive methods. A graft replacement that is substantially more lax than the native ACL, for example, a common long-term reconstruction outcome [203–205], will be particularly problematic in a knee joint with a large lateral tibial slope. In this instance, the more lax graft will take longer to arrest the rapidly accelerating tibia, resulting in greater and potentially debilitative deviations from the pre-injury articular cartilage contact profile [63]. Similarly, a graft tissue that is too large for the notch within which it is housed may be at a greater risk of impingement driven injury moving forward [192]. Further consideration of individual-specific joint geometric and resultant mechanical factors in the reconstructive process may thus be vital to long-term joint mobility and health. Such considerations seem equally critical for future injury risk screening efforts and associated prevention efforts.

1.5 Replacement graft mechanics

Currently, two types of tissue grafts are most commonly used for ACL replacements, the patellar tendon (PT) and the modulated semitendinosus- gracilis tendon, referred to clinically as simply the hamstrings tendon (HT). Grafts may be autografts or cadaveric allografts. Outcomes for ACL reconstruction using these techniques are limited by graft availability, risk of rejection, and increased morbidity. The region of the graft within the bone tunnel does not fully integrate with native tissue [45,206] and the initial response of the body to grafts is one that results in a lowering of the stiffness of the replacement [207]. Moreover, because the graft may not fully integrate with native tissue within the bone tunnel, the graft may not complete the ligamentization process nor restore the original biomechanics to the knee, even 2-3 years postoperatively [45,206,207]. Common sequelae of ACL injury include articular cartilage degeneration and osteoarthritis (OA). While the goal of ACL reconstruction should be to utilize tissues that replicate the structural and particularly mechanical properties of the native ACL tissue, this critical outcome is rarely achieved.

Because of the fact that the PT and HT grafts have significantly higher tangent moduli than that of the ACL at all strain levels [145,176,208], these grafts have been very successful historically in stabilizing the knee and allowing the patient to return to strenuous physical activities. Notwithstanding these satisfactory short-term clinical and functional outcomes [7,209–212], the ACL reconstructed patient still has a high risk of developing early-onset OA [7,213–215], with symptoms presenting 5-15 years post-surgery [7]. Studies show incidences of OA within 7-14 years following knee injury as high as 50% [7,213,216], and sub-optimal improvements in outcomes as a result of ACL reconstruction with current graft methods [2]. In addition to the risk of developing OA, the altered graft properties typically manifest in a similarly altered and potentially hazardous joint mechanical profile, during both functional and especially highly dynamic maneuvers [5,6]. The net result is an increased risk of “ligament” re-rupture compared to the original native tissue state [217]. Graft failure rates are nearing 25% for the youngest, most active patients (i.e. teens) [218,219]. Long-term follow-up studies of ACL reconstructions report increased knee laxity over time [220,221] placing the graft at a greater risk of rupture.

In attempts to more effectively replicate the native ACL condition, a number of studies have compared explicit structural and mechanical properties between this and a series of commonly used replacement tissues under various movement/load scenarios [49,50,100,151,208,222–226]. These data consistently highlight substantial differences in the mechanical properties between the native and graft tissue, as well as how these differences promoted concomitant differences in knee function. For example, Woo et al. 2002 compared the mechanical response of PT and HT autografts to intact and ACL deficient cadaveric knees under explicit combined external joint load applications. Specifically, either an anterior tibial translation (ATT) load of 134 N, or ATT combined internal tibial (10 N-m) and valgus moments (10 N-m) were applied at two different (15°

and 30°) knee flexion angles. For each loading condition, both the PT and HT graft conditions resulted in significantly greater (by approximately 3-4 mm) peak anterior tibial translation magnitudes compared to the intact ACL state. They did not result in as great an increase, however, as the ACL deficient condition (approximately 5-11 mm). That the addition of internal rotation and valgus torques produced only minor translation increases compared to the isolated ATT case is somewhat logical, since as noted, the ACL's orientation renders it a secondary restraint to in-plane loading [76,93,94].

Table 1.2: Gender and age differences in the human ACL. (*Quantities were calculated by the authors from available data in the literature.) [1]

Authors	Strain Rate (/s)	Failure Strain	Tensile Strength (MPa)	Tangent Modulus (MPa)	Notes
Noyes and Grood	1.0	0.485 ± 0.119	13 ± 5	62 ± 7*	old
Noyes and Grood	1.0	0.602 ± 0.068	38 ± 9	110 ± 15*	young
Chandrashekar et al.	1.0	0.30 ± 0.06	26 ± 10	128 ± 35	male
Chandrashekar et al.	1.0	0.27 ± 0.08	23 ± 9	99 ± 50	female
Kennedy et al.	0.6	0.23 ± 0.02			2 mm/s
Kennedy et al.	0.25	0.28 ± 0.03			8 mm/s

The fact that HT and PT grafts resulted in increased translations compared to the intact case is less intuitive, however, since they both possess comparatively higher tangent moduli and geometric stiffnesses [65,177,227]. It could be that each graft was positioned within the knee joint at a lower active tension compared to the native ACL, countering these increased stiffness characteristics. It is also plausible that the overly stiff graft may immediately slip upon application of the external load, resulting in a more lax outcome than the native ACL condition. Such details were not reported, however, meaning underlying causes remain speculative at best.

Patellar tendon autografts were tested in uniaxial tension at a strain rate of 1.0/s to failure in male and female cadaveric knees by Hashemi, Beynnon, and co-workers, comparing properties to those of the native ACL condition [134,177,228]. Initial and tangent moduli were reported for the PTs but they reported only tangent moduli for the ACLs. The initial and tangent moduli observed for male PTs were approximately 103 ± 64 MPa and 479 ± 141 MPa, respectively, compared to a tangent modulus of 128 ± 35 MPa for the native ACL. The initial and tangent moduli of the female tendons were 140 ± 75 MPa and 490 ± 131 MPa, compared to the ACL tangent modulus of 99 ± 50 MPa. The increased linear moduli observed in both male and female PTs compared to the native state again highlight an important mechanical mismatch that likely compromises long-term joint integrities. That failure strains in the male 0.30 ± 0.06 and female 0.27 ± 0.08 ACLs [134] were significantly greater compared to corresponding PT values 0.18 ± 0.03 for male and 0.18 ± 0.04 for female; [173] further supports this tenet, especially since injury risk is strain dependent [48,131,132]. Donahue et al. 2001 measured the mechanical properties of human HT at a strain rate of 0.02/s, and found a tangent modulus of 904 MPa, strength of 66 MPa and failure strain of 0.088 [227]. These data indicate the HT is more overdesigned for stiffness as well as strength (as shown in **Table 1.2**) and potentially carries a higher risk of (re)injury, than the PT. Donahue et al. also reported stress relaxation to about 80% of the original value for PT which is in contrast to results reported for the ACL of about 50% [145,150], but comparable to the results in **Figure 1.5**.

1.6 Use of animal models in ACL research

Animal models have been used frequently in a variety of experiments designed to give insight into the properties of the human knee joint and its various components. Many tests have been conducted on different animal species, including rhesus monkeys [77,229], rabbits [152,230–234], rats [235–238], dogs [6,43,239,240], sheep [223,241–244], pigs [145,156,245–248], and cows [153,227,249]. From a biomechanics perspective, joints and tissues with structural features and biomechanical properties similar to those of human tissues would provide appropriate animal models. For small animal ACL replacement studies, appropriately scaled grafts are required. However, debate exists as to whether these animal models accurately reflect the structures and biomechanics of the human ACL and knee joint [229,250–256]. Others have called small animal models clinically inaccurate, due to their inability to support common ACL replacement surgery techniques [257]. Seitz et al. 1997 also characterized the rabbit ACL vascularity as more sparse than that of humans, citing it as an inappropriate model, but it isn't clear whether the vascularity was scaled appropriately in this study [258]. For this reason and others, such as the inability of small animal models to support human sized loads, small animal models have been all but ruled out within the clinical test model. Direct comparison of structural characteristics affords limited insights, however, since they fail to take into consideration underlying size differences in the respective tissues. Some small animal models may therefore need to be revisited as appropriately scaled (e.g. body weight) loads or material level properties such as moduli and failure strength, rather than geometric stiffness and load magnitudes, should be the factors used in determining suitable animal surrogates.

Others have explored size independent properties to eliminate some small animal models. Noyes et al. 1976 compared the mechanical and structural properties of human (16-26 yrs) and rhesus monkey specimens loaded uniaxially under tension (1.0/s) to failure. Human ACL stiffness (~180 kN/m) and particularly peak load magnitudes (~1.7 kN) were noticeably different from those observed (~190 kN/m and ~0.8 kN) for the monkey specimens [77]. When accounting for underlying structural differences, Noyes et al. 1976 found the human ACL elastic modulus (111 MPa) and strength (38 MPa) to be significantly lower than corresponding values (186 MPa and 66 MPa) in the monkey specimens. These outcomes, highlighting important constitutive differences, suggest that the monkey ACL model does not adequately represent the human tissue response.

Danto and Woo 1993 used the rabbit model to explore strain rate dependent responses of the medial portion of the ACL and PT at three different strain rates: 0.00017/s, 0.017/s and 3.8/s. They calculated the tangent modulus as the fit of the linear portion of the stress-strain curve between strains of 0.040 and 0.065, and reported an increase of 31% in the tangent modulus at the highest rate over that at the lowest rate for the ACL. Measuring the tangent modulus between strains of 0.020 and 0.045 in the PT, they found a 94% difference between the low and high strain rate tangent moduli [259]. These results provide an indication of the inability of the PT to replicate the native ACL response, in this case its strain rate dependence. Particularly, the existing discrepancies between the moduli of the ACL and PT at low strain rates are amplified at high strain rates in the rabbit model.

Sheep have been increasingly used as a large animal model as their stifle joint properties are anatomically similar to the human knee joint [260]. The relatively large size of the ovine stifle joint and its mechanical, histological, and molecular biological similarities similarly renders it suitable for *in vivo* investigations of knee and ACL function [261,262]. The sheep ACL contains two distinct sections, the craniomedial and caudolateral bundles (comparable to the AM and PL respectively). The two bundles have more distinct separate tibial insertions than the human bundles [261], as human ACLs demonstrate more of a continuum ribbon-like structure. However, in sheep as in humans the bundles are readily separated as described earlier. Seitz, et al.1997 discovered that the vascular anatomy of the ovine ACL is similar to that observed in humans [258]. Murray et al. also concluded that cell number density, blood vessel density, and percentage of intrinsic cells expressing smooth muscle actin, which are known to influence the response to injury in other musculoskeletal tissues, are similar between human and ovine ACL cells [263]. Several investigators have reported geometric stiffness values for sheep ACL [243,244,257,264]. When converted to tangent modulus using the geometrical properties provided by these authors, a fairly uniform consensus value of 130 ± 15 MPa is attained. Recall from Table 1 the recent study by the Beynnon group [134] giving a human ACL a tangent modulus of 128 ± 35 MPa for males and 99 ± 50 MPa for females.

The sheep model is also appealing for ACL studies because of the similarities of its soft-tissue graft healing processes and biomechanical outcomes in response to current surgical techniques compared to those of humans [257]. Sheep tend to tolerate the surgical grafting procedure well, regain knee stability without visible restrictions of motion, and display little macroscopic evidence of osteoarthritis [257]. Disadvantages with the sheep model include the substantially different metabolic processes between animals and humans. Wound healing in sheep is found to be faster than in humans, which may affect the time-dependent changes of graft remodeling [244].

Other investigations have noted similar attributes between the ACLs of large animals other than sheep (and goats) and those of humans. Fuss et al. 1991 found that although the knee range of motion is different for humans vs. pigs, there is no functional difference between the ACL in either model [246]. However, the porcine ACL structure shows a distinct difference from that of the human as its AM is further divided into two distinct sections. Xerogeanes et al. 1998 compared the *in situ* forces present in the ACL overall and its individual AM and PL separately in humans, pigs, goats, and sheep [265]. Force, moment, and displacement data were acquired by applying an anterior displacement to the tibia of the intact knee at 90° of knee flexion to 100 N at a rate of 0.333 mm/s. All soft tissue other than the ACL was then removed from the specimen, the displacements found in the first test reapplied, and the resulting forces measured. The porcine model was found to be most similar to the human model in terms of the load carried by the ACL, with differences evident between both the goat and sheep model. However, one cannot attribute differences among the loads carried by the various animal tissues to size of the ligament, its constitution, or both, without knowledge of the relative sizes of the animal ACLs.

It was noted earlier that Donahue et al. 2001 examined the viscoelastic properties of human HT [227]. That study compared the properties of human HT to those of the bovine digital extensor. Stress relaxation tests were performed by pulling the tissue at an elongation rate of 250 mm/s (approximately 3/s) to a strain of 0.025, corresponding to a force of around 500 N, and holding the displacement constant for around 900 seconds. Creep tests were performed using load control (at a rate of 315 N/s) to around 250 N, and holding at constant load for approximately 900 seconds. The structural and material properties were found through uniaxial tension testing to failure at a rate of 0.02/s. They found no significant differences in the viscoelastic properties of the bovine and human grafts; the loads at the end of the stress relaxation tests differed by only around 5 N (393 N for the human and 388 N for the bovine specimens). In addition, the strains at the end of the creep tests were approximately 0.012 for both tissues. The structural and material properties were also similar in the human and bovine models. The linear stiffness was found to be 418 N/mm in human and 444 N/mm in bovine, while average peak loads and ultimate stresses were around 2914 N and 66 MPa for human and 2901 N and 72 MPa for bovine. Ultimate displacement and ultimate strains were 8.4 mm and 0.88 for the human and 8.6 mm and 0.90 for the bovine tissue [227].

In recent years the sheep (or goat) has pulled ahead of the pack as the most widely used animal model for ACL biomechanics because of the data described above. Whether smaller animals have been virtually discounted for the right reasons remains unclear. Sheep clearly exhibit important similarities – joint and ACL structure and anatomy, and ACL material properties. A paucity of similar data for smaller animals precludes identification of potential models from this cohort. Cost considerations may one day entice investigators to revisit the possibility of a substitute for sheep. To some extent, a paradigm shift away from structural parameters towards mechanical concepts of stress and strain rather than load and displacement and material properties such as modulus, strength, and strain to failure is also required.

1.7 Mathematical models

Structurally viable finite element (FE) computational knee models may be highly useful for understanding ACL biomechanics in normal and pathological conditions, extending information that can be obtained from experiments. The reliability of FE models strongly depends on accurate geometric representations of the knee structures, appropriate constitutive models of the tissues, and correct boundary conditions including contact algorithms. Many computational efforts to date have focused on building accurate geometrical models and computationally efficient schemes, and advances in these areas have been remarkable. Mathematical modeling approaches for the ACL have included bilinear elastic one-dimensional springs [266–269], isotropic neo-Hookean materials [270], and general isotropic hyperelastic models [271,272]. More recently investigators have turned to developing more accurate mathematical models of the ACL as well as other tissues of the knee within a computational framework. Several investigators isolate the ACL and its attachments to the femur and tibia. The bones are assumed to be rigid therefore the computational framework is limited to just the ACL [194,273–276]. Others digitize the bones, ligaments, tendons, cartilage, and menisci [277–279]. The majority of these models use a transversely isotropic, non-linear elastic constitutive law for the ACL, writing the strain energy density function as a linear combination of the dilatational (volumetric) and distortional (isochoric) parts of the deformation gradient [194,273,275,278–280]:

$$W = \overline{W_{ISO}}(\overline{I_1}, \overline{I_4}) + W_{VOL}(J) \tag{3}$$

where the isochoric part of the strain energy density function, $\overline{W_{ISO}}$, depends on the first and fourth invariants of the isochoric right Cauchy-Green tensor ($\bar{C}$), and the volumetric part, W_{VOL}, depends on the volume change, J [281]. Both terms in the strain energy density function are non-linear, and, depending on the specific form of the functions chosen, the models have between four and six elastic constants. The first invariant, $\overline{I_1} = trace(\bar{C})$, is a scalar and therefore provides isotropic behavior. The fourth invariant, $\overline{I_4} = \bar{C}: m_0 \otimes m_0$, in which m_0 is a unit vector that indicates an initial “fiber” direction, provides anisotropy. Peña et al. 2006 also incorporate an initial stretch into their model [278]. Other investigators studying cartilage or meniscus and requiring an ACL in their computational framework have opted for a non-linear 1D spring model [282,283].

The elastic constants in a constitutive model should ideally be determined from experiments. Caution must be exercised when determining the best fit of the model constants to experimental data as the constants used must also provide a strain energy density function that is an increasing function of deformation. Xie et al. 2009 did not fit their model to ACL data but used a model from the literature that was developed for skin and contained elastic constants that violate this requirement [284]. Park et al. 2010 used an anisotropic model from the literature and fit the model to experiments they conducted on strips of ACL tissue tested in tension along and perpendicular to the fiber direction [194]. Unfortunately their elastic constants resulted in a strain energy density function that is also not an increasing function of deformation. The same is potentially true for the form the of constitutive model used by Dhaher et al. 2010 in that the choice of elastic constants could result in an invalid strain energy density function but their particular choices for elastic constants do not render their function invalid [279]. Peña et al. 2006 fit their ACL model parameters to data obtained by Butler et al. 1990 [278,285]. The Peña approach was used by Zhang et al. 2008, who used the model constants determined by Peña et al. manually digitized one human ACL to map the local collagen bundle direction, and assigned the local bundle direction to m_0 [273]. Recently Kiapour et al. 2014 also using the form of Equation 3, fit the ACL tension data to their model but they did not report the specific form of the strain energy density function they used nor their modal constants [280].

1.8 Conclusions

An extensive review of the literature herein reveals that graft tissues most commonly used to reconstruct the injured ACL (e.g. PT and HT) are substantially stiffer than the native tissue [100]. Studies also show that when reconstructing the ligament with these tissues, the common long-term outcome is an overly lax graft [12], arising as noted either through graft loosening [15] or a devolved and increasingly compliant tissue [16], although this is not true clinically. As other sources for replacement graft tissue are not available, methods to engineer ACL grafts may one day yield an alternative approach. From a design perspective, the challenges associated with matching the structure, function, and biomechanical properties of native ACL and its interfaces with materials available for scaffolds are arduous and multifaceted, as recently reviewed by Lu 2012 [19]. Recent efforts have demonstrated that at least for the sheep, a tissue engineering approach in which the graft grows and remodels *in vivo* to histologically and mechanically approach the native tissue condition appears promising [18]. Others have focused on augmented repair of the torn ACL using a bio-enhanced regenerative approach [20].

A key limitation of current research into ACL and/or graft mechanics is that data have typically been obtained under simple assumed uniaxial loading (tension) conditions. Studies extending analyses to examine more complex joint loading scenarios, both *in vitro* [114,118] and *in vivo* [127], have still only produced overly simplistic (regional) mechanical descriptions. With the ACL possessing substantial anatomical and functional complexity [35], its resultant mechanical response will likely be equally complex. It is thus plausible that current data drastically underrepresent the

ACL mechanical response. Similarly, the methods used to characterize ACL strain assuming uniformity oversimplify reality. Novel full-field methods have become established in studies of the mechanics of non-biological structural materials and are becoming increasingly utilized in tissue mechanics studies [18,45,286–290].

Digital image correlation (DIC) analysis provides the strain contours from the displacement information. In either bundle it is clear that strain averaged along the entire bundle length grossly simplifies the actual strain state which may lead to inaccuracies in predicting injury mechanisms. DIC provides transverse and shear strains as well, vastly expanding the data collected from a single experiment. Increased utilization of innovations such as the full-field DIC method during structural and functional testing of the ACL and the knee joint is critically needed to enhance our understanding of the ACL response.

A torn anterior cruciate ligament is a traumatic knee joint injury that carries significant morbidities. Central to identifying and countering the mechanisms of these injuries and their long-term sequelae is a thorough knowledge of the native tissue’s mechanical properties. Over the past five decades, an abundance of (*in vitro*, *in vivo* and animal model) research has been undertaken with this direct intent, affording significant insights into the ligament’s response to various isolated and combined load states. Despite these extensive efforts, however, limited data exist that successfully characterize 3D ligament mechanical behaviors under highly dynamic physiologic loading conditions synonymous with injury. The net outcomes of this ongoing void include a lack of insight into the true mechanisms of ACL injury and means to successfully screen for and counter their debilitative impact. In addition, the ACL biomechanics community lags behind the rest of the mechanics community in the use of experimental techniques and computational tools to characterize, model, and predict biomechanics, kinematics, and injuries. Filling these knowledge gaps is critical and is a primary focus of the research discussed in this work.

The remaining chapters are organized as follows. In **Chapter 2**, a novel stochastic patterning method for soft biological tissue for use with digital image correlation is discussed. **Chapter 3** outlines the experimental results of the AM bundle of the ACL using digital image correlation and traditional strain measuring techniques. In **Chapter 4**, the experimental results for the PL bundle and the clinically relevant anterior tibial translation (ATT) test are discussed. **Chapter 5** details the development of a finite-element AM bundle model derived and validated from the experimental results. **Chapter 6** concludes, with a focus on proposed next steps for future work.

1.9 References

[1] S.G. McLean, K.F. Mallett, E.M. Arruda, Deconstructing the Anterior Cruciate Ligament: What We Know and Don’t Know About Function, Material Properties, and Injury Mechanics., J. Biomech. Eng. 137 (2015) 020906. doi:10.1115/1.4029278.

[2] L.S. Lohmander, a Ostenberg, M. Englund, H.P. Roos, High prevalence of knee osteoarthritis, pain, and functional limitations in female soccer players twelve years after anterior cruciate ligament injury., Arthritis Rheum. 50 (2004) 3145–52. doi:10.1002/art.20589.

[3] R.P. Csintalan, M.C.S. Inacio, T.T. Funahashi, Incidence rate of anterior cruciate ligament reconstructions., Perm. J. 12 (2008) 17–21. http://www.pubmedcentral.nih.gov/articlerender.fcgi?artid=3037119&tool=pmcentrez&rendertype=abstract.

[4] L.Y. Griffin, M.J. Albohm, E.A. Arendt, R. Bahr, B.D. Beynnon, M. Demaio, R.W. Dick, L. Engebretsen, W.E. Garrett Jr., J.A. Hannafin, T.E. Hewett, L.J. Huston, M.L. Ireland, R.J. Johnson, S. Lephart, B.R. Mandelbaum, B.J. Mann, P.H. Marks, S.W. Marshall, G. Myklebust, F.R. Noyes, C. Powers, C. Shields Jr., S.J. Shultz, H. Silvers, J. Slauterbeck, D.C. Taylor, C.C. Teitz, E.M. Wojtys, B. Yu, Understanding and preventing noncontact anterior cruciate ligament injuries: a review of the Hunt Valley II meeting, January 2005, Am. J. Sports Med. 34 (2006) 1512–1532. http://www.ncbi.nlm.nih.gov/entrez/query.fcgi?cmd=Retrieve&db=PubMed&dopt=Citation&list_uids=16905673.

[5] J.M. Deneweth, M.J. Bey, S.G. McLean, T.R. Lock, P.A. Kolowich, S. Tashman, Tibiofemoral joint kinematics of the anterior cruciate ligament-reconstructed knee during a single-legged hop landing, Am. J. Sports Med. 38 (2010) 1820–1828. doi:0363546510365531 [pii]10.1177/0363546510365531.

[6] S. Tashman, W. Anderst, P.A. Kolowich, S. Havstad, S.P. Arnoczky, Kinematics of the ACL-deficient canine knee during gait: serial changes over two years., J. Orthop. Res. 22 (2004) 931–41. doi:10.1016/j.orthres.2004.01.008.

[7] L.S. Lohmander, P.M. Englund, L.L. Dahl, E.M. Roos, The long-term consequence of anterior cruciate ligament and meniscus injuries: osteoarthritis, Am. J. Sports Med. 35 (2007) 1756–1769. doi:0363546507307396 [pii]10.1177/0363546507307396.

[8] P. Neuman, M. Englund, I. Kostogiannis, T. Fridén, H.P. Roos, L.E. Dahlberg, P. Neumann, M. Englund, I. Kostogiannis, T. Friden, H.P. Roos, L.E. Dahlberg, Prevalence of tibiofemoral osteoarthritis 15 years after nonoperative treatment of anterior cruciate ligament injury: a prospective cohort study, Am. J. Sports Med. 36 (2008) 1717–1725. doi:0363546508316770 [pii]10.1177/0363546508316770.

[9] C.W. Imhauser, C. Mauro, D. Choi, E. Rosenberg, S. Mathew, J. Nguyen, Y. Ma, T. Wickiewicz, Abnormal tibiofemoral contact stress and its association with altered kinematics after center-center anterior cruciate ligament reconstruction: an in vitro study, Am. J. Sports Med. 41 (2013) 815–825. doi:10.1177/0363546512475205.

[10] T.P. Andriacchi, A. Mundermann, R.L. Smith, E.J. Alexander, C.O. Dyrby, S. Koo, A framework for the in vivo pathomechanics of osteoarthritis at the knee, Ann. Biomed. Eng. 32 (2004) 447–457. http://www.ncbi.nlm.nih.gov/entrez/query.fcgi?cmd=Retrieve&db=PubMed&dopt=Citation&list_uids=15095819.

[11] M.C. Logan, E. Dunstan, J. Robinson, A. Williams, W. Gedroyc, M. Freeman, Tibiofemoral kinematics of the anterior cruciate ligament (ACL)-deficient weightbearing, living knee employing vertical access open “interventional” multiple resonance imaging, Am. J. Sports Med. 32 (2004) 720–726. http://www.ncbi.nlm.nih.gov/entrez/query.fcgi?cmd=Retrieve&db=PubMed&dopt=Citation&list_uids=15090390.

[12] S. Rupp, B. Muller, R. Seil, Knee laxity after ACL reconstruction with a BPTB graft, Knee Surg. Sports Traumatol. Arthrosc. 9 (2001) 72–76. http://www.ncbi.nlm.nih.gov/entrez/query.fcgi?cmd=Retrieve&db=PubMed&dopt=Citation&list_uids=11354856.

[13] A. Van Kampen, A.B. Wymenga, H.J.L. Van Der Heide, A. van Kampen, A.B. Wymenga, H.J. van der Heide, H.J. Bakens, The effect of different graft tensioning in anterior cruciate ligament reconstruction: a prospective randomized study, Arthroscopy. 14 (1998) 845–850. http://www.ncbi.nlm.nih.gov/pubmed/9848597.

[14] M. Cuppone, B.B. Seedhom, Effect of implant lengthening and mode of fixation on knee laxity after ACL reconstruction with an artificial ligament: a cadaveric study, J. Orthop. Sci. 6 (2001) 253–261. doi:10.1007/s0077610060253.

[15] P.J. Roos, M.L. Hull, S.M. Howell, Lengthening of double-looped tendon graft constructs in three regions after cyclic loading: a study using Roentgen stereophotogrammetric analysis, J. Orthop. Res. 22 (2004) 839–846. doi:10.1016/j.orthres.2003.11.002S0736026603002857 [pii].

[16] C.K. Smith, M.L. Hull, S.M. Howell, Lengthening of a single-loop tibialis tendon graft construct after cyclic loading: a study using Roentgen stereophotogrammetric analysis, J. Biomech. Eng. 128 (2006) 437–442. doi:10.1115/1.2187038.

[17] R.S. Boorman, G.M. Thornton, N.G. Shrive, C.B. Frank, Ligament grafts become more susceptible to creep within days after surgery: evidence for early enzymatic degradation of a ligament graft in a rabbit model, Acta Orthop. Scand. 73 (2002) 568–574. doi:10.1080/000164702321022866.

[18] J. Ma, M.J. Smietana, T.Y. Kostrominova, E.M. Wojtys, L.M. Larkin, E.M. Arruda, Three-Dimensional Engineered Bone–Ligament–Bone Constructs for Anterior Cruciate Ligament Replacement, Tissue Eng. 18 (2012) 103–116. doi:10.1089/ten.tea.2011.0231.

[19] H.H. Lu, Engineering Tissue-to-Tissue Interfaces and the Formation of Complex Tissues, Bridg. 42 (2012) 40–47.

[20] M.M. Murray, B.C. Fleming, Biology of anterior cruciate ligament injury and repair: Kappa Delta Ann Doner Vaughn award paper 2013., J. Orthop. Res. 31 (2013) 1501–6. doi:10.1002/jor.22420.

[21] E.S. Grood, W.J. Suntay, A joint coordinate system for the clinical description of three-dimensional motions: application to the knee, J. Biomech. Eng. 105 (1983) 136–144.

[22] D.K. Ramsey, P.F. Wretenberg, Biomechanics of the knee: methodological considerations in the in vivo kinematic analysis of the tibiofemoral and patellofemoral joint., Clin. Biomech. (Bristol, Avon). 14 (1999) 595–611. http://www.ncbi.nlm.nih.gov/pubmed/10521643.

[23] Y. Takeda, J.W. Xerogeanes, G.A. Livesay, F.H. Fu, S.L.-Y. Woo, Biomechanical function of the human anterior cruciate ligament, Arthroscopy. 10 (1994) 140–147.

[24] S.L.-Y. Woo, R.E. Debski, J.D. Withrow, M.A. Janaushek, Biomechanics of knee Ligaments, Am. J. Sports Med. 27 (1999) 533–543.

[25] H.J. Marans, R.W. Jackson, N.D. Glossop, C. Young, Anterior cruciate ligament insufficiency: a dynamic three-dimensional motion analysis, Am. J. Sports Med. 17 (1989) 325–332. http://www.ncbi.nlm.nih.gov/pubmed/2729481.

[26] R. Shiavi, T.J. Limbird, M. Frazer, K. Stivers, A. Strauss, J. Abramovitz, Helical motion analysis of the knee--II. Kinematics of uninjured and injured knees during walking and pivoting., J. Biomech. 20 (1987) 653–65.

http://www.ncbi.nlm.nih.gov/pubmed/3654664.

[27] B. Yu, C.F. Lin, W.E. Garrett, Lower extremity biomechanics during the landing of a stop-jump task, Clin. Biomech. 21 (2006) 297–305. http://www.ncbi.nlm.nih.gov/entrez/query.fcgi?cmd=Retrieve&db=PubMed&dopt=Citation&list_uids=16378667.

[28] T.E. Hewett, J.S. Torg, B.P. Boden, Video analysis of trunk and knee motion during non-contact anterior cruciate ligament injury in female athletes: lateral trunk and knee abduction motion are combined components of the injury mechanism, Br. J. Sports Med. 43 (2009) 417–422. doi:bjsm.2009.059162 [pii]10.1136/bjsm.2009.059162.

[29] S.G. McLean, B. Borotikar, S.M. Lucey, Lower limb muscle pre-motor time measures during a choice reaction task associate with knee abduction loads during dynamic single leg landings, Clin. Biomech. 25 (2010) 563–569. doi:S0268-0033(10)00062-8 [pii]10.1016/j.clinbiomech.2010.02.013.

[30] S.G. McLean, M.L. Beaulieu, Complex integrative morphological and mechanical contributions to ACL injury risk, Exerc Sport Sci Rev. 38 (2010) 192–200. doi:10.1097/JES.0b013e3181f450b400003677-201010000-00007 [pii].

[31] E.G. Meyer, R.C. Haut, Anterior cruciate ligament injury induced by internal tibial torsion or tibiofemoral compression., J. Biomech. 41 (2008) 3377–83. doi:10.1016/j.jbiomech.2008.09.023.

[32] Y.K. Oh, J.L. Kreinbrink, E.M. Wojtys, J.A. Ashton-Miller, Effect of axial tibial torque direction on ACL relative strain and strain rate in an in vitro simulated pivot landing., J. Orthop. Res. 30 (2012) 528–34. doi:10.1002/jor.21572.

[33] F. Girgis, J.L. Marshall, A. Monajem, A.R.S. Al Monajem, The cruciate ligaments of the knee joint: anatomical, functional and experimental analysis, Clin. Orthop. Relat. Res. 106 (1975) 216–231.

[34] S.F. Dye, W.D.J. Cannon, Anatomy and biomechanics of the anterior cruciate ligament, Clin. Sports Med. 7 (1988) 715–725. http://www.ncbi.nlm.nih.gov/pubmed/3052878 (accessed September 30, 2013).

[35] A.B. Moghaddam, A. Torkaman, A cadaver study of the structures and positions of the anterior cruciate ligament in humans, Int. J. Prev. Med. 4 (2013) S85–91. http://www.ncbi.nlm.nih.gov/pubmed/23717777.

[36] M. Odensten, J. Gillquist, Functional anatomy of the anterior cruciate ligament and a rationale for reconstruction, J-Bone-Joint-Surg-Am. 67 (1985) 257–9355. http://www.ncbi.nlm.nih.gov/pubmed/3968118.

[37] W. Petersen, T. Zantop, Anatomy of the anterior cruciate ligament with regard to its two bundles, Clin. Orthop. Relat. Res. 454 (2007) 35–47. doi:10.1097/BLO.0b013e31802b4a59.

[38] B.A. Smith, G.A. Livesay, S.L.-Y. Woo, Biology and biomechanics of the anterior cruciate ligament, Clin. Sports Med. 12 (1993) 637–670.

[39] R.P. Welsh, Knee joint structure and function, Clin. Orthop. Relat. Res. (1980) 7–14. http://www.pubmedcentral.nih.gov/articlerender.fcgi?artid=3171541&tool=pmcentrez&rendertype=abstract.

[40] F.H. Fu, C.D. Harner, D.L. Johnson, M.D. Miller, S.L.-Y. Woo, Biomechanics of Knee Ligaments; Basic Concepts and Clinical Application, J. Bone Jt. Surg. 75

(1993) 1716–1727.

[41] C.D. Harner, G.H. Baek, T.M. Vogrin, G.J. Carlin, S. Kashiwaguchi, S.L.-Y. Woo, Quantitative analysis of human cruciate ligament insertions, Arthroscopy. 15 (1999) 741–749. http://www.ncbi.nlm.nih.gov/pubmed/10524822.

[42] S.P. Arnoczky, Anatomy of the anterior cruciate ligament., Clin. Orthop. Relat. Res. 172 (1983) 19–25. http://www.ncbi.nlm.nih.gov/pubmed/6821989.

[43] S.L.-Y. Woo, M. a Gomez, Y. Seguchi, C.M. Endo, W.H. Akeson, Measurement of mechanical properties of ligament substance from a bone-ligament-bone preparation., J. Orthop. Res. 1 (1983) 22–9. doi:10.1002/jor.1100010104.

[44] M. Benjamin, E.J. Evans, L. Copp, The histology of tendon attachments to bone in man., J. Anat. 149 (1986) 89–100. http://www.pubmedcentral.nih.gov/articlerender.fcgi?artid=1261636&tool=pmcentrez&rendertype=abstract.

[45] K.L. Moffat, W.-H.S. Sun, P.E. Pena, N.O. Chahine, S.B. Doty, G.A. Ateshian, C.T. Hung, H.H. Lu, Characterization of the structure-function relationship at the ligament-to-bone interface., Proc. Natl. Acad. Sci. U. S. A. 105 (2008) 7947–52. doi:10.1073/pnas.0712150105.

[46] J.T. Andrish, Anterior cruciate ligament injuries in the skeletally immature patient, Am J Orthop. 30 (2001) 103–110. http://www.ncbi.nlm.nih.gov/entrez/query.fcgi?cmd=Retrieve&db=PubMed&dopt=Citation&list_uids=11234936.

[47] S.P. Arnoczky, R.F. Warren, M.A. Ashlock, Replacement of the anterior cruciate ligament using a patellar tendon allograft. An experimental study, J Bone Jt. Surg [Am]. 68 (1986) 376–385.

[48] J.M. Bach, M.L. Hull, H.A. Patterson, Direct measurement of strain in the posterolateral bundle of the anterior cruciate ligament, J. Biomech. 30 (1997) 1–3.

[49] D.L. Butler, M.D. Kay, D.C. Stouffer, Comparison of Material Properties in Fascicle-Bone Units from Human Patellar Tendon and Knee Ligaments, J. Biomech. 19 (1986) 435–432.

[50] D.L. Hamner, C.H. Brown, M.E. Steiner, a T. Hecker, W.C. Hayes, Hamstring tendon grafts for reconstruction of the anterior cruciate ligament: biomechanical evaluation of the use of multiple strands and tensioning techniques., J. Bone Joint Surg. Am. 81 (1999) 549–57. http://www.ncbi.nlm.nih.gov/pubmed/10225801.

[51] D.L. Butler, Anterior cruciate ligament: its normal response and replacement, J. Orthop. Res. 7 (1989) 910–21. doi:10.1002/jor.1100070618.

[52] J.M. Hollis, J.P. Marcin, S. Horibe, S.L.-Y. Woo, Load determination in ACL fibres under knee loading., Trans. Orthop. Res. Soc. 13 (1988) 196.

[53] L.A. Norwood, M.J. Cross, Anterior cruciate ligament: functional anatomy of its bundles in rotatory instabilities., Am. J. Sports Med. 7 (1979) 23–6. http://www.ncbi.nlm.nih.gov/pubmed/420384.

[54] J.C. Kennedy, H.W. Weinberg, A.S. Wilson, The anatomy and function of the anterior cruciate ligament - as determined by clinical and morphological studies, J. Bone Joint Surg. Am. 56-A (1974).

[55] S. Takai, S.L.-Y. Woo, G.A. Livesay, D.J. Adams, F.H. Fu, Determination of the in situ loads on the human anterior cruciate ligament, J. Orthop. Res. 11 (1993) 686–695.

[56] J.A. Sidles, R. V Larson, J.L. Garbini, D.J. Downey, F.A.D. Matsen, Ligament length relationships in the moving knee, J. Orthop. Res. 6 (1988) 593–610.

[57] C.J. Wang, P.S. Walker, B. Wolf, The effects of flexion and rotation on the length patterns of the ligaments of the knee., J. Biomech. 6 (1973) 587–96. http://www.ncbi.nlm.nih.gov/entrez/query.fcgi?cmd=Retrieve&db=PubMed&dopt=Citation&list_uids=4757478.

[58] J.M. Hollis, S. Takai, D.J. Adams, S. Horibe, S.L.-Y. Woo, The effects of knee motion and external loading on the length of the anterior cruciate ligament (ACL): a kinematic study., J. Biomech. Eng. 113 (1991) 208–14. http://www.ncbi.nlm.nih.gov/pubmed/1875695.

[59] T.J. Mommersteeg, J.G. Kooloos, L. Blankevoort, J.M. Kauer, R. Huiskes, F.Q. Roeling, The fibre bundle anatomy of human cruciate ligaments, J. Anat. 187 (1995) 461–471. http://www.pubmedcentral.nih.gov/articlerender.fcgi?artid=1167440&tool=pmcentrez&rendertype=abstract.

[60] S.W. Arms, M.H. Pope, R.J. Johnson, R.A. Fischer, I. Arvidsson, E. Eriksson, The biomechanics of anterior cruciate ligament rehabilitation and reconstruction, Am. J. Sports Med. 12 (1984) 8–18. http://www.ncbi.nlm.nih.gov/pubmed/6703185.

[61] G. Li, R. Papannagari, L.E. DeFrate, J.D. Yoo, S.E. Park, T.J. Gill, Comparison of the ACL and ACL graft forces before and after ACL reconstruction: an in-vitro robotic investigation, Acta Orthop. 77 (2006) 267–274. http://www.ncbi.nlm.nih.gov/entrez/query.fcgi?cmd=Retrieve&db=PubMed&dopt=Citation&list_uids=16752289.

[62] S. Tashman, P.A. Kolowich, D. Collon, K. Anderson, W. Anderst, Dynamic function of the ACL-reconstructed knee during running, Clin. Orthop. Relat. Res. 454 (2007) 66–73. doi:10.1097/BLO.0b013e31802bab3e.

[63] A.M. Chaudhari, P.L. Briant, S.L. Bevill, S. Koo, T.P. Andriacchi, Knee kinematics, cartilage morphology, and osteoarthritis after ACL injury, Med. Sci. Sports Exerc. 40 (2008) 215–222. doi:10.1249/mss.0b013e31815cbb0e.

[64] A. Kanamori, J. Zeminski, T.W. Rudy, G. Li, F.H. Fu, S.L.-Y. Woo, The effect of axial tibial torque on the function of the anterior cruciate ligament: a biomechanical study of a simulated pivot shift test, Arthrosc. J. Arthrosc. Relat. Surg. 18 (2002) 394–398. doi:10.1053/jars.2002.30638.

[65] J. Ma, Experimental and Computational Characterizations of Native Ligaments, Tendons and Engineered 3-D Bone-Ligament-Bone Constructs in the Knee, University of Michigan, Ann Arbor, 2012.

[66] F.R. Noyes, J.L. DeLucas, P.J. Torvik, Biomechanics of Anterior Cruciate Ligament Failure: An Analysis of Strain-Rate Sensitivity and Mechanisms of Failure in Primates, J. Bone Jt. Surg. (1974).

[67] F.R. Noyes, P.J. Torvik, W.B. Hyde, J.L. DeLucas, Biomechanics of Ligament Failure II: An Analysis of Immobilization, Exercise, and Reconditioning Effects in Primates, J. Bone Jt. Surg. (1974).

[68] H.E. Cabaud, W.G. Rodkey, J.A. Feagin, Experimental studies of acute anterior cruciate ligament injury and repair, Am. J. Sports Med. 7 (1979) 18–22.

[69] H.E. Cabaud, J.A. Feagin, W.G. Rodkey, Acute anterior cruciate ligament injury and augmented repair, Am. Orthop. Soc. Sport. Med. 8 (1980) 395–401.

[70] D.L. Butler, F.R. Noyes, E.S. Grood, Ligamentous Restraints to Anterior-Posterior Drawer in the Human Knee, J. Bone Jt. Surg. 62 (1980) 259–270.

[71] D.L. Butler, E.S. Grood, F.R. Noyes, A.N. Sodd, On the Interpretation of Our Anterior Cruciate Ligament Data, Clin. Orthop. Relat. Res. 196 (1985).

[72] T. Fukubayashi, P.A. Torzilli, M.F. Sherman, R.F. Warren, An in vitro biomechanical evaluation of anterior-posterior motion of the knee. Tibial displacement, rotation, and torque, J. Bone Joint Surg. Am. 64 (1982) 258–264.

[73] K.L. Markolf, J.S. Mensch, H.C. Amstutz, Stiffness and laxity of the knee--the contributions of the supporting structures. A quantitative in vitro study, J Bone Jt. Surg [Am]. 58 (1976) 583–594.

[74] J.L. Haimes, R.R. Wroble, E.S. Grood, F.R. Noyes, Role of the medial structures in the intact and anterior cruciate ligament-deficient knee. Limits of motion in the human knee, Am. J. Sports Med. 22 (1994) 402–409.

[75] D.L. Gollehon, P.A. Torzilli, R.F. Warren, The Role of the Posterolateral and Cruciate Ligaments in the Stability of the Human Knee, J. Bone Jt. Surg. 69-A (1987) 233–242.

[76] R.L. Piziali, W.P. Seering, D. a Nagel, D.J. Schurman, The function of the primary ligaments of the knee in anterior-posterior and medial-lateral motions., J. Biomech. 13 (1980) 777–84. http://www.ncbi.nlm.nih.gov/pubmed/7440592.

[77] F.R. Noyes, E.S. Grood, The Strength of the Anterior Cruciate Ligament in Humans and Rhesus Monkeys, J. Bone Jt. Surg. 58 (1976) 1074–1082.

[78] G. DeMorat, P. Weinhold, T. Blackburn, S. Chudik, W. Garrett, Aggressive Quadriceps Loading Can Induce Noncontact Anterior Cruciate Ligament Injury, Am. J. Sports Med. 32 (2004) 477–483. http://www.ncbi.nlm.nih.gov/entrez/query.fcgi?cmd=Retrieve&db=PubMed&dopt=Citation&list_uids=14977677.

[79] A. Cappozzo, F. Catani, A. Leardini, M.G. Benedetti, U.D. Croce, U. Della Croce, Position and orientation in space of bones during movement: experimental artifacts, Clin Biomech. 11 (1996) 90–100. doi:0268003395000461 [pii].

[80] E.Y. Chao, R.K. Laughman, E. Schneider, R.N. Stauffer, Normative data of knee joint motion and ground reaction forces in adult level walking, J. Biomech. 16 (1983) 219–233.

[81] M.A. Lafortune, P.R. Cavanagh, H.J. d Sommer, A. Kalenak, Three-dimensional kinematics of the human knee during walking, J. Biomech. 25 (1992) 347–357.

[82] S.G. McLean, J.E. Samorezov, Fatigue-induced ACL injury risk stems from a degradation in central control, Med. Sci. Sports Exerc. 41 (2009) 1661–1672. doi:10.1249/MSS.0b013e31819ca07b.

[83] H.K. Ramakrishnan, M.P. Kadaba, On the estimation of joint kinematics during gait, J. Biomech. 24 (1991) 969–977.

[84] D.B. Kettelkamp, R.J. Johnson, G.L. Smidt, E.Y. Chao, M. Walker, An Electrogoniometric Motion in Normal of Knee Gait, J. Bone Jt. Surg. 52-A (1970) 775–790.

[85] O.C. Brantigan, A.F. Voshell, The mechanics of the ligaments and menisci of the knee joint, J. Bone Jt. Surg. 23 (1941) 44–66.

[86] J.G. Lane, S.E. Irby, K. Kaufman, C. Rangger, D.M. Daniel, The anterior cruciate ligament in controlling axial rotation. An evaluation of its effect, Am. J. Sports

Med. 22 (1994) 289–293.
[87] J.D. Reuben, J.S. Rovick, R.J. Schrager, P.S. Walker, A.L. Boland, Three-dimensional dynamic motion analysis of the anterior cruciate ligament deficient knee joint, Am. J. Sports Med. 17 (1989) 463–471. http://www.ncbi.nlm.nih.gov/pubmed/2782529.
[88] H.N. Andersen, P. Dyhre-Poulsen, The anterior cruciate ligament does play a role in controlling axial rotation in the knee, Knee Surg. Sports Traumatol. Arthrosc. 5 (1997) 145–149.
[89] J.M. Lipke, C.J. Janecki, C.L. Nelson, P. McLeod, C. Thompson, J. Thompson, D.W. Haynes, The role of incompetence of the anterior cruciate and lateral ligaments in anterolateral and anteromedial instability. A biomechanical study of cadaver knees, J Bone Jt. Surg [Am]. 63 (1981) 954–960.
[90] K.L. Markolf, W.L. Bargar, S.C. Shoemaker, H.C. Amstutz, H.C. Amstuts, H.C. Amstutz, The role of joint load in knee stability, J Bone Jt. Surg [Am]. 63 (1981) 570–585.
[91] L.A. Norwood, J.R. Andrews, R.C. Meisterling, G.L. Glancy, Acute anterolateral rotatory instability of the knee, J. Bone Joint Surg. Am. 61 (1979) 704–709. http://www.ncbi.nlm.nih.gov/entrez/query.fcgi?cmd=Retrieve&db=PubMed&dopt=Citation&list_uids=582318.
[92] W.P. Seering, R.L. Piziali, D.A. Nagel, D.J. Schurman, The function of the primary ligaments of the knee in varus-valgus and axial rotation, J. Biomech. 13 (1980) 785–794.
[93] S.C. Shoemaker, K.L. Markolf, Effects of joint load on the stiffness and laxity of ligament-deficient knees. An in vitro study of the anterior cruciate and medial collateral ligaments, J Bone Jt. Surg [Am]. 67 (1985) 136–146.
[94] R.R. Wroble, E.S. Grood, J.S. Cummings, J.M. Henderson, F.R. Noyes, The role of the lateral extraarticular restraints in the anterior cruciate ligament-deficient knee, Am. J. Sports Med. 21 (1993) 257–62; discussion 263.
[95] E.M. Wojtys, M.L. Beaulieu, J.A. Ashton-Miller, New perspectives on ACL injury: On the role of repetitive sub-maximal knee loading in causing ACL fatigue failure, J. Orthop. Res. 34 (2016) 2059–2068. doi:10.1002/jor.23441.
[96] M.L. Beaulieu, E.M. Wojtys, J.A. Ashton-Miller, Risk of Anterior Cruciate Ligament Fatigue Failure Is Increased by Limited Internal Femoral Rotation During In Vitro Repeated Pivot Landings, Am. J. Sports Med. 43 (2015) 2233–2241. doi:10.1177/0363546515589164.
[97] E.S. Grood, F.R. Noyes, D.L. Butler, W.J. Suntay, Ligamentous and capsular restraints preventing straight medial and lateral laxity in intact human cadaver knees, J. Bone Joint Surg. Am. 63 (1981) 1257–1269.
[98] S. Nielsen, J. Ovesen, O. Rasmussen, The anterior cruciate ligament of the knee: an experimental study of its importance in rotatory knee instability, Arch Orthop Trauma Surg. 103 (1984) 170–174.
[99] M. Inoue, E. McGurk Burleson, J.M. Hollis, S.L.-Y. Woo, Treatment of the medial collateral ligament injury. I: The importance of anterior cruciate ligament on the varus-valgus knee laxity, Am. J. Sports Med. 15 (1987) 15–21.
[100] S.L.-Y. Woo, A. Kanamori, J. Zeminski, M. Yagi, C. Papageorgiou, F.H. Fu, The effectiveness of reconstruction of the anterior cruciate ligament with hamstrings

and patellar tendon . A cadaveric study comparing anterior tibial and rotational loads, J. Bone Joint Surg. Am. 84-A (2002) 907–14.

[101] H. Fujie, K. Mabuchi, S.L.-Y. Woo, G.A. Livesay, S. Arai, Y. Tsukamoto, The use of robotics technology to study human joint kinematics: a new methodology, J. Biomech. Eng. 115 (1993) 211–7.

[102] T.W. Rudy, G.A. Livesay, S.L.-Y. Woo, F.H. Fu, A combined robotic/universal force sensor approach to determine in situ forces of knee ligaments, J. Biomech. 29 (1996) 1357–60.

[103] H.R. Galway, A. Beaupre, D.L. MacIntosh, Pivot shift: a clinical sign of symptomatic anterior cruciate in suffiency, J. Bone Jt. Surg. 54 (1972) 763–764.

[104] H. Fujie, G.A. Livesay, S.L.-Y. Woo, S. Kashiwaguchi, G. Blomstrom, The use of a universal force-moment sensor to determine in-situ forces in ligaments: a new methodology, J. Biomech. Eng. 117 (1995) 1–7.

[105] G.A. Livesay, T.W. Rudy, S.L.-Y. Woo, T.J. Runco, M. Sakane, G. Li, F.H. Fu, Evaluation of the effect of joint constraints on the in situ force distribution in the anterior cruciate ligament, J. Orthop. Res. 15 (1997) 278–84.

[106] M. Sakane, R.J. Fox, S.L.-Y. Woo, G.A. Livesay, G. Li, F.H. Fu, In situ forces in the anterior cruciate ligament and its bundles in response to anterior tibial loads., J. Orthop. Res. 15 (1997) 285–93. doi:10.1002/jor.1100150219.

[107] M.T. Gabriel, E.K. Wong, S.L.-Y. Woo, M. Yagi, R.E. Debski, Distribution of in situ forces in the anterior cruciate ligament in response to rotatory loads., J. Orthop. Res. 22 (2004) 85–9. doi:10.1016/S0736-0266(03)00133-5.

[108] A. Kanamori, S.L.-Y. Woo, C.B. Ma, J. Zeminski, T.W. Rudy, G. Li, G.A. Livesay, The forces in the anterior cruciate ligament and knee kinematics during a simulated pivot shift test: A human cadaveric study using robotic technology., Arthroscopy. 16 (2000) 633–9. doi:10.1053/jars.2000.7682.

[109] A. Wineman, Mechanical Response of Polymers: an Introduction, Cambridge University Press, Cambridge, UK, UK, 2000.

[110] K.L. Markolf, D.M. Burchfield, M.M. Shapiro, M.F. Shepard, G.A. Finerman, J.L. Slauterbeck, Combined knee loading states that generate high anterior cruciate ligament forces, J. Orthop. Res. 13 (1995) 930–935.

[111] P.A. Renstrom, S.W. Arms, T.S. Stanwyck, R.J. Johnson, M.H. Pope, Strain within the anterior cruciate ligament during hamstring and quadriceps activity, Am. J. Sports Med. 14 (1986) 83–87.

[112] K. Mizuno, J.T. Andrish, A.J. van den Bogert, S.G. McLean, Gender dimorphic ACL strain in response to combined dynamic 3D knee joint loading: Implications for ACL injury risk, Knee. 16 (2009) 432–440. doi:10.1016/j.knee.2009.04.008.

[113] L.P. Maletsky, B.M. Hillberry, Simulating dynamic activities using a five-axis knee simulator, J. Biomech. Eng. 127 (2005) 123–133. http://www.ncbi.nlm.nih.gov/entrez/query.fcgi?cmd=Retrieve&db=PubMed&dopt=Citation&list_uids=15868795.

[114] T.J. Withrow, L.J. Huston, E.M. Wojtys, J.A. Ashton-Miller, The relationship between quadriceps muscle force, knee flexion, and anterior cruciate ligament strain in an in vitro simulated jump landing., Am. J. Sports Med. 34 (2006) 269–74. doi:10.1177/0363546505280906.

[115] T.J. Withrow, L.J. Huston, E.M. Wojtys, J.A. Ashton-Miller, Effect of varying

hamstring tension on anterior cruciate ligament strain during in vitro impulsive knee flexion and compression loading., J. Bone Joint Surg. Am. 90 (2008) 815–23. doi:10.2106/JBJS.F.01352.

[116] Y.K. Oh, D.B. Lipps, J.A. Ashton-Miller, E.M. Wojtys, What strains the anterior cruciate ligament during a pivot landing?, Am. J. Sports Med. 40 (2012) 574–83. doi:10.1177/0363546511432544.

[117] S.G. McLean, Y.K. Oh, M.L. Palmer, S.M. Lucey, D.G. Lucarelli, J.A. Ashton-Miller, E.M. Wojtys, The relationship between anterior tibial acceleration, tibial slope, and ACL strain during a simulated jump landing task, J. Bone Joint Surg. Am. 93 (2011) 1310–1317. doi:10.2106/JBJS.J.00259.

[118] D.B. Lipps, Y.K. Oh, J.A. Ashton-Miller, E.M. Wojtys, Morphologic characteristics help explain the gender difference in peak anterior cruciate ligament strain during a simulated pivot landing., Am. J. Sports Med. 40 (2012) 32–40. doi:10.1177/0363546511422325.

[119] J. Hashemi, R. Breighner, T.H. Jang, N. Chandrashekar, S. Ekwaro-Osire, J.R. Slauterbeck, Increasing pre-activation of the quadriceps muscle protects the anterior cruciate ligament during the landing phase of a jump: an in vitro simulation, Knee. 17 (2010) 235–241. doi:S0968-0160(09)00177-X [pii]10.1016/j.knee.2009.09.010.

[120] Z.J. Domire, R.L. Boros, J. Hashemi, An examination of possible quadriceps force at the time of anterior cruciate ligament injury during landing: A simulation study., J. Biomech. 44 (2011) 1630–2. doi:10.1016/j.jbiomech.2011.03.001.

[121] D.B. Lipps, E.M. Wojtys, J.A. Ashton-Miller, Anterior cruciate ligament fatigue failures in knees subjected to repeated simulated pivot landings., Am. J. Sports Med. 41 (2013) 1058–66. doi:10.1177/0363546513477836.

[122] S.G. McLean, A. Su, A.J. van den Bogert, Development and Validation of a 3-D Model to Predict Knee Joint Loading During Dynamic Movement, J. Biomech. Eng. 125 (2003) 864–874. doi:10.1115/1.1634282.

[123] M.A. Pflum, K.B. Shelburne, M.R. Torry, M.J. Decker, M.G. Pandy, Model prediction of anterior cruciate ligament force during drop-landings, Med. Sci. Sports Exerc. 36 (2004) 1949–1958. http://www.ncbi.nlm.nih.gov/entrez/query.fcgi?cmd=Retrieve&db=PubMed&dopt=Citation&list_uids=15514512.

[124] S.G. McLean, X. Huang, A. Su, A.J. Van Den Bogert, Sagittal plane biomechanics cannot injure the ACL during sidestep cutting, Clin. Biomech. 19 (2004) 828–838. doi:10.1016/j.clinbiomech.2004.06.006S0268-0033(04)00140-8 [pii].

[125] K.B. Shelburne, M.G. Pandy, F.C. Anderson, M.R. Torry, Pattern of anterior cruciate ligament force in normal walking, J. Biomech. 37 (2004) 797–805. http://www.ncbi.nlm.nih.gov/entrez/query.fcgi?cmd=Retrieve&db=PubMed&dopt=Citation&list_uids=15111067.

[126] J.P. Halloran, A. Erdemir, A.J. van den Bogert, Adaptive surrogate modeling for efficient coupling of musculoskeletal control and tissue deformation models, J. Biomech. Eng. 131 (2009) 11014. doi:10.1115/1.3005333.

[127] G. Cerulli, D.L. Benoit, M. Lamontagne, A. Caraffa, A. Liti, In vivo anterior cruciate ligament strain behaviour during a rapid deceleration movement: case report, Knee Surg. Sports Traumatol. Arthrosc. 11 (2003) 307–11.

[128] M.R. Torry, K.B. Shelburne, D.S. Peterson, J.E. Giphart, J.P. Krong, C. Myers, J.R. Steadman, S.L.-Y. Woo, Knee kinematic profiles during drop landings: a biplane fluoroscopy study, Med. Sci. Sports Exerc. 43 (2011) 533–541. doi:10.1249/MSS.0b013e3181f1e491.

[129] M.R. Torry, C. Myers, K.B. Shelburne, D. Peterson, J.E. Giphart, W.W. Pennington, J.P. Krong, S.L.-Y. Woo, J.R. Steadman, Relationship of knee shear force and extensor moment on knee translations in females performing drop landings: A biplane fluoroscopy study, Clin. Biomech. 26 (2011) 1019–1024. doi:10.1016/j.clinbiomech.2011.06.010.

[130] M.R. Torry, C. Myers, W.W. Pennington, K.B. Shelburne, J.P. Krong, J.E. Giphart, J.R. Steadman, S.L.-Y. Woo, Relationship of anterior knee laxity to knee translations during drop landings: a bi-plane fluoroscopy study, Knee Surg. Sports Traumatol. Arthrosc. 19 (2011) 653–662. doi:10.1007/s00167-010-1327-6.

[131] G.S. Berns, M.L. Hull, H.A. Patterson, Strain in the anteromedial bundle of the anterior cruciate ligament under combination loading, J. Orthop. Res. 10 (1992) 167–176.

[132] S.L.-Y. Woo, Mechanical properties of tendons and ligaments. I. Quasi-static and nonlinear viscoelastic properties, Biorheology. 19 (1982) 385–396.

[133] D.L. Butler, Y. Guan, M.D. Kay, J.F. Cummings, S.M. Feder, M.S. Levy, Location-dependent variations in the material properties of the anterior cruciate ligament, J. Biomech. 25 (1992) 511–8. http://www.ncbi.nlm.nih.gov/pubmed/1592856.

[134] N. Chandrashekar, H. Mansouri, J. Slauterbeck, J. Hashemi, Sex-based differences in the tensile properties of the human anterior cruciate ligament., J. Biomech. 39 (2006) 2943–50. doi:10.1016/j.jbiomech.2005.10.031.

[135] J.C. Kennedy, R.J. Hawkins, R.B. Willis, K.D. Danylchuck, Tension studies of human knee ligaments. Yield point, ultimate failure, and disruption of the cruciate and tibial collateral ligaments, J. Bone Joint Surg. Am. 58 (1976) 350–355.

[136] F.R. Noyes, D.L. Butler, E.S. Grood, R.F. Zernicke, M.S. Hefzy, Biomechanical Analysis of Human Ligament Grafts used in Knee-Ligament Repairs and Reconstructions, J. Bone Joint Surg. Am. (1984) 344–352.

[137] S.L.-Y. Woo, M.A. Gomez, W.H. Akeson, The time and history-dependent viscoelastic properties of the canine medical collateral ligament, J. Biomech. Eng. 103 (1981) 293–298.

[138] B.D. Beynnon, R.J. Johnson, Anterior cruciate ligament injury rehabilitation in athletes. Biomechanical considerations, Sport. Med. 22 (1996) 54–64.

[139] M.S. Hefzy, E.S. Grood, Sensitivity of insertion locations on length patterns of anterior cruciate ligament fibers, J. Biomech. Eng. 108 (1986) 73–82.

[140] R.S. Jones, N.S.S. Nawana, M.J.J. Pearcy, D.J.A. Learmonth, D.R.R. Bickerstaff, J.J.J. Costi, R.S.S. Paterson, J.R. S, N.S.S. Nawana, M.J.J. Pearcy, D.J.A. Learmonth, D.R.R. Bickerstaff, J.J.J. Costi, R.S.S. Paterson, Mechanical properties of the human anterior cruciate ligament, Clin. Biomech. (Bristol, Avon). 10 (1995) 339–344.

[141] S.L.-Y. Woo, J.M. Hollis, D.J. Adams, R.M. Lyon, S. Takai, Tensile properties of the human femur- anterior cruciate ligament-tibia complex: The effects of specimen age and orientation, Am. J. Sports Med. 19 (1991) 217–225.

[142] T.J. Mommersteeg, L. Blankevoort, R. Huiskes, J.G. Kooloos, J.M. Kauer,

Characterization of the mechanical behavior of human knee ligaments: a numerical-experimental approach, J. Biomech. 29 (1996) 151–160.
[143] W. Furman, J.L. Marshall, F. Girgis, The anterior cruciate ligament: a functional analysis based on postmortem studies, J. Bone Jt. Surg. 58-A (1976) 179–185.
[144] A.A. Amis, G.P.C. Dawkins, Functional Anatomy of the Anterior Cruciate Ligament, J. Bone Jt. Surg. (1991) 260–267.
[145] M.K. Kwan, T.W. Lin, S.L.-Y. Woo, On the viscoelastic properties of the anteromedial bundle of the anterior cruciate ligament., J. Biomech. 26 (1993) 447–52. http://www.ncbi.nlm.nih.gov/pubmed/8478348.
[146] B.D. Beynnon, B.C. Fleming, R.J. Johnson, C.E. Nichols, P.A. Renstrom, M.H. Pope, Anterior cruciate ligament strain behavior during rehabilitation exercises in vivo, Am. J. Sports Med. 23 (1995) 24–34. doi:10.1177/036354659502300105.
[147] B.D. Beynnon, R.J. Johnson, B.C. Fleming, C.J. Stankewich, P.A. Renstrom, C.E. Nichols, The strain behavior of the anterior cruciate ligament during squatting and active flexion-extension. A comparison of an open and a closed kinetic chain exercise, Am. J. Sports Med. 25 (1997) 823–829. doi:10.1177/036354659702500616.
[148] B.D. Beynnon, R.J. Johnson, B.C. Fleming, G.D. Peura, P.A. Renstrom, C.E. Nichols, M.H. Pope, The effect of functional knee bracing on the anterior cruciate ligament in the weightbearing and nonweightbearing knee, Am. J. Sports Med. 25 (1997) 353–359. doi:10.1177/036354659702500314.
[149] B.D. Beynnon, B.C. Fleming, Anterior cruciate ligament strain in-vivo: a review of previous work., J. Biomech. 31 (1998) 519–25. http://www.ncbi.nlm.nih.gov/pubmed/9755036.
[150] E. Yamamoto, K. Hayashi, N. Yamamoto, Mechanical properties of collagen fascicles from the rabbit patellar tendon., J. Biomech. Eng. 121 (1999) 124–31. http://www.ncbi.nlm.nih.gov/pubmed/16502659.
[151] G. a Johnson, D.M. Tramaglini, R.E. Levine, K. Ohno, N.Y. Choi, S.L.-Y. Woo, Tensile and viscoelastic properties of human patellar tendon., J. Orthop. Res. 12 (1994) 796–803. doi:10.1002/jor.1100120607.
[152] G.M. Thornton, a Oliynyk, C.B. Frank, N.G. Shrive, Ligament creep cannot be predicted from stress relaxation at low stress: a biomechanical study of the rabbit medial collateral ligament., J. Orthop. Res. 15 (1997) 652–6. doi:10.1002/jor.1100150504.
[153] D.P. Pioletti, L.R. Rakotomanana, P.F. Leyvraz, Strain rate effect on the mechanical behavior of the anterior cruciate ligament-bone complex., Med. Eng. Phys. 21 (1999) 95–100. http://www.ncbi.nlm.nih.gov/pubmed/10426509.
[154] C.K. Smith, M.L. Hull, S.M. Howell, Does graft construct lengthening at the fixations cause an increase in anterior laxity following anterior cruciate ligament reconstruction in vivo?, J. Biomech. Eng. 132 (2010) 0810011–0810017. doi:10.1115/1.4001027.
[155] D.M. Elliott, P.S. Robinson, J.A. Gimbel, J.J. Sarver, J.A. Abboud, R. V. Iozzo, L.J. Soslowsky, Effect of Altered Matrix Proteins on Quasilinear Viscoelastic Properties in Transgenic Mouse Tail Tendons, Ann. Biomed. Eng. 31 (2003) 599–605. doi:10.1114/1.1567282.
[156] S. Martelli, A. Joukhadar, S. Zaffagnini, M. Marcacci, S. Lavallee, G.

Champleboux, Fiber-based anterior cruciate ligament model for biomechanical simulations., J. Orthop. Res. 16 (1998) 379–85. doi:10.1002/jor.1100160315.

[157] P.P. Provenzano, R.S. Lakes, T. Keenan, J.. R. Vanderby, Nonlinear Ligament Viscoelasticity, Ann. Biomed. Eng. 29 (2001) 908–914. doi:10.1114/1.1408926.

[158] E.M. Arruda, S. Calve, R.G. Dennis, K. Mundy, K. Baar, Regional variation of tibialis anterior tendon mechanics is lost following denervation., J. Appl. Physiol. 101 (2006) 1113–7. doi:10.1152/japplphysiol.00612.2005.

[159] E.A. Arendt, R. Dick, Knee injury patterns among men and women in collegiate basketball and soccer. NCAA data and review of literature, Am. J. Sports Med. 23 (1995) 694–701.

[160] S.G. McLean, S.W. Lipfert, A.J. van den Bogert, Effect of gender and defensive opponent on the biomechanics of sidestep cutting, Med. Sci. Sports Exerc. 36 (2004) 1008–1016. doi:00005768-200406000-00014 [pii].

[161] S.G. McLean, R.J. Neal, P.T. Myers, M.R. Walters, Knee joint kinematics during the sidestep cutting maneuver: potential for injury in women, Med. Sci. Sports Exerc. 31 (1999) 959–968. http://www.ncbi.nlm.nih.gov/entrez/query.fcgi?cmd=Retrieve&db=PubMed&dopt=Citation&list_uids=10416556.

[162] T.E. Hewett, G.D. Myer, K.R. Ford, Anterior cruciate ligament injuries in female athletes: Part 1, mechanisms and risk factors, Am. J. Sports Med. 34 (2006) 299–311. http://www.ncbi.nlm.nih.gov/entrez/query.fcgi?cmd=Retrieve&db=PubMed&dopt=Citation&list_uids=16423913.

[163] G.D. Myer, K.R. Ford, T.E. Hewett, G.D. Myer, T.E. Hewett, The effects of gender on quadriceps muscle activation strategies during a maneuver that mimics a high ACL injury risk position, J Electromyogr Kinesiol. 15 (2005) 181–189. http://www.ncbi.nlm.nih.gov/entrez/query.fcgi?cmd=Retrieve&db=PubMed&dopt=Citation&list_uids=15664147.

[164] L.J. Huston, E.M. Wojtys, Neuromuscular performance characteristics in elite female athletes, Am. J. Sports Med. 24 (1996) 427–36.

[165] D.E. Gwinn, J.H. Wilckens, E.R. McDevitt, G. Ross, T.C. Kao, The relative incidence of anterior cruciate ligament injury in men and women at the United States Naval Academy, Am. J. Sports Med. 28 (2000) 98–102.

[166] B. Yu, D. Herman, J. Preston, W. Lu, D.T. Kirkendall, W.E. Garrett, Immediate effects of a knee brace with a constraint to knee extension on knee kinematics and ground reaction forces in a stop-jump task, Am. J. Sports Med. 32 (2004) 1136–1143.

[167] T.E. Hewett, K.R. Ford, G.D. Myer, Anterior Cruciate Ligament Injuries in Female Athletes: Part 2, A Meta-analysis of Neuromuscular Interventions Aimed at Injury Prevention, Am. J. Sports Med. 34 (2006) 490–498. http://www.ncbi.nlm.nih.gov/entrez/query.fcgi?cmd=Retrieve&db=PubMed&dopt=Citation&list_uids=16382007.

[168] S.G. McLean, K.B. Walker, A.J. van den Bogert, Effect of gender on lower extremity kinematics during rapid direction changes: an integrated analysis of three sports movements, J. Sci. Med. Sport. 8 (2005) 411–422. http://www.ncbi.nlm.nih.gov/entrez/query.fcgi?cmd=Retrieve&db=PubMed&dopt=

Citation&list_uids=16602169.

[169] A.F. Anderson, D.C. Dome, S. Gautam, M.H. Awh, G.W. Rennirt, Correlation of anthropometric measurements, strength, anterior cruciate ligament size, and intercondylar notch characteristics to sex differences in anterior cruciate ligament tear rates, Am. J. Sports Med. 29 (2001) 58–66. http://www.ncbi.nlm.nih.gov/entrez/query.fcgi?cmd=Retrieve&db=PubMed&dopt=Citation&list_uids=11206258.

[170] N. Chandrashekar, J. Slauterbeck, J. Hashemi, Sex-based differences in the anthropometric characteristics of the anterior cruciate ligament and its relation to intercondylar notch geometry: a cadaveric study, Am. J. Sports Med. 33 (2005) 1492–1498. http://www.ncbi.nlm.nih.gov/entrez/query.fcgi?cmd=Retrieve&db=PubMed&dopt=Citation&list_uids=16009992.

[171] J. Hashemi, R. Breighner, N. Chandrashekar, D.M. Hardy, A.M. Chaudhari, S.J. Shultz, J.R. Slauterbeck, B.D. Beynnon, Hip extension, knee flexion paradox: a new mechanism for non-contact ACL injury., J. Biomech. 44 (2011) 577–85. doi:10.1016/j.jbiomech.2010.11.013.

[172] T. Muneta, K. Takakuda, H. Yamamoto, Intercondylar notch width and its relation to the configuration and cross-sectional area of the anterior cruciate ligament. A cadaveric knee study, Am. J. Sports Med. 25 (1997) 69–72.

[173] J. Hashemi, N. Chandrashekar, H. Mansouri, J.R. Slauterbeck, D.M. Hardy, The human anterior cruciate ligament: sex differences in ultrastructure and correlation with biomechanical properties, J. Orthop. Res. 26 (2008) 945–950. doi:10.1002/jor.20621.

[174] S.J. Shultz, S.E. Kirk, M.L. Johnson, T.C. Sander, D.H. Perrin, Relationship between sex hormones and anterior knee laxity across the menstrual cycle, Med. Sci. Sports Exerc. 36 (2004) 1165–1174. http://www.ncbi.nlm.nih.gov/entrez/query.fcgi?cmd=Retrieve&db=PubMed&dopt=Citation&list_uids=15235320.

[175] S.J. Shultz, R.J. Schmitz, A.D. Nguyen, A.M. Chaudhari, D.A. Padua, S.G. McLean, S.M. Sigward, ACL Research Retreat V: an update on ACL injury risk and prevention, March 25-27, 2010, Greensboro, NC, J. Athl. Train. 45 (2010) 499–508. doi:10.4085/1062-6050-45.5.499.

[176] S.G. McLean, X. Huang, A.J. Van Den Bogert, Investigating isolated neuromuscular control contributions to non-contact anterior cruciate ligament injury risk via computer cimulation methods, Clin. Biomech. 23 (2008) 926–937.

[177] N. Chandrashekar, J. Hashemi, J. Slauterbeck, B.D. Beynnon, Low-load behaviour of the patellar tendon graft and its relevance to the biomechanics of the reconstructed knee, Clin. Biomech. (Bristol, Avon). 23 (2008) 918–25. doi:10.1016/j.clinbiomech.2008.03.070.

[178] Y. Yoshioka, D. Siu, T.D. Cooke, The anatomy and functional axes of the femur, J. Bone Joint Surg. Am. 69 (1987) 873–880. http://www.ncbi.nlm.nih.gov/entrez/query.fcgi?cmd=Retrieve&db=PubMed&dopt=Citation&list_uids=3597501.

[179] Y. Yoshioka, D.W. Siu, R.A. Scudamore, T.D. Cooke, Tibial anatomy and functional axes, J. Orthop. Res. 7 (1989) 132–137.

http://www.ncbi.nlm.nih.gov/entrez/query.fcgi?cmd=Retrieve&db=PubMed&dopt=Citation&list_uids=2908904.

[180] R.A. Simon, J.S. Everhart, H.N. Nagaraja, A.M. Chaudhari, A case-control study of anterior cruciate ligament volume, tibial plateau slopes and intercondylar notch dimensions in ACL-injured knees, J. Biomech. 43 (2010) 1702–1707. doi:S0021-9290(10)00142-9 [pii]10.1016/j.jbiomech.2010.02.033.

[181] V. Stein, L. Li, A. Guermazi, Y. Zhang, C. Kent Kwoh, C.B. Eaton, D.J. Hunter, The relation of femoral notch stenosis to ACL tears in persons with knee osteoarthritis, Osteoarthritis Cartilage. 18 (2010) 192–199. doi:S1063-4584(09)00247-7 [pii]10.1016/j.joca.2009.09.006.

[182] J.M. Uhorchak, C.R. Scoville, G.N. Williams, R.A. Arciero, P. St Pierre, D.C. Taylor, Risk factors associated with noncontact injury of the anterior cruciate ligament: a prospective four-year evaluation of 859 West Point cadets, Am. J. Sports Med. 31 (2003) 831–842. http://www.ncbi.nlm.nih.gov/entrez/query.fcgi?cmd=Retrieve&db=PubMed&dopt=Citation&list_uids=14623646.

[183] T.J. Davis, K.D. Shelbourne, T.E. Klootwyk, Correlation of the intercondylar notch width of the femur to the width of the anterior and posterior cruciate ligaments, Knee Surg. Sports Traumatol. Arthrosc. 7 (1999) 209–214. http://www.ncbi.nlm.nih.gov/entrez/query.fcgi?cmd=Retrieve&db=PubMed&dopt=Citation&list_uids=10462209.

[184] M. Dienst, G. Schneider, K. Altmeyer, K. Voelkering, T. Georg, B. Kramann, D. Kohn, Correlation of intercondylar notch cross sections to the ACL size: a high resolution MR tomographic in vivo analysis, Arch Orthop Trauma Surg. 127 (2007) 253–260. doi:10.1007/s00402-006-0177-7.

[185] W.P. Charlton, T.A. St John, M.G. Ciccotti, N. Harrison, M. Schweitzer, Differences in femoral notch anatomy between men and women: a magnetic resonance imaging study, Am. J. Sports Med. 30 (2002) 329–333. http://www.ncbi.nlm.nih.gov/entrez/query.fcgi?cmd=Retrieve&db=PubMed&dopt=Citation&list_uids=12016071.

[186] L. Stijak, V. Radonjic, V. Nikolic, Z. Blagojevic, M. Aksic, B. Filipovic, Correlation between the morphometric parameters of the anterior cruciate ligament and the intercondylar width: gender and age differences, Knee Surg. Sports Traumatol. Arthrosc. 17 (2009) 812–817. doi:10.1007/s00167-009-0807-z.

[187] C.C. Teitz, B.K. Lind, B.M. Sacks, Symmetry of the femoral notch width index, Am. J. Sports Med. 25 (1997) 687–90.

[188] M.L. Ireland, B.T. Ballantyne, K. Little, I.S. McClay, A radiographic analysis of the relationship between the size and shape of the intercondylar notch and anterior cruciate ligament injury, Knee Surg. Sports Traumatol. Arthrosc. 9 (2001) 200–5.

[189] L. Stijak, V. Nikolic, Z. Blagojevic, V. Radonjic, G. Santrac-Stijak, G. Stankovic, N. Popovic, [Influence of morphometric intercondylar notch parameters in ACL ruptures], Acta Chir Iugosl. 53 (2006) 79–83. http://www.ncbi.nlm.nih.gov/entrez/query.fcgi?cmd=Retrieve&db=PubMed&dopt=Citation&list_uids=17688039.

[190] T.O. Souryal, T.R. Freeman, Intercondylar notch size and anterior cruciate ligament injuries in athletes. A prospective study [published erratum appears in

Am J Sports Med 1993 Sep-Oct;21(5):723], Am. J. Sports Med. 21 (1993) 535–539.

[191] L. Stijak, R.F. Herzog, P. Schai, Is there an influence of the tibial slope of the lateral condyle on the ACL lesion? A case-control study, Knee Surg. Sports Traumatol. Arthrosc. 16 (2008) 112–117. doi:10.1007/s00167-007-0438-1.

[192] D.T. Fung, L.Q. Zhang, Modeling of ACL impingement against the intercondylar notch, Clin. Biomech. 18 (2003) 933–941. doi:S0268003303001748 [pii].

[193] D.T. Fung, R.W. Hendrix, J.L. Koh, L.Q. Zhang, ACL impingement prediction based on MRI scans of individual knees, Clin. Orthop. Relat. Res. 460 (2007) 210–218. doi:10.1097/BLO.0b013e31804d2339.

[194] H.-S.S. Park, C. Ahn, D.T. Fung, Y. Ren, L.-Q.Q. Zhang, A knee-specific finite element analysis of the human anterior cruciate ligament impingement against the femoral intercondylar notch, J. Biomech. 43 (2010) 2039–2042. doi:10.1016/j.jbiomech.2010.03.015.

[195] J.S. Everhart, D.C. Flanigan, R.A. Simon, A.M. Chaudhari, Association of noncontact anterior cruciate ligament injury with presence and thickness of a bony ridge on the anteromedial aspect of the femoral intercondylar notch, Am. J. Sports Med. 38 (2010) 1667–1673. doi:0363546510367424 [pii]10.1177/0363546510367424.

[196] C.S. Shin, A.M. Chaudhari, C.O. Dyrby, T.P. Andriacchi, Influence of patellar ligament insertion angle on quadriceps usage during walking in anterior cruciate ligament reconstructed subjects, J. Orthop. Res. 27 (2009) 730–735. doi:10.1002/jor.20806.

[197] C.F. van Eck, C.A. Martins, S.M. Vyas, U. Celentano, C.N. van Dijk, F.H. Fu, Femoral intercondylar notch shape and dimensions in ACL-injured patients, Knee Surg. Sports Traumatol. Arthrosc. 18 (2010) 1257–1262. doi:10.1007/s00167-010-1135-z.

[198] M.L. Brandon, P.T. Haynes, J.R. Bonamo, M.I. Flynn, G.R. Barrett, M.F. Sherman, The association between posterior-inferior tibial slope and anterior cruciate ligament insufficiency, Arthroscopy. 22 (2006) 894–899. http://www.ncbi.nlm.nih.gov/entrez/query.fcgi?cmd=Retrieve&db=PubMed&dopt=Citation&list_uids=16904590.

[199] M.S. Todd, S. Lalliss, E. Garcia, T.M. DeBerardino, K.L. Cameron, The relationship between posterior tibial slope and anterior cruciate ligament injuries, Am. J. Sports Med. 38 (2010) 63–67. doi:0363546509343198 [pii]10.1177/0363546509343198.

[200] J. Hashemi, N. Chandrashekar, H. Mansouri, B. Gill, J.R. Slauterbeck, R.C. Schutt Jr., E. Dabezies, B.D. Beynnon, Shallow medial tibial plateau and steep medial and lateral tibial slopes: new risk factors for anterior cruciate ligament injuries, Am. J. Sports Med. 38 (2010) 54–62. doi:0363546509349055 [pii]10.1177/0363546509349055.

[201] S.G. McLean, S.M. Lucey, S. Rohrer, C. Brandon, Knee joint anatomy predicts high-risk in vivo dynamic landing knee biomechanics., Clin. Biomech. (Bristol, Avon). 25 (2010) 781–8. doi:10.1016/j.clinbiomech.2010.06.002.

[202] K.M. Bojicic, M.L. Beaulieu, D.Y. Imaizumi Krieger, J.A. Ashton-Miller, E.M. Wojtys, Association Between Lateral Posterior Tibial Slope, Body Mass Index,

and ACL Injury Risk, Orthop. J. Sport. Med. 5 (2017) 232596711668866. doi:10.1177/2325967116688664.
[203] J.L. Lewis, W.D. Lew, J.A. Hill, P. Hanley, K. Ohland, S. Kirstukas, R.E. Hunter, Knee joint motion and ligamental forces before and after ACL reconstruction, J. Biomech. Eng. 111 (1989) 97–106. http://www.ncbi.nlm.nih.gov/pubmed/2733414.
[204] S.F. Dye, E.M. Wojtys, F.H. Fu, D.C. Fithian, I. Gillquist, Factors contributing to function of the knee joint after injury or reconstruction of the anterior cruciate ligament, Instr. Course Lect. 48 (1999) 185–198. http://www.ncbi.nlm.nih.gov/pubmed/10098044.
[205] C.D. Harner, J.R. Giffin, R.C. Dunteman, C.C. Annunziata, M.J. Friedman, Evaluation and treatment of recurrent instability after anterior cruciate ligament reconstruction, Instr. Course Lect. 50 (2001) 463–474. http://www.ncbi.nlm.nih.gov/pubmed/11372347.
[206] K.L. Moffat, W.-H.S. Sun, N.O. Chahine, P.E. Pena, S.B. Doty, C.T. Hung, G. a Ateshian, H.H. Lu, Characterization of the mechanical properties and mineral distribution of the anterior cruciate ligament-to-bone insertion site., Conf. Proc. ... Annu. Int. Conf. IEEE Eng. Med. Biol. Soc. IEEE Eng. Med. Biol. Soc. Annu. Conf. 1 (2006) 2366–9. doi:10.1109/IEMBS.2006.259299.
[207] S.U. Scheffler, F.N. Unterhauser, A. Weiler, Graft remodeling and ligamentization after cruciate ligament reconstruction., Knee Surg. Sports Traumatol. Arthrosc. 16 (2008) 834–42. doi:10.1007/s00167-008-0560-8.
[208] S.L. Keays, J.E. Bullock-Saxton, A.C. Keays, P.A. Newcombe, M.I. Bullock, A 6-year follow-up of the effect of graft site on strength, stability, range of motion, function, and joint degeneration after anterior cruciate ligament reconstruction: patellar tendon versus semitendinosus and Gracilis tendon graft, Am. J. Sports Med. 35 (2007) 729–739. doi:10.1177/0363546506298277.
[209] J.O. Anders, R. a Venbrocks, M. Weinberg, Proprioceptive skills and functional outcome after anterior cruciate ligament reconstruction with a bone-tendon-bone graft., Int. Orthop. 32 (2008) 627–33. doi:10.1007/s00264-007-0381-2.
[210] D.M. Hopper, G.R. Strauss, J.J. Boyle, J. Bell, Functional recovery after anterior cruciate ligament reconstruction: a longitudinal perspective., Arch. Phys. Med. Rehabil. 89 (2008) 1535–41. doi:10.1016/j.apmr.2007.11.057.
[211] F.W. Smith, Subjective functional assessments and the return to competitive sport after anterior cruciate ligament reconstruction, Br. J. Sports Med. 38 (2004) 279–284. doi:10.1136/bjsm.2002.001982.
[212] E. Ageberg, A. Pettersson, T. Fridén, 15-Year Follow-Up of Neuromuscular Function in Patients With Unilateral Nonreconstructed Anterior Cruciate Ligament Injury Initially Treated With Rehabilitation and Activity Modification: a Longitudinal Prospective Study., Am. J. Sports Med. 35 (2007) 2109–17. doi:10.1177/0363546507305018.
[213] M.A. Kessler, H. Behrend, S. Henz, G. Stutz, A. Rukavina, M.S. Kuster, Function, osteoarthritis and activity after ACL-rupture: 11 years follow-up results of conservative versus reconstructive treatment., Knee Surg. Sports Traumatol. Arthrosc. 16 (2008) 442–8. doi:10.1007/s00167-008-0498-x.
[214] J.O. Drogset, T. Grontvedt, O.R. Robak, A. Molster, A.T. Viset, L. Engebretsen, A sixteen-year follow-up of three operative techniques for the treatment of acute

ruptures of the anterior cruciate ligament, J. Bone Joint Surg. Am. 88 (2006) 944–952. doi:88/5/944 [pii]10.2106/JBJS.D.02876.

[215] M. Marcacci, S. Zaffagnini, G. Giordano, F. Iacono, M. Lo Presti, Anterior cruciate ligament reconstruction associated with extra-articular tenodesis: A prospective clinical and radiographic evaluation with 10- to 13-year follow-up., Am. J. Sports Med. 37 (2009) 707–14. doi:10.1177/0363546508328114.

[216] A. von Porat, E.M. Roos, H.P. Roos, High prevalence of osteoarthritis 14 years after an anterior cruciate ligament tear in male soccer players: a study of radiographic and patient relevant outcomes, Ann. Rheum. Dis. 63 (2004) 269–273. http://www.ncbi.nlm.nih.gov/entrez/query.fcgi?cmd=Retrieve&db=PubMed&dopt=Citation&list_uids=14962961.

[217] K.D. Shelbourne, T. Gray, M. Haro, Incidence of subsequent injury to either knee within 5 years after anterior cruciate ligament reconstruction with patellar tendon autograft., Am. J. Sports Med. 37 (2009) 246–51. doi:10.1177/0363546508325665.

[218] C.C. Kaeding, B. Aros, A. Pedroza, E. Pifel, A. Amendola, J.T. Andrish, W.R. Dunn, R.G. Marx, E.C. McCarty, R.D. Parker, R.W. Wright, K.P. Spindler, Allograft Versus Autograft Anterior Cruciate Ligament Reconstruction: Predictors of Failure From a MOON Prospective Longitudinal Cohort., Sports Health. 3 (2011) 73–81. doi:10.1177/1941738110386185.

[219] K.P. Spindler, R.W. Wright, Clinical Practice. Anterior Cruciate Ligament Tear, N. Engl. J. Med. 359 (2008) 2135–2142.

[220] T. Aït Si Selmi, D. Fithian, P. Neyret, The evolution of osteoarthritis in 103 patients with ACL reconstruction at 17 years follow-up., Knee. 13 (2006) 353–8. doi:10.1016/j.knee.2006.02.014.

[221] L.J. Salmon, V.J. Russell, K. Refshauge, D. Kader, C. Connolly, J. Linklater, L. a Pinczewski, Long-term outcome of endoscopic anterior cruciate ligament reconstruction with patellar tendon autograft: minimum 13-year review., Am. J. Sports Med. 34 (2006) 721–32. doi:10.1177/0363546505282626.

[222] R.T. Ballock, S.L.-Y. Woo, R.M. Lyon, J.M. Hollis, W.H. Akeson, Use of patellar tendon autograft for anterior cruciate ligament reconstruction in the rabbit: a long-term histologic and biomechanical study., J. Orthop. Res. 7 (1989) 474–85. doi:10.1002/jor.1100070404.

[223] U. Bosch, B. Decker, W. Kasperczyk, A. Nerlich, H.J. Oestern, H. Tscherne, The relationship of mechanical properties to morphology in patellar tendon autografts after posterior cruciate ligament replacement in sheep., J. Biomech. 25 (1992) 821–30. http://www.ncbi.nlm.nih.gov/pubmed/1639826.

[224] D.W. Jackson, E.S. Grood, J.D. Goldstein, M.A. Rosen, P.R. Kurzweil, J.F. Cummings, T.M. Simon, A comparison of patellar tendon autograft and allograft used for anterior cruciate ligament reconstruction in the goat model., Am. J. Sports Med. 21 (1992) 176–85. http://www.ncbi.nlm.nih.gov/pubmed/8465909.

[225] B.T. Haraldsson, P. Aagaard, M. Krogsgaard, T. Alkjaer, M. Kjaer, S.P. Magnusson, Region-specific mechanical properties of the human patella tendon., J. Appl. Physiol. 98 (2005) 1006–12. doi:10.1152/japplphysiol.00482.2004.

[226] V. Chouliaras, S. Ristanis, C. Moraiti, N. Stergiou, A.D. Georgoulis, Effectiveness

of reconstruction of the anterior cruciate ligament with quadrupled hamstrings and bone-patellar tendon-bone autografts: an in vivo study comparing tibial internal-external rotation., Am. J. Sports Med. 35 (2007) 189–96. doi:10.1177/0363546506296040.

[227] T.L. Haut Donahue, C. Gregersen, M.L. Hull, S.M. Howell, T.L. Donahue, C. Gregersen, M.L. Hull, S.M. Howell, Comparison of Viscoelastic, Structural, and Material Properties of Double-Looped Anterior Cruciate Ligament Grafts Made From Bovine Digital Extensor and Human Hamstring Tendons, J. Biomech. Eng. 123 (2001) 162–169. doi:10.1115/1.1351889.

[228] J. Hashemi, N. Chandrashekar, J. Slauterbeck, The mechanical properties of the human patellar tendon are correlated to its mass density and are independent of sex., Clin. Biomech. (Bristol, Avon). 20 (2005) 645–52. doi:10.1016/j.clinbiomech.2005.02.008.

[229] W.G. Clancy, R.G. Narechania, T.D. Rosenberg, J.G. Gmeiner, D.D. Wisnefske, T.A. Lange, Anterior and Posterior Cruciate Ligament Reconstruction in Rhesus Monkeys, J. Bone Jt. Surg. 63-A (1981) 1270–1284.

[230] S.L.-Y. Woo, R.H. Peterson, K.J. Ohland, T.J. Sites, M.I. Danto, The effects of strain rate on the properties of the medial collateral ligament in skeletally immature and mature rabbits: a biomechanical and histological study., J. Orthop. Res. 8 (1990) 712–21. doi:10.1002/jor.1100080513.

[231] R.A. Hart, S.L.-Y. Woo, P.O. Newton, Ultrastructural morphometry of anterior cruciate and medial collateral ligaments: an experimental study in rabbits., J. Orthop. Res. 10 (1992) 96–103. doi:10.1002/jor.1100100112.

[232] M.L. Roemhildt, K.M. Coughlin, G.D. Peura, G.J. Badger, D. Churchill, B.C. Fleming, B.D. Beynnon, Effects of increased chronic loading on articular cartilage material properties in the lapine tibio-femoral joint., J. Biomech. 43 (2010) 2301–8. doi:10.1016/j.jbiomech.2010.04.035.

[233] D. Amiel, C.B. Frank, F. Harwood, J. Fronek, W.H. Akeson, Tendons and ligaments: a morphological and biochemical comparison., J. Orthop. Res. 1 (1984) 257–65. doi:10.1002/jor.1100010305.

[234] M.L. Zec, P. Thistlethwaite, C.B. Frank, N.G. Shrive, Characterization of the Fatigue Behavior of the Medial Collateral Ligament Utilizing Traditional and Novel Mechanical Variables for the Assessment of Damage, J. Biomech. Eng. 132 (2010) 011001. doi:10.1115/1.4000108.

[235] S. Thomopoulos, G.R. Williams, J.A. Gimbel, M. Favata, L.J. Soslowsky, Variation of biomechanical, structural, and compositional properties along the tendon to bone insertion site., J. Orthop. Res. 21 (2003) 413–9. doi:10.1016/S0736-0266(03)00057-3.

[236] S. Calve, I.F. Lytle, K. Grosh, D.L. Brown, E.M. Arruda, Implantation increases tensile strength and collagen content of self-assembled tendon constructs., J. Appl. Physiol. 108 (2010) 875–81. doi:10.1152/japplphysiol.00921.2009.

[237] M.E. Stasiak, D. Wiznia, S. Alzoobaee, M.C. Ciccotti, C.W. Imhauser, C. Voigt, P.A. Torzilli, X.-H. Deng, S.A. Rodeo, A novel device to apply controlled flexion and extension to the rat knee following anterior cruciate ligament reconstruction., J. Biomech. Eng. 134 (2012) 041008. doi:10.1115/1.4006341.

[238] J. Ma, K. Goble, M.J. Smietana, T.Y. Kostrominova, L.M. Larkin, E.M. Arruda,

Morphological and functional characteristics of three-dimensional engineered bone-ligament-bone constructs following implantation., J. Biomech. Eng. 131 (2009) 1010171–1010179. doi:10.1115/1.4000151.

[239] L.A. Setton, V.C. Mow, F.J. Müller, J.C. Pita, D.S. Howell, F.J. Muller, J.C. Pita, D.S. Howell, Mechanical properties of canine articular cartilage are significantly altered following transection of the anterior cruciate ligament, J. Orthop. Res. 12 (1994) 451–463. doi:10.1002/jor.1100120402.

[240] H.E. Figgie, E.H. Bahniuk, K.G. Heiple, D.T. Davy, The effects of tibial-femoral angle on the failure mechanics of the canine anterior cruciate ligament, J. Biomech. 19 (1986) 89–91. http://www.ncbi.nlm.nih.gov/entrez/query.fcgi?cmd=Retrieve&db=PubMed&dopt=Citation&list_uids=3957947.

[241] M. Therin, P. Christel, F. Crespeau, L. Dürselen, L. Claes, Functional Evaluation of Polyarylamide Fibers for Use in a Prosthesis for Anterior Cruciate Ligament Replacement in Sheep, Clin. Mater. 15 (1994) 69–75.

[242] L. Claes, L. Dürselen, S. Rübenacker, Comparative Investigation on the Biomechanical Properties of Ligament Replacement in the Sheep Knee Using Six Different Ligament Prostheses, Clin. Mater. 15 (1994) 15–22.

[243] R. Meller, E. Willbold, E. Hesse, B. Dreymann, M. Fehr, C. Haasper, C. Hurschler, C. Krettek, F. Witte, Histologic and biomechanical analysis of anterior cruciate ligament graft to bone healing in skeletally immature sheep, Arthroscopy. 24 (2008) 1221–1231. doi:S0749-8063(08)00515-X [pii]10.1016/j.arthro.2008.06.021.

[244] M. Dustmann, T. Schmidt, I. Gangey, F.N. Unterhauser, A. Weiler, S.U. Scheffler, The extracellular remodeling of free-soft-tissue autografts and allografts for reconstruction of the anterior cruciate ligament: a comparison study in a sheep model., Knee Surg. Sports Traumatol. Arthrosc. 16 (2008) 360–369. doi:10.1007/s00167-007-0471-0.

[245] G. Papachristou, A. Kalliakmanis, K. Papachristou, E. Magnissalis, J. Sourlas, S. Plessas, Comparison of fixation methods of double-bundle double-tibial tunnel ACL reconstruction and double-bundle single-tunnel technique, Int. Orthop. 32 (2008) 483–488. doi:10.1007/s00264-007-0343-8.

[246] F.K. Fuss, Anatomy and function of the cruciate ligaments of the domestic pig (Sus scrofa domestica): a comparison with human cruciates., J. Anat. 178 (1991) 11–20. http://www.pubmedcentral.nih.gov/articlerender.fcgi?artid=1260531&tool=pmcentrez&rendertype=abstract.

[247] O. Martel, J.F. Cárdenes, G. Garcés, J.A. Carta, Influence of the crosshead rate on the mechanical properties of fixation systems of ACL tendon grafts., J. Appl. Biomech. 25 (2009) 313–21. http://www.ncbi.nlm.nih.gov/pubmed/20095452.

[248] S.E. Duenwald, J.. R. Vanderby, R.S. Lakes, Stress relaxation and recovery in tendon and ligament: experiment and modeling., Biorheology. 47 (2010) 1–14. doi:10.3233/BIR-2010-0559.

[249] J.A. Maes, T.L. Haut Donahue, Time dependent properties of bovine meniscal attachments: stress relaxation and creep., J. Biomech. 39 (2006) 3055–61. doi:10.1016/j.jbiomech.2005.09.025.

[250] D. Amiel, J.B. Kleiner, R.D. Roux, F.L. Harwood, W.H. Akeson, The phenomenon

of “ligamentization”: anterior cruciate ligament reconstruction with autogenous patellar tendon., J. Orthop. Res. 4 (1986) 162–72. doi:10.1002/jor.1100040204.
[251] K. Blickenstaff, W.A. Grana, D. Egle, Analysis of a Semitendinosus Autograft in a Rabbit Model, Am. J. Sports Med. 25 (1997) 554–559.
[252] W.A. Grana, D.M. Egle, R. Mahnken, C.W. Goodhart, An analysis of autograft fixation after anterior cruciate ligament reconstruction in a rabbit model., Am. J. Sports Med. 22 (1994) 344–51. http://www.ncbi.nlm.nih.gov/pubmed/8037275.
[253] K. Labs, C. Perka, F. Schneider, The biological and biomechanical effect of different graft tensioning in anterior cruciate ligament reconstruction: an experimental study., Arch. Orthop. Trauma Surg. 122 (2002) 193–9. doi:10.1007/s00402-002-0409-4.
[254] H. Sakai, N. Fukui, A. Kawakami, H. Kurosawa, Biological fixation of the graft within bone after anterior cruciate ligament reconstruction in rabbits: effects of the duration of postoperative immobilization., J. Orthop. Sci. 5 (2000) 43–51.
[255] A.K. Aune, M. Hukkanen, J.E. Madsen, J.M. Polak, L. Nordsletten, Nerve regeneration during patellar tendon autograft remodelling after anterior cruciate ligament reconstruction: an experimental and clinical study., J. Orthop. Res. 14 (1996) 193–9. doi:10.1002/jor.1100140205.
[256] S. Yamazaki, K. Yasuda, F. Tomita, A. Minami, H. Tohyama, The effect of graft-tunnel diameter disparity on intraosseous healing of the flexor tendon graft in anterior cruciate ligament reconstruction., Am. J. Sports Med. 30 (2002) 498–505. http://www.ncbi.nlm.nih.gov/pubmed/12130404.
[257] P. Hunt, S.U. Scheffler, F.N. Unterhauser, A. Weiler, A model of soft-tissue graft anterior cruciate ligament reconstruction in sheep., Arch. Orthop. Trauma Surg. 125 (2005) 238–48. doi:10.1007/s00402-004-0643-z.
[258] H. Seitz, T. Hausner, I. Schlenz, S. Lang, J. Eschberger, Vascular anatomy of the ovine anterior cruciate ligament. A macroscopic, histological and radiographic study., Arch. Orthop. Trauma Surg. 116 (1997) 19–21. http://www.ncbi.nlm.nih.gov/pubmed/9006759.
[259] M.I. Danto, S.L.-Y. Woo, The mechanical properties of skeletally mature rabbit anterior cruciate ligament and patellar tendon over a range of strain rates., J. Orthop. Res. 11 (1993) 58–67. doi:10.1002/jor.1100110108.
[260] W.J.P. Radford, A.A. Amis, A.C. Stead, The Ovine Stifle as a Model for Human Cruciate Ligament Surgery, Vet. Comp. Orthop. Traumatol. (1996) 44–49.
[261] M.J. Allen, J.E. Houlton, S.B. Adams, N. Rushton, The surgical anatomy of the stifle joint in sheep, Vet. Surg. 27 (1998) 596–605. http://www.ncbi.nlm.nih.gov/pubmed/9845224.
[262] J.E. Tapper, J.L. Ronsky, M.J. Powers, C. Sutherland, T. Majima, C.B. Frank, N.G. Shrive, In Vivo Measurement of the Dynamic 3-D Kinematics of the Ovine Stifle Joint, J. Biomech. Eng. 126 (2004) 301–318. doi:10.1115/1.1695576.
[263] M.M. Murray, A. Weiler, K.P. Spindler, Interspecies variation in the fibroblast distribution of the anterior cruciate ligament., Am. J. Sports Med. 32 (2004) 1484–91. doi:10.1177/0363546504263700.
[264] L. Dürselen, L. Claes, A. Ignatius, S. Rübenacker, Comparative animal study of three ligament prostheses for the replacement of the anterior cruciate and medial collateral ligament., Biomaterials. 17 (1996) 977–82. doi:10.1016/0142-

9612(96)84671-0.
[265] J.W. Xerogeanes, R.J. Fox, Y. Takeda, H.S. Kim, Y. Ishibashi, G.J. Carlin, S.L.-Y. Woo, A functional comparison of animal anterior cruciate ligament models to the human anterior cruciate ligament., Ann. Biomed. Eng. 26 (1998) 345–52. http://www.ncbi.nlm.nih.gov/pubmed/9570217.
[266] G. Li, J. Gil, A. Kanamori, S.-Y.S.L.-Y.Y. Woo, A validated three-dimensional computational model of a human knee joint., J. Biomech. Eng. 121 (1999) 657–62. doi:10.1115/1.2800871.
[267] G. Li, J. Suggs, T. Gill, The effect of anterior cruciate ligament injury on knee joint function under a simulated muscle load: a three-dimensional computational simulation, Ann. Biomed. Eng. 30 (2002) 713–720. doi:10.1114/1.1484219.
[268] C.S. Shin, A.M. Chaudhari, T.P. Andriacchi, The influence of deceleration forces on ACL strain during single-leg landing: a simulation study, J. Biomech. 40 (2007) 1145–1152. http://www.ncbi.nlm.nih.gov/entrez/query.fcgi?cmd=Retrieve&db=PubMed&dopt=Citation&list_uids=16797556.
[269] J. Yao, G.-M. Kuang, D.W.-C. Wong, W.-X. Niu, M. Zhang, Y.-B. Fan, Influence of screw length and diameter on tibial strain energy density distribution after anterior cruciate ligament reconstruction, Acta Mech. Sin. 30 (2014) 241–249.
[270] E. Peña, B. Calvo, M.A. Martínez, D. Palanca, M. Doblaré, Finite element analysis of the effect of meniscal tears and meniscectomies on human knee biomechanics., Clin. Biomech. (Bristol, Avon). 20 (2005) 498–507. doi:10.1016/j.clinbiomech.2005.01.009.
[271] Y. Song, R.E. Debski, V. Musahl, M. Thomas, S.L.Y. Woo, A three-dimensional finite element model of the human anterior cruciate ligament: A computational analysis with experimental validation, J. Biomech. 37 (2004) 383–390. doi:10.1016/S0021-9290(03)00261-6.
[272] Y. Wang, Y. Fan, M. Zhang, Comparison of stress on knee cartilage during kneeling and standing using finite element models, Med. Eng. Phys. 36 (2014) 439–447. doi:10.1016/j.medengphy.2014.01.004.
[273] X. Zhang, G. Jiang, C. Wu, S.-Y.S.L.-Y.Y. Woo, A subject-specific finite element model of the anterior cruciate ligament., Conf. Proc. IEEE Eng. Med. Biol. Soc. 2008 (2008) 891–894. doi:10.1109/IEMBS.2008.4649297.
[274] G. Limbert, M. Taylor, J. Middleton, Three-dimensional finite element modelling of the human ACL: simulation of passive knee flexion with a stressed and stress-free ACL., J. Biomech. 37 (2004) 1723–31. doi:10.1016/j.jbiomech.2004.01.030.
[275] S. Hirokawa, R. Tsuruno, Three-dimensional deformation and stress distribution in an analytical/computational model of the anterior cruciate ligament, J. Biomech. 33 (2000) 1069–1077. http://www.sciencedirect.com/science/article/B6T82-40GHY88-4/2/8faf6c6a33fd77ff12a73e02387abd80.
[276] G. Li, L.E. Defrate, H.E. Rubash, T.J. Gill, In vivo kinematics of the ACL during weight-bearing knee flexion., J. Orthop. Res. 23 (2005) 340–4. doi:10.1016/j.orthres.2004.08.006.
[277] P. Beillas, G. Papaioannou, S. Tashman, K.H. Yang, A new method to investigate in vivo knee behavior using a finite element model of the lower limb., J. Biomech. 37 (2004) 1019–30. doi:10.1016/j.jbiomech.2003.11.022.

[278] E. Peña, B. Calvo, M.A. Martínez, M. Doblaré, A three-dimensional finite element analysis of the combined behavior of ligaments and menisci in the healthy human knee joint, J. Biomech. 39 (2006) 1686–1701. doi:10.1016/j.jbiomech.2005.04.030.

[279] Y.Y. Dhaher, T.-H. Kwon, M. Barry, The effect of connective tissue material uncertainties on knee joint mechanics under isolated loading conditions., J. Biomech. 43 (2010) 3118–25. doi:10.1016/j.jbiomech.2010.08.005.

[280] A. Kiapour, A.M. Kiapour, V. Kaul, C.E. Quatman, S.C. Wordeman, T.E. Hewett, C.K. Demetropoulos, F. Grati, Finite element model of the knee for investigation of injury mechanisms: development and validation., J. Biomech. Eng. 136 (2014) 011002. doi:10.1115/1.4025692.

[281] G.A. Holzapfel, Nonlinear solid mechanics: a continuum approach for engineering, Wiley, Chichester, 2000.

[282] T.L. Haut Donahue, M.L. Hull, M.M. Rashid, C.R. Jacobs, T.L. Donahue, M.L. Hull, M.M. Rashid, C.R. Jacobs, A Finite Element Model of the Human Knee Joint for the Study of Tibio-Femoral Contact, J. Biomech. Eng. 124 (2002) 273. doi:10.1115/1.1470171.

[283] M.Z. Bendjaballah, A. Shirazi-Adl, D.J. Zukor, Finite element in varus-valgus analysis of human knee joint, Clin. Biomech. 12 (1997) 139–148.

[284] F. Xie, L. Yang, L. Guo, Z. Wang, G. Dai, A study on construction three-dimensional nonlinear finite element model and stress distribution analysis of anterior cruciate ligament., J. Biomech. Eng. 131 (2009) 121007. doi:10.1115/1.4000167.

[285] D.L. Butler, M.Y. Sheh, D.C. Stouffer, V. a Samaranayake, M.S. Levy, Surface strain variation in human patellar tendon and knee cruciate ligaments., J. Biomech. Eng. 112 (1990) 38–45. http://www.ncbi.nlm.nih.gov/pubmed/2308302.

[286] Z.L. Shen, H. Kahn, R. Ballarini, S.J. Eppell, Viscoelastic properties of isolated collagen fibrils., Biophys. J. 100 (2011) 3008–15. doi:10.1016/j.bpj.2011.04.052.

[287] M.A. Sutton, X. Ke, S.M. Lessner, M. Goldbach, M. Yost, F. Zhao, H.W. Schreier, Strain field measurements on mouse carotid arteries using microscopic three-dimensional digital image correlation, J. Biomed. Mater. Res. Part A. 84A (2007) 178–190. doi:10.1002/jbm.a.31268.

[288] D. Zhang, D.D. Arola, Applications of digital image correlation to biological tissues., J. Biomed. Opt. 9 (2004) 691–9. doi:10.1117/1.1753270.

[289] T.K. Tonge, L.S. Atlan, L.M. Voo, T.D. Nguyen, Full-field bulge test for planar anisotropic tissues: part I--experimental methods applied to human skin tissue., Acta Biomater. 9 (2013) 5913–25. doi:10.1016/j.actbio.2012.11.035.

[290] T.K. Tonge, L.M. Voo, T.D. Nguyen, Full-field bulge test for planar anisotropic tissues: part II--a thin shell method for determining material parameters and comparison of two distributed fiber modeling approaches., Acta Biomater. 9 (2013) 5926–42. doi:10.1016/j.actbio.2012.11.034.

Chapter 2: Development of a Stochastic Patterning Technique for Use with Digital Image Correlation Analysis of Biological Soft Tissues

2.1 Introduction

Developed as a non-contact, full-field displacement measurement technique with no intrinsic length scale, digital image correlation (DIC) takes as inputs digital images of a specimen undergoing mechanical strain. It functions by optically identifying unique subsets of pixels throughout the entire area of interest on the surface of the specimen. As shown in **Figure 2.1**, these subsets deform with the specimen, not necessarily in an affine manner, and each deformed subset throughout each image frame is uniquely identified using a least squares algorithm and related back to its original undeformed orientation. The DIC algorithm computes the deformations of these subsets, from which strains are calculated. Because the subsets exist on the specimen surface, 2D displacements and strains are the usual outputs of the DIC analysis.

3D DIC is a variation of the 2D DIC method. Two cameras (with known orientations relative to each other) are used to generate two sets of camera images. The position of the specimen in the out-of-plane direction is determined by triangulating the two sets of images. This technique provides 2D displacements and strains along the surface of the specimen (similar to 2D DIC), as well as out-of-plane displacements. Due to the surface-only input information from the cameras, 3D DIC does not provide out-of-plane strains. However, it has several advantages over 2D DIC, namely that in providing positional data in the out-of-plane direction, it has the capability to correlate surface strains of non-planar specimens. It also provides surface strains for specimens that move in or out-of-plane during deformation, which is not uncommon for specimens undergoing finite deformations, such as many biological soft tissues.

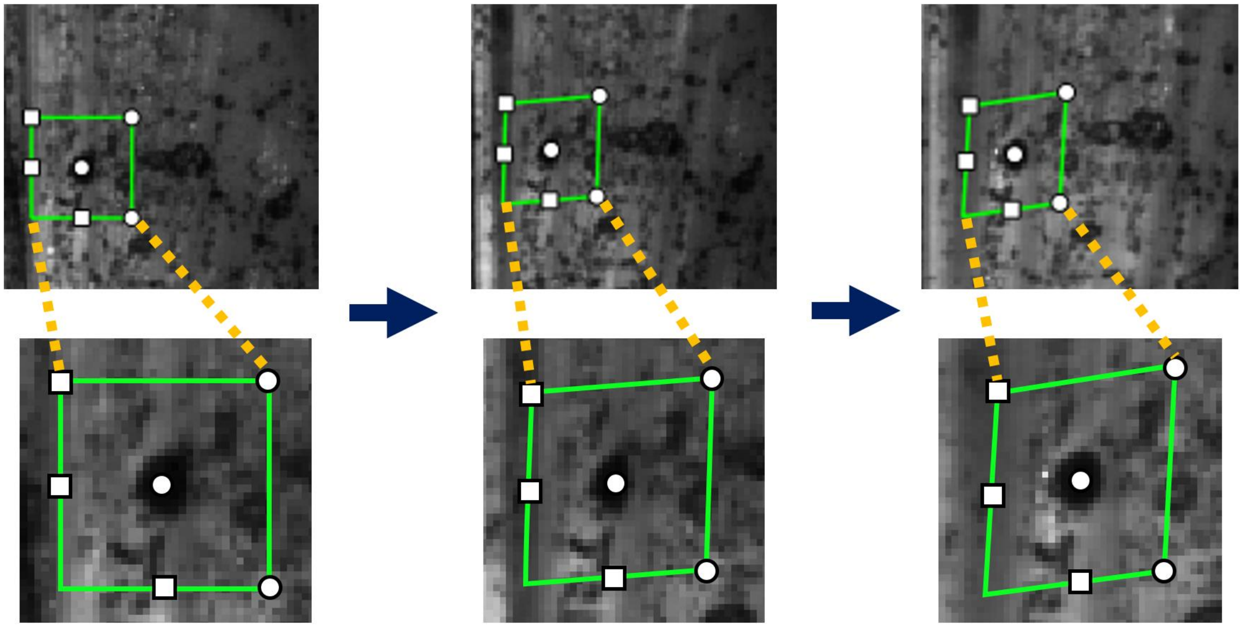

Figure 2.1: Example of DIC subsets tracking the deformation of a specimen. The undeformed specimen (**left**) contains originally undeformed subsets of a certain size (measured in pixels). After deformation, subsets in each image frame (**center** and **right**) are uniquely identified, and related to the undeformed frame, providing displacement data. Pseudo-random stochastic patterns are needed to uniquely identify the subsets in each frame.

DIC is well known in the mechanics community for the great advantages it has in obtaining full-field surface strains without invasively interacting with the material under consideration. However, the crux of the technique is the requirement of uniquely identified subsets throughout the area of interest. This necessitates the use of a pseudo-random high contrast stochastic (speckle) pattern on the surface of the material (as seen in **Figure 2.2**). There has been success in generating patterns for DIC to study a variety of structural materials, from uniaxial loading of woven-fiber ceramic matrix composites to deformations present in cold-rolling processes [1,2]. With these materials, the stochastic pattern can be relatively easily achieved using layers of paint, often applied with commonly available spray paints. By overlaying white and black layers of paint, it is usually not difficult to apply a high-contrast pseudo-random pattern to hard surfaces. The density of the pattern is also of critical importance (**Figure 2.2**), as areas of low density will not have enough information to calculate displacements. Density is often accomplished in traditional DIC patterning methods by controlling the distance between the pattern applicator and the specimen. However, as will be discussed in detail in Section 2.1.2, there are significant challenges in adapting traditional patterning methods to soft biological tissue.

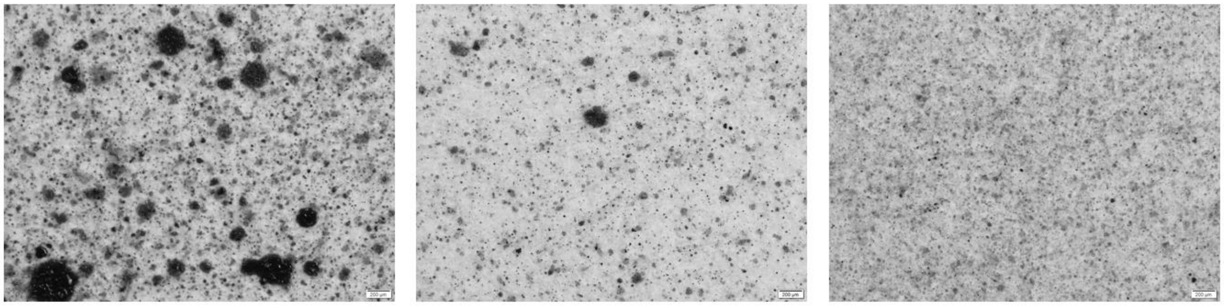

Figure 2.2: Examples of pseudo-random stochastic patterns for DIC. For many macro-scale non-soft material experiments, the density and overall particle size can be controlled to provide a variety of patterns according to the requirements of the test setup.

The size of the speckles is also crucial. DIC algorithms typically recommend a '3 x 3' rule (individual speckles contained within a 3 x 3 pixel area), as described in Sutton et al. 2009 [3]. Patterns containing speckles of highly varying size will require different image magnifications, and optimizing the DIC analysis for one size will cause lack of correlation, due either to low resolution for speckles smaller than the optimal size, or areas that are too dense/sparse due to larger speckles. Regarding pattern density, Sutton et al. recommends that subsets should contain 3 x 3 pixels for accuracy of the subset matching process. [3]. The specific density and speckle size of the stochastic pattern is largely constrained by the material under consideration, especially the size of the material, and by the capability of the imaging systems utilized. Achieving this recommended density and size is another challenge with biological materials and there is a need to develop methods rendering DIC more amenable to use with soft tissues.

2.1.1 Traditional ligament strain measurement techniques

Far-field displacement measurement systems have been widely used to measure deformation of soft biological tissue, usually by measuring tissue displacement via the movement of the test frame. However, compliance along the load train of the specimen due to components of the testing apparatus, including the test frame itself or tissue fixation techniques, can contribute to higher measured strains than those actually experienced by the tissue. Notwithstanding this issue with compliance, several foundational ACL mechanics studies have utilized these types of strain measurement devices [4–6]. Other studies have gathered displacement data of biological specimens directly at the tissue surface. Several studies on the knee ligaments have used a linear variable differential transformer (LVDT), a point-to-point measurement system that operates by clamping onto a specimen at two locations and measuring the absolute displacement between those points during deformation [7–9]. For example, Butler et al. [7] studied individual bone-ligament-bone ACL bundles using an LVDT, and reported mechanical properties of the bundles. There are several limitations with this kind of system. Point-to-point systems are one-dimensional in nature, and provide average displacements and strains across the gauge length of a specimen. In addition, the local mechanical deformation of the tissue is highly likely to be adversely affected by the direct contact of the measurement prongs.

The use of surface-level markings has been utilized to contribute to mechanics data of soft tissue. Woo et al. and Wren et al. used tissue-surface markers to measure the gauge length, and Butler et al. used similar markers to visualize slippage of specimens within the test grip system [10–12]. Others have used small numbers (~9-15) of beads or markers to measure strains optically. However, in each of these cases, only data along the axis of loading was reported, neglecting the rich amount of data full-field techniques such as DIC can provide [13–15]. Indeed, little attention has been given to the strain response of soft tissues specifically outside of strains along the axis of loading, leading to a paucity of data on and understanding of their full-field intrinsic behavior.

2.1.2 Challenges of applying DIC to soft tissues

There are significant challenges in adapting the pattern requirements of DIC to soft tissue. The traditionally used spray paint medium can adversely affect the material properties of softer materials, and thus is not an effective medium for soft biological tissue. In addition, maintaining tissue hydration during loading is greatly important for biological materials. The use of full layers of spray paint can contribute to tissue desiccation, further affecting the measured material properties. Over-coverage of the specimen surface during application of the patterning medium is another serious challenge in the creation of viable DIC patterns. This is often unintentional, as minor shifts in the position or pressure applied to the medium applicator (i.e. an aerosol air can or airbrush with compressed air tank) can cause a burst of patterning fluid or particles to cover the specimen surface. If the patterning medium is extremely difficult to remove or permanent, this over-coverage can result in untestable specimens. Patterning biological tissue is challenging, and the ability to remove and reapply patterns is essential. Thus, the optimal DIC patterning medium would be both biologically-friendly and amenable to pattern reapplication.

Graphite particles have been used to pattern soft biological tissue [16]. These are sometimes referred to as powdered graphite lubricant, and extra fine particles range in size from 44-75 μm. This medium has advantages in its non-harmful nature, and it can be used in combination with talcum powder to create a high-contrast pattern. However, the use of graphite particles as a patterning medium is often subject to particle clumping. The application of DIC patterns for soft biological tissue testing is ideally performed once the specimen is mounted in the test system, as motion of the tissue post-patterning can cause movement of the pattern, clumping particles in some regions while removing particles completely in others. Grids can be utilized to sift graphite particles in order to minimize this problem, but grids are more amenable to horizontally-oriented specimens; vertically-aligned test systems further the difficulty of creating a consistent particle density and speckle size throughout the specimen surface. As mentioned previously, unintentional over-coverage of the surface can necessitate the removal of the particles to repeat patterning afresh. These multiple applications of graphite powder often render the tissue surface gray, as it is extremely challenging to remove all particles after application. Hydrating the tissue during testing exacerbates this ‘graying out’ phenomenon, as particles tend to aggregate in areas of heavy hydration. Other patterning mediums have been used for optical tracking and for 2D DIC of soft biological tissue, including Verhoeff’s stain [17]. However, these types of ink are often permanent in nature, necessitating the creation of optimal patterns on the first patterning attempt and risking the loss of specimens with any excess pattern coverage.

Another challenge in patterning biological tissue is the controllability of the speckle size and density, as required for optimal DIC contour coverage. Airbrushes and compressed air tanks are an option for applying fluid-based patterns for DIC. With an airbrush, the user manually controls the speckle size and density during pattern application, often by prescribing a set air pressure and needle/nozzle configuration, and adjusting the distance of the airbrush from the specimen surface to achieve the desired speckle size and density. This 'free-form' manner of application offers a variety of particle size and pattern densities (as seen in **Figure 2.2**), but can suffer from the issue of unintentional over-coverage as discussed previously. As the optimal speckle size parameters are largely constrained by the requirements of the test setup (including camera resolution and specimen dimensions), larger speckles can be desired. To achieve this with an airbrush, the needle is commonly positioned further back in the airbrush assembly, allowing larger drops of ink to flow from the airbrush [18]. However, the size of these drops is often unpredictable, and can lead to higher uncontrollability of the final pattern. For these reasons, the use of the free-form airbrush alone is not sufficient to provide uniform coverage. It was hypothesized that the use of the airbrush in conjunction with a stencil to apply a stochastic larger speckle size to control the pattern size and density would produce the optimal speckle pattern. The goal of this work is to develop a pattern design, fabrication technique, and application method that produces a stochastic pattern with controlled pattern density and individual speckle size, providing enhanced and more repeatable DIC patterns for data correlation in soft tissue testing.

2.2 Methods

A non-toxic alcohol-based ink (ShowOffs Body Art LC, Clarkston, MI) was identified as a potentially attractive patterning medium for DIC on soft tissue. This medium is commonly used for temporary ‘tattoos’. It is designed to be water-insoluble, and this specifically allows for hydration of the tissue while maintaining ink coverage. Its alcohol-solvable nature renders it temporary, allowing for easy and complete removal with isopropyl alcohol in the case of unintentional over-coverage.

As mentioned previously, the optimal speckle size and pattern density for DIC is largely dependent on the experimental setup, camera resolution, and field of view (FOV) required for the specimen to be tested. Fastcam SA1.1 cameras (Photron USA, Inc., San Diego, CA) and Nikon AF Micro-Nikkor 200 mm lenses (Nikon Inc., Melville, NY) were used in this investigation. The ligament chosen was the anteromedial (AM) bundle of the ACL, and it was positioned within the 1024x1024 pixel field of view (FOV), leaving space in the FOV above and below the ligament to allow for the tissue to remain in view while undergoing axial deformation during testing. In order to determine a baseline for the goal speckle size, a representative tissue length of 35mm was selected (based on data from preliminary ACL tissue experiments under the same test conditions), and the representative overall test setup and tissue orientation within the FOV provided an estimate of the speckle size according to the 3x3 speckle rule of 100 μm. The test setup varies with the size of the bundle to be viewed and its orientation within the camera FOV (based on the physical position of the cameras relative to each other and to the bundle, as well as the camera lens' positions). Variation in setups for different bundles are unavoidable, and are necessary to obtain the optimal position and focus of each bundle in the FOV. The estimated 100 μm speckle size was set as the goal speckle size for pattern generation prior to testing the patterns experimentally, with the understanding that the optimal experimental goal speckle size would vary according to each individual specimen's dimensions and test setup. In the experimental tests detailed later, the optimal speckle size for the eight specimens tested was 152 ± 9 μm. This variation in optimal speckle size from specimen to specimen was sufficiently small to enable the use of a single stencil pattern for all specimens (see Results section for further detail).

A stencil approach was identified as a method to control the size, density and pseudo-random nature of the DIC pattern. Masking tape and washi (和紙, 'Japanese paper') tape were examined as candidate stencil materials due to their thin and adhesive nature (i.e. ability to stick to the soft, pliable, and hydrated surface of the ACL).

A laser cutter was utilized to fabricate the stencil pattern. Laser cutters function by taking as input a 2D drawing object, and as output a prescription of the x-y motion of a laser crosshead over a bed positioned at a particular z distance from the crosshead. Laser cutters interface with CAD or technical drawing software and function similarly to traditional laser printers, however, the intensity of the laser beam allows the "printing" operation to generate a perforated pattern on the stencil material.

An Epilog Mini 24 Laser Helix model (Epilog Laser, Golden, CO), located at MakerWorks, a member-based workshop (Ann Arbor, MI) was used for fabrication of the stencil patterns. The maximum laser power (intensity of the beam) was 50 W, and maximum crosshead speed was 160 in/s (4.1 m/s). The laser wavelength was 10.6 μm with a spot size of 76 - 127 μm. The maximum crosshead x-y travel was 610 x 305 mm, with a resolution (at 1200 dpi) of 21 μm. The commercial software package controlling the laser allowed for variation in the input settings of laser power and crosshead speed, and both parameters were defined as percentages of the maximum speed and power.

All patterns were generated using MATLAB R2014 (MathWorks, Natick, MA) (see last paragraph in this section for more detail on MATLAB pattern generation). After the pattern designs were created in MATLAB, they were converted to a compatible image file and exported to the graphics editor CorelDRAW X6 (Corel Corporation, Ottawa, ON). Within CorelDRAW, the pattern image was scaled to the desired physical size and sent to the laser cutter's commercial software package to be printed as a raster (pixelated) image. The laser cutter system used to fabricate the stencil patterns is shown in **Figure 2.3.**

A fixture was designed to position the stencil material within the laser cutter system. Within this fixture, the tape was suspended on two raised platforms beneath the laser crosshead. These raised platforms suspended the stencil over the laser cutter bed and provided an intact stencil, by preventing melting and adherence of the stencil to the laser cutter bed due to the intensity of the laser beam. Investigations were carried out to identify the optimal pattern for DIC, by studying the capabilities of the laser to print the actual individual speckle sizes prescribed, as well as collections of speckles. These

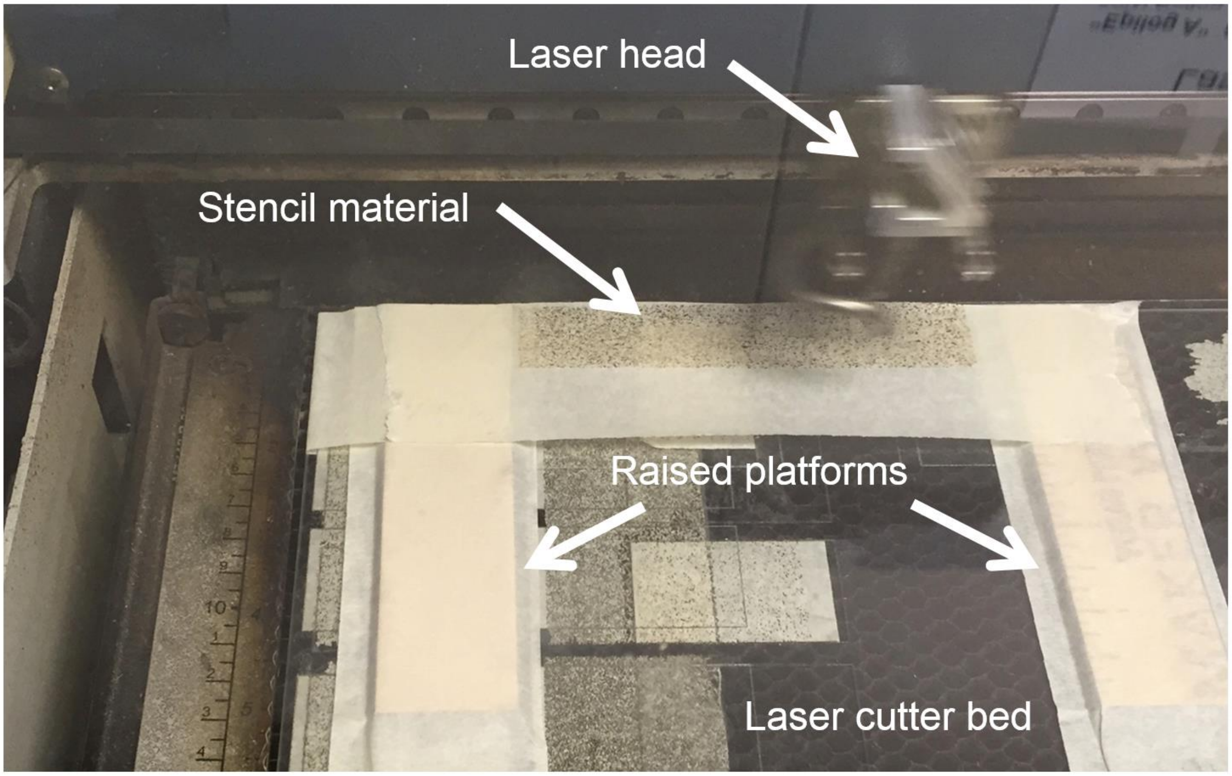

Figure 2.3: Epilog laser cutter used for pattern fabrication. The stencil material shown here (masking tape) was suspended between raised platforms, creating a ‘substrate’ of air between the material and the bed of the laser. The adhesive side of the material faced away from the laser source. The bed of the laser was set at a prescribed z distance from the laser head, and the laser head was controlled in the x-y plane above the material.

investigations served three purposes: to identify 1) the smallest individual speckle and 2) the smallest spacing between two speckles the laser could produce, and 3) to extend the individual and paired speckle size and density to a full pattern of a stochastic collection of speckles.

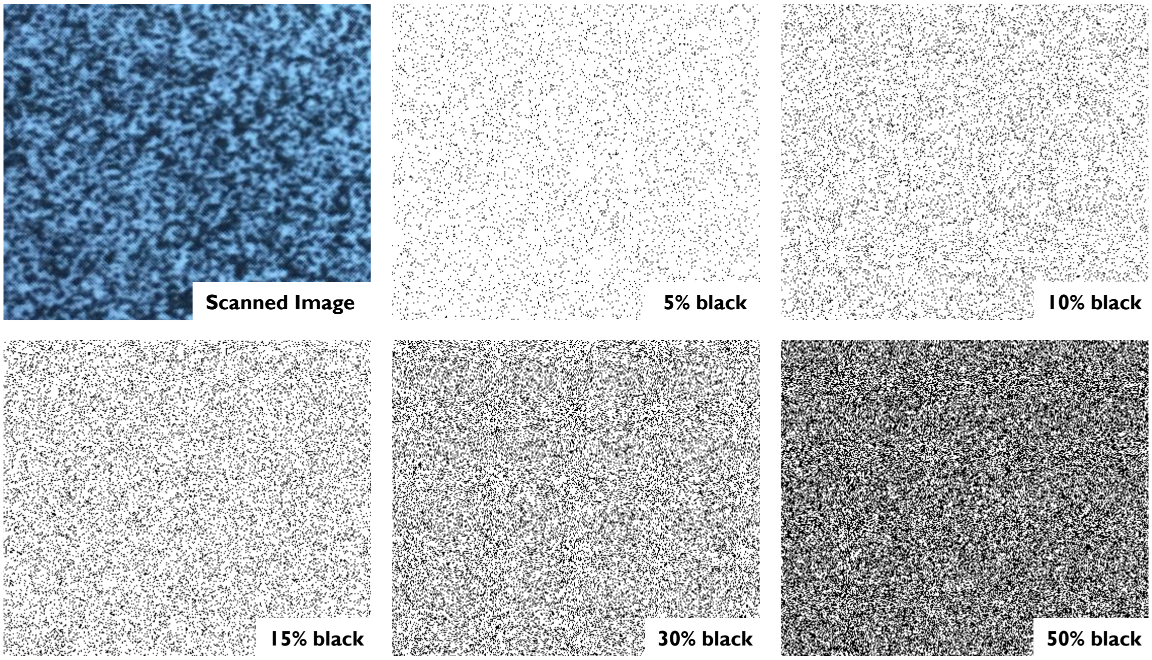

Figure 2.4: Pseudo-random patterns generated in MATLAB R2014. The density of the patterns was controlled as a percentage of black particles and specified to 5, 10, 15, 30 and 50%. The speckle size was also controlled using the MATLAB script. The scanned image of a traditional spray paint pattern is shown for reference, taken from [3].

For the individual speckle tests, speckle size control was first investigated by varying the speed of the laser crosshead as a function of the prescribed size of the speckles (at a constant power setting of 100%). This prescribed speckle size was specified within the CorelDRAW software that interfaced with the laser. To investigate the effect of laser power on the speckle size, laser speed vs. power tests were performed (at a prescribed speckle size of 100 μm). Paired speckle patterns were also created by prescribing the spacing between two speckles in the original pattern created in MATLAB. For the paired speckle tests, the distance between the two speckles was controlled using a spacing parameter ‘j’ in the MATLAB script, and the speed vs. power tests were repeated.

Sample patterns were generated within MATLAB at densities of 5 - 50% of black particles within an area of interest (**Figure 2.4**). These patterns were created through a script to generate a pseudo-random spatial distribution of ‘particles’ in order to demonstrate control over the density of the stencil pattern design within MATLAB. This was done by first defining a grid, with all spaces initially specified to be white. Next, the percentage of speckles to add was specified, and this percentage was pseudo-randomly distributed throughout the grid. However, without any prescription of the spacing between particles, clusters of particles can occur (**Figure 2.5, left**), which could contribute to burning.

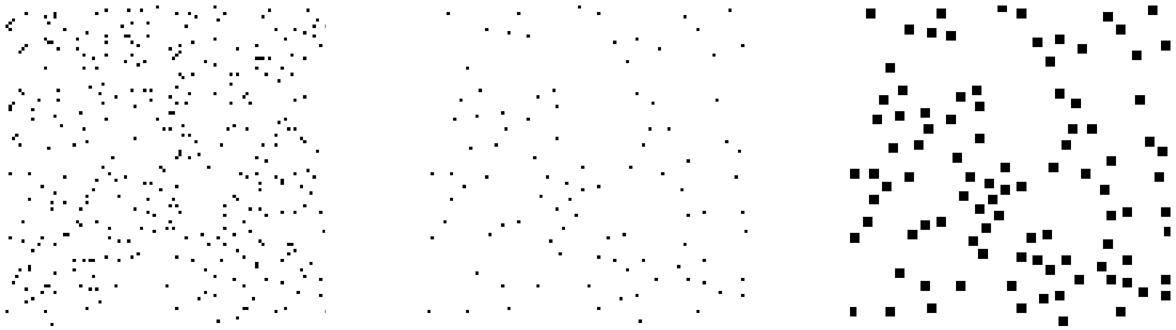

Figure 2.5: Optimal pattern density determination. **Left**: original pattern with no specification on spacing between particles. **Center**: ‘sparse’ pattern, with a minimum spacing prescribed between all points. **Right**: ‘grown’ pattern, where all speckles from the sparse pattern have been enlarged.

Prescribing the minimum spacing between individual particles can be used to control the densities of the pseudo-randomly distributed patterns and prevent burning due to long laser dwell times. This exclusion process was prescribed to the original speckle pattern (**Figure 2.5, left**) by removing all but one particle in clustered areas on the pattern, generating a sparser pattern (**Figure 2.5, center)**. **Figure 2.5 (right)** is another adaptation; created by enlarging the particle size in the MATLAB script by converting the points in the neighborhood of each existing particle from white to black, effectively enlarging the speckle size.

Fabricated stencils were directly applied to the surfaces of the test specimens. The minimally tacky nature of the stencil allowed for adhesion during ink application, but easy removal of the stencil as well. The ink was applied to the surface through the stencil using an Iwata Custom Micron Series B Airbrush (Iwata Medea, Portland, OR). The airbrush compressed air tank was set to a pressure of ~40psi (maximum pressure possible). The stencil pattern was removed after applying the ink. If needed (due to unintentional over-coverage during pattern application), excess ink was easily removable from the tissue surface using a 70% Isopropyl rubbing alcohol (Vi-Jon Laboratories Inc., Saint Louis, MO). After application of the speckles through the stencil, the free-form airbrush was used to augment the stencil pattern with a finer speckle. The free-form speckles were created by manually controlling the speckle size and density during application of the pattern, by adjusting the distance of the airbrush from the specimen surface. **Figure 2.6** shows an example of the stencil on the surface of the tissue (**Figure 2.6, left**), and the speckle pattern on the surface of the tissue after removal of the stencil (**Figure 2.6, center and right**).

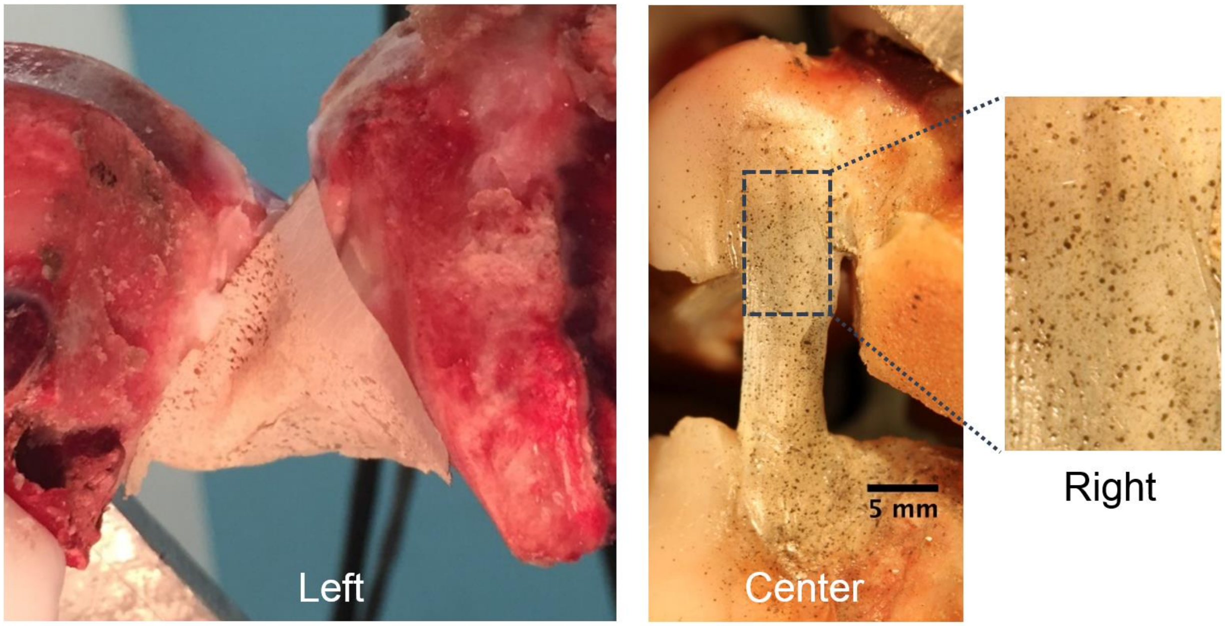

Figure 2.6: Left: Stencil applied to test specimen. Stencil material has minimal adherence to tissue and was easily removed after application of ink medium. **Center:** Stencil pattern overlay showing high contrast and fidelity in the majority of the tissue surface. **Right:** Close-up view of pattern on tissue surface.

As mentioned previously, DIC requires a pseudo-random distribution of speckles, which necessitates that no portion of the pattern can be repeated within the FOV. This was ensured by using a large random stencil, and care was taken to apply unique areas of the stencil pattern to any particular specimen. After applying the stencil patterning and free-form airbrush speckle patterns, the Fastcam SA1.1 cameras (1024x1024 pixels) were utilized to visualize AM bundle specimens with dimensions 31.7±12.3 mm by 5.5±0.5 mm (n=8) [19]. The resolution of the Fastcam cameras based on the position of the specimens within the camera FOV was 51 ± 3 μm (n=8). Tests were then performed to elucidate the full-field axial, transverse, and shear strain responses of the ACL bundles under tensile loading.

2.3 Results

As mentioned previously, 100 μm was estimated as the optimal speckle size based on the representative test setup discussed previously. **Figure 2.7** shows the results of investigating the speckle size as a function of crosshead speed at constant power of 100%. Microscopic images were taken at 5x magnification using an Olympus microscope (Center Valley, PA), with a resolution of 1 μm. Speckle diameters were measured from the dark region where the stencil has been fully perforated, not including the damaged area around the perforation. The speckle produced at 1% speed and 100 μm prescribed speckle size was larger (839 μm) than 100 μm, due to the long dwell time (i.e. slow speed) of the laser.

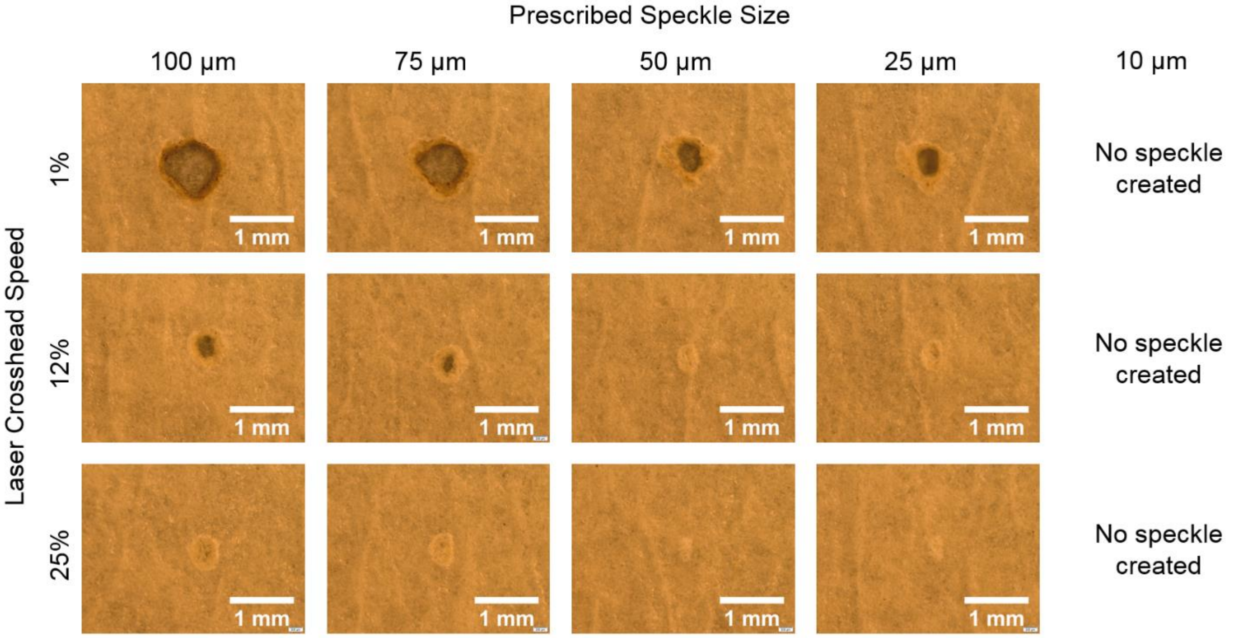

Figure 2.7: Microscopic images (5x mag) of prescribed speckle size vs. speed test at 100% power on final produced speckle size. As the speed increased, the speckle size decreased, due to shorter laser dwell times. The produced speckle size decreased as the prescribed speckle size in the software decreased. The smallest speckles produced were 242 ± 1 μm; these were achieved at 12% crosshead speed and 75 μm prescribed speckle size.

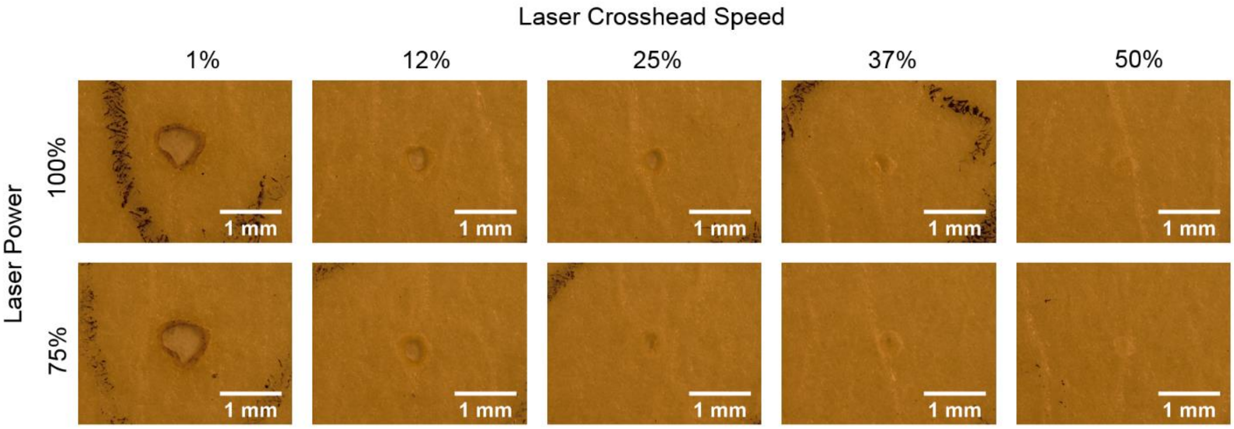

Figure 2.9: Effects of laser head speed vs. laser power at a constant prescribed speckle size of 100 μm on final produced speckle size. In this test, 75% power/25% speed produced the smallest speckle (150 ± 1 μm). Microscopic images at 5x mag.

As the laser speed was increased, the speckle produced at 100 μm prescribed size decreased to 317 μm at 12% speed. However, at 25% speed the laser did not dwell long enough at the speckle location to fully perforate the stencil. For smaller prescribed speckle sizes (10 μm – 75 μm), the resulting speckle size decreased, and increasing the crosshead speed further decreased the resulting speckle. The minimum speckle

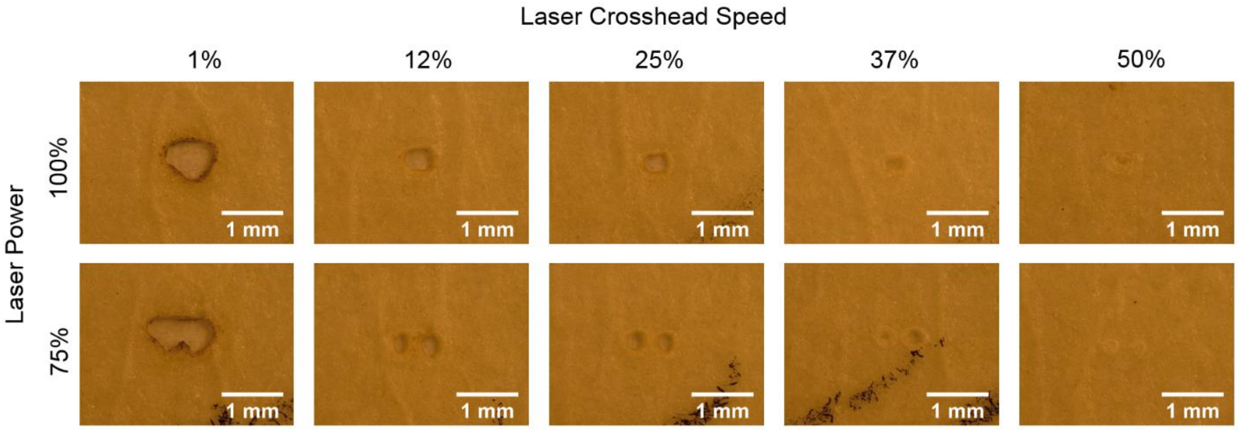

Figure 2.8: Paired speckle trials of at constant prescribed speckles of 100 μm. As speed decreased, the longer laser dwell time caused the laser to burn though the material between the two holes (as seen at 75% power/1% speed). The smallest produced pairs of speckles were 263 ± 1 μm, with a spacing 254 ± 1 μm between them, at 75% power/25% speed. Microscopic images at 5x mag.

size for a constant laser power (100%) was 242 ± 1 μm at 75 μm prescribed size and 12% speed. Smaller prescribed speckle sizes and faster speeds failed to generate full-thickness holes in the stencil.

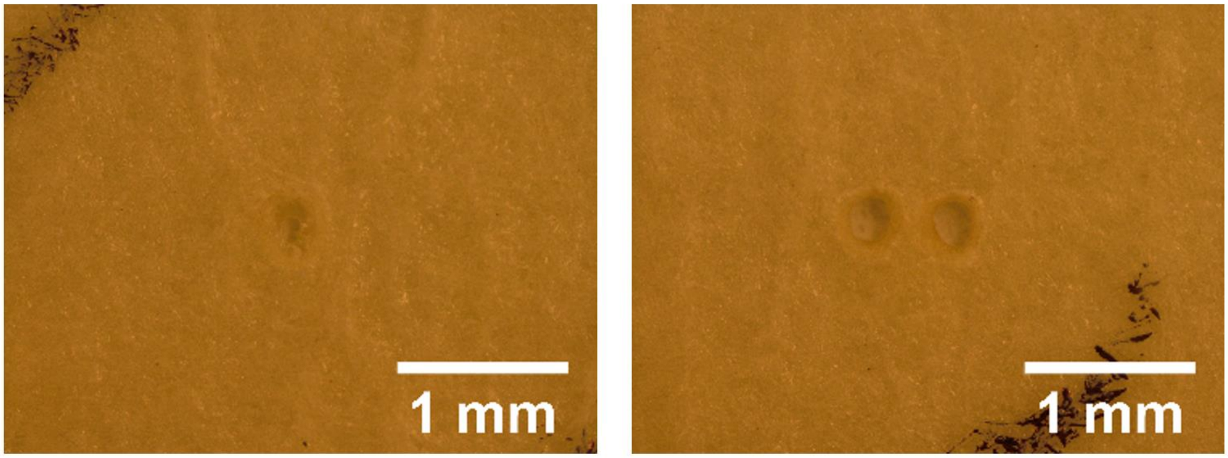

Figure 2.10: Microscopic images at 5x mag of best individual speckle and spacing between paired speckles in this set of experiments. Left: 75% power/25% speed, final diameter: 150 ± 1 μm. Right: 75% power/25% speed, final diameter: 263 ± 1 μm. Spacing between speckles: 254 ± 1 μm.

The results for the individual speckle size as a function of varying speed and power (at constant prescribed speckle size of 100 μm) are shown in **Figure 2.8**. Similarly to the previous tests on speckle size vs. speed, increasing the speed of the laser reduced the speckle size, but often resulted in an un-perforated stencil at high speeds. Reducing the power reduced the speckle size, and the smallest achieved speckle size with this method was 150 ± 1 μm at 75% power/25% speed.

The paired speckle laser speed and power tests are shown in **Figure 2.9**. As before, the smallest perforated pair of speckles occurred at 75% power/25% speed (and constant prescribed speckle size 100 μm). At higher power or slower speed settings, the laser, in

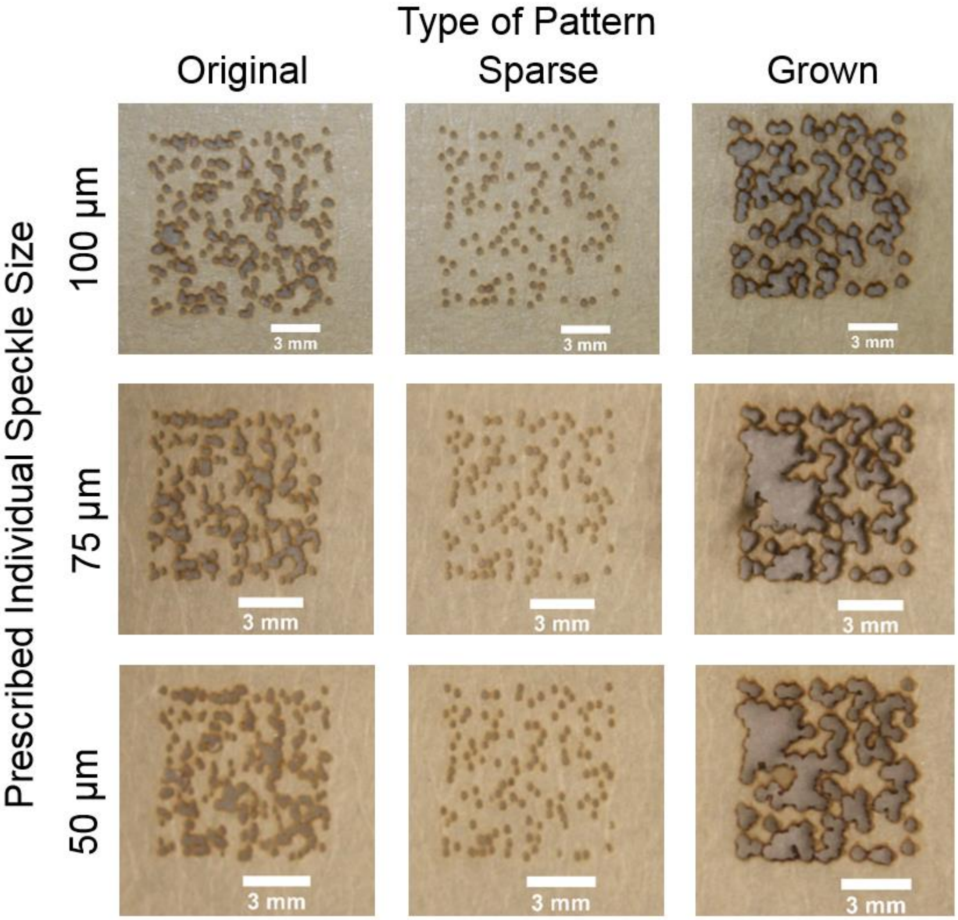

Figure 2.11: Example printed stencil patterns at various densities. The original and grown patterns exhibit enlarged ‘burnt’ areas due to the high dwell time of the laser at these positions, either to create a group of speckles at one point (original pattern) or to create larger individual speckles (grown). The sparse pattern is ideal, containing distinct speckles without presence of excessive burning and controlled speckle size.

addition to increasing the size of each speckle, effectively burned the stencil material between individual speckles, eliminating the spacing between them. **Figure 2.10** shows the smallest completely perforated individual and paired speckles generated. For the individual speckle, the diameter was 150 ± 1 μm taken at a power/speed setting of 75%/25%. The minimum paired test speckle size was 263 ± 1 μm with 254 ± 1 μm between the speckles.

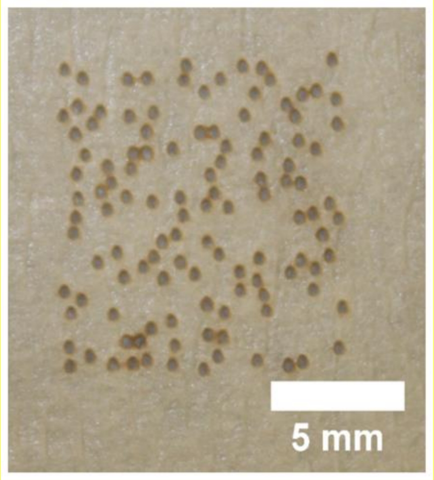

Figure 2.12: Sparse pattern with speckle diameter 264 ± 20 μm (n=28) and average spacing 429 ± 160 μm (n=28).

The printed full stencil patterns vs. prescribed speckle size are shown in **Figure 2.11**. These images were taken with a Canon Rebel T1i camera with resolution of 13 ± 0 μm (Canon U.S.A. Inc., Lake Success, NY). As mentioned previously, the 'original' patterns are created without any specification on the spacing between particles, while the 'sparse' pattern specifies a minimum spacing between individual particles. The 'grown' patterns additionally enlarge the size of the particles in the sparse pattern. Patterns were printed at several power/speed combinations, and 100% power/12% speed was found to provide the optimal results; all patterns in **Figure 2.11** were printed at this setting. The brown edges surrounding portions of the original pattern are evidence of burning. This was exaggerated in the grown pattern, along with greater merging of individual speckles where the space between particles disintegrated, and this degradation is apparent as the prescribed speckle size decreases as well. However, burning was not apparent for the majority of the sparse patterns, where the integrity of the individual particles and the spacing between particles were preserved. As the prescribed particle size decreased, the spacing between the particles decreased, with evidence of speckles merging together in all patterns. For this reason, the sparse pattern at 100 μm was selected as the optimal stencil. This sparse pattern is shown in **Figure 2.12 (right)**. The average speckle size and spacing was measured within a 5 mm x 5 mm subset of the stencil, this region contained 28 speckles. In this pattern, the average size of the particles was 264 ± 20 μm (n=28), and the average minimum spacing between any two particles (measured from speckle outside edge to outside edge) was 429 ± 160 μm (n=28).

The sparse patterns chosen as the final stencil were used in conjunction with the freeform airbrush to produce patterns for DIC. A representative final pattern and DIC contour overlay at peak displacement is shown in **Figure 2.13**. This work (detailed in **Chapter 3**) patterned and tested 8 AM specimens in a tensile test setup using the stencils outlined in this work.

Briefly, the focus of these experiments was to utilize DIC to quantify the full-field strain response of the bundles of the ACL undergoing deformation in a well-known loading state. Samples were aligned in an MTS 810 Material Test System (MTS Systems Corporation, Eden Prairie, MN) and visualized with the Fastcam cameras mentioned previously. A LabVIEW DAQ device (National Instruments Corporation, Austin, TX) and custom script were used for control of the MTS, and a Tektronix function generator (Tektronix, Inc, Beaverton, OR) synced the

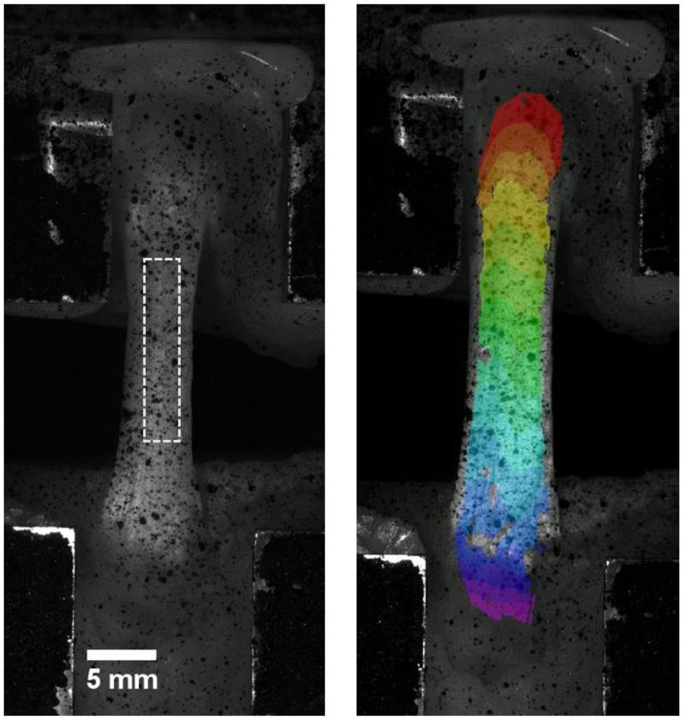

Figure 2.13: Final pattern for DIC deformation measurement. Specimen is an AM bundle aligned for tensile testing, with mid-substance outlined in gray. **Right:** DIC contour overlay on AM bundle at peak vertical displacement, adapted from [19].

Fastcam cameras with the LabVIEW program. DIC data was analyzed using VIC 3D 2010 (Correlated Solutions, Inc., Colombia, SC), and strain data was exported to MATLAB for presentation of the axial strain figures. Each specimen was loaded along the long axis of the tissue to ~12% global (grip-to-grip) nominal strain at a true strain rate of 0.05/s.

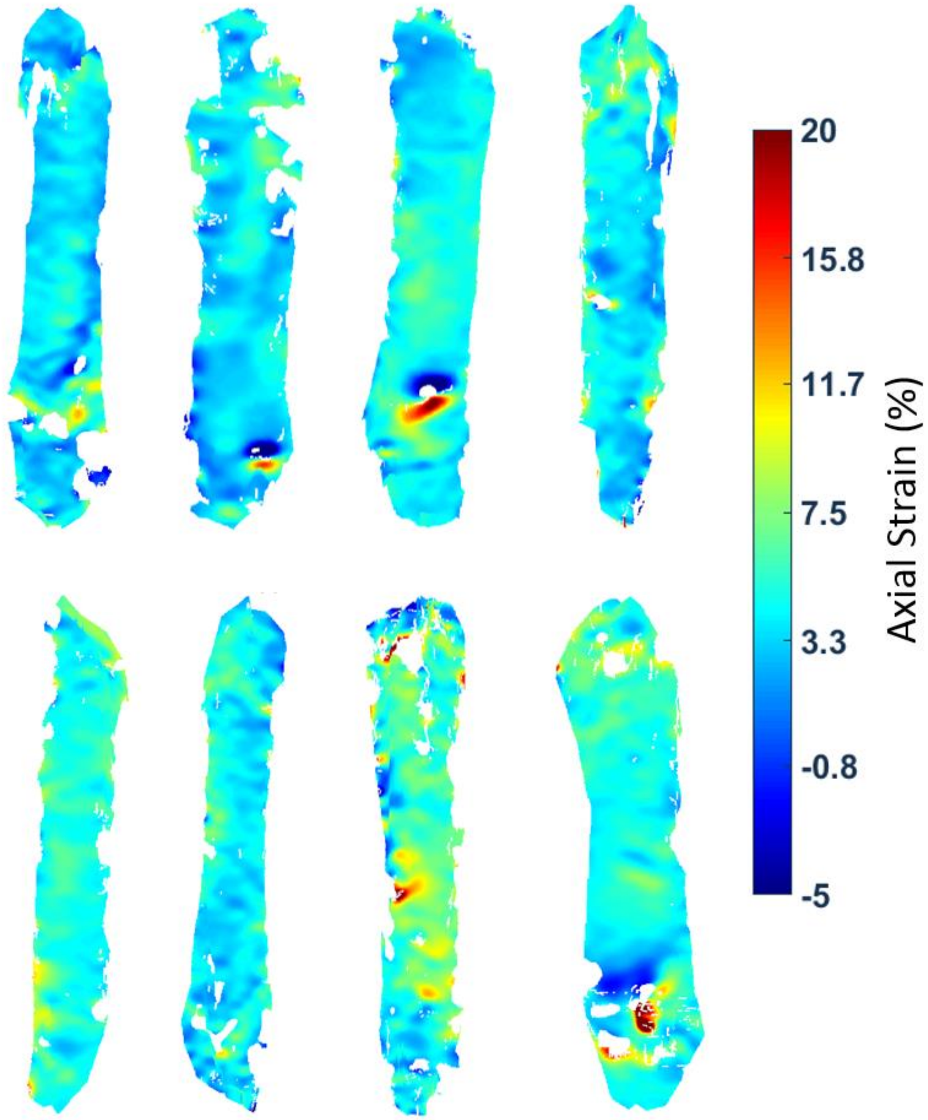

Figure 2.14: Experimental DIC strain contours of 8 AM bundles at peak displacement. For the majority of the specimens, the contours maintain high coverage, especially in the bundle mid-substance.

DIC can be used to validate the final pattern achieved with the combination sparse stencil and freeform airbrush, namely in providing the ideal speckle size, spacing, and amount of contour coverage loss at the edges of the sample from the experimental data. Although the goal speckle size was estimated to be 100 μm with an "assumed representative test setup", the actual goal speckle size according to Sutton et al. 2009 [3] varies according to test conditions, especially the length of the specimen and its size within the camera FOV. As mentioned in the Methods section, the AM bundle specimens tested in **Chapter 3** had dimensions 31.7 ± 12.3 mm by 5.5 ± 0.5 mm [19]. This variation in actual length and small variations in test setup change the experimental speckle size from the estimated 100 μm size. As a validation of the actual size required, the average DIC recommended speckle size for the set of experiments can be calculated. By taking the final resolution of the experimental tests in **Chapter 3** (51 ± 3 μm, n=8), and assuming 3 x 3 pixels per speckle ([3]), the recommended speckle size for the 8 experimental data sets is 152 ± 9 μm (n=8). For the specific experiment in **Figure 2.13**, the recommended speckle size is 150 ± 50 μm. For comparison, measurements of 20 speckles were taken in the mid-substance region of the specimen (outlined in white in **Figure 2.13**), and manifested an average size of 223 ± 114 μm (n=20), with minimum speckle 88 ± 50 μm and maximum 515 ± 50 μm). Within the 3D DIC software subsets of pixels are monitored for each set of image data, and should ideally contain 3 speckles (and two spaces between speckles) across the subset. For the representative contour shown in **Figure 2.13**, the subset was chosen to maximize contour coverage without loss of correlation, with a resulting subset size of 15 pixels. This subset size and the average speckle size for the representative bundle provide an estimate of the ideal spacing parameter in the final pattern as 41 ± 56 μm.

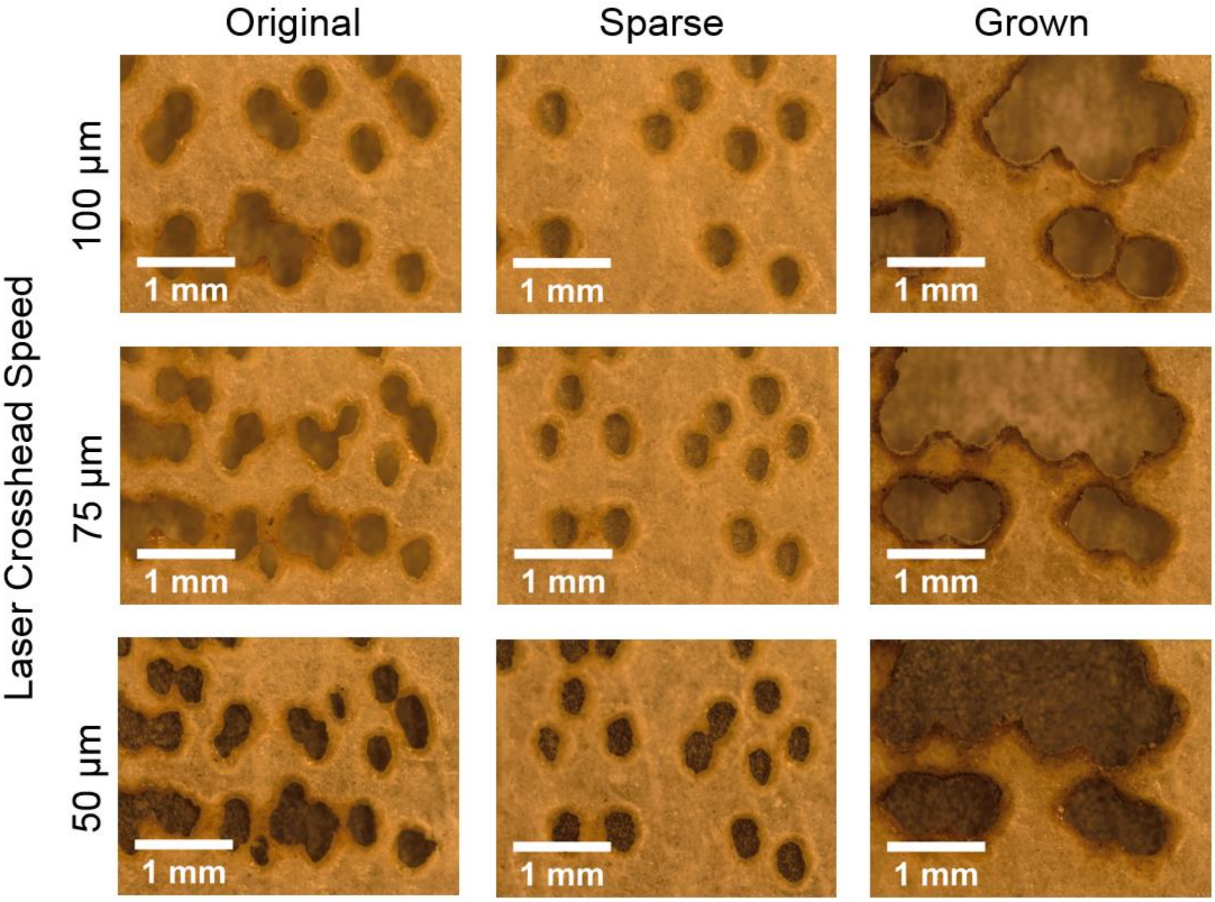

Figure 2.15: Microscopic (5x mag) view of different patterning densities. The dwell time of the laser (original and grown patterns) created a limitation for controlling the spacing and density of the laser.

The efficacy of the underlying DIC pattern can also be discussed in terms of the coverage loss at the edges of the final contour overlay. The width of the tissue lacking a pattern was measured in 5 locations in the representative contour overlay shown in **Figure 2.13, (right)**, with an average width of 362 ± 48 μm (n=5). This compares well with the subset size for this pattern of 15 pixels (750 μm). A final measure of the pattern fidelity is its capability to maintain correlation during specimen deformation. As shown in **Figure 2.14**, the patterns generated using this technique correlated throughout the full loading path of the tissue, even up to strains of ~5% axial and ~35% transverse strains the patterns maintain high contour coverage for the majority of the sample surface.

2.4 Discussion

The difference in speckle size in the single speckle test (150 ± 1 μm) compared with that of the paired (263 ± 1 μm) and sparse pattern (264 ± 20 μm, n=28) is likely due to the longer dwell time of the laser to print multiple speckles at once. Good agreement is shown between the paired and sparse pattern individual speckles. In addition, the low variability for the final sparse stencil pattern is a demonstration of the controllability of the speckle size with the laser cutter stencil perforation technique.

Regarding density, the smallest spacing with the sparse stencil pattern (chosen at 100 μm prescribed size) was 429 ± 160 μm (n=28). Further insight on the choice of stencil pattern can be gained from **Figure 2.15**, showing microscopic images of the stencil patterns at 5x magnification. Both the original and grown patterns demonstrate disintegration of the space between individual particles, due to the longer time the laser spent in specific locations to create multiple particles. This disintegration was also apparent in the sparse patterns at 50 μm and 70 μm prescribed speckle size. The sparse pattern at 100 μm did not contain this pattern degradation, and was the optimal choice for final stencil. The spacing and particle size of the final stencil is a limitation of the density capable by the laser cutter, but is mitigated by combining the sparse stencil with the freeform airbrush, resulting in the final pattern with satisfactory density and fidelity.

Prior to patterning tissue samples, the freeform airbrush was utilized to print patterns on a paper substrate as a measure of its capability to produce speckles. As seen in **Figure 2.16**, the freeform airbrush contains the initially estimated goal speckle size (100 μm) within the range of speckles produced: 8 ± 1 μm to 495 ± 1 μm (n=20). However, the lack of consistency in particle size demonstrates the uncontrollability of the freeform airbrush technique at this length scale.

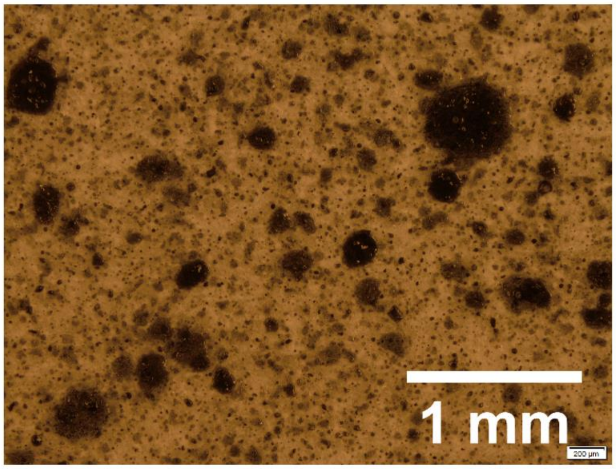

Figure 2.16: Pattern generated using freeform airbrush technique, speckle size 8 ± 1 to 495 ± 1 μm. The uncontrollability of the speckle pattern at this length scale is evident in the range of speckle sizes.

A section of the mid-substance region in **Figure 2.13** was selected for measurement of the average speckle size, and twenty speckles in this region averaged 223 ± 114 μm (n=20). This lies within the experimental error of the average hole size produced with the sparse stencil patterns (264 ± 20 μm, measured from 28 speckles in **Figure 2.12**). The experimental speckle size is above the recommendation by Sutton et al. (150 ± 50 μm), and although a spacing parameter can be calculated from the Sutton et al. subset recommendation (41 ± 56 μm), it lies below the resolution of the cameras utilized in this study. However, an extremely low subset size of 15 pixels (750 μm) was attainable using this pattering method; the minimum possible subset size in the VIC 3D software is 9 pixels. The subset of 15 is quite close to this minimum possible subset size, indicating fine detail of the speckle pattern for correlation. In addition, the small loss of contour coverage seen at the specimen edges, averaging 362 ± 48 μm (n=5), is possible with such a small subset. Some pattern loss on the edges is unavoidable with the DIC technique, as subsets on the edge of the contour cannot be compared to their neighbors. The subset size achieved in the test shown in **Figure 2.13**, is a testament to the good coverage possible with this patterning method.

The efficacy of this patterning technique is also demonstrated in the consistency of the pattern generation process, with most bundles patterned within 2-3 applications. Unlike graphite powder, any re-applications with the non-toxic alcohol-based ink could be done with no holdover of previous patterning attempts, as the pattern could be virtually completely removed with isopropyl alcohol. This patterning technique also allows for small subsets of the DIC technique, difficult to achieve with biological tissue, taking advantage of the camera resolution and macro-lens used in testing.

Finally, a major advantage of this patterning technique is the capability of the pattern to deform with the large deformation of soft biological tissue, while demonstrating high DIC contour coverage: the initial pattern (**Figure 2.13, left**) deforms with the specimen, and the contour overlay demonstrates high fidelity up to the peak displacement (**Figure 2.13, right**). This is also present in the axial strain contours of 8 bundles, as seen in **Figure 2.14**.

2.5 Summary

The goal of this work was to develop a patterning technique using a non-toxic patterning medium, and allowing user control over the pattern density, contrast, and individual particle size. A biologically friendly alcohol-based ink was identified and used in conjunction with a novel stencil design for stochastic patterning of soft biological structures. This water-insoluble, yet removable, patterning medium allows for continual tissue hydration without loss of pattern integrity, while also allowing for pattern reapplication. Using laser cutting technology, a novel stencil design was identified as a random speckle pattern fabrication method, and used to create a final pattern at the limits of the laser capabilities. The pattern fabrication method produces speckles for DIC as required by the camera resolution, specimen dimensions, and test setup. This pattern design and fabrication technique produces a stencil pattern with controlled pattern density and individual speckle size, providing enhanced and more repeatable DIC patterns for data correlation.

2.6 References

[1] V.P. Rajan, M.N. Rossol, F.W. Zok, Optimization of Digital Image Correlation for High-Resolution Strain Mapping of Ceramic Composites, Exp. Mech. 52 (2012) 1407–1421. doi:10.1007/s11340-012-9617-1.

[2] Analysis of Speckle Patterns for Deformation Measurements by Digital Image Correlation, in: Conf. Speckles, From Grains to Flowers, 2006.

[3] M.A. Sutton, J. Orteu, H.W. Schreier, Digital image correlation (DIC), Image Correl. Shape, Motion Deform. Meas. Basic Concepts, Theory Appl. (2009).

[4] F.R. Noyes, E.S. Grood, The Strength of the Anterior Cruciate Ligament in Humans and Rhesus Monkeys, J. Bone Jt. Surg. 58 (1976) 1074–1082.

[5] J.M. Hollis, S. Takai, D.J. Adams, S. Horibe, S.L.-Y. Woo, The effects of knee motion and external loading on the length of the anterior cruciate ligament (ACL): a kinematic study, J. Biomech. Eng. 113 (1991) 208–214.

[6] A. Kanamori, S.L.-Y. Woo, C.B. Ma, J. Zeminski, T.W. Rudy, G. Li, G.A. Livesay, The forces in the anterior cruciate ligament and knee kinematics during a simulated pivot shift test: A human cadaveric study using robotic technology., Arthroscopy. 16 (2000) 633–9. doi:10.1053/jars.2000.7682.
[7] D.L. Butler, Y. Guan, M.D. Kay, J.F. Cummings, S.M. Feder, M.S. Levy, Location-dependent variations in the material properties of the anterior cruciate ligament, J. Biomech. 25 (1992) 511–8.
[8] E. Gentleman, A.N. Lay, D.A. Dickerson, E.A. Nauman, G.A. Livesay, K.C. Dee, Mechanical characterization of collagen fibers and scaffolds for tissue engineering, Biomaterials. 24 (2003) 3805–3813. doi:10.1016/S0142-9612(03)00206-0.
[9] S. Arms, J. Boyle, R.J. Johnson, M. Pope, Strain measurement in the medial collateral ligament of the human knee: an autopsy study., J. Biomech. 16 (1983) 491–6. http://www.ncbi.nlm.nih.gov/pubmed/6619166.
[10] S.L.-Y. Woo, M.A. Gomez, W.H. Akeson, The Time and History-Dependent Viscoelastic Properties of the Canine Medial Collateral Ligament, J. Biomech. Eng. 103 (1981) 293–298.
[11] F.R. Noyes, D.L. Butler, E.S. Grood, R.F. Zernicke, M.S. Hefzy, Biomechanical Analysis of Human Ligament Grafts used in Knee-Ligament Repairs and Reconstructions, J. Bone Joint Surg. Am. (1984) 344–352.
[12] T.A.. Wren, S.A. Yerby, G.S. Beaupré, D.R. Carter, Mechanical properties of the human achilles tendon, Clin. Biomech. 16 (2001) 245–251. doi:10.1016/S0268-0033(00)00089-9.
[13] J.C. Gardiner, J.A. Weiss, T.D. Rosenberg, Strain in the human medial collateral ligament during valgus loading of the knee, Clin Orthop. (2001) 266–74.
[14] C.Y. Huang, V.M. Wang, R.J. Pawluk, J.S. Bucchieri, W.N. Levine, L.U. Bigliani, V.C. Mow, E.L. Flatow, Inhomogeneous mechanical behavior of the human supraspinatus tendon under uniaxial loading, J. Orthop. Res. 23 (2005) 924–930. doi:10.1016/j.orthres.2004.02.016.
[15] S. Rigozzi, R. Müller, J.G. Snedeker, Local strain measurement reveals a varied regional dependence of tensile tendon mechanics on glycosaminoglycan content, J. Biomech. 42 (2009) 1547–1552. doi:10.1016/j.jbiomech.2009.03.031.
[16] S.G. McLean, K.F. Mallett, E.M. Arruda, Deconstructing the Anterior Cruciate Ligament: What We Know and Don't Know About Function, Material Properties, and Injury Mechanics., J. Biomech. Eng. 137 (2015) 020906. doi:10.1115/1.4029278.
[17] S.E. Szczesny, J.M. Peloquin, D.H. Cortes, J.A. Kadlowec, L.J. Soslowsky, D.M. Elliott, Biaxial tensile testing and constitutive modeling of human supraspinatus tendon, J. Biomech. Eng. 134 (2012) 21004.
[18] B. Reedlunn, S. Daly, L. Hector, P. Zavattieri, J. Shaw, Tips and tricks for characterizing shape memory wire part 5: Full-field strain measurement by digital image correlation, Exp. Tech. 37 (2013) 62–78. doi:10.1111/j.1747-1567.2011.00717.x.
[19] K.F. Mallett, E.M. Arruda, Digital Image Correlation-Aided Mechanical Characterization of the Anteromedial and Posterolateral Bundles of the Anterior Cruciate Ligament, Acta Biomater. (2017).

Chapter 3: Experimental Characterization of the AM Bundle

3.1 Introduction

The anterior cruciate ligament (ACL) plays a significant role as a major stabilizer of the articular knee joint [2–8]. The ACL is also the most commonly injured soft tissue structure in the knee, and demonstrates a low ability to self-heal [9–12]. Many patients with ACL tears opt for surgical replacements, and upwards of 300,000 ACL replacement (ACLr) surgeries are performed in the U.S. each year [13]. There is also growing concern for the populations most affected by ACL tears and replacements, specifically females aged 14-19, which represent the group with both the largest incidence of ACL injuries and the largest rate of increase of these injuries [14–20]. In addition, long-term outcomes of ACLr reconstructions manifest as degraded knee kinematics, tears of the replacement tissue, and early onset osteoarthritis [21–29]. Several reasons have been postulated for re-failure, especially the inability of tissue replacement options to restore native ACL response [21,30,22,31–42,29,43–45]. There is a pressing need to understand the intrinsic mechanical behavior of the ACL and its role in knee stabilization. To this end, a plethora of research has been performed to investigate these mechanical properties, in order to better identify possible replacement materials. However, the complex nature of the ACL, including its heterogeneity, orientation, and enthesis morphology, have made performing traditional mechanical characterization tests with well-defined boundary conditions difficult [46–52,8].

Much of the previously conducted work to characterize ACL mechanics has sought to elucidate the mechanical properties of the entire ACL in various loading states. Noyes and Grood tested entire human ACL femur-ligament-tibia complexes of young (16-26 yrs) and old (48-86 yrs) human cadaveric knees at a strain rate of 1/s and a knee flexion angle of 45° [48]. While no tangent modulus values were reported, McLean et al. later calculated the terminal tangent moduli in the Noyes and Grood study to be 110 ± 15 MPa and 62 ± 7 MPa for the young and old populations, respectively [53]. In two different studies, Weiler et al. tested intact ovine ACLs at 90° knee flexion and loading rates of 1 mm/s [54,55]. While neither paper reported tangent moduli, the reported tensile strength was 54 ± 14 MPa in one study [54], and 42 ± 5 MPa in the other [55]. Chandrashekar et al. tested entire human ACL specimens with femur and tibia bone plugs attached at a strain rate of 1/s, with reported tangent moduli of 128 ± 35 MPa and 99 ± 50 MPa for male and female populations, respectively [52]. Meller et al. reported a Young’s modulus of 217 ± 58 MPa at an unreported strain level for ovine ACLs [56]. While these studies form a basis for understanding the range of ACL mechanical properties, significant differences in loading rates, specimen orientations, and data reported have made direct comparisons among studies difficult, if not impossible.

The heterogeneity of the ACL is seen in its anteromedial (AM) and posterolateral (PL) bundles, with their distinct geometric and mechanical properties [57,16,17,58,59,18,60–62,46,63–71]. Despite their differences, the bundles of the ACL have received little individualized attention in the biomechanics community. Butler et al. tested the human ACL as three distinct bundles, testing bone-ligament-bone samples in uniaxial tension at strain rates of ‘100% of the initial subunit (bundle) length per second’ [49]. The reported tangent moduli were 283 ± 114 MPa, 286 ± 141 MPa, and 155 ± 120 MPa for the anteromedial, anterolateral, and posterolateral bundles, respectively. It is now widely accepted that the ACL consists of two bundles, namely the anteromedial (AM) and posterolateral (PL) bundles [53]. Ma et al. studied fresh ovine AM and PL bundles at a strain rate of 0.05/s [47]. In these tests, the tibia was split at the ACL tibial footprint to separate the AM and PL bundles, with each bundle connected to a distinct tibial bony section. Each bundle was tested in isolation at 0.05/s, to obtain its distinct mechanical properties. Ma et al. reported tangent moduli of 105 ± 67 MPa and 210 ± 58 MPa for the AM and PL bundles, respectively; the bundles were tested up to ~5% applied strain. The isolation of the bundles is a crucial first step to elucidate the intrinsic mechanical properties of the ACL, but further consideration of the bundle definitions, alignment procedures, and strain measurement approaches should be taken into account when comparing studies.

It is of critical importance to report mechanical properties of soft tissues in well-defined loading states as measured from un-deformed reference states. These properties may be used to design better ACL replacement grafts, or they may be implemented into FE models to provide insight into the strain response of complex materials in orientations unable to be reproduced in experimental studies. One example is the clinically relevant anterior tibial translation (ATT) test to determine knee laxity or diagnose an ACL deficiency. However, the efficacy of FE models relies on experimental data that comply with boundary conditions matching constitutive modeling assumptions. Test system compliance is an unavoidable consequence of both the methods of interfacing the specimens with the testing system, and the characteristics of the bone-ligament interfaces – especially the circular femoral insertions of both bundles and the tibial AM insertion along the anterior aspect of the tibial spines. System compliance can be overcome using digital image correlation (DIC), a non-contact, direct, tissue level displacement measurement technique. With DIC, local strains can be focused on, particularly those of the mid-substance of bundles undergoing uniaxial loading. The heterogeneity of the strain field can also be assessed. At the bone-ligament interfaces, because of their irregular shapes, the loading state is not well known. DIC also allows for visualizing surface strains (through post-processing of the displacement field images) across the surface of the tissue, without having to rely on the point-to-point measurements available from traditional LVDT sensors. However, away from the interfaces, the mid-substance is in a much more uniform axial deformation state. The purpose of this work is to elucidate the properties of the AM and PL bundles in uniaxial tension beyond the strain range seen in physiological loading situations using DIC displacement measurements and strain calculations, and to compare their responses with those determined via traditional strain measurement techniques.

3.2 Materials

20 fresh ovine knees were tested in this study. Knees were obtained from a local butcher ~12 hours after sacrifice, and refrigerated until testing. Knees came as a paired set from one animal (breed: Suffolk, age: <1yr). All knees were dissected to remove all soft tissue except the intact ACL, and each ACL was visually inspected for damage. Each knee in a pair was randomly assigned for testing of the PL or AM bundle, and the bundles of the intact ACL were then separated using forceps. The non-tested bundle was transected with a scalpel and removed at the tibial and femoral insertions, with care taken not to damage the remaining bundle. A MM30 Multi-Max™ Oscillating Power Tool (Robert Bosch Tool Corporation, Mt. Prospect, IL) was used to trim excess bone from both the tibia and femur to create 'bone plugs' for bone-ligament-bone specimens. The bone sections were cut to align the femoral and tibial entheses of the bundle, orienting the tissue along its long axis (see **Figure 3.1**). The alignment and bone-ligament-bone (BLB) isolation processes are described in detail below.

In the native ACL orientation, the AM bundle tibial insertion can be seen on the anterior aspect of the tibia (**Figure 3.1a**). At the femoral insertion, the AM is visualized between the femoral condyles, facing towards the lateral part of the knee (**Figure 3.1b**). After removing the PL bundle (**Figure 3.1c**), an initial ~90° twist of external rotation of the femur relative to the tibia is needed to align the entheses (**Figure 3.1d**). Next, a ~90° flexion of the tibia relative to the femur aligns the tissue in a uniaxial orientation, and excess bone from the tibia must be removed to allow this rotation (**Figures 3.1e** and **3.1f** show the bundle orientation prior to this removal). The final orientation of the AM BLB specimen aligned uniaxially is shown in **Figure 3.1g**. The PL bundle BLB specimens were created in a similar manner. To align the PL uniaxially, a ~90° twist about the PL longitudinal axis of the femur in external rotation relative to the tibia is required to untwist the PL bundle completely. The aligned BLB PL specimen is shown in **Figure 3.1h**.

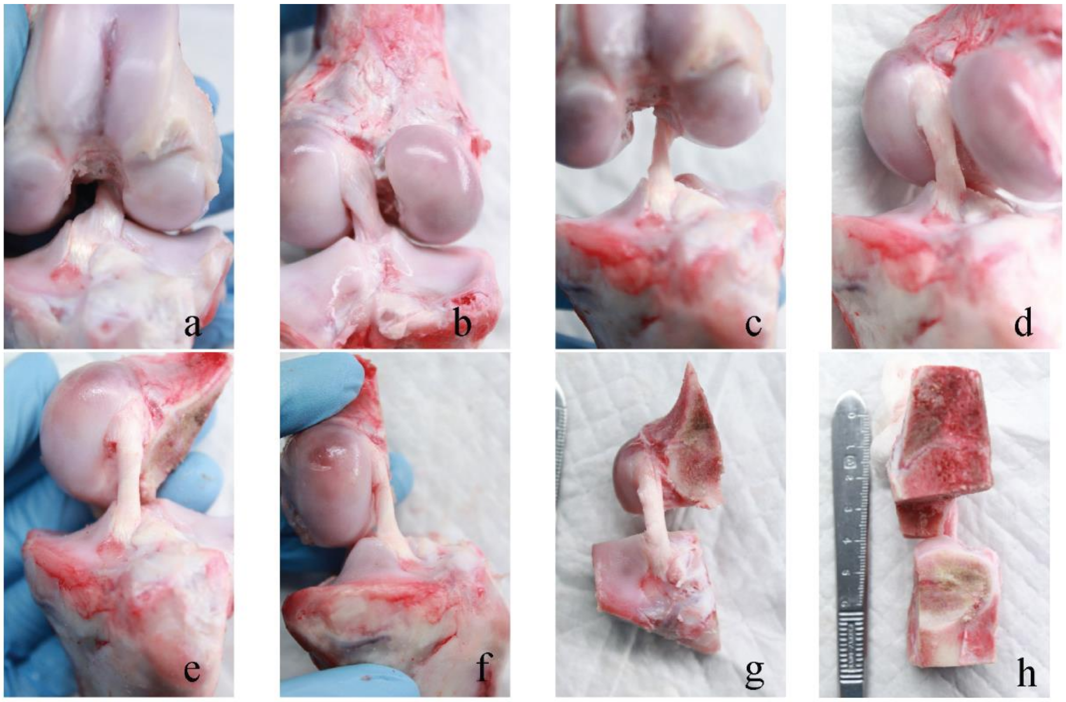

Figure 3.1: Creation of AM bundle BLB specimens. a) anterior view of complete ACL at ~90° knee flexion in physiological 'native' orientation. b) posterior view of complete ACL ~0° knee flexion in native orientation. c) Anterior view of femur, tibia and AM after removal of the PL, showing the 'twist' of AM bundle in the native orientation. d) Medial view of AM bundle after ~90° external rotation of femur relative to tibia. e) Medial view of AM bundle after removing excess femur. f) Profile view of AM bundle with femoral bone removed, note that additional bone must be removed from the tip of the remaining femoral condyle and the posterior aspect of the tibia to fully orient the AM bundle in uniaxial tension. g) Final BLB specimen with AM bundle oriented in uniaxial tension. h) Final BLB specimen of the PL bundle oriented in uniaxial tension. [1]

3.3 Methods

After isolating and aligning the BLB specimens, they were potted in custom grips using a biodegradable and non-toxic thermoplastic (McMaster-Carr, Aurora, OH). The grips holding the BLB specimens were installed in a servo-hydraulic MTS 810 Material Test System (MTS Systems Corporation, Eden Prairie, MN). As seen in **Figure 3.2a**, Specimens were manually aligned with the loading axis of the MTS. In addition, the MTS was custom-built with two opposing actuators, enabling the center of specimens to remain stationary during loading, keeping the region of interest in full view of the cameras throughout the entire loading excursion.

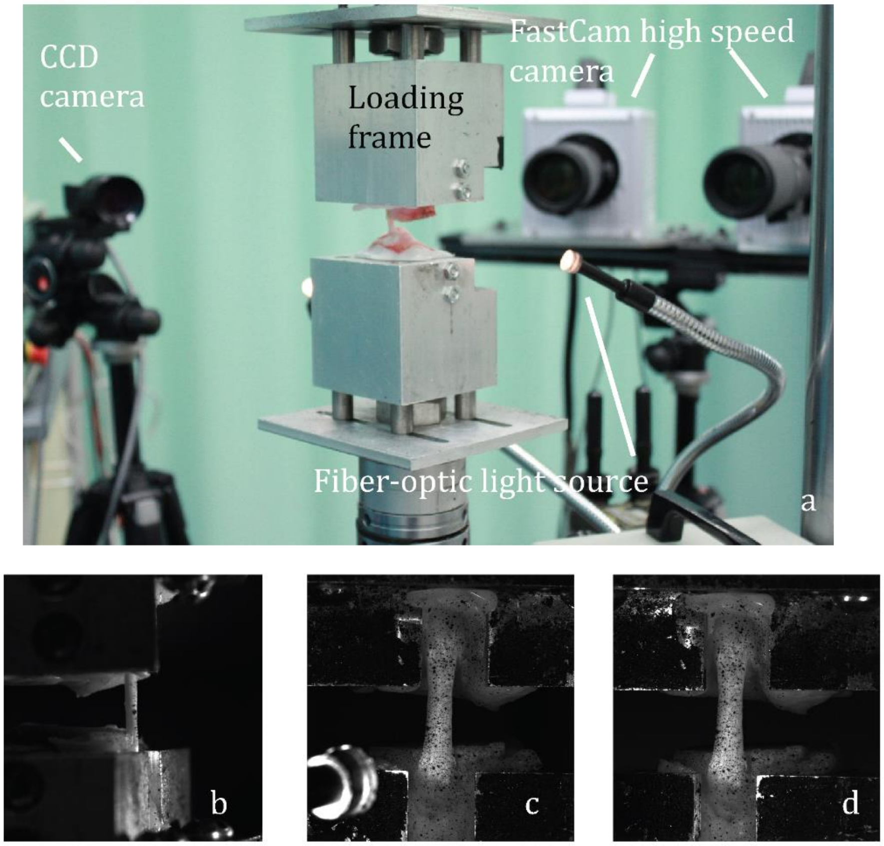

Figure 3.2: a) Uniaxial tension testing of an AM bundle in a MTS 810 Material Test System with dual actuators. Two Photron Fastcam SA1.1cameras are used to visualize the 3D surface strain contours c, left front and d, right front), while one Point Grey Gras-50SM-C camera captures the profile (b). [1]

The MTS interfaced with a custom data acquisition program built in LabVIEW (National Instruments Corporation, Austin, TX). The analog voltage signals for force and displacement from the MTS were acquired and recorded with a NI USB-6361 DAQ device (National Instruments Corporation, Austin, TX). The custom LabVIEW program prescribed a load-unload path under displacement control to a user-defined final 'grip-to-grip' strain (essentially the strain computed from the applied displacement of the servo-hydraulic actuators). This grip-to-grip strain may be greater than the actual tissue strain if there is compliance in the grips. The approximate length of each specimen was measured with an ABSOLUTE Solar Caliper Series 500 caliper (Mitutoyo America Corporation, Aurora, IL). This measurement was used to calculate and prescribe the approximate grip-to-grip final strain for the load-unload tests. The mid-substance cross-sectional area (CSA) of the AM bundle was calculated assuming a rectangular CSA with rounded semi-circular edges, using the width and thickness of the middle section of the tissue. The PL bundle demonstrates a more ‘undulated’ surface than the AM, where fascicles are oriented more randomly in the anterior-posterior direction (into and out of the page from an anterior view). A rectangular CSA was assumed for the PL, due to this undulation. In both cases several options for the shape of the CSA were considered, and, for the AM in particular, this CSA assumption matches the flat surface of the AM bundle. Thus the E_{33} strains reported by the DIC data are representative of the majority of the surface the specimen.

Three cameras were used for full-field displacement measurement of the tissue during loading. In this case, the term ‘full-field’ refers to the surface view of the tissue visible within the field of view of the camera(s). Two Fastcam SA1.1 cameras (Photron USA, Inc., San Diego, CA) were used to visualize the front surface of the BLB specimens during testing in uniaxial tension, in conjunction with Nikon AF Micro-Nikkor 200 mm lenses (Nikon Inc., Melville, NY). In addition, one Grasshopper Gras-50SM-C (Point Grey Research Inc., Richmond, BC, Canada) visualized the narrow medial or lateral surface at the mid-substance of the tissue (profile view). This profile view camera was intended to measure the change in thickness of the bundles during testing, as negative Poisson's ratios for soft tissues have been reported [72]. The FASTCAM cameras were chosen for their excellent resolution of the front surface of the tissue. However, the lower resolution of the Grasshopper camera, combined with the difficulty of lighting two surfaces (front and profile) during testing, resulted in less accuracy for the thickness measurements compared to the width and length measurements.

Reference images were taken from each camera with a scale for measurement of the actual length, width, and thickness of the tissue specimens, and ImageJ software (National Institutes of Health, Bethesda, MD) was utilized to obtain dimensions. The acquisition of load and displacement data was synchronized with image capture using an AFG3021C single channel arbitrary/function generator (Tektronix, Inc, Beaverton, OR). All three cameras were triggered by a 3 V TTL signal from the function generator, and this voltage was recorded by the data acquisition system. Load and displacement data were acquired at 500 Hz, and the Fastcam SA1.1 and Grasshopper Gras-50SM-C cameras acquired images at 50 Hz and ~12 Hz respectively.

For full-field displacement measurements over the surface of each specimen, DIC, a non-contact and length scale independent technique, was used. This technique measures displacements and calculates strains on the surface of a material undergoing deformation. The correlation algorithm functions by identifying unique pixel subsets within a pseudo-random high-contrast pattern on the surface. By tracking the translation, rotation and deformation of each subset, the algorithm can measure the full-field surface displacements and calculate the corresponding strains. Two types of DIC are commonly used. 2D DIC calculates full-field strains of planar test specimens. In addition to this, the 3D DIC technique utilizes two sets of camera images for the same test, and is capable of tracking out-of-plane deformation by triangulating the position of the specimen in 3D space. 3D DIC was performed for all test specimens, and the stereo angle between the cameras was 18.75 ± 0.85° from six camera calibrations.

For many materials, an artificial pseudo-random stochastic pattern is required for the tracking of material displacements. For these experiments, a non-toxic alcohol-based ink (ShowOffs Body Art LC, Clarkston, MI) was applied to the front surface of the specimen using a Custom Micron CM-B airbrush and Power Jet air compressor (Iwata Medea Inc., Portland, OR). This alcohol-based ink is easily removable using a 70% solution of isopropyl alcohol (Vi-Jon Laboratories Inc., St. Louis, MO), but water-insoluble. This provides great flexibility in creating patterns with optimal density and contrast, as it allows for easy removal and reapplication if necessary e.g., if the initial pattern is not adequate, or for subsequent load excursions. A humidifier was also utilized during testing to hydrate the environment (EE-5301 drop humidifier, Crane USA Inc., Bensenville, IL).

During testing, each knee was pre-tensioned to 3 mN (to ensure the tissue was not slack), in a procedure similar to that used previously and loaded to 12% grip-to-grip strain at a 0.05/s true strain rate [73,74]. The strain rate is consistent with strain rates traditionally chosen [75]. The maximum strain was chosen outside of the physiological range in order to fully capture the tissue's physiological response, including unloading, without causing tearing during the loading excursion. Each specimen was then unloaded at the same strain rate and allowed to relax for 15 minutes, then tested to failure at 0.05/s. The stochastic ink pattern was reapplied prior to the test to failure if necessary, and the tissue kept hydrated throughout testing by spritzing with Dulbecco's Phosphor Buffered Saline (ThermoFisher Scientfic, Waltham, MA). Data were acquired through the full load/unload path of the test, in order to quantify the hysteresis of the material response, measured as the difference between the load and unload curves, in MPa. The raw load and actuator displacement data are converted to nominal stress (load divided by mid-substance CSA) and grip-to-grip nominal strain (displacement divided by initial length) curves. Raw camera images were correlated using VIC-3D (Correlated Solutions, Inc., Columbia, SC). The DIC data from VIC-3D was extracted to MATLAB (The MathWorks, Inc., Natick, MA). The output DIC data was extracted as Green-Lagrange strain, a finite strain measure given by

$$\boldsymbol{E} = \frac{1}{2}(\boldsymbol{C} - \boldsymbol{I}) \tag{1}$$

where $\boldsymbol{C}$ is the right Cauchy-Green tensor and $\boldsymbol{I}$ is the identity tensor (tensors indicated in boldface). The nominal axial strain is used for plotting the stress/strain response, and is defined in terms of the axial component of the Green-Lagrange strain tensor as

$$e_{33} = \sqrt{2E_{33} + 1} - 1 \qquad (2)$$

3.4 Results

The specimen dimensions of the AM and PL BLB specimens are shown in **Table 3.1**. Two of the AM bundles were excluded due to changes in the testing environment and data synchronization issues. The AM bundle is longer than the PL bundle, but it has a smaller average and mid-substance cross-sectional area. The AM bundle has a ribbon-like CSA, almost three times as wide as it is thick, while the PL bundle has a more rectangular CSA.

Representative displacement contours of the front surface of an AM bundle are shown in **Figure 3.3**. The displacement path of the test machine was prescribed using a

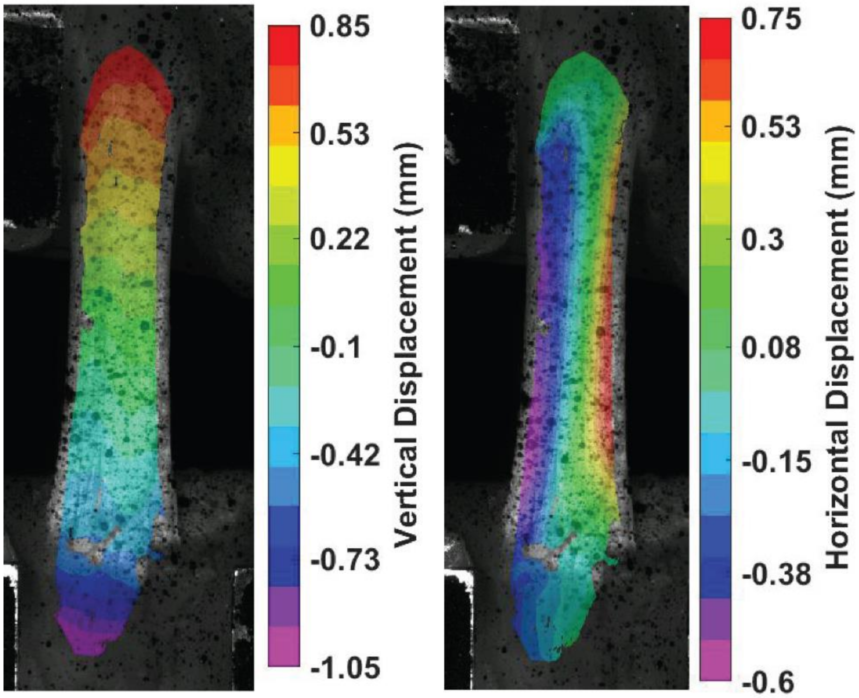

Figure 3.3: Full-field AM bundle vertical (left) and horizontal (right) displacement contours at peak displacement. [1]

constant true strain rate formulation. Thus, the displacement is quasi-linear in the small strain regime. These contours show the full-field tissue response of the AM at a peak applied grip-to-grip strain of 12%. The use of dual actuators keeps the specimen in the center of the camera frames, and the resulting vertical displacement shows this, with 0.85 mm and -1.05 mm displacement at the femoral and tibial ends of the tissue, respectively. The horizontal contours reveal significant transverse expansion of this AM bundle of a total of 1.35 mm from an original mid-substance width of 4.80 mm.

Table 3.1: Dimensional data of AM and PL bundles

Bundle	Length (mm)	Mid-substance Width (mm)	Mid-substance Thickness (mm)	Mid-substance Cross Sectional Area (mm^2)
AM (n=8)	31.7± 12.3	5.5 ± 0.5	2.3 ± 0.6	11.8 ± 4.3
PL (n=10)	18.9 ± 2.6	5.0 ± 0.8	4.2 ± 0.9	21.1 ± 7.1

There is debate in the field about whether soft tissue tendons and ligaments demonstrate a negative Poisson’s ratio [76–78]. However, many of these works have ignored changes in the third direction. In this work, low resolution in the profile view camera, as well as lighting and camera placement constraints hindered measurement of the bundle thickness. Although these issues reduced the accuracy of the profile thickness displacement, dilatation from 5 of the bundles (calculated using the strains in the axial, transverse and thickness directions as well as the initial tissue volume of the mid-substance) was found to be 1.7e-3 ± 1.8e-3 /mm^3 at an axial tissue strain of 3%. Thus, overall, this AM bundle slightly increased in volume under a tensile load, which is typical for elastic materials in tension.

Figure 3.4 illustrates the strain contour of a typical AM bundle at maximum 12% grip-to-grip strain. The contours are those at pre-load, mid-displacement, and peak displacement (~12% global strain). It should be noted that the applied global displacement was based on the caliper estimate of the bundle length, whereas the actual bundle length was determined after testing from camera images using ImageJ software as described above, so the actual applied grip-to-grip strains varied. **Figure 3.4a** shows the pre-load response, with essentially zero strain on the specimen, as expected. By mid-displacement (**Figure 3.4b**), the AM bundle shows a homogenous axial strain (E_{33}) response, and a band of an expanding fascicle is visible in the transverse strain (E_{22}) contour. This positive transverse strain is in agreement with the outward horizontal displacement contours shown in **Figure 3.4**.

Shear is also present (E_{23}). At the peak applied displacement (**Figure 3.4c**), the axial strain is still homogeneous in the mid-substance and the lateral expansion of the AM bundle is strongly evident, with local strains as much as 55%.

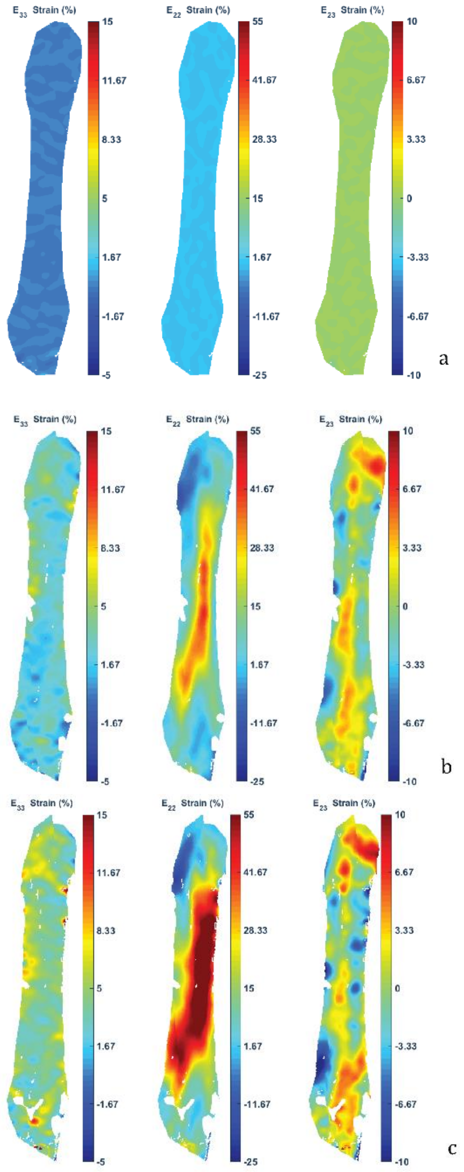

Figure 3.4: Strain contour evolution of an AM bundle during loading under uniaxial tension a) Pre-displacement axial (vertical direction, E_{33}), transverse (horizontal, E_{22}), and shear (E_{23}) strains b) Mid-displacement axial, transverse, and shear strain contours c) Peak displacement axial, transverse, and shear strain contours at ~12% applied global strain. [1]

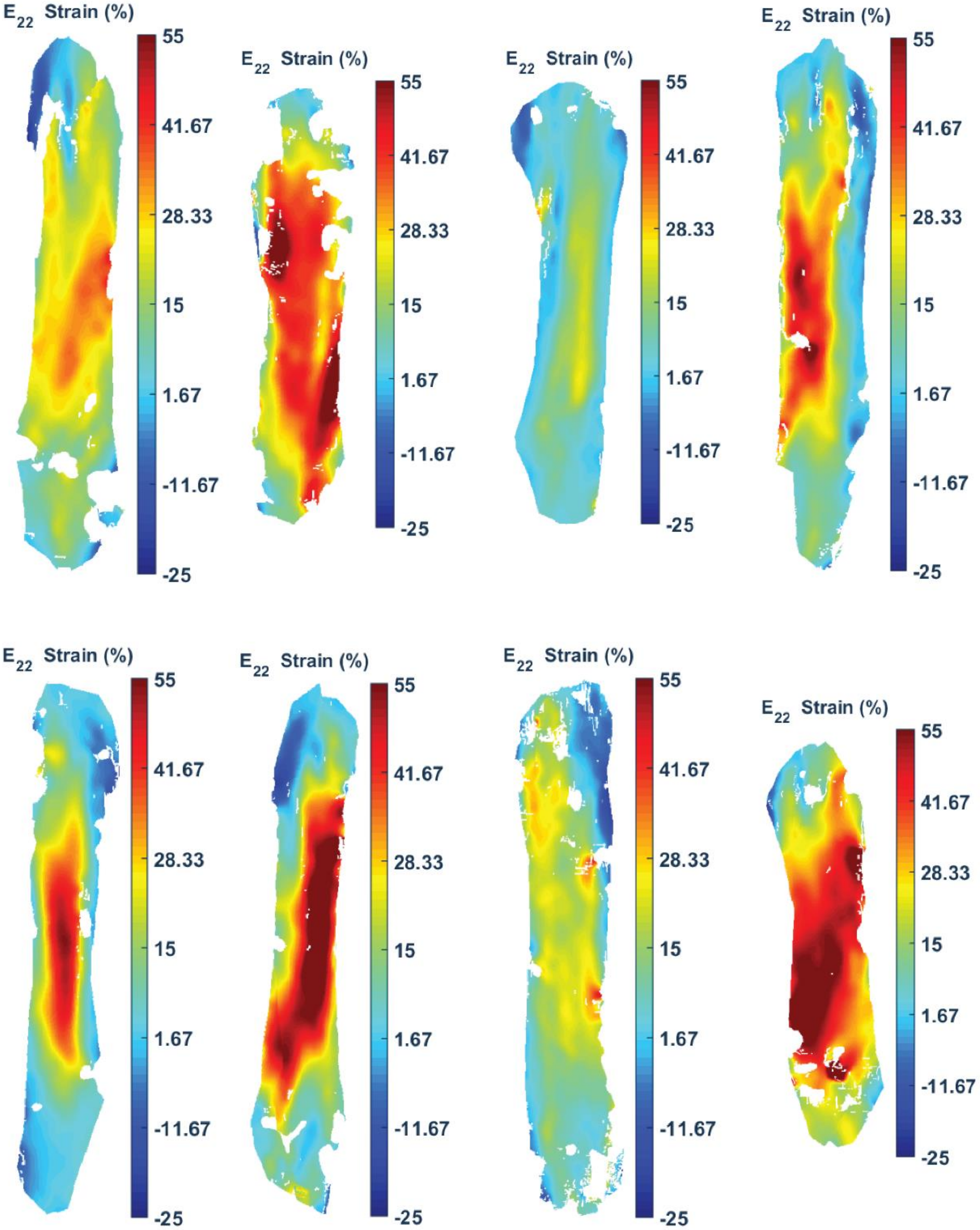

Figure 3.5: AM bundle axial (vertical) strains at an average DIC-computed mid-substance

Figure 3.6: AM bundle transverse (horizontal) strains at an average DIC-computed mid-substance Green-Lagrange strain of 3%. [1]

The axial strains in **Figure 3.5** show relative homogeneity within the mid-substance region of the bundle surface contours (see **Figure 3.8** for an example of the

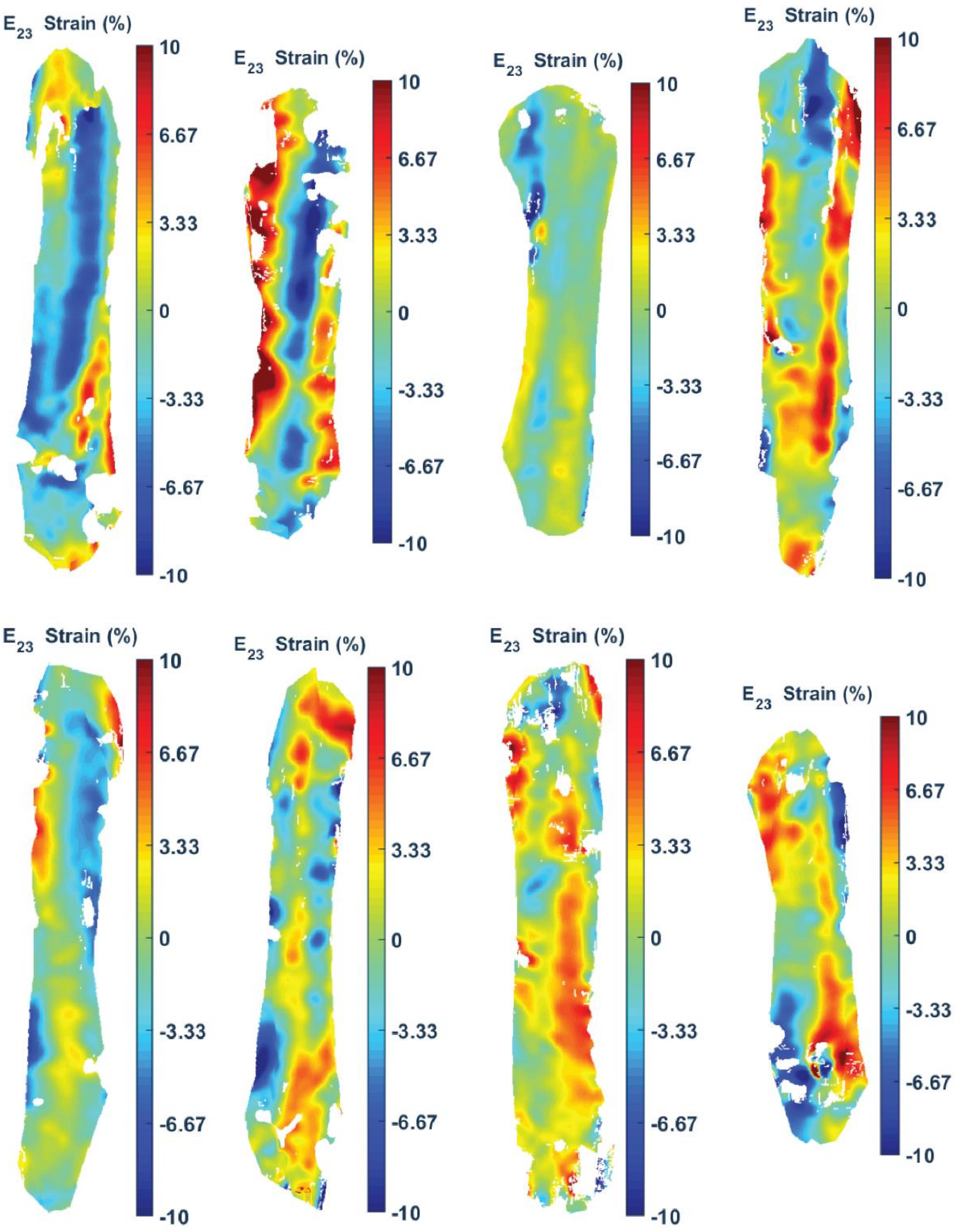

Figure 3.7: AM bundle shear strains at an average DIC-computed mid-substance Green-Lagrange strain of 3%. [1]

mid-substance region). Inhomogeneity and higher strain regions manifest in the axial strain contours in the regions of the tissue where the AM bundle attaches to the femur and tibia. It is critical to recognize the loading state in these regions cannot be defined as uniaxial, as the bone-enthesis-ligament geometries are complex morphologically. The mid-substance region sufficiently far from the bones experiences uniaxial loading, therefore it is the appropriate region for determining bundle mechanical properties.

Transverse strains are shown in **Figure 3.6**. All AM bundles manifested high transverse strains, with many exceeding 55% local strain. The profile camera view data was observed and it was verified that with loading, the thickness of the AM bundles decreases. While the thickness direction had lower accuracy, overall the thickness direction of the AM bundles did decrease.

The shear response (**Figure 3.7**) is also distinct, and not zero, which is what would be expected for traditional materials tested in uniaxial tension. This shear response is likely due to inherent misalignment of the fascicles in the AM to PL bundles, and is covered in more detail in the Discussion section.

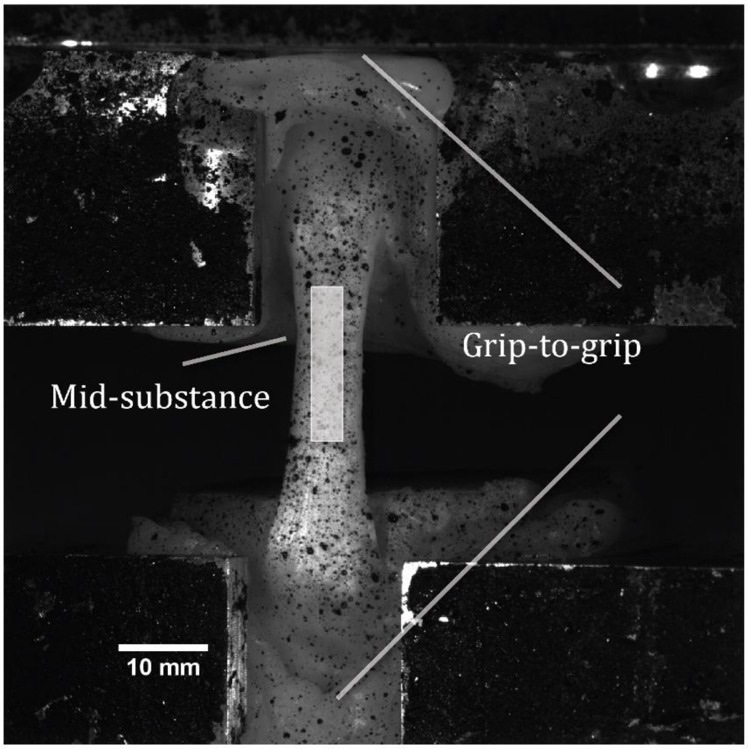

Figure 3.8: Representative region of strain analysis used in the generation of the stress vs. strain response curves of the AM bundles. The shaded mid-substance region of the tissue is used, whereas 'grip-to-grip' indicates measurements taken from the point-to-point measurement capability of standard uniaxial tension test equipment. [1]

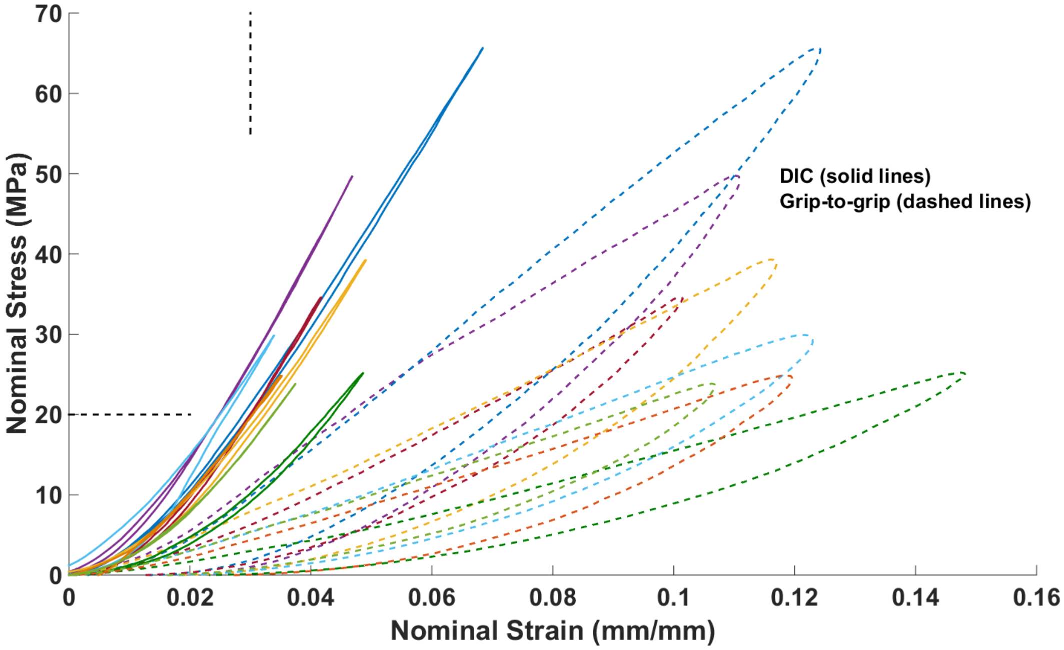

Figure 3.9: Stress vs. strain responses of eight AM bundles, with DIC curves shown with solid lines and grip-to-grip shown with dashed lines. Each color represents a unique bundle. Dashed lines at 20 MPa and 3% nominal strain mark locations of tangent moduli calculation, as discussed in Figures 3.10a and 3.10b. [1]

The homogenous longitudinal strains measured via DIC within the mid-substance of the AM bundles provide the basis for determining the mechanical properties of the AM bundles. **Figure 3.8** shows a representative mid-substance region selected from the DIC strain contours used in calculating the stress/strain response of an AM bundle. This mid-substance region was selected away from the edges of the tissue to avoid regions of sparse DIC data. This region is also well away from the femoral and tibial insertion regions of the tissue, to ensure the characterization is that of a tissue undergoing a well-defined uniaxial loading state.

The DIC strain data from the mid-substance of the AM bundles was used to compute the nominal-stress vs. nominal strain response curves of the tissue, and these are shown in **Figure 3.9**. Also in **Figure 3.9** are response curves generated using the grip-to-grip strains. All of the curves demonstrate an initial ‘toe’ region, with low nominal stress for the initial applied strains, followed by stiffening in the stress response. This response is common for ligament tissue, with the toe region understood to be the straightening of initially crimped collagen fibers. Hysteresis, a measure of the viscoelastic response of a material, can be observed in a variety of experimental testing techniques. For materials deformed at constant strain rate, the viscoelastic behavior will manifest as the area between the load/unload paths of the stress/strain response, and is evident in the curves calculated using grip-to-grip

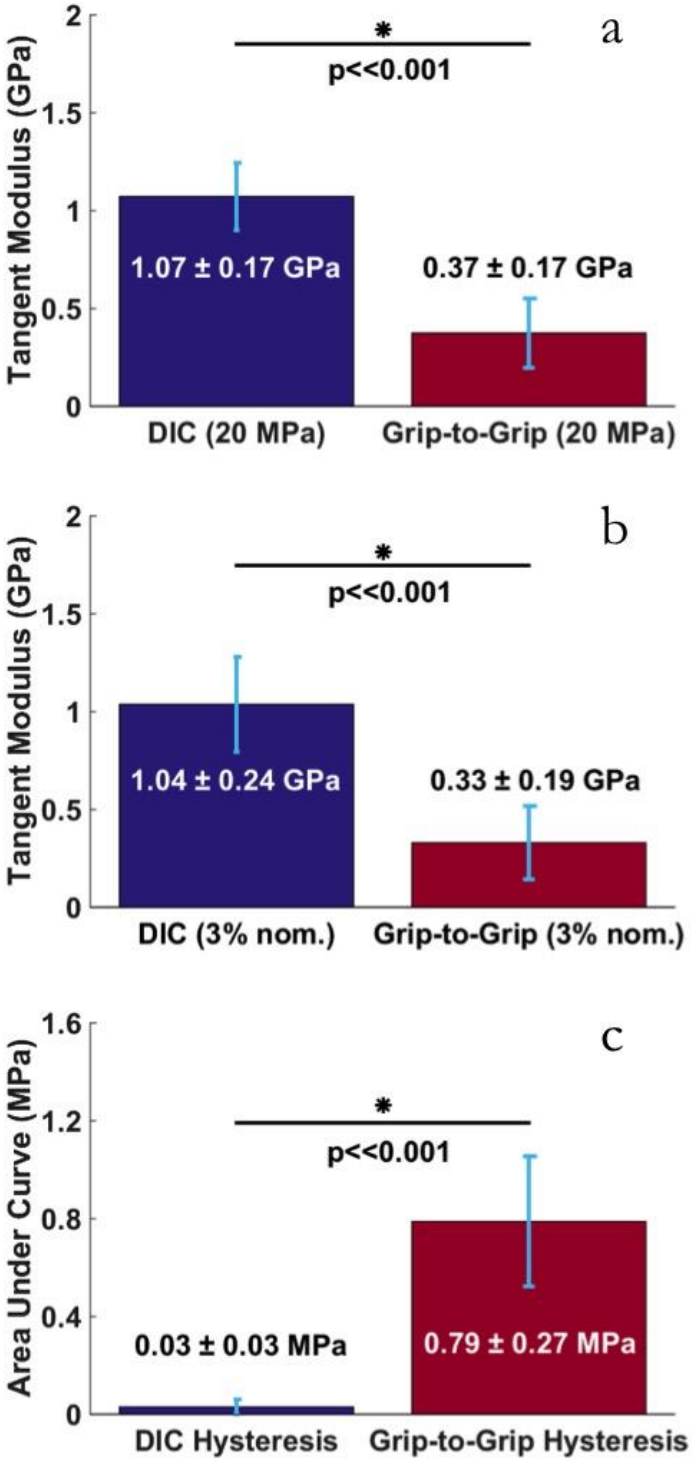

Figure 3.10: Tangent moduli at 20 MPa and 3% nominal strain (a,b). c) Hysteresis difference between DIC and Grip-to-trip responses. [1]

displacements.

As can be inferred from the low strains of the homogenous contours of **Figures 3.9**, the DIC based curves (solid lines) demonstrate much lower strain levels compared to the measured grip-to-grip strain levels for all bundles. There is also more variability of the grip-to-grip response vs. the mid-substance response. Comparing the DIC and grip-to-grip data, it should be noted that the grip-to-grip method cannot differentiate what is

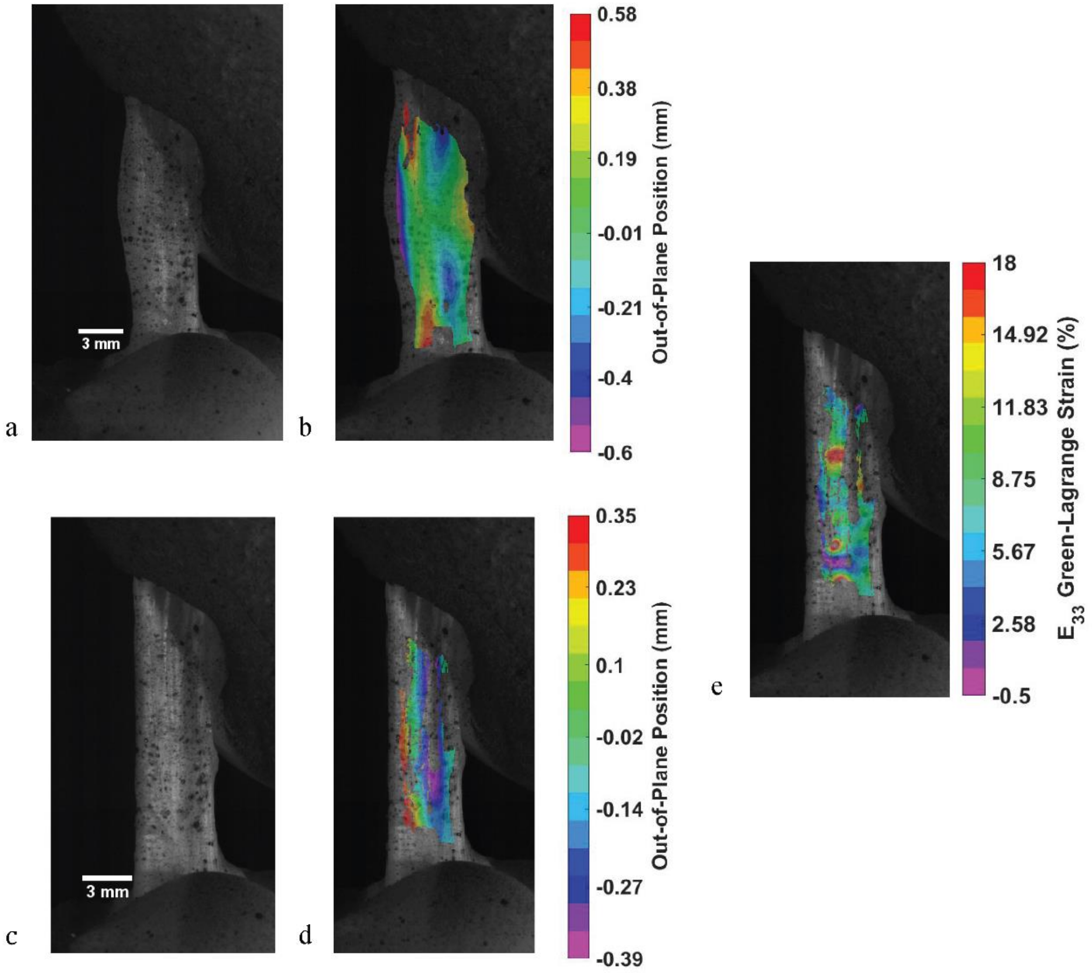

Figure 3.11: a) PL bundle prior to loading b) Pl bundle raw DIC contour image coverage in the depth (into the page) direction. c) and d) PL bundle expansion and contour coverage at image before de-correlation occurs. e) PL bundle axial strain data. [1]

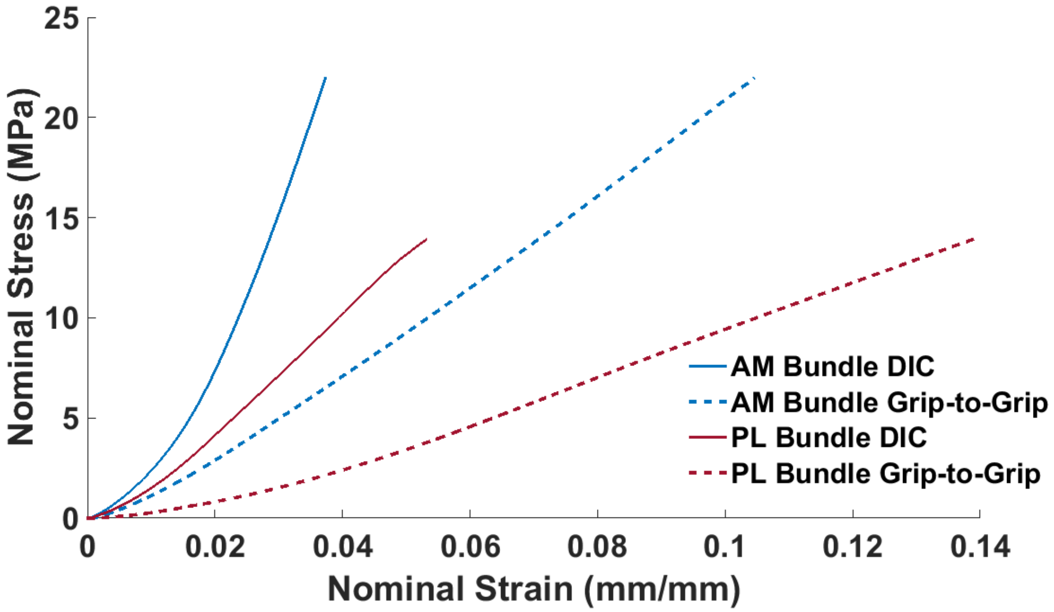

Figure 3.12: Loading response to 12% grip-to-grip strain of representative AM and PL bundles measured via DIC and grip-to-grip. Test specimens were taken from paired knees of the same donor, with the AM bundle demonstrating higher stiffness, lower strain to failure, and higher stress at failure than the PL bundle. [1]

happening on the surface of the material from compliant grip related information; DIC more accurately shows the strain response of the tissue during loading.

Figures 3.10a and **3.10b** show the average tangent moduli of the eight AM bundles at a constant stress of 20 MPa and a constant strain of 3%, respectively. Tangent moduli computed both ways (1.07 ± 0.17 GPa at 20 MPa and 1.04 ± 0.24 GPa at 3% nominal strain) were significantly higher using DIC contour strain data compared to traditional grip-to-grip strain measurement techniques. The grip-to-grip data agree with previous studies of the bundles of the ACL when the spread of that data is considered (Butler et al. [49]). **Figure 3.10c** is the hysteresis response of the DIC vs. grip-to-grip strain methods. The hysteresis is drastically reduced when DIC is used to compute strains vs. when grip-to-grip strains are used (n=8), and there is virtually no hysteresis in the mid-substance regions at the applied strain rate of 0.05/s.

The PL bundle poses additional challenges in obtaining surface level strains during load/unload testing. **Figure 3.11a** and **3.11b** show a representative PL bundle prior to loading, and an un-deformed DIC contour of out-of-plane distance relative to an arbitrary zero on the tissue surface. This un-deformed contour shows good coverage of the bundle, especially the bundle mid-substance. The PL bundle lacks the flat, ribbon-like geometry of the AM bundle, and individual fascicles move out-of-plane during loading (**Figures 3.11c and 3.11d**). For this reason, one representative contour is shown from the PL results due to poor correlation. However, axial strain data from regions retaining correlation demonstrate peak nominal strains ~6%.

A comparison between the AM and PL bundle stress/strain responses is shown in **Figure 3.12**. The data for these curves were taken from the same animal, to avoid differences due to biological variability. The AM bundle manifests a stiffer response with a lower strain to failure compared to the PL, with the PL experiencing a peak stress prior to failure of 60% of that of the AM. This diverse response of the AM and PL bundles supports the need to characterize them separately, as single bundle models cannot capture the complete mechanical response of both bundles.

3.5 Discussion

Several challenges were faced in this work, including the use of specimens from a local butcher, and the design of the experimental testing protocol. Knees were obtained from a local butcher via a commercial slaughterhouse, and it was not possible to control for specimen gender. In addition, the adaptation of DIC for biological specimens, and the alignment and uniaxial loading of the AM and PL bundles is particularly challenging. The use of DIC allows for non-contact full-field deformation visualizations, and provides a wealth of information for material characterization. Previous studies of ligaments and tendons have utilized surface markers to optically measure tissue strains. Woo et al. and Wren et al. used markers to measure the gauge length of specimens during testing, while Butler et al. optically tracked grip slippage with marks at the tissue-grip interface [79–81]. 2D marker bead arrays have also been used to calculate surface strains [82–84]. However, in each of these cases, these studies only reported strains along the axis of loading, and did not include transverse or shear strains. In addition, small numbers of markers were employed, ranging from ~9-15 per specimen, likely due to the labor-intensive process of manually placing each marker. These techniques do not have the resolution DIC provides and cannot assess homogeneity vs. heterogeneity. In addition, although 2D displacement measurement techniques have been employed, little attention has been given to the non-axial strains (i.e. transverse and shear strains), leading to lack of insight on complex tissue deformations [82–84]. In a study of Achilles tendons, Rigozzi et al. in particular compares the optically measured strains with the traditional point to point measurement, and reports that '...strains in the [mid-substance] were typically half that of the machine-based tendon strains." [84] The study concludes this difference is due to a combination of ‘relative movement between internal tendon substructures’ or slippage of the tissue within the grip system. It should be emphasized that while compliance is a challenge for soft tissue experiments, DIC measures the tissue-level response only, and is not affected by the rest of the testing system (bone plugs, grips, load train). ACL fibers are known to fail around 6% strain; this is supported by the strains computed via DIC as opposed to the strains computed via traditional grip-to-grip measurement methods.

Another challenge was the alignment of the bundles under uniaxial loading. In addition to the twist of the AM around the PL, the AM entheses insert along curved aspects of the femur and tibia. At the tibia, the AM inserts along the anterior aspect of the tibial spine, and is attached to the tibial spine at all points of the bone. At the femur, the AM inserts superiorly to the PL at the interior aspect of the lateral femoral condyle, again along the curved surface of the bone. The PL bundle femoral enthesis inserts along the interior aspect of the lateral femoral condyle. The PL splays out from the femur, inserting into the middle of the tibia with an oblong morphology. At the tibial insertion the PL bundle can be visualized from the anterior side of the knee. At the femur, the PL can only be fully visualized along its entire length from the posterior side of the knee. This is due to the AM wrapping around the PL at the medial and anterior viewpoints of the knee. In addition, from the lateral viewpoint, the lateral femoral condyle extends past the enthesis, obscuring it from view. However, isolating the tibial bone plug for the PL is relatively straightforward, due to the normal insertion of the PL into the tibia.

The axial response of the AM bundle is relatively homogenous within the mid-substance of the tissue, making this section ideal for mechanical characterization. The femoral and tibial insertions are regions where the boundary conditions diverge from the uniaxial tension loading state, and, as would be expected, these regions demonstrate inhomogeneity in the axial strain response. As mentioned in the introduction, previous work in this area has focused on a variety of challenges in ACL characterization, and there is a paucity of work isolating the individual ACL bundles in well-known loading states. The work by Butler et al. [49] is one of very few studies of individual BLB specimens of the ACL bundles. In these tests, ‘anterolateral’ and ‘anteromedial’ bundles were defined and tested independently by separating the ‘anterior’ ACL bundle (likely a split of the now commonly defined AM bundle). In addition to this bundle separation, strains were measured using a linear variable differential transformer (LVDT), in this case a grip-to-grip measurement device. Butler et al. reports tangent moduli of 283 ± 114 and 286 ± 141 MPa for the anteromedial and anterolateral bundles, while this work reports 1.07 ± 0.17 GPa for DIC and 0.37 ± 0.17 GPa for grip-to-grip (at constant 20 MPa stress) and 1.04 ± 0.24 GPa for DIC and 0.33 ± 0.19 GPa for grip-to-grip (at constant 3% strain) for the AM bundle. The grip-to-grip measurements encompass the results reported by Butler et al. when the spread of that data is considered. The large differences in the testing methods, especially bundle definitions and strain measurement approaches, contribute to the differences between the tissue-level DIC data and point-to-point measurements. This work contained good alignment of the entire tissue bundle, and axial strains were uniform in the mid-substance and larger outside the mid-substance region (**Figure 3.5**).

The transverse strains of the AM bundle are high, especially for a specimen in uniaxial loading, and positive, likely due to individual fascicles expanding laterally. This expansion may be explained by the fact that the fascicles flatten out as they insert into the enthesis, and are rounded in the mid-substance. The shear response of **Figure 3.7** is unexpected for an orthotropic material in uniaxial tension that has its principal material direction aligned with the loading direction. **Figure 3.13** shows the un-contoured bundle with a selected contour from **Figure 3.8**. As can be seen by the red and blue markers, some fascicles are aligned on the right side of the bundle at the femur, but insert into the tibia on the left side of the bundle (blue arrows). Other bundles are more aligned axially (red arrows). This indicates that some level of shear deformation is due to the detailed level of misalignment of the stiff fascicles within the AM bundle, rather than a systemic problem stemming from the grips or possible differences in left and right knees.

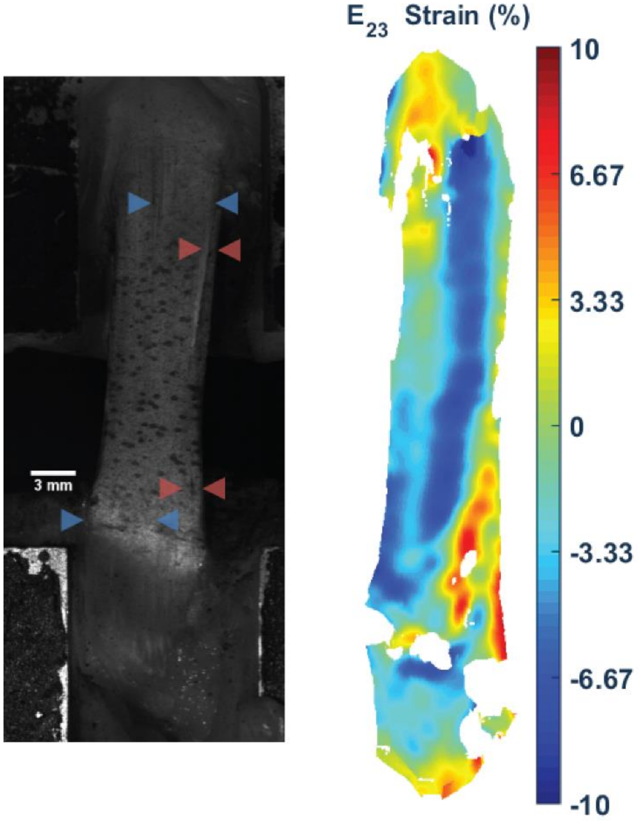

Figure 3.13: AM bundle at peak displacement (left) and the resulting shear strains (right). The blue and red markers indicate specific fascicles at the femur and tibia. The blue markers show a band of fascicles misaligned vertically, originating into the femur near the right side of the image at the top and inserting into the tibia at the left on the bottom. The red show a relative vertical fascicle band. This intrinsic fascicle orientation dominates the shear response. [1]

The undeformed PL contour (**Figure 3.11a**) demonstrates undulation of the bundle surface; the section of tissue on the right inserts into the tibia more anteriorly or towards the camera. During loading (**Figures 3.11c** and **3.11d**), it is common for individual fascicles to move anteriorly, further undulating the surface, resulting in loss of correlation. However, axial strain data from regions retaining correlation can be used for stress/strain analysis, and the lower left region of this representative PL bundle shows strains around 6% close to peak displacement.

Failure tests were also conducted on all 20 bundles. In 17 of 19 data sets, the BLB specimens failed at the bone rather than the ligament proper or even the enthesis. The uniaxial testing configuration is not the physiological orientation, so drawing conclusions about clinical relevancy could be problematic. Great care was taken in gripping and orientating the tissue such that specimens were uniaxially loaded; however in some cases a small amount of bending was indicated (1.24 mm overall out-of-plane displacement along a 38 mm bundle in the case shown in **Figure 3.3**). Due to the complex structure of the bundles, fascicles are longer on the anterior surface than the posterior, and DIC only provides measurements on the front surface. Full-volumetric displacement measurements would be needed to accurately determine the through-thickness material response of the tissue.

This work achieves better alignment of full bone-ligament-bone specimens than that seen in the literature to date, and that is likely the source of the presented higher moduli. Good alignment and minimized compliance provides stiffer measurements even in the grip-to-grip. The mid-substance is less affected by regional loading condition variations, as the DIC analysis is limited to a region that is undergoing uniform loading, exhibiting homogenous uniaxial strains in that region, and is a true tissue level measurement with no system compliance.

In addition to direct bundle axial strains, DIC provides transverse and shear strain data, pointing to the further complexity of the bundles of the ACL. Future applications of this work would include the development of mathematical models for the bundles and their implementation into computational models. The individual bundle mechanical responses can be used to develop individually characterized computational structures, and the ACL can then be computationally reconstructed to determine the pre-strained state of the ACL in its physiologically relevant state at any knee flexion angle. This sequence of steps would provide the needed information to generate truly accurate computational models of the ACL.

3.6 Conclusions

This work demonstrates that DIC is an attractive way to characterize the longitudinal response of soft tissue due to its non-contact and full-field nature. The use of DIC provides local full-field deformation data. However, DIC patterning requirements have created challenges for its use in biological tissue testing, as traditional patterning mediums can adversely affect the tissue surface and mechanical response. In this study custom-designed pattern stencils were implemented in combination with airbrush applicators and a water insoluble ink. This method allows for the control of the pattern density and speckle size, while allowing multiple reapplications (if needed), and the ability to keep soft tissues hydrated during testing.

In this work, DIC axial strains are significantly lower than data provided from the grip-to-grip response, and shear and transverse strain data would typically not even be measured using traditional techniques. This full tissue information gives valuable insight on the unexpected transverse and shear responses of the ACL in uniaxial tension. Taking the shear especially into account, it is recognized that E_{33} is not a principal strain, but despite this, DIC greatly reduces the specimen-to-specimen variability that has come to take for granted in biological tissue testing, signifying that some of these issues could come from alignment and compliance effects.

The results of this work provide new information on the mechanical response of the bundles of the ACL under a well-understood loading configuration. The mid-substance axial DIC data, used to develop the stress/strain response of the tissue, demonstrate lower strains in the AM bundle than that of traditional grip-to-grip methods. The actual bundle mechanical properties are stiffer than previously thought. The hysteresis in the AM bundle is low at this strain rate, and specimen-to-specimen variability is less of an issue than previously thought. The AM is also stiffer than the PL bundle, and care should be taken to characterize each of these structures independently, in order to provide meaningful experimental results and contributions to computational models.

3.7 References

[1] K.F. Mallett, E.M. Arruda, Digital image correlation-aided mechanical characterization of the anteromedial and posterolateral bundles of the anterior cruciate ligament, Acta Biomater. (2017). doi:10.1016/j.actbio.2017.03.045.

[2] D.L. Butler, E.S. Grood, F.R. Noyes, A.N. Sodd, On the Interpretation of Our Anterior Cruciate Ligament Data, Clin. Orthop. Relat. Res. 196 (1985).

[3] G. Cerulli, D.L. Benoit, M. Lamontagne, A. Caraffa, A. Liti, In vivo anterior cruciate ligament strain behaviour during a rapid deceleration movement: case report, Knee Surg. Sports Traumatol. Arthrosc. 11 (2003) 307–11.

[4] B.D. Beynnon, B.C. Fleming, R.J. Johnson, C.E. Nichols, P.A. Renstrom, M.H. Pope, Anterior cruciate ligament strain behavior during rehabilitation exercises in vivo, Am. J. Sports Med. 23 (1995) 24–34. doi:10.1177/036354659502300105.

[5] B.D. Beynnon, R.J. Johnson, B.C. Fleming, C.J. Stankewich, P.A. Renstrom, C.E. Nichols, The strain behavior of the anterior cruciate ligament during squatting and active flexion-extension. A comparison of an open and a closed kinetic chain exercise, Am. J. Sports Med. 25 (1997) 823–829. doi:10.1177/036354659702500616.

[6] B.D. Beynnon, R.J. Johnson, B.C. Fleming, G.D. Peura, P.A. Renstrom, C.E. Nichols, M.H. Pope, The effect of functional knee bracing on the anterior cruciate ligament in the weightbearing and nonweightbearing knee, Am. J. Sports Med. 25 (1997) 353–359. doi:10.1177/036354659702500314.

[7] B.D. Beynnon, B.C. Fleming, Anterior cruciate ligament strain in-vivo: a review of previous work., J. Biomech. 31 (1998) 519–25. http://www.ncbi.nlm.nih.gov/pubmed/9755036.

[8] D.L. Butler, Kappa Delta Award paper. Anterior cruciate ligament: its normal response and replacement, J. Orthop. Res. 7 (1989) 910–921.

[9] S.G. McLean, M.L. Beaulieu, Complex integrative morphological and mechanical contributions to ACL injury risk, Exerc Sport Sci Rev. 38 (2010) 192–200. doi:10.1097/JES.0b013e3181f450b400003677-201010000-00007 [pii].

[10] E.G. Meyer, R.C. Haut, Anterior cruciate ligament injury induced by internal tibial torsion or tibiofemoral compression., J. Biomech. 41 (2008) 3377–83. doi:10.1016/j.jbiomech.2008.09.023.

[11] Y.K. Oh, J.L. Kreinbrink, E.M. Wojtys, J.A. Ashton-Miller, Effect of axial tibial torque direction on ACL relative strain and strain rate in an in vitro simulated pivot landing., J. Orthop. Res. 30 (2012) 528–34. doi:10.1002/jor.21572.

[12] M.M. Murray, P. Vavken, B.C. Fleming, The ACL Handbook: Knee Biology, Mechanics, and Treatment, Springer New York, New York, NY, 2013.

[13] D.B. Lipps, Y.K. Oh, J.A. Ashton-Miller, E.M. Wojtys, Effect of increased quadriceps tensile stiffness on peak anterior cruciate ligament strain during a simulated pivot landing., J. Orthop. Res. 32 (2013) 423–30. doi:10.1002/jor.22531.

[14] R.P. Csintalan, M.C.S. Inacio, T.T. Funahashi, Incidence rate of anterior cruciate ligament reconstructions., Perm. J. 12 (2008) 17–21. http://www.pubmedcentral.nih.gov/articlerender.fcgi?artid=3037119&tool=pmcentrez&rendertype=abstract.

[15] L.Y. Griffin, M.J. Albohm, E.A. Arendt, R. Bahr, B.D. Beynnon, M. Demaio, R.W. Dick, L. Engebretsen, W.E. Garrett Jr., J.A. Hannafin, T.E. Hewett, L.J. Huston, M.L. Ireland, R.J. Johnson, S. Lephart, B.R. Mandelbaum, B.J. Mann, P.H. Marks, S.W. Marshall, G. Myklebust, F.R. Noyes, C. Powers, C. Shields Jr., S.J. Shultz, H. Silvers, J. Slauterbeck, D.C. Taylor, C.C. Teitz, E.M. Wojtys, B. Yu, Understanding and preventing noncontact anterior cruciate ligament injuries: a review of the Hunt Valley II meeting, January 2005, Am. J. Sports Med. 34 (2006) 1512–1532. http://www.ncbi.nlm.nih.gov/entrez/query.fcgi?cmd=Retrieve&db=PubMed&dopt=Citation&list_uids=16905673.

[16] S.F. Dye, W.D.J. Cannon, Anatomy and biomechanics of the anterior cruciate ligament, Clin. Sports Med. 7 (1988) 715–725. http://www.ncbi.nlm.nih.gov/pubmed/3052878 (accessed September 30, 2013).

[17] M. Odensten, J. Gillquist, Functional anatomy of the anterior cruciate ligament and a rationale for reconstruction, J-Bone-Joint-Surg-Am. 67 (1985) 257–9355. http://www.ncbi.nlm.nih.gov/pubmed/3968118.

[18] F.H. Fu, C.D. Harner, D.L. Johnson, M.D. Miller, S.L.-Y. Woo, Biomechanics of Knee Ligaments; Basic Concepts and Clinical Application, J. Bone Jt. Surg. 75 (1993) 1716–1727.

[19] J. Hashemi, N. Chandrashekar, H. Mansouri, J.R. Slauterbeck, D.M. Hardy, The human anterior cruciate ligament: sex differences in ultrastructure and correlation with biomechanical properties, J. Orthop. Res. 26 (2008) 945–950. doi:10.1002/jor.20621.

[20] P.A. Renstrom, A. Ljungqvist, E.A. Arendt, B.D. Beynnon, T. Fukubayashi, W. Garrett, T. Georgoulis, T.E. Hewett, R. Johnson, T. Krosshaug, B. Mandelbaum, L. Micheli, G. Myklebust, E.M. Roos, H.P. Roos, P. Schamasch, S. Shultz, S. Werner, E.M. Wojtys, L. Engebretsen, Non-contact ACL injuries in female athletes: an International Olympic Committee current concepts statement, Br. J. Sports Med. 42 (2008) 394–412. http://www.ncbi.nlm.nih.gov/entrez/query.fcgi?cmd=Retrieve&db=PubMed&dopt=Citation&list_uids=18539658.

[21] J.M. Deneweth, M.J. Bey, S.G. McLean, T.R. Lock, P.A. Kolowich, S. Tashman, Tibiofemoral joint kinematics of the anterior cruciate ligament-reconstructed knee during a single-legged hop landing, Am. J. Sports Med. 38 (2010) 1820–1828. doi:0363546510365531 [pii]10.1177/0363546510365531.

[22] L.S. Lohmander, P.M. Englund, L.L. Dahl, E.M. Roos, The long-term consequence of anterior cruciate ligament and meniscus injuries: osteoarthritis, Am. J. Sports Med. 35 (2007) 1756–1769. doi:0363546507307396 [pii]10.1177/0363546507307396.

[23] G. Li, R. Papannagari, L.E. DeFrate, J.D. Yoo, S.E. Park, T.J. Gill, Comparison of the ACL and ACL graft forces before and after ACL reconstruction: an in-vitro robotic investigation, Acta Orthop. 77 (2006) 267–274.

http://www.ncbi.nlm.nih.gov/entrez/query.fcgi?cmd=Retrieve&db=PubMed&dopt=Citation&list_uids=16752289.

[24] S. Tashman, P.A. Kolowich, D. Collon, K. Anderson, W. Anderst, Dynamic function of the ACL-reconstructed knee during running, Clin. Orthop. Relat. Res. 454 (2007) 66–73. doi:10.1097/BLO.0b013e31802bab3e.

[25] M.A. Kessler, H. Behrend, S. Henz, G. Stutz, A. Rukavina, M.S. Kuster, Function, osteoarthritis and activity after ACL-rupture: 11 years follow-up results of conservative versus reconstructive treatment., Knee Surg. Sports Traumatol. Arthrosc. 16 (2008) 442–8. doi:10.1007/s00167-008-0498-x.

[26] J.O. Drogset, T. Grontvedt, O.R. Robak, A. Molster, A.T. Viset, L. Engebretsen, A sixteen-year follow-up of three operative techniques for the treatment of acute ruptures of the anterior cruciate ligament, J. Bone Joint Surg. Am. 88 (2006) 944–952. doi:88/5/944 [pii]10.2106/JBJS.D.02876.

[27] M. Marcacci, S. Zaffagnini, G. Giordano, F. Iacono, M. Lo Presti, Anterior cruciate ligament reconstruction associated with extra-articular tenodesis: A prospective clinical and radiographic evaluation with 10- to 13-year follow-up., Am. J. Sports Med. 37 (2009) 707–14. doi:10.1177/0363546508328114.

[28] A. von Porat, E.M. Roos, H.P. Roos, High prevalence of osteoarthritis 14 years after an anterior cruciate ligament tear in male soccer players: a study of radiographic and patient relevant outcomes, Ann. Rheum. Dis. 63 (2004) 269–273. http://www.ncbi.nlm.nih.gov/entrez/query.fcgi?cmd=Retrieve&db=PubMed&dopt=Citation&list_uids=14962961.

[29] P. Neumann, M. Englund, I. Kostogiannis, T. Friden, H.P. Roos, L.E. Dahlberg, Prevalence of tibiofemoral osteoarthritis 15 years after nonoperative treatment of anterior cruciate ligament injury: a prospective cohort study, Am. J. Sports Med. 36 (2008) 1717–1725. doi:0363546508316770 [pii]10.1177/0363546508316770.

[30] S. Tashman, W. Anderst, P.A. Kolowich, S. Havstad, S.P. Arnoczky, Kinematics of the ACL-deficient canine knee during gait: serial changes over two years., J. Orthop. Res. 22 (2004) 931–41. doi:10.1016/j.orthres.2004.01.008.

[31] C.W. Imhauser, C. Mauro, D. Choi, E. Rosenberg, S. Mathew, J. Nguyen, Y. Ma, T. Wickiewicz, Abnormal tibiofemoral contact stress and its association with altered kinematics after center-center anterior cruciate ligament reconstruction: an in vitro study, Am. J. Sports Med. 41 (2013) 815–825. doi:10.1177/0363546512475205.

[32] T.P. Andriacchi, A. Mundermann, R.L. Smith, E.J. Alexander, C.O. Dyrby, S. Koo, A framework for the in vivo pathomechanics of osteoarthritis at the knee, Ann. Biomed. Eng. 32 (2004) 447–457. http://www.ncbi.nlm.nih.gov/entrez/query.fcgi?cmd=Retrieve&db=PubMed&dopt=Citation&list_uids=15095819.

[33] M.C. Logan, E. Dunstan, J. Robinson, A. Williams, W. Gedroyc, M. Freeman, Tibiofemoral kinematics of the anterior cruciate ligament (ACL)-deficient weightbearing, living knee employing vertical access open “interventional” multiple resonance imaging, Am. J. Sports Med. 32 (2004) 720–726. http://www.ncbi.nlm.nih.gov/entrez/query.fcgi?cmd=Retrieve&db=PubMed&dopt=Citation&list_uids=15090390.

[34] S. Rupp, B. Muller, R. Seil, Knee laxity after ACL reconstruction with a BPTB graft, Knee Surg. Sports Traumatol. Arthrosc. 9 (2001) 72–76. http://www.ncbi.nlm.nih.gov/entrez/query.fcgi?cmd=Retrieve&db=PubMed&dopt=Citation&list_uids=11354856.

[35] P.J. Roos, M.L. Hull, S.M. Howell, Lengthening of double-looped tendon graft constructs in three regions after cyclic loading: a study using Roentgen stereophotogrammetric analysis, J. Orthop. Res. 22 (2004) 839–846. doi:10.1016/j.orthres.2003.11.002S0736026603002857 [pii].

[36] C.K. Smith, M.L. Hull, S.M. Howell, Lengthening of a single-loop tibialis tendon graft construct after cyclic loading: a study using Roentgen stereophotogrammetric analysis, J. Biomech. Eng. 128 (2006) 437–442. doi:10.1115/1.2187038.

[37] K.L. Moffat, W.-H.S. Sun, P.E. Pena, N.O. Chahine, S.B. Doty, G.A. Ateshian, C.T. Hung, H.H. Lu, Characterization of the structure-function relationship at the ligament-to-bone interface., Proc. Natl. Acad. Sci. U. S. A. 105 (2008) 7947–52. doi:10.1073/pnas.0712150105.

[38] M.K. Kwan, T.W. Lin, S.L.-Y. Woo, On the viscoelastic properties of the anteromedial bundle of the anterior cruciate ligament., J. Biomech. 26 (1993) 447–52. http://www.ncbi.nlm.nih.gov/pubmed/8478348.

[39] S.G. McLean, X. Huang, A.J. Van Den Bogert, Investigating isolated neuromuscular control contributions to non-contact anterior cruciate ligament injury risk via computer cimulation methods, Clin. Biomech. 23 (2008) 926–937.

[40] K.L. Moffat, W.-H.S. Sun, N.O. Chahine, P.E. Pena, S.B. Doty, C.T. Hung, G. a Ateshian, H.H. Lu, Characterization of the mechanical properties and mineral distribution of the anterior cruciate ligament-to-bone insertion site., Conf. Proc. ... Annu. Int. Conf. IEEE Eng. Med. Biol. Soc. IEEE Eng. Med. Biol. Soc. Annu. Conf. 1 (2006) 2366–9. doi:10.1109/IEMBS.2006.259299.

[41] S.U. Scheffler, F.N. Unterhauser, A. Weiler, Graft remodeling and ligamentization after cruciate ligament reconstruction., Knee Surg. Sports Traumatol. Arthrosc. 16 (2008) 834–42. doi:10.1007/s00167-008-0560-8.

[42] S.L. Keays, J.E. Bullock-Saxton, A.C. Keays, P.A. Newcombe, M.I. Bullock, A 6-year follow-up of the effect of graft site on strength, stability, range of motion, function, and joint degeneration after anterior cruciate ligament reconstruction: patellar tendon versus semitendinosus and Gracilis tendon graft, Am. J. Sports Med. 35 (2007) 729–739. doi:10.1177/0363546506298277.

[43] A. van Kampen, A.B. Wymenga, H.J. van der Heide, H.J. Bakens, The effect of different graft tensioning in anterior cruciate ligament reconstruction: a prospective randomized study, Arthroscopy. 14 (1998) 845–850. http://www.ncbi.nlm.nih.gov/pubmed/9848597.

[44] M. Cuppone, B.B. Seedhom, Effect of implant lengthening and mode of fixation on knee laxity after ACL reconstruction with an artificial ligament: a cadaveric study, J. Orthop. Sci. 6 (2001) 253–261. doi:10.1007/s0077610060253.

[45] R.S. Boorman, G.M. Thornton, N.G. Shrive, C.B. Frank, Ligament grafts become more susceptible to creep within days after surgery: evidence for early enzymatic degradation of a ligament graft in a rabbit model, Acta Orthop. Scand. 73 (2002) 568–574. doi:10.1080/000164702321022866.

[46] D.L. Butler, M.D. Kay, D.C. Stouffer, Comparison of Material Properties in Fascicle-Bone Units from Human Patellar Tendon and Knee Ligaments, J. Biomech. 19 (1986) 435–432.

[47] J. Ma, Experimental and Computational Characterizations of Native Ligaments, Tendons and Engineered 3-D Bone-Ligament-Bone Constructs in the Knee, University of Michigan, Ann Arbor, 2012.

[48] F.R. Noyes, E.S. Grood, The Strength of the Anterior Cruciate Ligament in Humans and Rhesus Monkeys, J. Bone Jt. Surg. 58 (1976) 1074–1082.

[49] D.L. Butler, Y. Guan, M.D. Kay, J.F. Cummings, S.M. Feder, M.S. Levy, Location-dependent variations in the material properties of the anterior cruciate ligament, J. Biomech. 25 (1992) 511–8. http://www.ncbi.nlm.nih.gov/pubmed/1592856.

[50] J.C. Kennedy, R.J. Hawkins, R.B. Willis, K.D. Danylchuck, Tension studies of human knee ligaments. Yield point, ultimate failure, and disruption of the cruciate and tibial collateral ligaments, J. Bone Joint Surg. Am. 58 (1976) 350–355.

[51] F.R. Noyes, D.L. Butler, E.S. Grood, R.F. Zernicke, M.S. Hefzy, Biomechanical Analysis of Human Ligament Grafts used in Knee-Ligament Repairs and Reconstructions, J. Bone Joint Surg. Am. (1984) 344–352.

[52] N. Chandrashekar, J. Slauterbeck, J. Hashemi, Sex-based differences in the anthropometric characteristics of the anterior cruciate ligament and its relation to intercondylar notch geometry: a cadaveric study, Am. J. Sports Med. 33 (2005) 1492–1498. http://www.ncbi.nlm.nih.gov/entrez/query.fcgi?cmd=Retrieve&db=PubMed&dopt=Citation&list_uids=16009992.

[53] S.G. McLean, K.F. Mallett, E.M. Arruda, Deconstructing the Anterior Cruciate Ligament: What We Know and Don’t Know About Function, Material Properties, and Injury Mechanics., J. Biomech. Eng. 137 (2015) 020906. doi:10.1115/1.4029278.

[54] A. Weiler, G. Peters, J. Mäurer, F.N. Unterhauser, N.P. Südkamp, Biomechanical properties and vascularity of an anterior cruciate ligament graft can be predicted by contrast-enhanced magnetic resonance imaging. A two-year study in sheep., Am. J. Sports Med. 29 (2001) 751–761. http://www.ncbi.nlm.nih.gov/pubmed/11734489.

[55] A. Weiler, C. Förster, P. Hunt, R. Falk, T. Jung, F.N. Unterhauser, V. Bergmann, G. Schmidmaier, N.P. Haas, The Influence of Locally Applied Platelet-Derived Growth Factor – BB on Free Tendon Graft Remodeling After Anterior Cruciate Ligament Reconstruction, Sport. Med. (2004) 881–891. doi:10.1177/0363546503261711.

[56] R. Meller, E. Willbold, E. Hesse, B. Dreymann, M. Fehr, C. Haasper, C. Hurschler, C. Krettek, F. Witte, Histologic and biomechanical analysis of anterior cruciate ligament graft to bone healing in skeletally immature sheep, Arthroscopy. 24 (2008) 1221–1231. doi:S0749-8063(08)00515-X [pii]10.1016/j.arthro.2008.06.021.

[57] F. Girgis, J.L. Marshall, A. Monajem, A.R.S. Al Monajem, The cruciate ligaments of the knee joint: anatomical, functional and experimental analysis, Clin. Orthop. Relat. Res. 106 (1975) 216–231.

[58] B.A. Smith, G.A. Livesay, S.L.-Y. Woo, Biology and biomechanics of the anterior cruciate ligament, Clin. Sports Med. 12 (1993) 637–670.

[59] R.P. Welsh, Knee joint structure and function, Clin. Orthop. Relat. Res. (1980) 7–14. http://www.pubmedcentral.nih.gov/articlerender.fcgi?artid=3171541&tool=pmcentrez&rendertype=abstract.

[60] S.P. Arnoczky, Anatomy of the anterior cruciate ligament., Clin. Orthop. Relat. Res. 172 (1983) 19–25. http://www.ncbi.nlm.nih.gov/pubmed/6821989.

[61] S.P. Arnoczky, R.F. Warren, M.A. Ashlock, Replacement of the anterior cruciate ligament using a patellar tendon allograft. An experimental study, J Bone Jt. Surg [Am]. 68 (1986) 376–385.

[62] J.M. Bach, M.L. Hull, H.A. Patterson, Direct measurement of strain in the posterolateral bundle of the anterior cruciate ligament, J. Biomech. 30 (1997) 1–3.

[63] D.L. Hamner, C.H. Brown, M.E. Steiner, a T. Hecker, W.C. Hayes, Hamstring tendon grafts for reconstruction of the anterior cruciate ligament: biomechanical evaluation of the use of multiple strands and tensioning techniques., J. Bone Joint Surg. Am. 81 (1999) 549–57. http://www.ncbi.nlm.nih.gov/pubmed/10225801.

[64] J.M. Hollis, J.P. Marcin, S. Horibe, S.L.-Y. Woo, Load determination in ACL fibres under knee loading., Trans. Orthop. Res. Soc. 13 (1988) 196.

[65] L.A. Norwood, M.J. Cross, Anterior cruciate ligament: functional anatomy of its bundles in rotatory instabilities., Am. J. Sports Med. 7 (1979) 23–6. http://www.ncbi.nlm.nih.gov/pubmed/420384.

[66] J.C. Kennedy, H.W. Weinberg, A.S. Wilson, The anatomy and function of the anterior cruciate ligament - as determined by clinical and morphological studies, J. Bone Joint Surg. Am. 56-A (1974).

[67] S. Takai, S.L.-Y. Woo, G.A. Livesay, D.J. Adams, F.H. Fu, Determination of the in situ loads on the human anterior cruciate ligament, J. Orthop. Res. 11 (1993) 686–695.

[68] J.A. Sidles, R. V Larson, J.L. Garbini, D.J. Downey, F.A.D. Matsen, Ligament length relationships in the moving knee, J. Orthop. Res. 6 (1988) 593–610.

[69] C.J. Wang, P.S. Walker, B. Wolf, The effects of flexion and rotation on the length patterns of the ligaments of the knee., J. Biomech. 6 (1973) 587–96. http://www.ncbi.nlm.nih.gov/entrez/query.fcgi?cmd=Retrieve&db=PubMed&dopt=Citation&list_uids=4757478.

[70] J.M. Hollis, S. Takai, D.J. Adams, S. Horibe, S.L.-Y. Woo, The effects of knee motion and external loading on the length of the anterior cruciate ligament (ACL): a kinematic study., J. Biomech. Eng. 113 (1991) 208–14. http://www.ncbi.nlm.nih.gov/pubmed/1875695.

[71] T.J. Mommersteeg, J.G. Kooloos, L. Blankevoort, J.M. Kauer, R. Huiskes, F.Q. Roeling, The fibre bundle anatomy of human cruciate ligaments, J. Anat. 187 (1995) 461–471. http://www.pubmedcentral.nih.gov/articlerender.fcgi?artid=1167440&tool=pmcentrez&rendertype=abstract.

[72] R. Gatt, M. Vella Wood, A. Gatt, F. Zarb, C. Formosa, K.M. Azzopardi, A. Casha, T.P. Agius, P. Schembri-Wismayer, L. Attard, N. Chockalingam, J.N. Grima, Negative Poisson’s ratios in tendons: An unexpected mechanical response, Acta Biomater. 24 (2015) 201–208. doi:10.1016/j.actbio.2015.06.018.

[73] V.D. Mahalingam, N. Behbahani-Nejad, S. V Horine, T.J. Olsen, M.J. Smietana,

E.M. Wojtys, D.M. Wellik, E.M. Arruda, L.M. Larkin, Allogeneic versus autologous derived cell sources for use in engineered bone-ligament-bone grafts in sheep anterior cruciate ligament repair., Tissue Eng. Part A Part A. 21 (2015) 1047–54. doi:10.1089/ten.TEA.2014.0422.

[74] V.D. Mahalingam, N. Behbahani-Nejad, E.A. Ronan, T.J. Olsen, M.J. Smietana, E.M. Wojtys, D.M. Wellik, E.M. Arruda, L.M. Larkin, Fresh versus frozen engineered bone-ligament-bone grafts for sheep anterior cruciate ligament repair., Tissue Eng. Part C. Methods. 21 (2015) 548–56. doi:10.1089/ten.TEC.2014.0542.

[75] D.P. Pioletti, L.R. Rakotomanana, P.F. Leyvraz, Strain rate effect on the mechanical behavior of the anterior cruciate ligament-bone complex., Med. Eng. Phys. 21 (1999) 95–100. http://www.ncbi.nlm.nih.gov/pubmed/10426509.

[76] R. Gatt, M. Vella Wood, A. Gatt, F. Zarb, C. Formosa, K.M. Azzopardi, A. Casha, T.P. Agius, P. Schembri-Wismayer, L. Attard, N. Chockalingam, J.N. Grima, Negative Poisson's ratios in tendons: An unexpected mechanical response, Acta Biomater. 24 (2015) 201–208. doi:10.1016/j.actbio.2015.06.018.

[77] H. Ahmadzadeh, B.R. Freedman, B.K. Connizzo, L.J. Soslowsky, V.B. Shenoy, Micromechanical poroelastic finite element and shear-lag models of tendon predict large strain dependent Poisson's ratios and fluid expulsion under tensile loading, Acta Biomater. 22 (2015) 83–91. doi:10.1016/j.actbio.2015.04.035.

[78] S.P. Reese, S.A. Maas, J.A. Weiss, Micromechanical Models of Helical Superstructures in Ligament and Tendon Fibers Predict Large Poisson's Ratios, J. Biomechancs. 43 (2010) 1394–1400. doi:10.1016/j.pestbp.2011.02.012.Investigations.

[79] S.L.-Y. Woo, M.A. Gomez, W.H. Akeson, The time and history-dependent viscoelastic properties of the canine medical collateral ligament, J. Biomech. Eng. 103 (1981) 293–298.

[80] T.A.. Wren, S.A. Yerby, G.S. Beaupré, D.R. Carter, Mechanical properties of the human achilles tendon, Clin. Biomech. 16 (2001) 245–251. doi:10.1016/S0268-0033(00)00089-9.

[81] D.L. Butler, E.S. Grood, F.R. Noyes, R.F. Zernicke, K. Brackett, Effects of structure and strain measurement technique on the material properties of young human tendons and fascia., J. Biomech. 17 (1984) 579–96. http://www.ncbi.nlm.nih.gov/pubmed/6490671.

[82] J.C. Gardiner, J.A. Weiss, T.D. Rosenberg, Strain in the human medial collateral ligament during valgus loading of the knee, Clin Orthop. (2001) 266–74.

[83] C.Y. Huang, V.M. Wang, R.J. Pawluk, J.S. Bucchieri, W.N. Levine, L.U. Bigliani, V.C. Mow, E.L. Flatow, Inhomogeneous mechanical behavior of the human supraspinatus tendon under uniaxial loading, J. Orthop. Res. 23 (2005) 924–930. doi:10.1016/j.orthres.2004.02.016.

[84] S. Rigozzi, R. Müller, J.G. Snedeker, Local strain measurement reveals a varied regional dependence of tensile tendon mechanics on glycosaminoglycan content, J. Biomech. 42 (2009) 1547–1552. doi:10.1016/j.jbiomech.2009.03.031.

Chapter 4: Experimental Characterization of the Posterolateral Bundle and Anterior Tibial Translation Experiments

Introduction

This chapter focuses on the experimental results of PL bundle tensile tests and anterior tibial translation tests of entire ACLs. As discussed in **Chapter 1**, it is critically important to elucidate the properties of the anteromedial (AM) and posterolateral (PL) bundles separately for accurate characterization of the ACL. Several studies have investigated the PL, often in a combined study of both the AM and PL. Many of these studies are focused on the kinematics or gross displacement of the entire knee due to removal of one or both bundles [1–4]. As discussed in **Chapter 3**, research on the characterization of the ACL has largely focused on the entire tissue as a homogenous structure [5–9] . The mechanical properties of the isolated AM and PL bundles have received little attention. In a rare study, Butler et al. divided the ACL into 3 bundles (anteromedial, anterolateral and posterolateral) and further divided these bundles into subunits [10–12] for mechanical testing. This paper is one of few available for comparison of the mechanical properties of the individual bundles of the ACL.

Anterior tibial translation (ATT) is commonly employed as a method to identify possible ACL failures. As discussed in **Chapter 1**, the role of the ACL in restraining ATT has been heavily investigated, and the ATT test is accepted as an established method for probing ACL failure. With this technique, the tibia is loaded along an axis directed anteriorly and oriented perpendicular to the tibial shaft. As anterior translation is a benchmark for ACL rupture, ATT tests are also performed in laboratory settings to understand the role of the ACL in normal and injured knee kinematics. Gabriel et al. 2004 utilized a 5DOF system to measure the kinematics of the knee undergoing ATT with missing AM or PL bundles, and reported knee kinematics for a range of knee flexion angles [13]. Furman et al. 1976 also investigated the displacements and rotations that occur with portions of the knee's soft tissues removed under ATT loading [14]; these studies will be highlighted in the discussion of this chapter.

4.1 Methods

The results in this chapter include 9 PL and 8 ATT specimens from fresh ovine knees, and the testing protocol utilized is outlined in detail in **Chapter 3**. Briefly, knees were obtained from a local butcher and refrigerated prior to testing. All soft tissue was removed from each knee, leaving attached to the tibia and femur either the PL bundle for the PL tension tests, or the entire ACL for ATT testing. A MM30 Multi-Max™ Oscillating Power Tool (Robert Bosch Tool Corporation, Mt. Prospect, IL) was used to trim excess bone in order to visualize the entire PL for DIC. A custom grip system was used for testing of the PL BLB and ATT specimens. Specimens were mounted in a servo-hydraulic MTS 810 Material Test System, with a 661.20 force transducer and DC load controller with resolution 0.001 ± 2 N (MTS Systems Corporation, Eden Prairie, MN). The final orientation of the aligned PL BLB is shown in **Figure 4.1**, with the tissue aligned with the axis of the loading. **Figure 4.2** shows the experimental setup of the ATT specimens, with the knee oriented at 30° knee flexion.

Motion for both the PL and ATT specimens was prescribed with the dual actuators of the MTS, keeping the specimen in the cameras' view during loading. The MTS was controlled through a custom LabVIEW program (National Instruments Corporation, Austin, TX) in displacement control. 3D DIC was performed through the use of two Fastcam SA1.1 cameras (Photron USA, Inc., San Diego, CA) focused on the surface of the PL and ATT specimens throughout loading. The cameras had a field of view (FOV) of 1024 x 1024 pixels and a resolution of 0.051 ± 0.003 mm (n=8). The pseudo-random stochastic patterns discussed in **Chapter 2** were applied to the surface of the specimens for DIC displacement measurements and strain calculations. A 3 mN tare load was used to ensure the tissue was not slack prior to testing, and tests were performed at 0.05/s true strain rate. 4 of the PL specimens discussed in this chapter were a part of the study discussed in **Chapter 3**, in which load-unload paths were prescribed to 12% grip-to-grip strain, as opposed to the load-unload paths to 8% grip-to-grip strain for PL bundles in a similar study. For comparison,

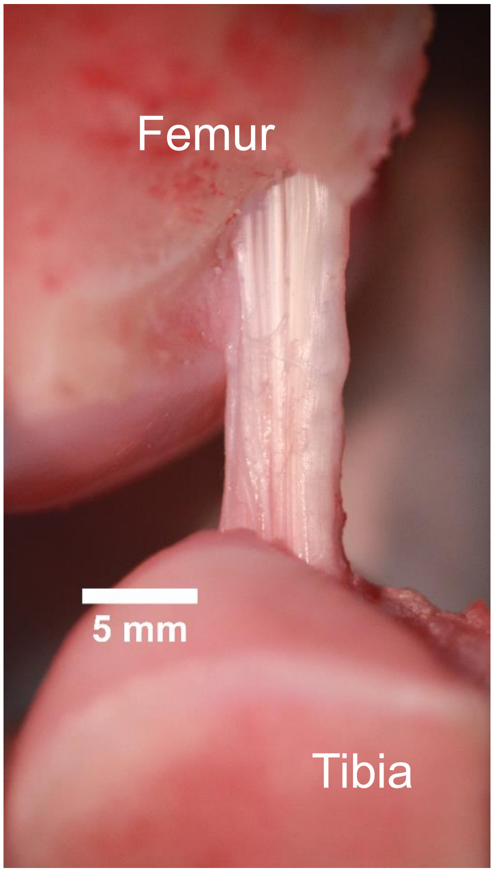

Figure 4.1: Experimental setup of posterolateral bundle in uniaxial tension. Excess femur and tibia has been removed to visualize the tissue at both insertions.

the contour plots shown in this chapter are reported at 8% grip-to-grip strain. The tissue was hydrated using Dulbecco's Phosphor Buffered Saline (ThermoFisher Scientfic, Waltham, MA). The initial mid-substance width and thickness were measured from the digital images, and used to calculate the cross-sectional area (CSA), assuming a rectangular CSA for the PL bundle, as discussed in **Chapter 3**. The raw load and actuator displacement data (along the axis of loading) were converted to nominal stress (load divided by mid-substance CSA, with a load cell resolution of 0.001 ± 2 N) and grip-to-grip nominal strain (displacement divided by initial length) curves. Strains computed via DIC were generated in VIC-3D (Correlated Solutions, Inc., Columbia, SC), and the contours shown created with MATLAB R2014 (The MathWorks, Inc., Natick, MA).

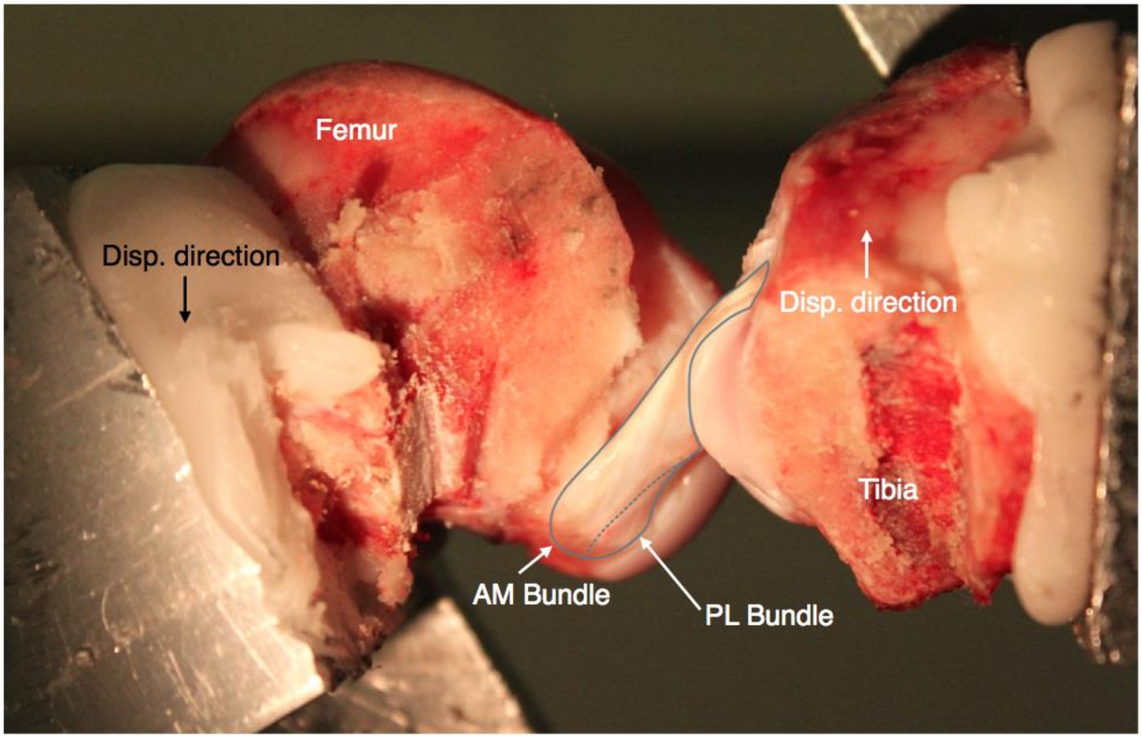

Figure 4.2: Experimental setup of anterior tibial translation test. Anterior translation of the tibia occurs in the sagittal plane of the knee. The ACL is visible after removal of the medial femoral condyle, and can be visualized spanning from the femoral to tibial insertions.

4.2 Results

4.2.1 Posterolateral bundle tests

The displacement contours for a representative PL bundle are shown in **Figure 4.3**. The vertical displacement contour (**Figure 4.3, left**) shows upwards displacement of the femur and downwards displacement of the tibia, due to the dual actuators used in testing. The displacement at the femur also follows the angle of the insertion of the bundle into the bone (top right), showing higher displacements along the sharp angle of the femoral insertion. **Figure 4.3 (right)** demonstrates lateral expansion similar to that of the AM bundle discussed in **Chapter 3**.

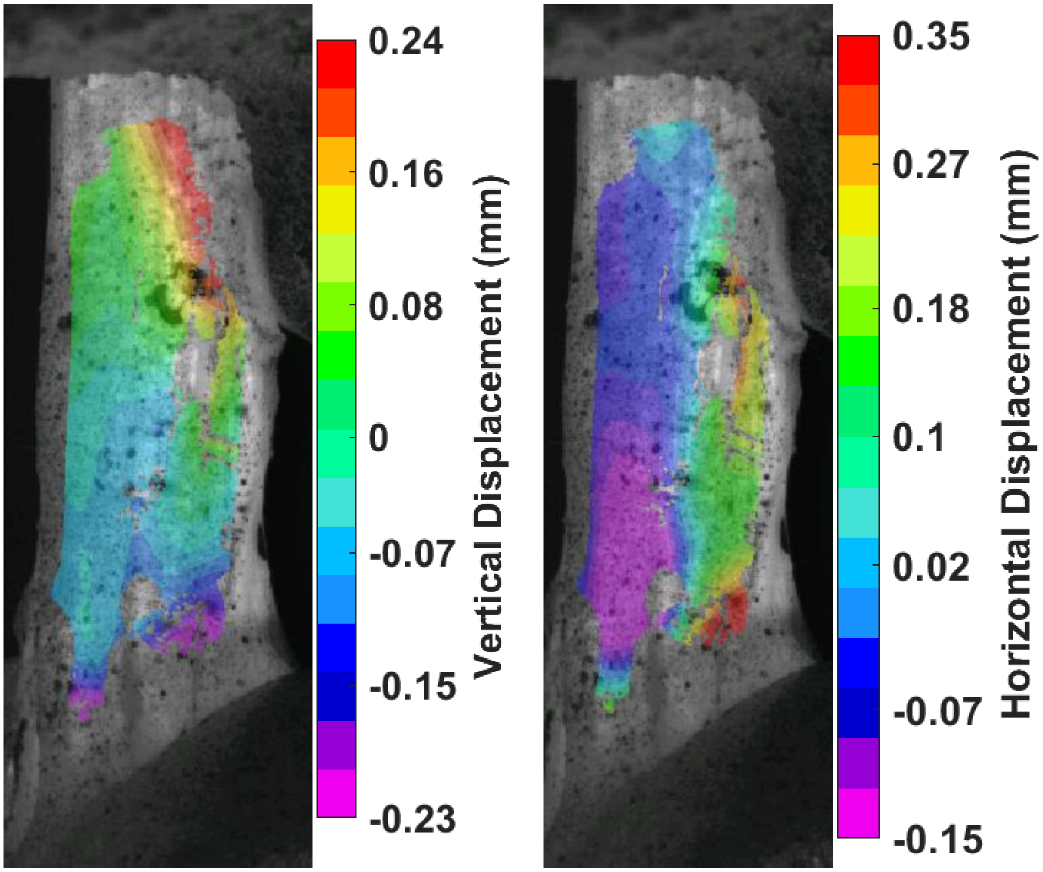

Figure 4.3: Full-field (8% strain) PL bundle vertical (**left**) and horizontal (**right**) displacement contours at peak displacement.

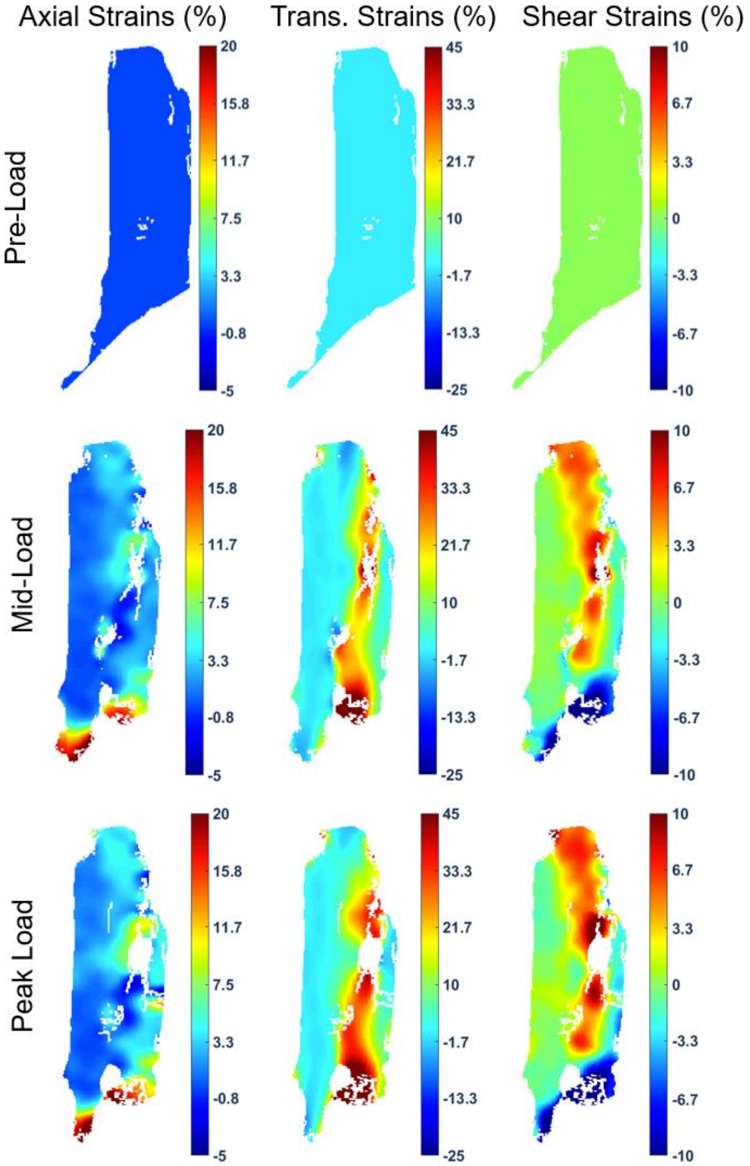

Figure 4.4: Strain contour evolution of a PL bundle during loading to 8% grip-to-grip applied strain. **Left:** Axial strains are along the axis of loading (vertical in the plane of the page), and demonstrate homogeneity in the mid-substance of the tissue during loading. **Center:** Strains transverse to the axis of loading (horizontal in the plane of the page) demonstrate lateral expansion, unexpected for traditional uniaxial loading. **Right:** Shear strains (in-plane) are non-zero, another unexpected result that is possible to visualize through the use of full-field tissue-level measurements.

As seen in **Figure 4.1**, the front surface of the PL is not flat, but wavy, with certain fascicles appearing closer to the camera than others. This variation in position of the tissue surface relative to the camera is exacerbated during loading, as certain fascicles move towards the camera while others shrink from view, leading to decorrelation of the contour coverage in regions in the resulting DIC contours.

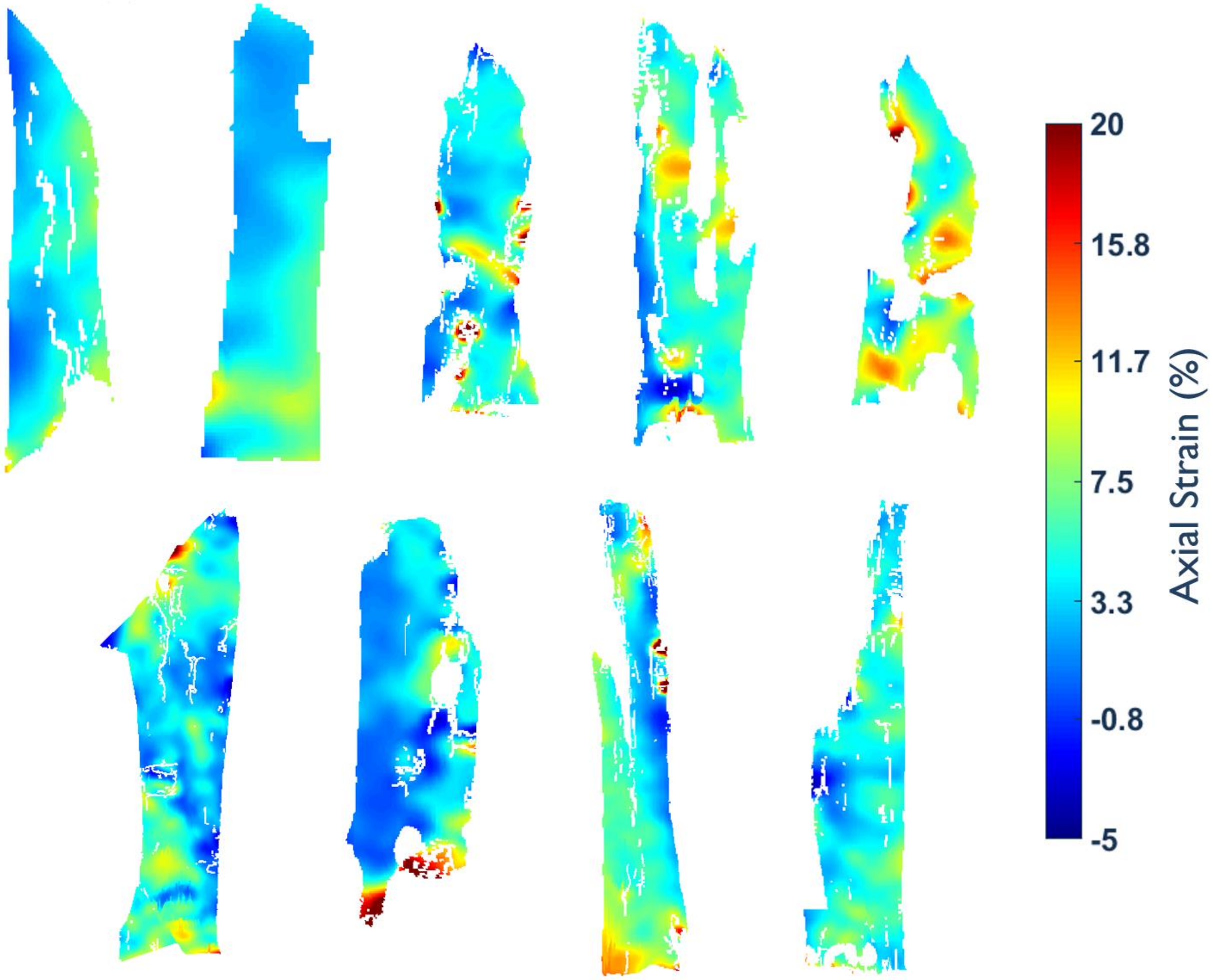

Figure 4.5: PL bundle axial (along the axis of loading, vertical in the plane of the page) strain contours for all PL bundles loaded to 8% true strain (calculated from grip-to-grip displacement measurements. Stress vs. strain data and tangent moduli are calculated from the 5 bundles in the top row.

The axial, transverse, and in-plane strain contour evolution for a representative PL bundle is shown in **Figure 4.4**. High contour coverage of the bundle is seen in the top row prior to loading. At mid-load, a band manifesting high transverse and shear strains can be seen along the central portion of the tissue (**Figure 4.4, center row, center and right columns**). At peak load, strains are localized within this band to more than 55% transverse strain and 10% shear strain (**Figure 4.4, lower row, center and right columns**).

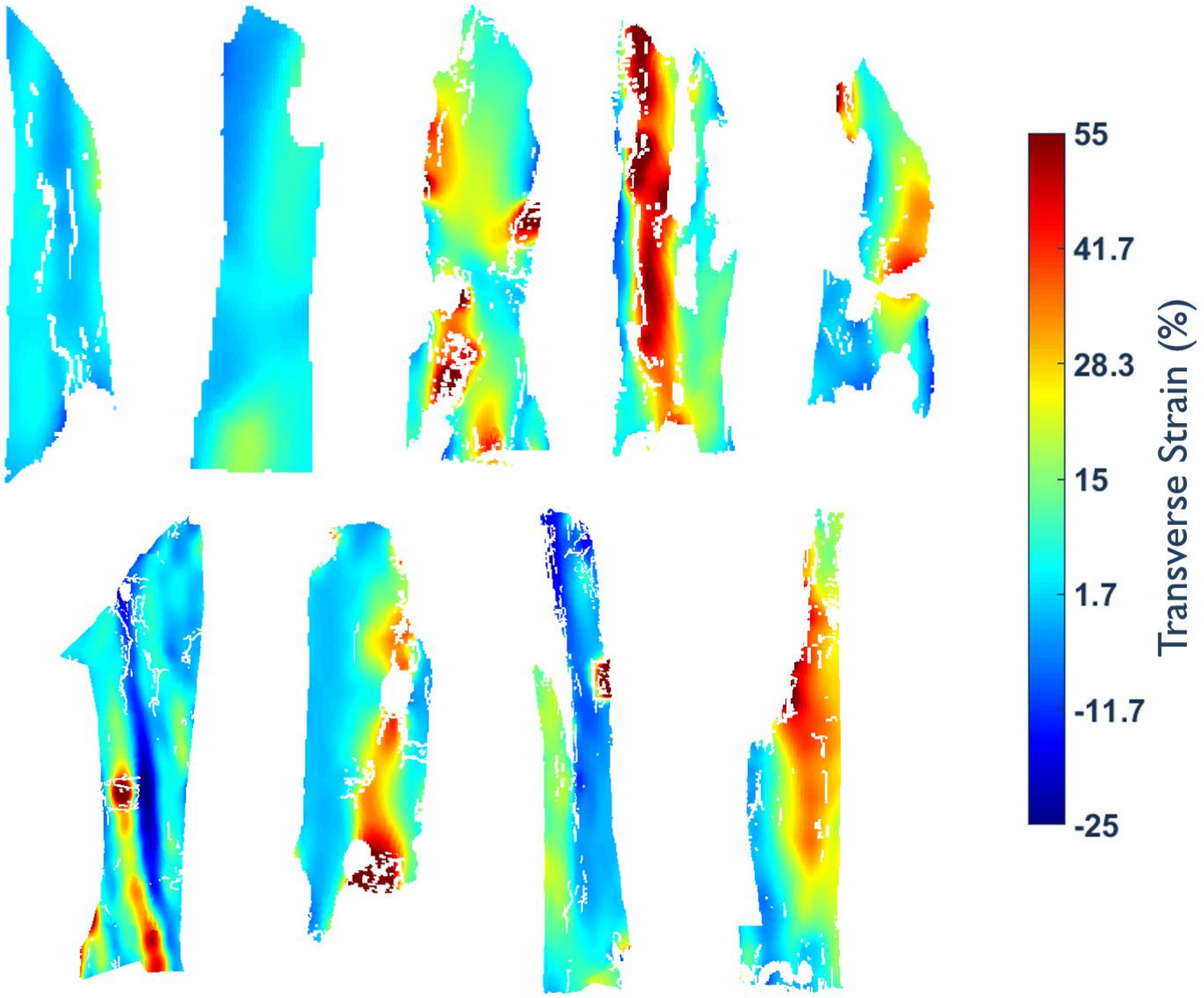

Figure 4.6: PL bundle transverse (to the axis of loading, horizontal in the plane of the page) strain contours for bundles loaded to 8% true strain (calculated from grip-to-grip displacement measurements. Stress vs. strain data and tangent moduli are calculated from the 5 bundles in the top row.

The axial strain contours (along the axis of loading) at an applied average axial strain of 8% are shown for the 9 PL bundles in **Figure 4.5**. The PL response is typically somewhat homogenous, although the response is more heterogeneous throughout the tissue surface and within the mid-substance for the PL bundles compared to the AM experiments.

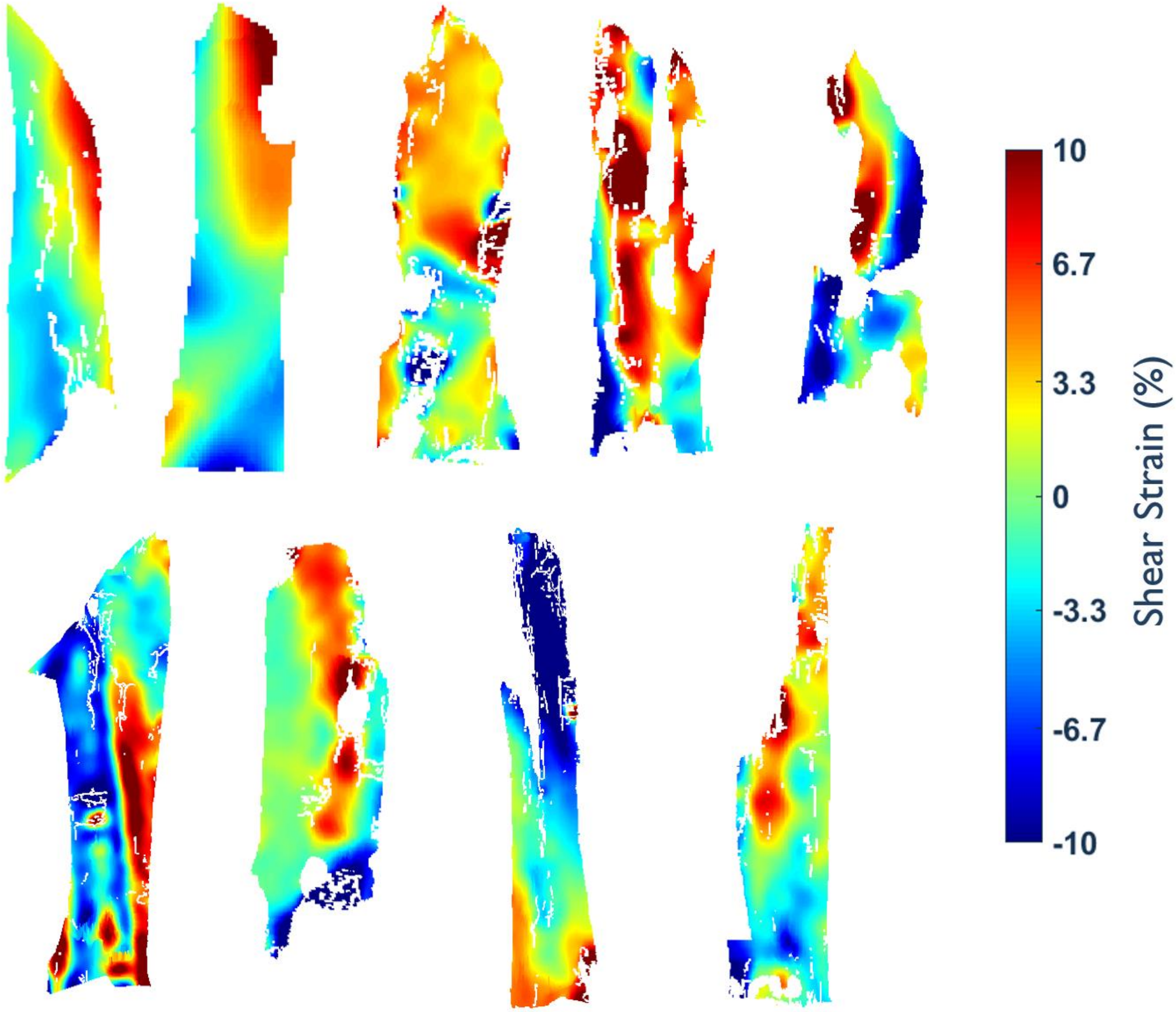

Figure 4.7: PL bundle shear strain contours (shear in the plane of the page) at an average DIC-computed mid-substance true strain of 8%. Stress vs. strain data and tangent moduli are calculated from the 5 bundles in the top row.

Transverse strain contours for all 9 PL bundles are depicted in **Figure 4.6**. The majority of bundles show high lateral expansion, especially within certain bands of the tissue. These strains are often in excess of 55% strain. The loss of correlation can also been seen in certain portions of the tissue surface for the PL bundle, likely due to the variation in tissue surface position mentioned previously.

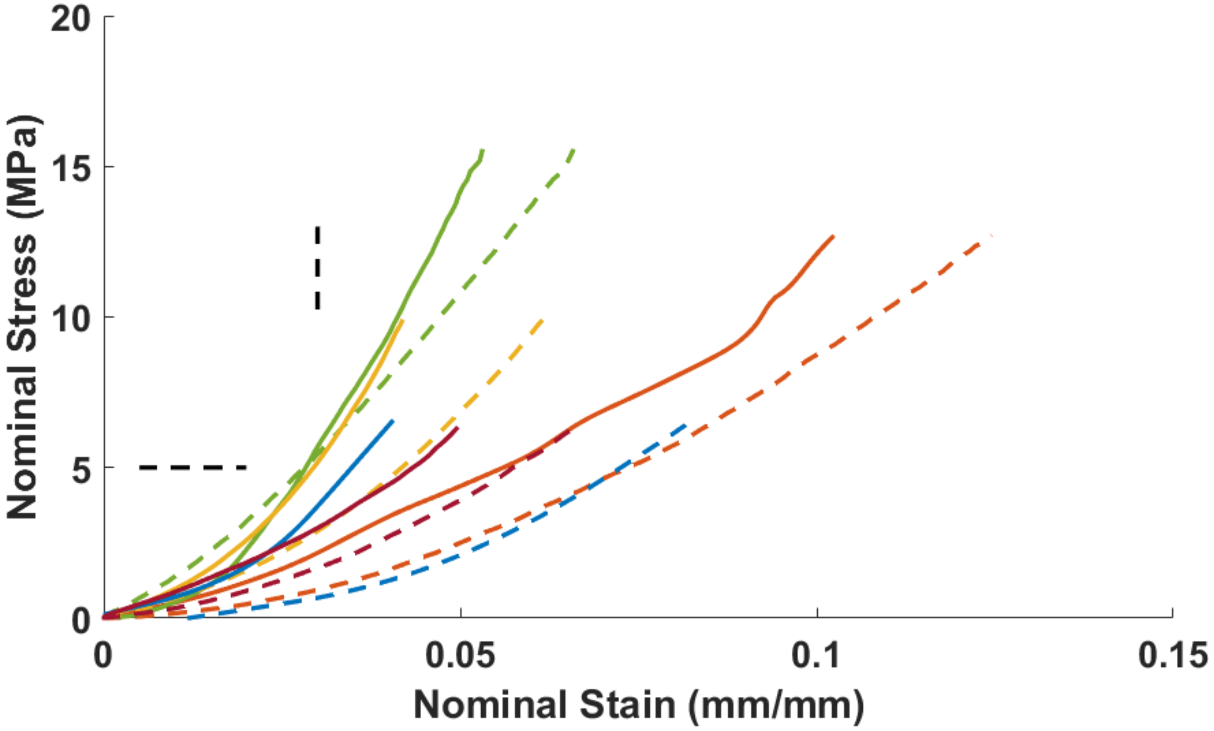

Figure 4.8: Stress vs. strain responses of 5 PL bundles. The response curves based on strains calculated from DIC measured displacements are shown with solid lines. The corresponding bundle's response curve based on strains calculated from grip-to-grip data is shown with a dashed line. Colors represent distinct bundles. Tangent moduli were calculated at the black dashed line indicators: 5 MPa nominal stress and 3% nominal strain.

Shear contours are shown in **Figure 4.7**. Shear manifests for all the bundles shown, similar to the data for the AM bundle. However, the shear for the PL bundle is often in excess of 10% strain, indicating significant motion of individual fascicles relative to each other.

The stress vs. strain data are shown in **Figure 4.8**. For 4 of the PL bundles (those in the bottom row of **Figures 4.5, 4.6** and **4.7**), some data from image frames during loading did not correlate, but later images did correlate (including the peak displacement image frame). As strains were calculated with respect to the reference image frame, the strain contours at peak displacement can be used for comparison, as seen in **Figures 4.5** to **4.7**.

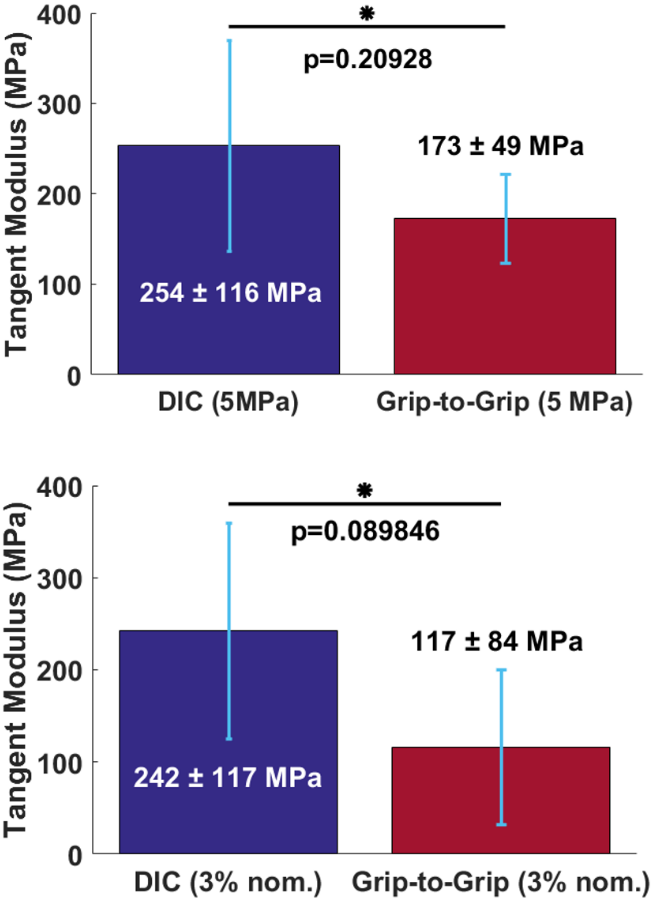

Figure 4.9: Tangent moduli at 5 MPa (nominal stress, **top**) and 3% nominal strain (**bottom**) (n=5).

The remaining 5 PL bundles with correlation throughout the loading path (top row, **Figures 4.5, 4.6** and **4.7**) were used to generate full stress-strain response curves and compute tangent moduli, and are shown in **Figure 4.8**. Strains from grip-to-grip displacement data are shown with dashed lines, and strains computed via DIC (indicated with solid lines) were calculated from the mid-substance of the tissue, as described in **Chapter 3** for the AM bundle. The toe region of the stress vs. strain response, expected in ligaments, is evident, followed by a stiffened response. Similar to the AM bundle, the PL manifests smaller strains computed via DIC than those computed grip-to-grip displacements.

Figure 4.9 shows the tangent stiffness of the 5 PL bundles taken at 3% nominal strain and 5 MPa nominal stress. The tangent moduli at 3% nominal strain were 242 ± 117 and 117 ± 84 MPa for the strains computed via DIC and grip-to-grip displacements respectively, and 254 ± 116 and 173 ± 49 MPa for the strains computed via DIC and grip-to-grip displacements at 5 MPa. In both cases, the tangent moduli measured via DIC strains were higher than those measured via grip-to-grip strains, although these differences were not significant.

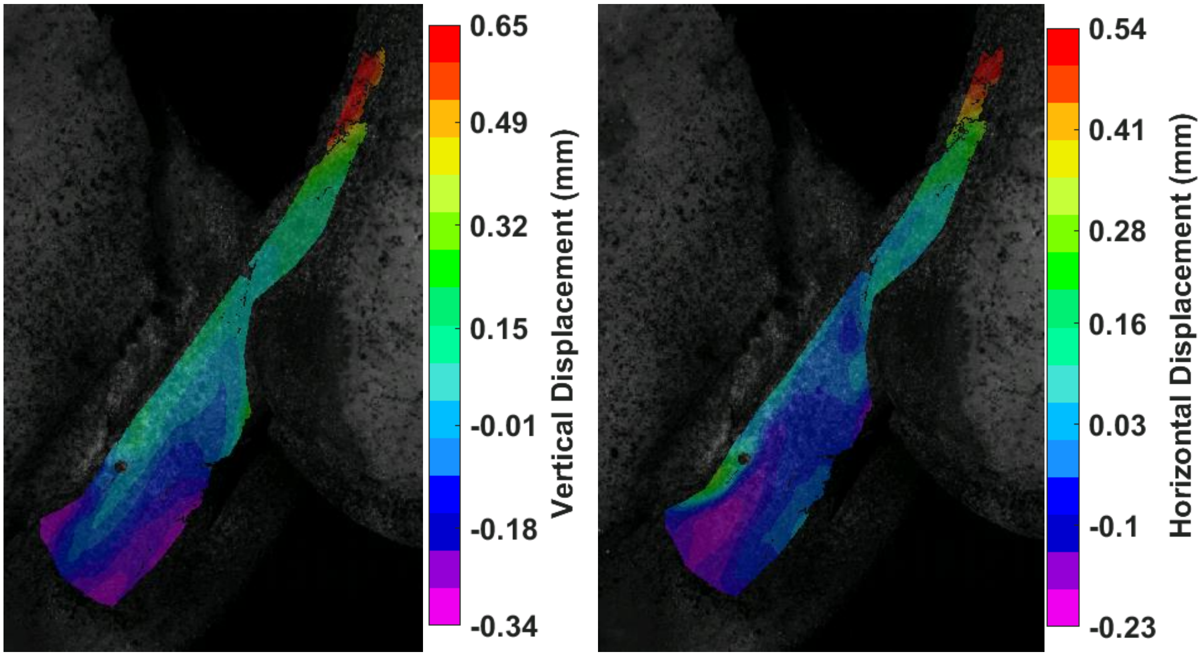

Figure 4.10: Full-field ATT test vertical (**left**) and horizontal (**right**) displacement contours at peak displacement.

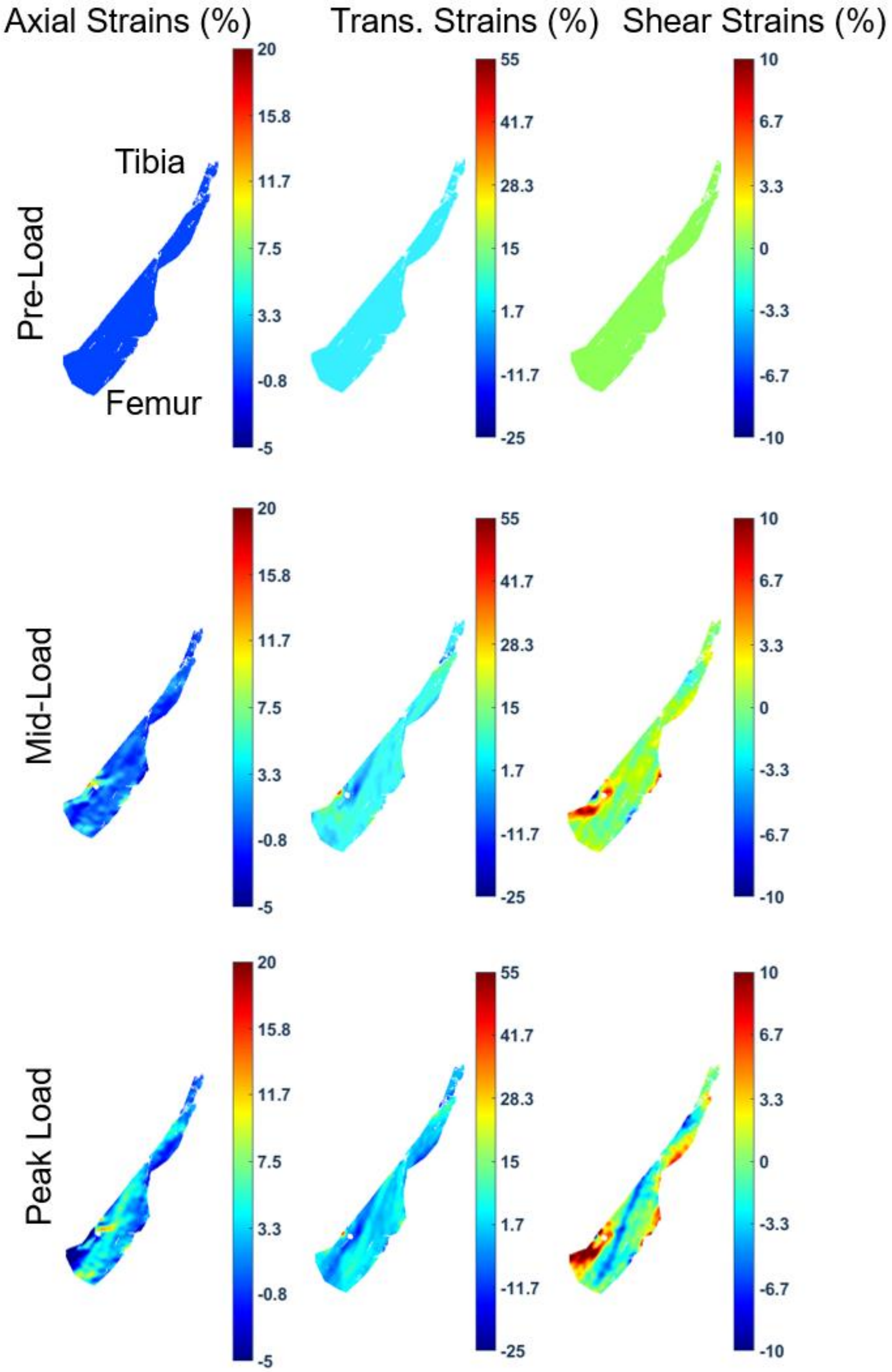

Figure 4.11: Strain contour evolution of the ACL during ATT loading to peak applied grip-to-grip strain. **Left:** Strains are along the axis of loading (vertical in the plane of the page), and appear fairly homogeneous during loading in comparison with the PL strain contour evolutions in **Figure 4.4. Center:** Strains transverse to the axis of loading (horizontal in the plane of the page) demonstrate a somewhat banded nature during loading (peak load shear contour). **Right:** Shear strains (in-plane of the page) are highest at the bony insertions, and in excess of 10% at

4.2.2 Anterior tibial translation tests

Figure 4.10 shows the displacement contours at peak displacement of a representative ATT test. The vertical displacement demonstrates motion of the femur downwards and tibia upwards in the sagittal plane of the tissue, while the horizontal displacement shows lateral expansion in the mid-substance.

The contour evolution during ATT is shown in **Figure 4.11.** The high contour coverage of the bundle pre-load (**Figure 4.11, top row**) is maintained during loading at mid and peak load (**Figure 4.11, center and bottom rows**). For the shear strains in particular, strains exceeding 10% concentrate at the AM bundle femoral insertion.

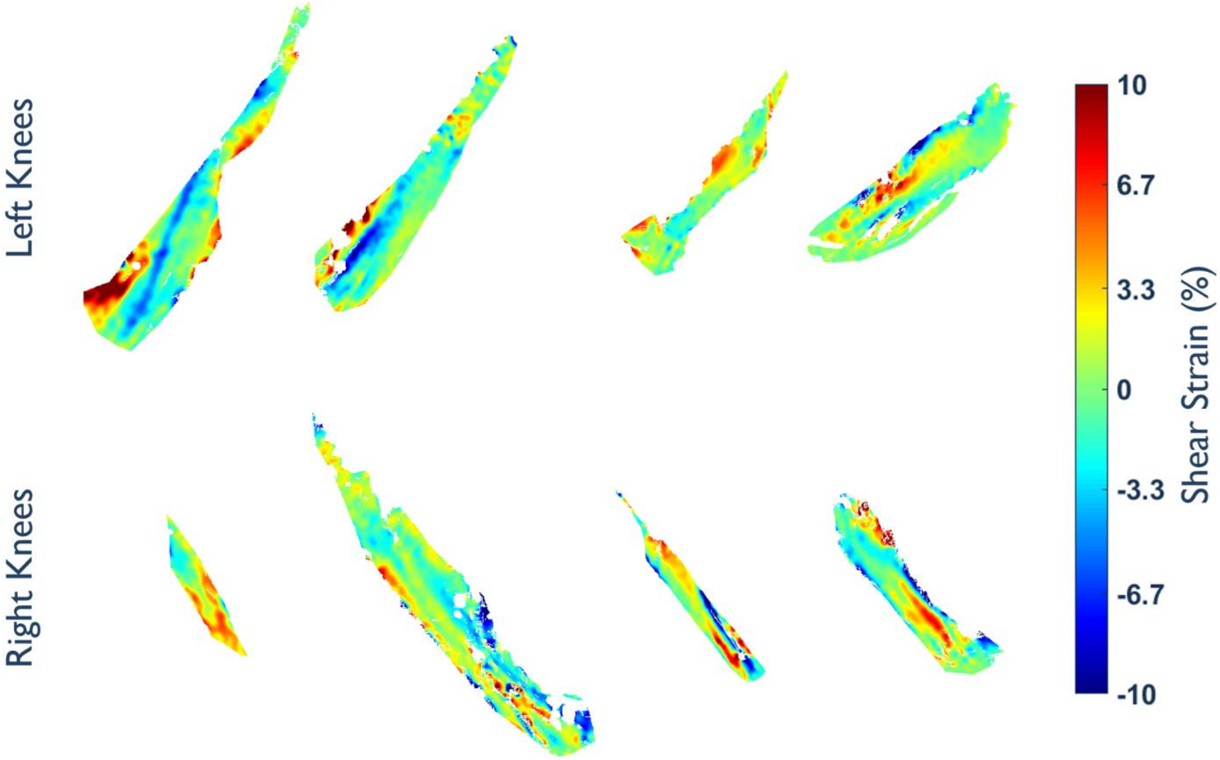

Figure 4.12: ATT shear strain (shear in the plane of the page) contours at peak applied grip-to-grip strain. Left knees are shown in the top row and right knees in the bottom row. The femoral insertion occurs at the bottom of the contour, and tibial insertions at the top.

The shear strain contours of 8 ATT specimens are shown in **Figure 4.12**. The femoral insertion of all knees occurs at the bottom of the contour, and tibial insertions are at the top of the contour. 4 right and 4 left knees are shown, with left knees originating at the femur and inserting into the tibia from the left to right side of the contours, and vice versa for the right knee. The contours demonstrate the AM bundle of the ACL in ATT develops shear strains of ~10% at the femoral insertion (see Discussion for further detail).

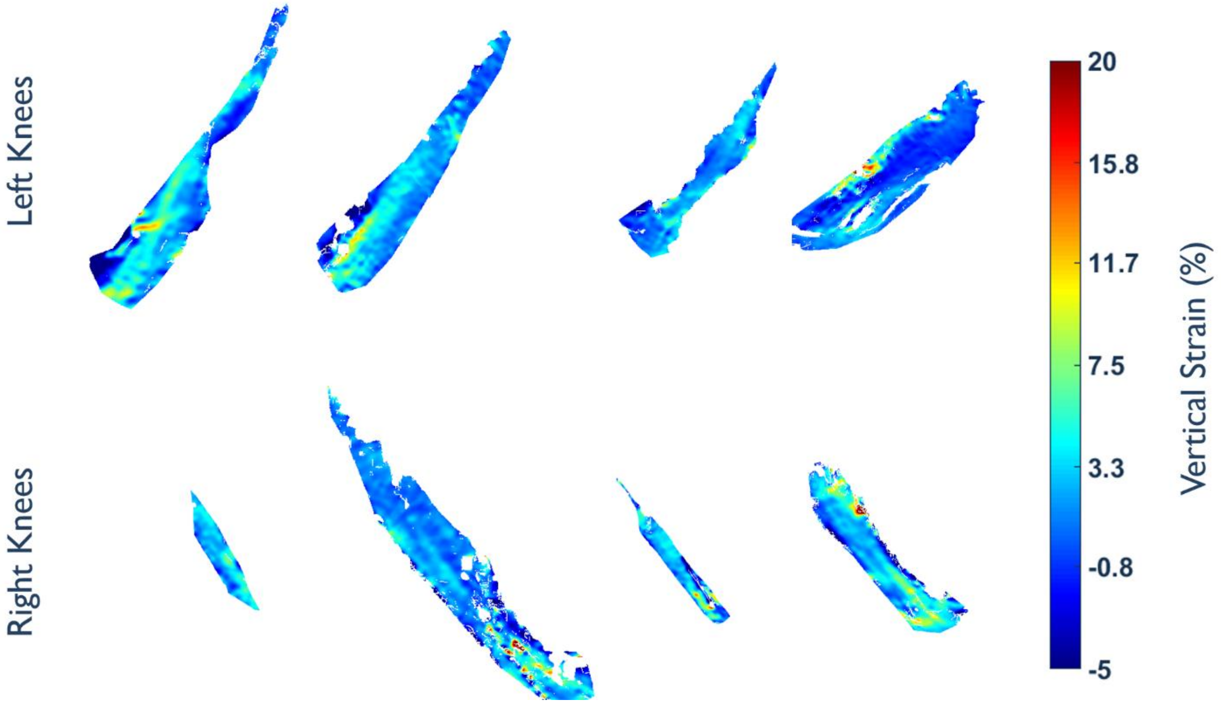

Figure 4.13: ATT vertical strain contours (along the axis of loading, vertical in the plane of the page) at peak applied grip-to-grip strain.

Vertical strain contours for the ATT tests are shown in **Figure 4.13** and horizontal strain contours are seen in **Figure 4.14**. As the ATT test represents a complex loading state of the ACL, and includes both bundles, these strain contours cannot be used to calculate stress vs. strain curves. However, both sets of contours show relative homogeneity along the surface of the specimen.

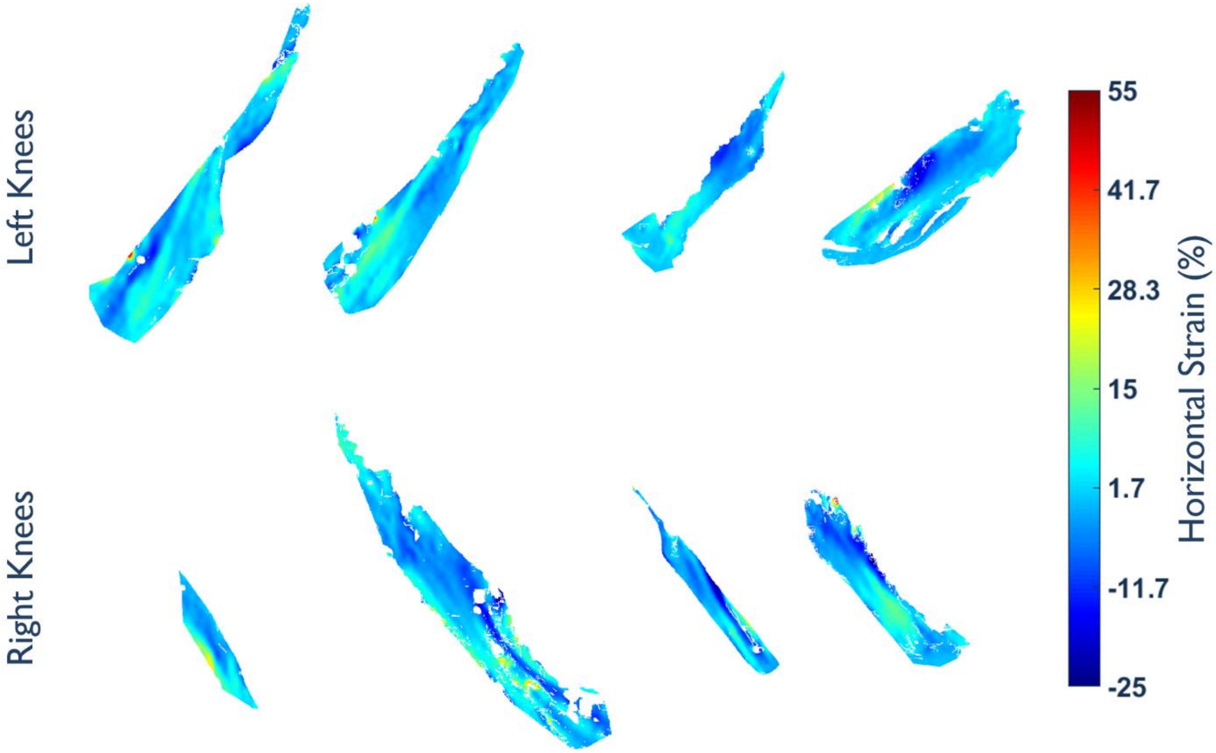

Figure 4.14: ATT horizontal strain contours (transverse to the axis of loading, horizontal in the plane of the page) at peak applied grip-to-grip strain.

Figure 4.15 shows the load vs. displacement data from 7 ATT experiments. With the use of dual MTS actuators, the peak displacements occur at the femoral and tibial insertions. For the plot in **Figure 4.15**, the DIC displacement data was taken at the femoral insertion, and 1 of the 8 bundles shown in **Figures 4.12** to **4.14** was excluded, as it did not contain correlated DIC data at the insertion. The displacements measured via DIC are lower than those measured via grip-to-grip for all cases. The dashed line indicates 0.134 kN, selected for comparison of the displacements measured via DIC and grip-to-grip in this study with those reported in the literature. For the two curves that manifested a force of 0.134 kN, the displacements were 0.176 mm and 0.179 mm for the DIC data, and 1.97 mm and 2.473 mm for the grip-to-grip data. **Figure 4.16** shows the DIC data only, with notable specimen-to-specimen variability, as would be expected for force and displacement data, where specimen dimensions are not taken into account.

4.3 Discussion

Previous studies have investigated the displacement response of the knee to anterior tibial translation. Furman et al. 1976 performed ATT tests in an investigation on the displacements and rotations that occur in the knee after removal of the AM or PL bundles, as well as the resultant motions due to cutting the entire ACL, LCL, superficial

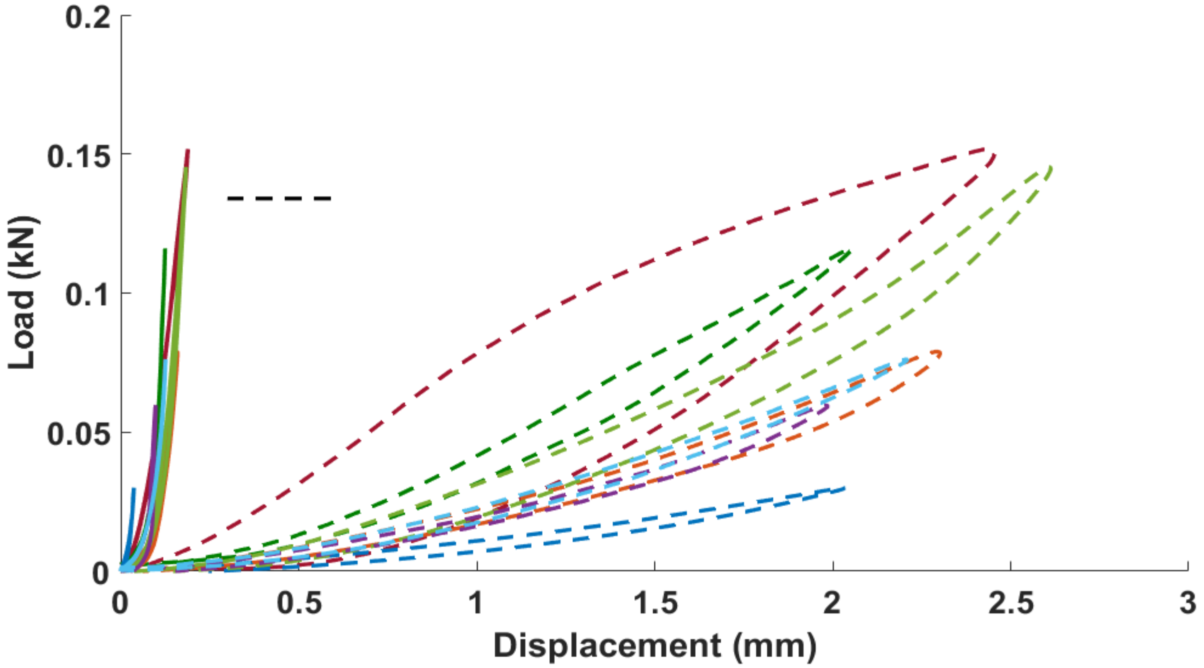

Figure 4.15: Load vs. displacement curves from 7 ATT tests. The response curves based on strains calculated from DIC are shown with solid lines and strains from grip-to-grip displacement data with dashed lines. Colors represent distinct bundles. The dashed black line indicates 0.134 kN for comparison of results of DIC and grip-to-grip data sets.

portion of the MCL, the posterior part of the joint capsule, or combinations of removing these tissues. For the intact knee control, they manually performed anterior translation of the tibia “until firm resistance was reached”, and reported displacements of 1.8 ± 0.2 mm at 0° flexion and 2.9 ± 0.5 mm at 45° flexion [14]. It is difficult to compare the data in this chapter with this study, as the force applied was not specified. Gabriel et al. 2004 performed ATT tests and measured the resulting kinematics, reporting 5.9 ± 2.6 mm of displacement with the application of 134 N load at 30° of knee flexion, whereas this work reports 1.97 mm and 2.473 mm for the grip-to-grip data. The difference in reported data is likely due to variations in test setup (and possible sources of compliance), as well as the difficulty in comparing non-normalized data between studies. Beynnon et al. 1997 reported strains as a function of knee flexion/extension, measured in the ACL

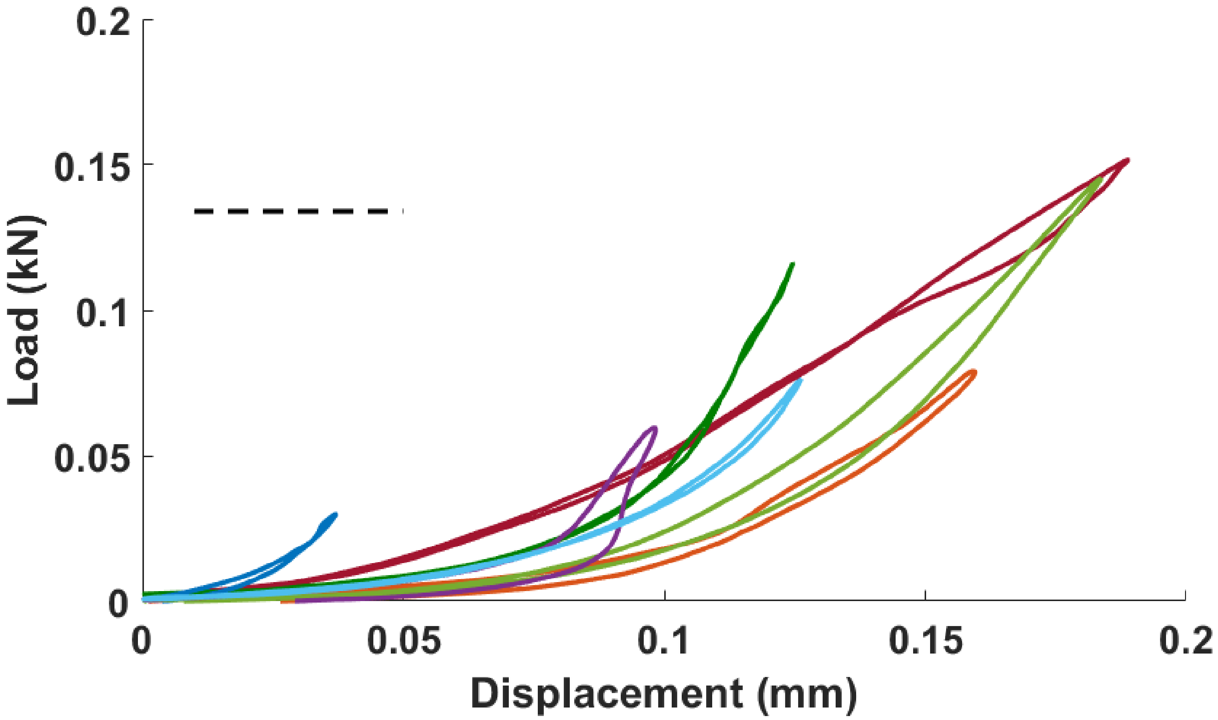

Figure 4.16: Load vs. displacement curves from DIC data for 7 ATT tests. The dashed black line indicates 0.134 kN for comparison of DIC and grip-to-grip displacements.

using an arthroscopically implanted DVRT (positioned in the mid-substance of the AM bundle) [15]. Although a direct comparison is difficult to make between the point-to-point measurements in this previous work and the full-field contours presented here, it is notable that Beynnon et al. found strains of less than 2% at a knee flexion angle of 30°.

In this work, the shear strain contours of 8 ATT specimens (**Figure 4.12**) manifest an excess of ~10% strain at the femoral insertion at 30° knee flexion. This demonstrates that in ATT, the ACL develops large shear strains, especially at the femoral insertion. This result could be indicative of tears originating at the femoral insertion, and point to ACL injury mechanisms.

The tangent moduli of the PL bundles discussed in this chapter are comparable to previous studies. Butler et al. 1992 reported a modulus of 155 ± 120 MPa for the PL, with a reported CSA resolution of 0.01 mm^2 and length measurement resolution of 0.05 mm (the resolution of the load cell utilized in the study was not reported) [10]. In this chapter, tangent moduli computed via grip-to-grip motion were 117 ± 84 MPa at 3% nominal strain and 173 ± 49 MPa at 5 MPa nominal stress, both well within experimental error of the values reported in the previous work. The tangent moduli computed via DIC (242 ± 117 MPa at 3% nominal strain and 254 ± 116 MPa at 5 MPa) are stiffer than both the tangent moduli computed using grip-to-grip motion and those of the previous work. It is not surprising that the results via grip-to-grip motion are within the range of the study by Butler et al., as that work utilized an Instron LVDT to obtain grip-to-grip displacement measurements.

The PL bundle tangent moduli can also be compared to those of the AM bundle. At 3% nominal strain, the AM manifested tangent moduli of 1.04 ± 0.24 GPa (n=8) from strains computed via DIC and 0.33 ± 0.19 GPa (n=8) for strains computed via grip-to-grip motion [16], compared to PL levels of 242 ± 117 MPa (n=5) or strains computed via DIC and 117 ± 184 MPa (n=5) for strains computed via grip-to-grip motion. When comparing the mean response of the AM and PL bundles, it is apparent that the AM is stiffer than the PL for both DIC and grip-to-grip data. In a comparison of a single AM and PL from the same animal, the AM also manifested a stiffer response than the PL (**Figure 3.12** in **Chapter 3**).

As mentioned earlier, the PL bundle surface is notably wavy on the front surface when aligned for tensile testing—it is not flat and smooth like the AM bundle—and this is not conducive to maintaining a good speckle pattern in the camera FOV during tensile loading. As discussed in **Chapter 3**, certain portions of the tissue move anteriorly and others posteriorly during loading. This motion is not possible to predict prior to deformation of the tissue, and causes decorrelation of the DIC pattern as portions of the tissue move into or out of the field of view, and this phenomena creates a limitation on measuring the surface level displacements and strains of the PL bundle via DIC.

4.4 Conclusions

The ATT data demonstrate lower displacements sustained by the tissue during loading as measured via DIC as opposed to grip-to-grip motion. Full-field surface strain data gives insight into the response of the ACL in loading states both familiar to clinicians and indicative of injury. For the PL data, tangent moduli measured grip-to-grip compare well with those found in previous studies. In addition, the tangent moduli of the PL are less than those of the AM bundle (284.0 ± 80.1 MPa for PL vs. 1.04 ± 0.24 GPa for the AM at the same strain level), demonstrating the need to individually characterize the bundles for accurate models of the ACL mechanical response. The PL bundle demonstrates a variation in its frontal profile during tensile loading resulting in loss of correlation in regions, and is a limitation of this work. However, the portions of the surface that did maintain correlation were useful for obtaining data for characterization. Reports of full-field contour information are extremely rare for ATT studies and difficult to obtain for PL bundle tensile tests; this work provides new insight on the both the full-field and tissue level mechanical response of the PL bundle and the entire ACL under anterior tibial translation.

4.5 References

[1] J.M. Bach, M.L. Hull, H.A. Patterson, Direct measurement of strain in the posterolateral bundle of the anterior cruciate ligament, J. Biomech. 30 (1997) 1–3.

[2] L.A. Norwood, M.J. Cross, Anterior cruciate ligament: functional anatomy of its bundles in rotatory instabilities., Am. J. Sports Med. 7 (1979) 23–6. http://www.ncbi.nlm.nih.gov/pubmed/420384.

[3] M. Sakane, R.J. Fox, S.L.-Y. Woo, G.A. Livesay, G. Li, F.H. Fu, In situ forces in the anterior cruciate ligament and its bundles in response to anterior tibial loads., J. Orthop. Res. 15 (1997) 285–93. doi:10.1002/jor.1100150219.

[4] A.A. Amis, G.P.C. Dawkins, Functional Anatomy of the Anterior Cruciate Ligament, J. Bone Jt. Surg. (1991) 260–267.

[5] F.R. Noyes, E.S. Grood, The Strength of the Anterior Cruciate Ligament in Humans and Rhesus Monkeys, J. Bone Jt. Surg. 58 (1976) 1074–1082.

[6] A. Weiler, G. Peters, J. Mäurer, F.N. Unterhauser, N.P. Südkamp, Biomechanical properties and vascularity of an anterior cruciate ligament graft can be predicted by contrast-enhanced magnetic resonance imaging. A two-year study in sheep., Am. J. Sports Med. 29 (2001) 751–761.

http://www.ncbi.nlm.nih.gov/pubmed/11734489.

[7] A. Weiler, C. Förster, P. Hunt, R. Falk, T. Jung, F.N. Unterhauser, V. Bergmann, G. Schmidmaier, N.P. Haas, The Influence of Locally Applied Platelet-Derived Growth Factor – BB on Free Tendon Graft Remodeling After Anterior Cruciate Ligament Reconstruction, Sport. Med. (2004) 881–891. doi:10.1177/0363546503261711.

[8] N. Chandrashekar, H. Mansouri, J. Slauterbeck, J. Hashemi, Sex-based differences in the tensile properties of the human anterior cruciate ligament., J. Biomech. 39 (2006) 2943–50. doi:10.1016/j.jbiomech.2005.10.031.

[9] R. Meller, E. Willbold, E. Hesse, B. Dreymann, M. Fehr, C. Haasper, C. Hurschler, C. Krettek, F. Witte, Histologic and biomechanical analysis of anterior cruciate ligament graft to bone healing in skeletally immature sheep, Arthroscopy. 24 (2008) 1221–1231. doi:S0749-8063(08)00515-X [pii]10.1016/j.arthro.2008.06.021.

[10] D.L. Butler, Y. Guan, M.D. Kay, J.F. Cummings, S.M. Feder, M.S. Levy, Location-dependent variations in the material properties of the anterior cruciate ligament, J. Biomech. 25 (1992) 511–8. http://www.ncbi.nlm.nih.gov/pubmed/1592856.

[11] D.L. Butler, Anterior cruciate ligament: its normal response and replacement, J. Orthop. Res. 7 (1989) 910–21. doi:10.1002/jor.1100070618.

[12] D.L. Butler, M.D. Kay, D.C. Stouffer, Comparison of Material Properties in Fascicle-Bone Units from Human Patellar Tendon and Knee Ligaments, J. Biomech. 19 (1986) 435–432.

[13] M.T. Gabriel, E.K. Wong, S.L.-Y. Woo, M. Yagi, R.E. Debski, Distribution of in situ forces in the anterior cruciate ligament in response to rotatory loads., J. Orthop. Res. 22 (2004) 85–9. doi:10.1016/S0736-0266(03)00133-5.

[14] W. Furman, J.L. Marshall, F. Girgis, The anterior cruciate ligament: a functional analysis based on postmortem studies, J. Bone Jt. Surg. 58-A (1976) 179–185.

[15] B.D. Beynnon, R.J. Johnson, B.C. Fleming, C.J. Stankewich, P.A. Renstrom, C.E. Nichols, The strain behavior of the anterior cruciate ligament during squatting and active flexion-extension. A comparison of an open and a closed kinetic chain exercise, Am. J. Sports Med. 25 (1997) 823–829. doi:10.1177/036354659702500616.

[16] K.F. Mallett, E.M. Arruda, Digital image correlation-aided mechanical characterization of the anteromedial and posterolateral bundles of the anterior cruciate ligament, Acta Biomater. (2017). doi:10.1016/j.actbio.2017.03.045.

Chapter 5: Finite Element Modeling of the Hyperelastic Full-Field Response of the Anteromedial Bundle of the Anterior Cruciate Ligament

5.1 Introduction

The ACL is the most commonly injured soft tissue structure in the knee, and often requires invasive surgery to restore pre-injury kinematics. Due to its tendency for injury, and its role as a major stabilizing ligament within the knee, understanding the mechanical responses of the native ACL and proposed ACL replacements is of critical importance. Finite element (FE) frameworks are valuable tools to study ACL injury, as simulations can recreate diverse loading conditions difficult to perform in a laboratory environment, often with lower cost and time requirements. However, the accuracy of FE simulations greatly depends on the experimental data used for validation, the constitutive models used to mathematically capture the experimental data, as well as the ability of the computational geometry to mimic tissue physiology. A plethora of computational studies have been performed in the biomechanics community. Many of these studies focus on a particular soft tissue structure, such as the responses of articular cartilage, menisci or medial collateral ligament (MCL) [1–5] and whole knee models incorporating most soft tissues within the knee [6–19]. The ACL in particular has also received attention, often with a focus on the biomechanics of ACL graft replacements [20–23]. Other works in the computational biomechanics field have focused on the development of FE methods and constitutive models for analyzing soft tissue structures [24–28].

A variety of models exist for the constitutive behavior of ligaments. While some works still use linear elastic descriptions to describe ligament response [16,29], it is widely understood that ligaments are non-linear, and comprised of collagen fibers embedded in a ground substance matrix [3,9,10,19,30–34]. The matrix is often modeled as a neo-Hookean or Mooney-Rivlin material, and is significantly less stiff than the collagen fibers [32,35]. The collagen fibers are commonly modeled using a phenomenological approach, assuming a piecewise continuous strain energy density function wherein the fibers do not support compressive loads, and contain a nonlinear term governing the small strain regime and a linear expression for finite strains. Microstructurally-based strain energy density functions combined with three-dimensional networks offer an alternative approach to constitutive modeling, and have the advantage of providing model parameters with physical meaning.

There is a lack of connection between experimental results and the computational models that depend on them, especially in the geometry of the FE models and the experimental characterization data used for model validation. The vast majority of FE studies of the articular knee joint use computed tomography (CT) or magnetic resonance (MR) scans of intact cadaver knees to produce 3D FE models of relevant tissue structures, with great detail on the *in-vivo* knee anatomy, while some studies have used experimental measurements of tissue orientations [31,33,35].

However, with *in*-vivo models, it is difficult to ascertain the full-field response of tissue structures, and the complicated tissue loading state is an additional barrier to connecting the simulation results to traditional mechanics concepts. The gap between experiments and FE models is compounded by the experimental data utilized in many FE studies. The studies by Butler et al. ([36,37]) are frequently used as the basis for the material properties of the ACL in FE models. These studies studied the mechanical properties of the ACL by dividing it into bone-fascicle-bone units for uniaxial tensile testing and demonstrated a difference in the mechanical properties of the distinct ACL bundles. However, these studies used grip-to-grip displacement measurements, and, as discussed in **Chapter 3**, the lack of tissue-level measurements leads to a significant over-prediction of tissue strains and under-estimation of tangent moduli.

Of the studies that develop FE models for the intact ACL, few base those models on individual anteromedial (AM) and posterolateral (PL) bundle structures. Most studies that include the ACL treat it as a homogenous solid with a preferred material direction, and do not develop distinct constitutive models for the AM and PL. Orsi et al. 2015 focused on the failure response of the entire knee, using a constitutive model for the AM and PL bundles that consisted of a combined Mooney Rivlin and three term phenomenological model to capture the tissues’ responses [34]. This is one of a few studies with a focus on the native AM and PL, but no information was reported on the resulting bundle mechanical properties.

There is clearly a need for tissue-level full-field experimental data for accurate validation of FE models and for comparison of numerical results over the entire surface of investigated biological structures. The vast majority of FE models present the full-field mechanical results in the form of stress distributions, regardless of the tissue structure under investigation. As is discussed in Limbert et al. 2004 [35], the stress distribution alone is not sufficient for validation of FE models, but there is a paucity of full-field experimental data available for comparison. Weiss et al. 2005 and Gardiner and Weiss 2003 are rare studies that report the strain distribution within ligament tissue in an FE model [4,26]. Gardiner and Weiss 2003 created an FE model of the MCL, femur and tibia from CT scans, with the MCL modeled as a transversely isotropic hyperelastic material. The matrix component of the MCL was modeled with a neo-Hookean model, and the collagen fibers with a piecewise strain energy density function with separate terms for the compressive, small strain and finite strain regimes. In addition to reporting the FE strain contours, this study also made a comparison of the FE contours with full-field MCL experimental strain contours as a validation of the model. The MCL has been afforded attention not given to the ACL regarding its full-field strain response and its transverse mechanical response [4,38,39]. There remains a need to expand the knowledge base of ACL biomechanics in a similar manner.

Digital image correlation is well known in the mechanics community for the great advantages it has in obtaining full-field surface strains without invasively interacting with the material under consideration. In **Chapter 3**, the full-field experimental surface strains of the AM and PL bundles, as well as the mechanical responses of both bundles were reported [40]. The response of the AM bundle in tension was surprising, demonstrating lateral local strains exceeding 50%. Shear strains of or exceeding ~10% were also present in all tested AM bundles, and this is unexpected for an orthotropic material uniaxially loaded along its principal material direction.

The shear response confirms the presence of separate structures within the individual bundles of the ACL, i.e. several collagen fascicles separated and surrounded by extracellular matrix [3,9,10,19,20,30–35]. These fascicles are further divided into collections of fibrils at the macroscale. The expansion demonstrated in the lateral direction could be due to the ‘flattening’ out of fascicles as they insert into the femoral and tibial entheses; these fascicles are initially rounded in the bundle mid-substance. Both the lateral and shear strain responses demonstrate the need for a complex model of the bundles that replicates the bundle physiology. It is hypothesized that the surprising experimental results can be captured in the geometry of an FE model, and the combination of this geometry and a physically relevant constitutive model can be utilized to capture the experimental mechanical response of the AM bundle. The goal of this work is to develop a computational FE model of the AM bundle of the ACL that demonstrates both the constitutive and full-field experimental responses of the AM under tensile loading.

5.2 Methods

5.2.1 Bundle geometry formation

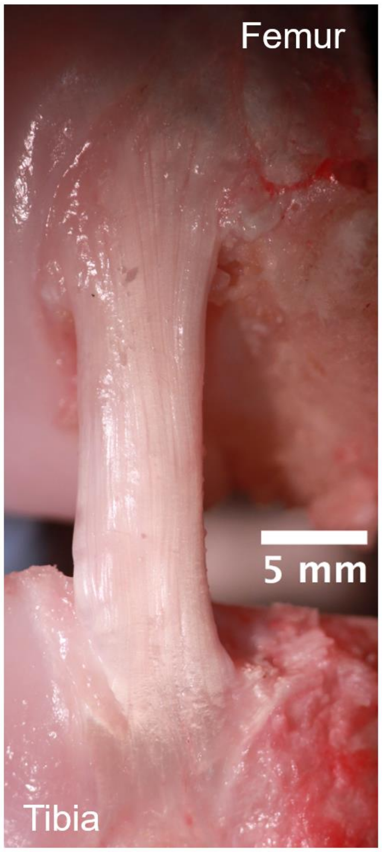

Figure 5.1: Alignment of AM bundle specimen for tension testing. The aligned fibrils of the AM bundle can be seen spanning from femur to tibia.

The AM bundle geometry was created from AM bone-ligament-bone (BLB) specimens isolated according to the protocol discussed in **Chapter 3** [40]. Briefly, this method aligned the AM bundle of the ACL for tensile testing. This was done by first dissecting all soft tissues except the ACL from fresh ovine knees. The PL bundle was also removed, leaving the AM bundle intact. Excess bone was trimmed to create femoral and tibial bone plugs. This facilitated alignment of the bundle by untwisting the AM from its native configuration and orienting the fascicles such that they spanned longitudinally from the femur to the tibia, as seen in **Figure 5.1**. A pseudo-random stochastic speckle pattern (using a non-toxic, biologically-friendly patterning medium) was placed on the surface of the bundle for measurement of displacements using digital image correlation (DIC). Speckle patterns were created using the custom pattern application technique developed for soft biological tissue discussed in **Chapter 2,** allowing for control of the speckle size and density according to the constraints of the test setup. DIC was used to obtain full-field surface displacements, and to determine axial (along the direction of loading), transverse (perpendicular to the direction of loading in the plane of the page), and in-plane shear strains. The bundle shown in **Figure 5.1** is representative of an aligned bundle prior to DIC patterning and testing.

After patterning, the experimental AM bundles (n=8) were tested in uniaxial tension up to ~12% grip-to-grip strain at 0.05/s true strain rate, although surface-level strains determined through DIC demonstrated tissue surface strains of ~5% at peak displacement. These tissue-level strains calculated via DIC were set as the benchmark for the simulation discussed in this chapter.

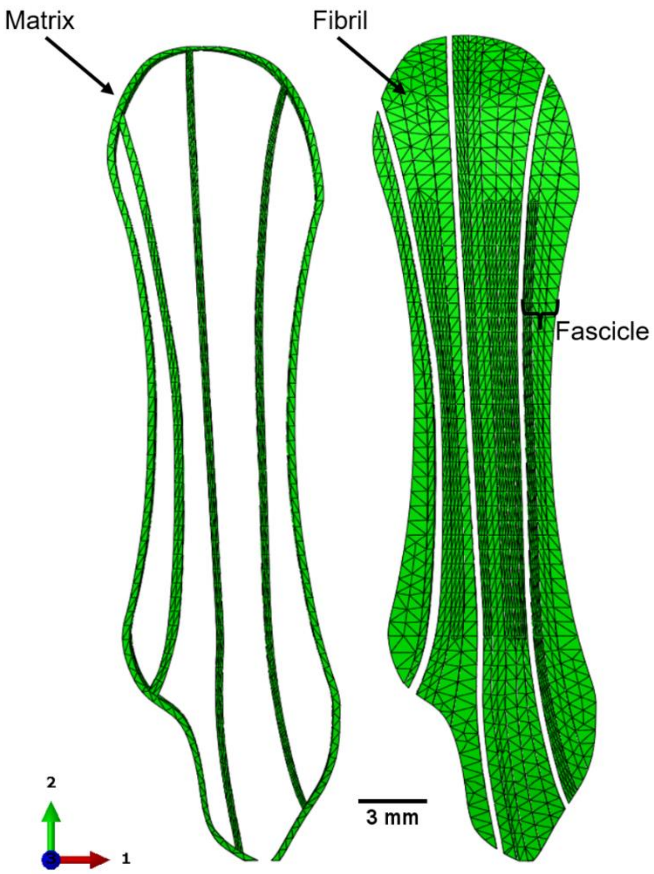

Figure 5.2: Inner components of the FE AM bundle. Matrix and fibril components within the FE model of AM bundle. The tissue is sectioned into fascicles and matrix. Each fascicle is further sectioned into individual fibrils, and the fascicles are separated by matrix

To capture the AM bundle geometry within an FE model, digital images were taken of the front and profile views of an aligned AM BLB specimen. This specimen was not included in the study discussed in **Chapter 3**, but its dimensions align well with the bundles in that study. The length of this representative specimen was 35.71 ± 0.01 mm, within the range of the average length of the AM bundles in the experimental study (31.7 ± 12.3 mm, n=8). The mid-substance of the FE bundle was contoured to achieve the hourglass mid-substance shape seen in the majority of the bundles in the experimental study. The width of the FE bundle was 5.54 ± 0.01 mm and the thickness of 2.37 ± 0.01 mm, matching the average dimensions of the bundles in the experimental study (width 5.5 ± 0.5 mm and thickness 2.3 ± 0.6 mm, n=8 [40]).

2D sketches of the bundle and bones were outlined in CorelDRAW X6 (Corel Corporation, Ottawa, ON). The 2D sketches of the front and profile views of the bundle were imported to the commercial finite element (FE) analysis code ABAQUS 2016 (Dassault Systèmes Americas Corp., Waltham, MA). Within ABAQUS, the 2D sketches

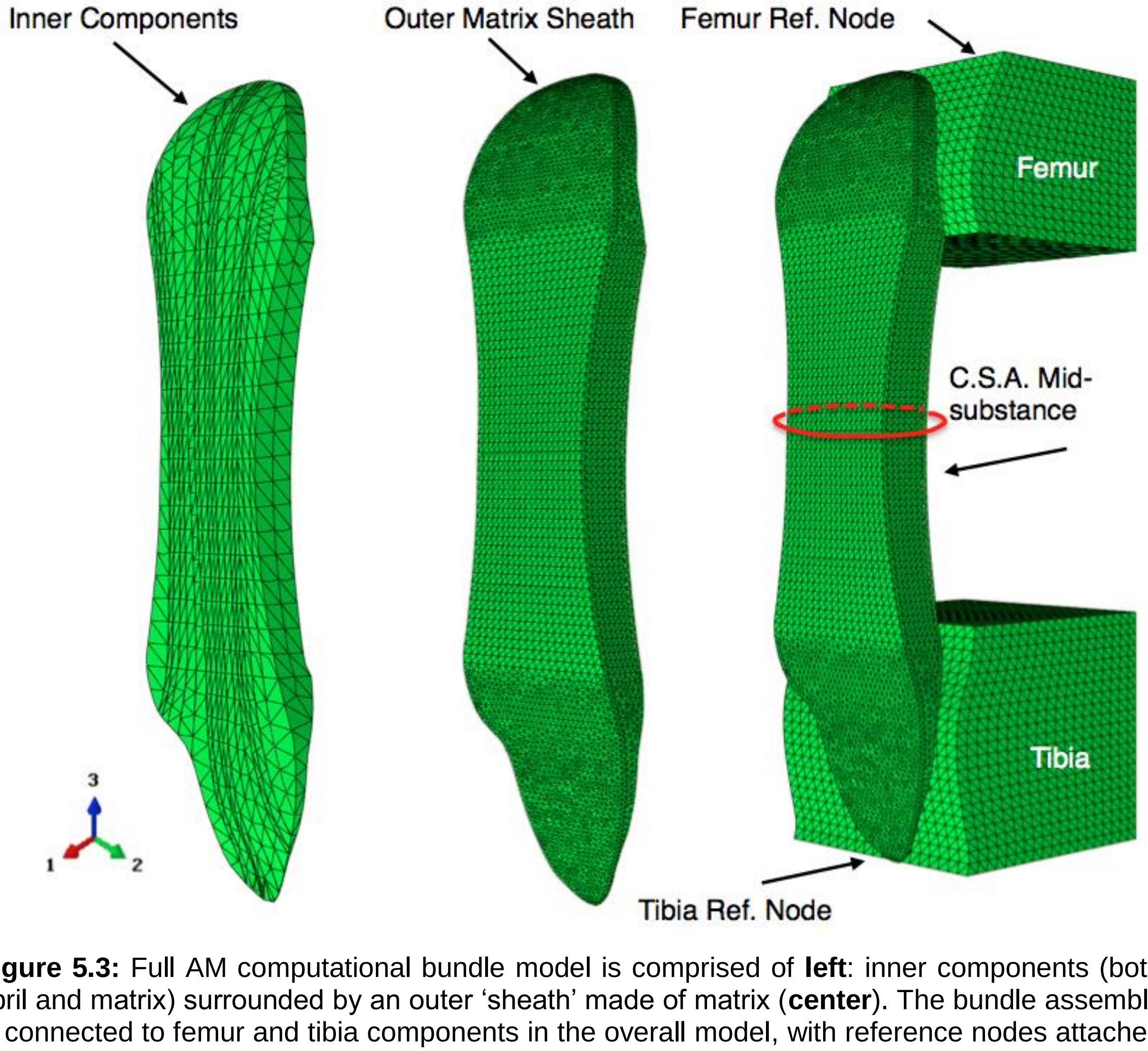

Figure 5.3: Full AM computational bundle model is comprised of **left**: inner components (both fibril and matrix) surrounded by an outer ‘sheath’ made of matrix (**center**). The bundle assembly is connected to femur and tibia components in the overall model, with reference nodes attached to the rigid femur and tibia (**right**). The length of the full bundle is 35.71 ± 0.01 mm and has a mid-substance width of 5.54 ± 0.01 mm and thickness of 2.37 ± 0.01 mm.

were extruded to a 3D deformable solid of the AM bundle. The femoral and tibial bone plugs were also outlined as 2D sketches and extruded as 3D discrete rigid shells. The AM bundle was discretized into fascicle, fibril, and matrix components, shown in **Figure 5.2**. Using the digital image of a physical bundle as a guide, the computational AM bundle was delineated into four fascicles spanning the length of the bundle from the femur to the tibia. These fascicles where separated by matrix components (defined to be 0.25 mm in width at the tissue mid-substance). Each fascicle was divided into individual fibrils, again using the physical bundle as a basis. The fibril and matrix components form the 'inner components' of the bundle, shown in **Figure 5.3**.

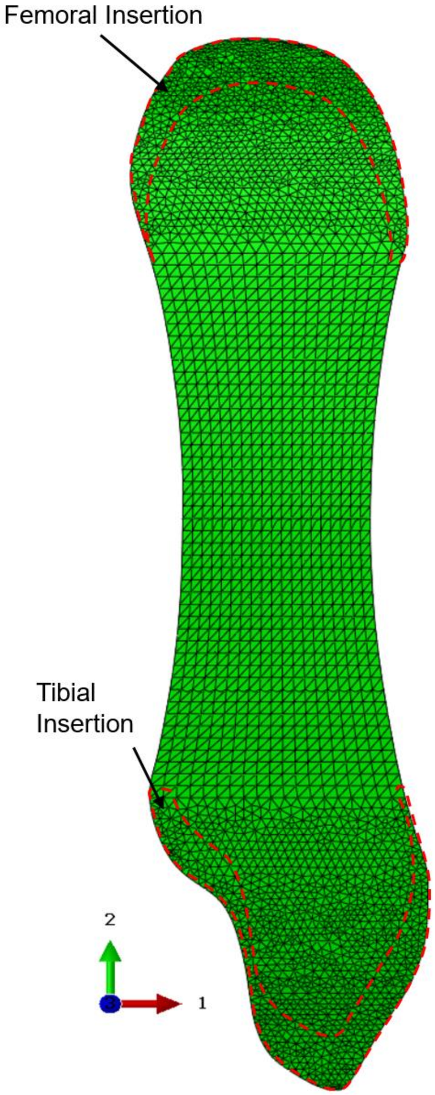

Figure 5.4: Femoral and tibial insertions. The back surface of the inner fibril and matrix components outlined in red are tied to the femur and tibia during deformation.

A matrix sheath was created to encompass the inner fibril and matrix components. This matrix sheath was created using the profile digital image of the bundle and specifying the sheath to have the same width (0.25 mm) as the inner component matrix. Bone plugs were also created using the digital images. The full assembly can be seen **Figure 5.3 (right)**. Fibril and matrix components were meshed with 10-node quadratic tetrahedron elements, and 3 node 3D rigid triangular facets for the rigid bone plugs. Tie constraints were used to connect the fibril and matrix in the inner component of the bundle (**Figure 5.3, left**). The surfaces of each matrix were tied to their respective neighboring fibril surfaces, and the outer matrix sheath (**Figure 5.3, center**) was selectively tied to fibrils in the inner component. Portions of the FE femur and tibial bone plugs were removed at both insertions; **Figure 5.4** shows the insertions at the femur and tibia, outlined in red. The back surface of the bundle within the femur and tibia insertions were tied to the femoral and tibial bone plugs using surface tie constraints. A general contact interaction was also prescribed between the fascicles (with finite sliding and hard contact), such that no fascicle was permitted to penetrate its neighbor fascicles during deformation.

The entire model was computationally deformed using ABAQUS Standard, with a static general step accounting for non-linear geometry. Displacement boundary conditions were applied to reference points attached to the rigid femur and tibia (**Figure 5.3, right**), and for the simulation discussed, all rotations and translations were fixed except for translation along the vertical '3' axis. Displacement of the femur and tibial reference nodes along the axial (‘3’) direction (**Figure 5.3, right**) were prescribed to the level necessary to produce ~4.3% nominal strain in the mid-substance of the bundle, matching the experimental strains calculated via DIC. Numerical nominal strain values were extracted from a set of nodes within the mid- substance (**Figure 5.3, right**), similar to the mid-substance region selected for evaluation of the experimental properties of the AM bundle (see [40] for more detail). The numerical nominal stress was calculated by dividing the reaction force output at the femoral reference node by the cross-sectional area of the mid-substance of the FE bundle.

5.2.2 Fiber and matrix constitutive models

The constitutive model for the computations utilized the experimental stress vs. strain response of the AM bundle data discussed in **Chapter 3**. **Figure 5.5** shows the mean response of 8 AM bundles (with standard deviation bars in black). The smallest peak stretch of the eight bundles was 1.0339; the mean response is calculated and plotted up to this point. A representative bundle from the set of 8 knees was selected as the basis of the constitutive model (**Figure 5.5**).

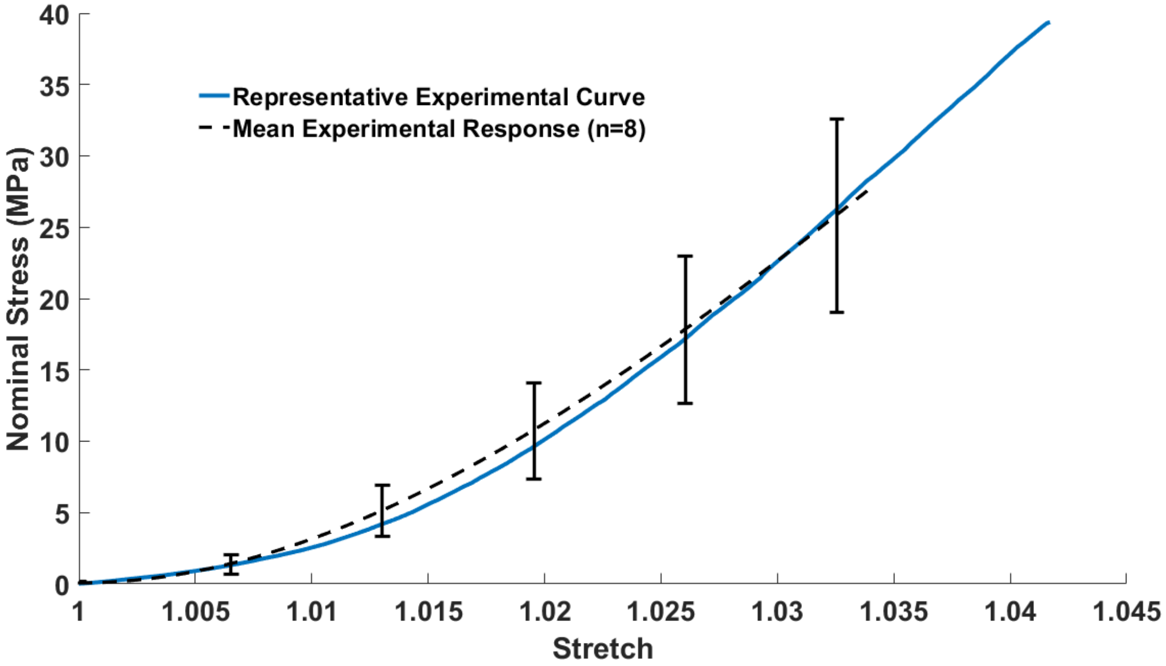

Figure 5.5: Mean response of 8 AM bundles tested in uniaxial tension. The representative experimental bundle chosen for the basis of the simulations lies within the standard deviation of the mean bundle response, and is chosen for direct comparison of the computational model with the experimental full-field strain contours.

An actual experimental contour was selected as opposed to the average response in order to make direct comparisons between the full-field computational strain contours and the full-field experimental strain contours for that particular bundle. The representative bundle chosen lies within the standard deviation of the mean response, and has a R^2 of 0.997 to the mean response, indicating it is a reasonable choice for the constitutive model. **Figure 5.6** shows the decomposition of the experimental AM stress vs. stretch response into estimated fibril and matrix responses. The individual fibril and matrix contributions to the overall AM bundle response were determined by calculating the tangent modulus of each component assuming the fibril was 200 times stiffer than the matrix, and utilizing rule-of-mixtures for the tangent modulus as seen in **Equation 1**:

$$E_{total} = \nu_f E_f + (1 - \nu_f) E_m \qquad (1)$$

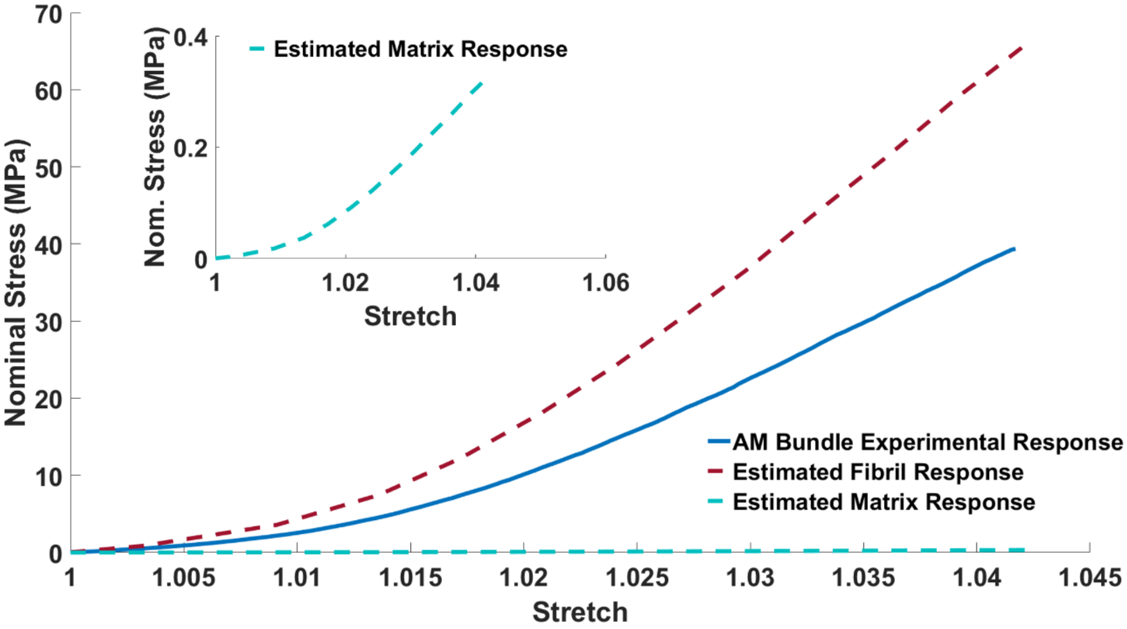

Figure 5.6: Decomposition of experimental AM bundle stress vs. stretch response into fibril and matrix contributions. Experimental data are from an AM bundle tension test to ~4.3% nominal strain. Fibril and matrix responses are derived assuming the fibril material is 200 times stiffer than the matrix, and applying rule of mixtures based on the cross-sectional area of the computational AM model (having a ratio of 60.9% fibril and 39.1% matrix).

where E_{total}, E_f, and $E_m$are the tangent moduli of the entire bundle, fascicle components, and matrix components respectively, and ν_f is the fiber volume fraction.

The constitutive model used for the fibrils in this model is based on the work by Palmer and Boyce 2008 [41]. Other works have combined the worm-like and eight-chain models to capture the constitutive response of anisotropic biopolymer networks [42,43]. Palmer and Boyce 2008 utilized a combination of the Kratky-Porod chain and Arruda-Boyce eight-chain model to capture the constitutive response of densely cross-linked cytoskeletal networks. Specifically, Palmer and Boyce invented the MacKintosh derivation of the Kratky-Porod model to describe the 1D force-extension behavior of single actin filaments. This 1D force-extension model was then extended to an incompressible isotropic 3D network of actin filaments using the Arruda-Boyce eight-chain model [44], capable of capturing non-affine deformations in an idealized network structure [41]. This work by Palmer and Boyce 2008 was recently developed into a slightly compressible form and then incorporated into a custom ABAQUS UMAT by B.C. Marchi. The strain energy density function for the fibrils has the form:

$$\begin{aligned} U_{Mac} = {} & \frac{C_r}{12\Lambda - 4\rho_0\sqrt{3I_1}}\left(3\Lambda^2 + \left(4\rho_0\sqrt{3I_1} - 12\Lambda\right)\ln\left(\frac{A\left(3\Lambda^2 - 6\Lambda + 2\rho_0\sqrt{3I_1}\right)}{\rho_0\sqrt{3I_1} - 3\Lambda}\right)\right) \\ & + \frac{B}{2}(J-1)^2 - \frac{C_r\Lambda^2\rho_0\left(6\rho_0 + \Lambda^2 - 6\Lambda\right)}{12(\Lambda - \rho_0)^2\left(2\rho_0 + \Lambda^2 - 2\Lambda\right)}\ln(J) \end{aligned} \qquad (2)$$

where the first two terms derive from the model developed by Palmer and Boyce 2008 and the second two terms are the volumetric components needed for compressibility. In the equation, J is the Jacobian, I_1 is the first invariant of the right Cauchy-Green deformation tensor, C_r is the rubbery modulus, B is the compressibility, $\Lambda = {}^{L}\!/_{A}$ and $\rho_0 = {}^{r_0}\!/_{A}$ where L is the final contour length, r_0 is the chain length in its reference configuration, and A is its persistence length. It should be noted that while the persistence length A appears in the strain energy density, it drops out in the final Cauchy stress expression. The matrix components in this work were modeled using the standard neo-Hookean model provided within ABAQUS 2016 (Dassault Systèmes Americas Corp., Waltham, MA), with the form:

$$U_{NH} = C_{10}(\bar{I}_1 - 3) + \frac{1}{D_1}(J_{el} - 1)^2 \tag{3}$$

where C_{10} is the stiffness parameter proportional to the shear modulus, D_1 is for compressibility (proportional to the inverse of the bulk modulus), $\bar{I}_1$ is the deviatoric first strain invariant of the left Cauchy-Green strain tensor, and J_{el} is the elastic volume strain. The standard neo-Hookean model provided within ABAQUS 2016 (Dassault Systèmes Americas Corp., Waltham, MA) was used for the matrix constitutive formulation. The neo-Hookean model is commonly used in the literature for the modeling of matrix for ligament models [3,4,9,10,19,20,33,35,38]. This model lacks the necessary curvature to capture the typical response of soft collagenous tissue, i.e. a ‘toe region’ of low stress followed by a stiffening of the stress vs. strain curve.

However, with matrix stiffness 200 times less than the fibril stiffness, the matrix does not significantly contribute to the longitudinal (along the axis of loading) response of the material, and thus the neo-Hookean material is reasonable for this model.

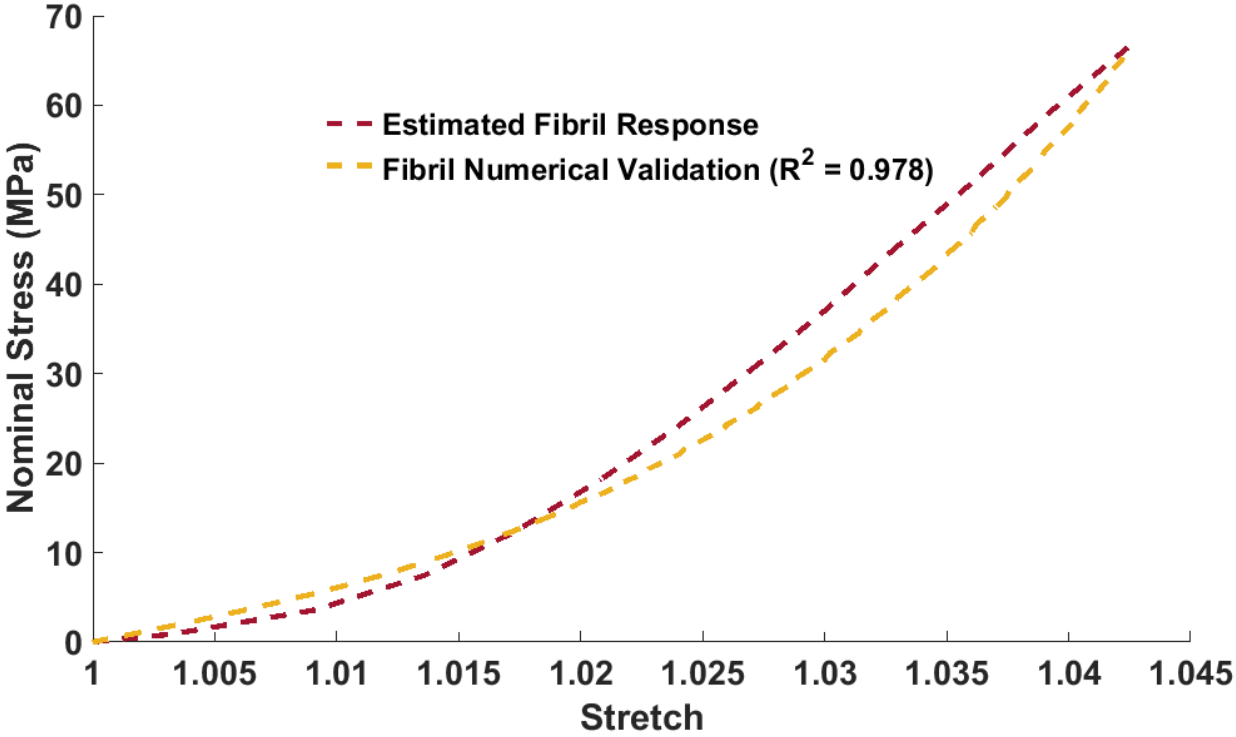

Figure 5.7: One-element validation of fibril constitutive model of **Equation 2**. This model is based on the MacKintosh derivation of the Kratky-Porod chain model, with the eight-chain model used to extend the 1D force extension behavior to three dimensions. This model is capable of capturing the toe response and stiffening response characteristic of ligament constitutive behavior.

One-element validations of the MacKintosh and neo-Hookean models were performed to determine the constitutive model parameters to the estimated fibril and matrix responses, as shown in **Figure 5.7** and **Figure 5.8**. The fibril model has an R^2 of 0.978. The matrix model has a R^2 of 0.977 (smaller compared to that of the fibril model), indicating a slightly better fit with the fibril model. **Table 5.1** contains the material parameters used in the simulation, with slight compressibility enforced for both the fibril

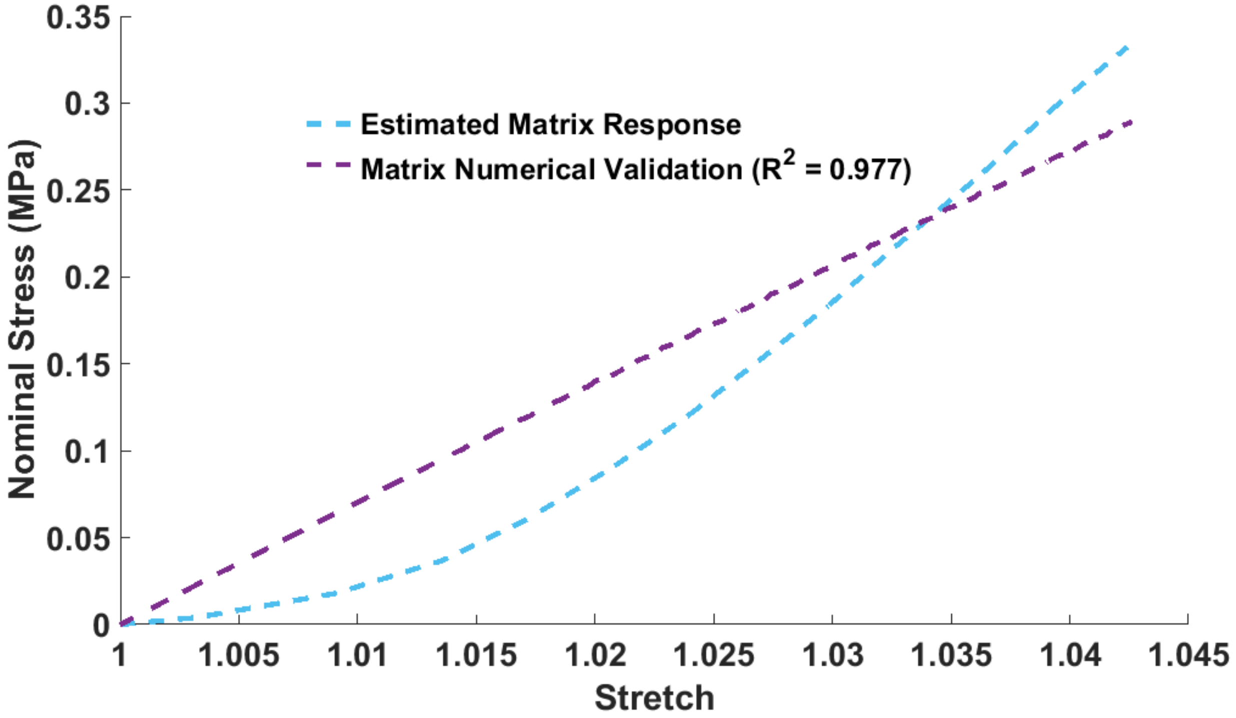

Figure 5.8: One-element validation of neo-Hookean matrix constitutive model. The neo-Hookean model lacks the curvature to capture the toe region and subsequent stiffened response of the tissue, and manifests a lower R^2 value compared to the fibril validation.

and matrix constitutive models (i.e. the bulk modulus is 1-2 orders of magnitude higher than the shear modulus for both material models) The initial Poisson's ratios are 0.452 and 0.490 for the fibril and matrix material models, respectively.

Table 5.1: Constitutive parameters for AM bundle simulation. The fibril components are modeled with Equation 2 and the matrix components with Equation 3.

Component	Material Properties
Fibril (MacKintosh)	$C_r = 7.290e^{10}$ Pa $B = 7.290e^{11}$ Pa $\rho_0 = 1.228$ $\Lambda = 1.722$
Matrix (neo-Hookean)	$C_{10} = 1.031e^{6}$ Pa $D_1 = 1.940e^{-8}$ Pa^{-1}

5.3 Results

Figure 5.9 (left) shows the vertical displacement contours of the AM FE model to the prescribed 1.50 mm displacement (selected to generate 4.24% nominal strain in the mid-substance of the bundle for a FE bundle initial length of 35.71 ± 0.011 mm). The experimental vertical displacement contour is shown in **Figure 5.9 (right,** adapted from

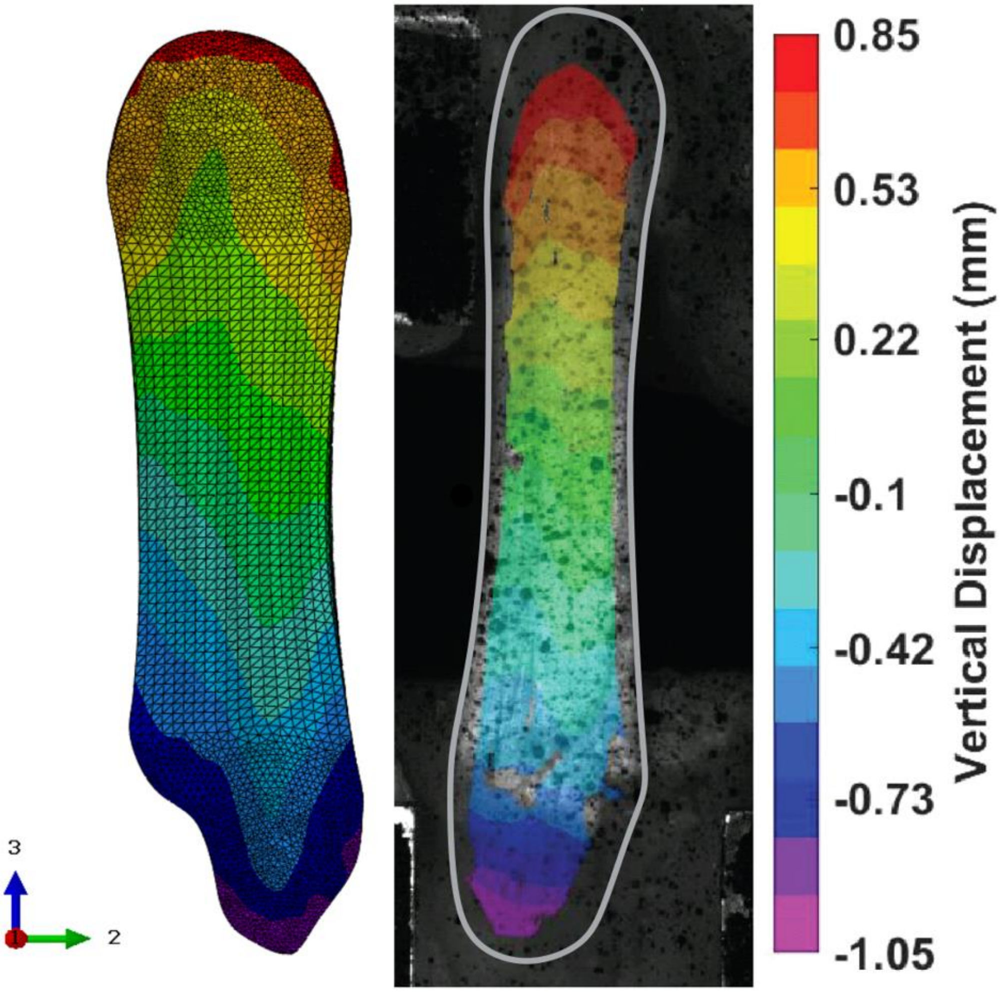

Figure 5.9: Comparison of the vertical displacement contours of the numerical response and experimental AM bundle data (adapted from [40]). The shorter AM computational bundle displacement scale has been adjusted to match the experimental bundle displacements. The simulation prescribed vertical displacement along the ‘3’ axis to both the femoral and tibial reference nodes, with all other translations and rotations held fixed. The numerical contour demonstrates the striated displacement ranges visible in the experimental contour. The entire AM bundle is outlined in grey in the experimental image.

[40]), at peak displacement (for a bundle with length of 38.10 ± 0.050 mm). The FE bundle is compared to the displacement and strain contours obtained via DIC of the representative bundle selected in **Figure 5.5** and used as the constitutive basis for the

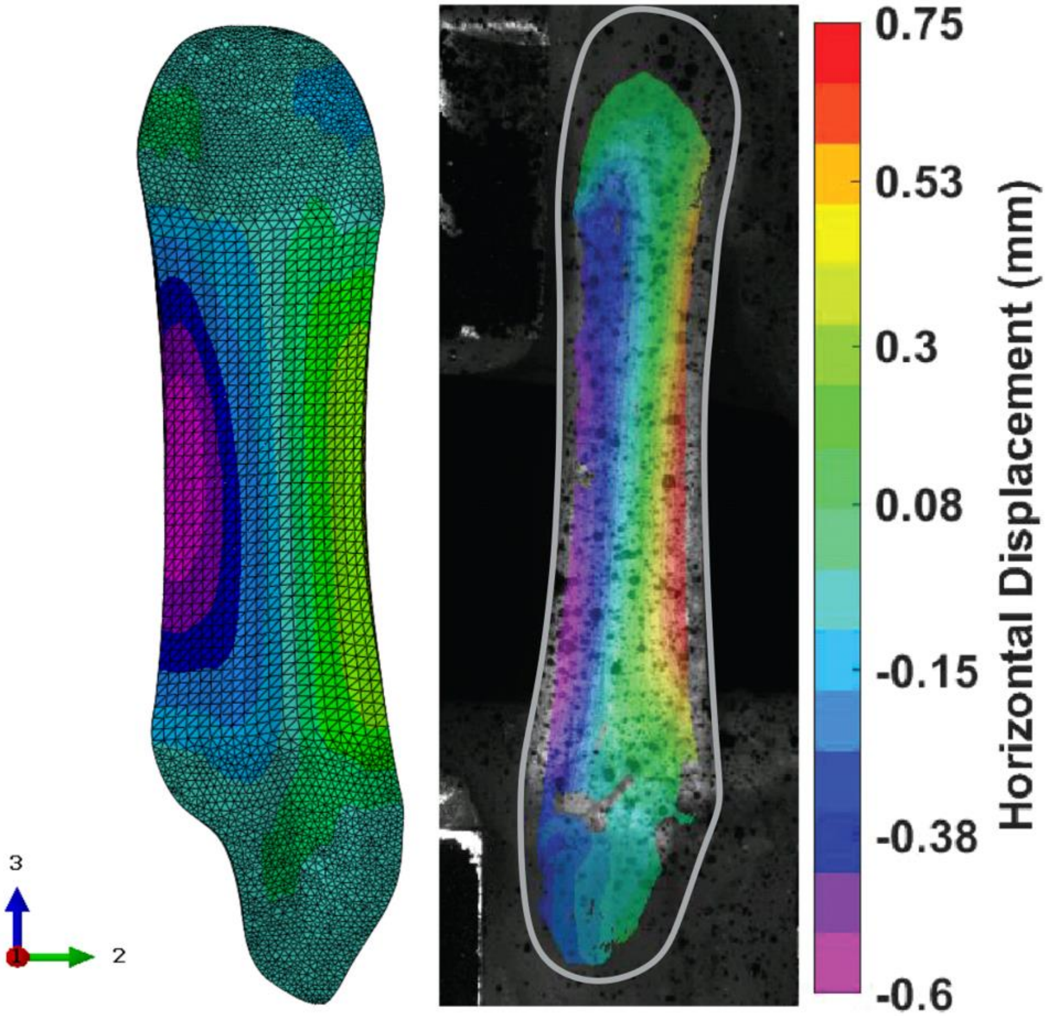

Figure 5.10: Comparison of the horizontal displacement contours of the numerical response and experimental AM bundle data (adapted from [40]). The AM computational bundle displacement scale has been adjusted to match the experimental bundle displacements (i.e. all contours are shown on the experimental bundle scale). This is the horizontal displacement resulting from a prescribed vertical displacement along the '3' axis. The numerical contour demonstrates the striated displacement ranges visible in the experimental contour, and demonstrates lateral expansion of the numerical bundle, matching the unexpected expansion in the experimental bundle. The entire AM bundle is outlined in grey in the experimental image.

FE model. Although the absolute displacement values differ (partially due to the difference in length, the FE geometry is slightly smaller than the dimensions of the experimental bundle), agreement can be seen between the numerical and experimental results, with the simulation capturing the striated displacement ranges at both insertions seen experimentally. The entire AM has been outlined in grey; some loss of DIC

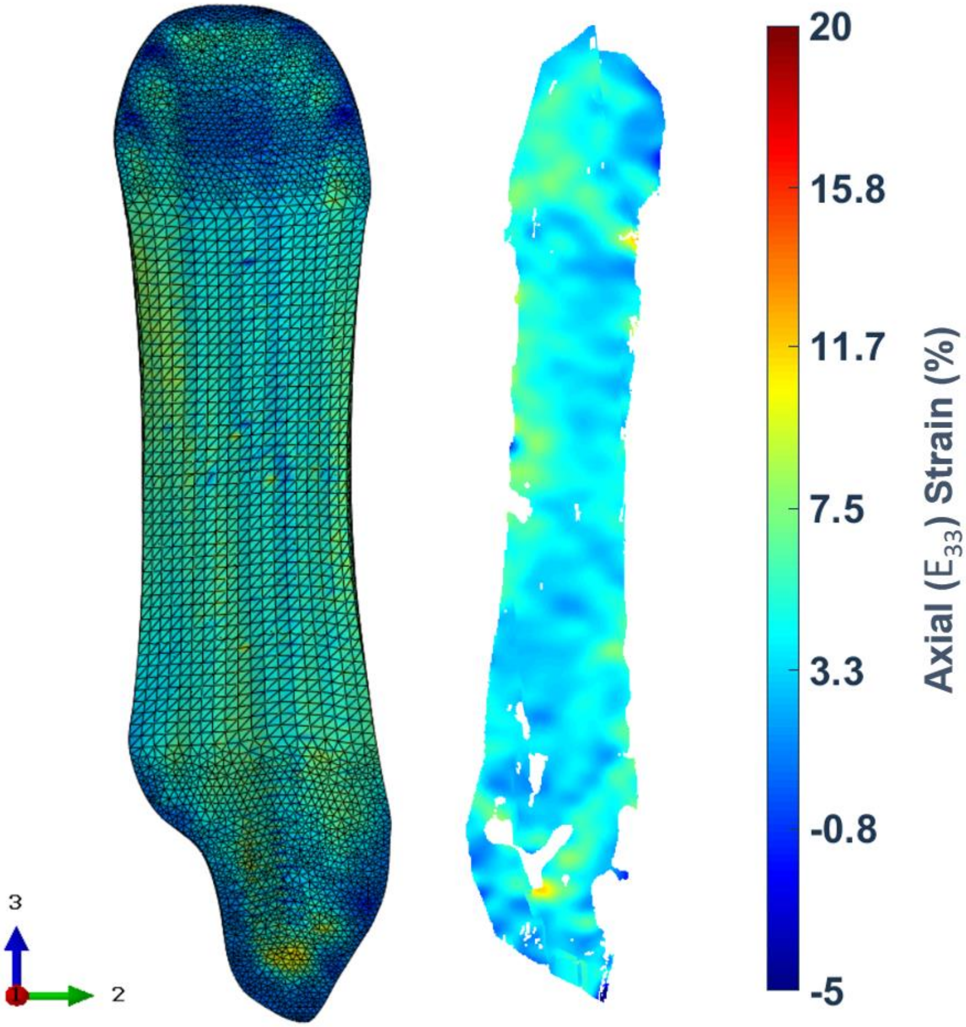

Figure 5.11: Comparison of numerical and experimental axial true strains (along '3' axis). Both contours are scaled to -5% to 20% true strain, and use the same color scheme. The computational element strains have been averaged within ABAQUS 2016.The numerical bundle shows a similar response as that of the experimental bundle, demonstrating the relative homogeneity in the mid-substance of the tissue. The experimental contour is adapted from the study detailed in [40]).

correlation is unavoidable at the edges of the tissue.

Figure 5.10 shows the horizontal displacement contours. The computational model demonstrates a similar expansion as that of the experimental AM bundle, with both the left and right edges of the computational and experimental contours moving outward laterally. The constructed geometry allows the individual fibrils to translate

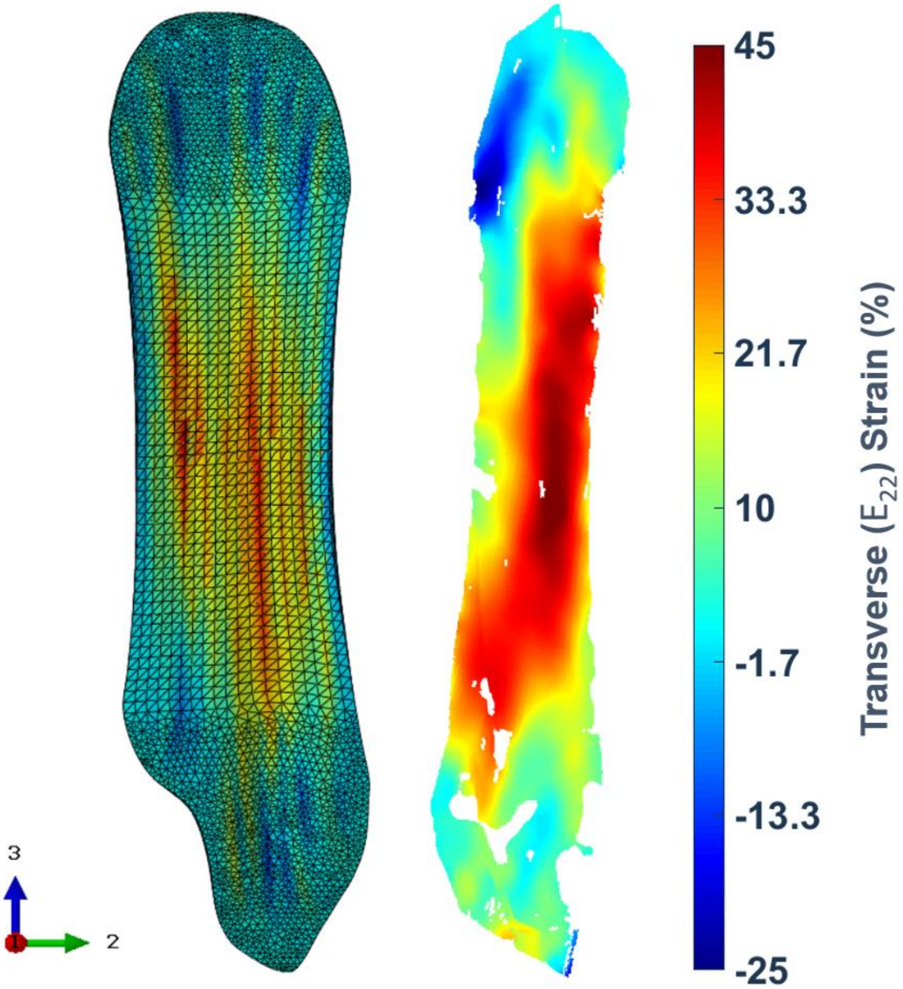

Figure 5.12: Comparison of numerical and experimental transverse true strains (along the '2' axis). The computational element strains have been averaged within ABAQUS 2016. Both contours are scaled between -25% and 45% true strain with the same color scheme. The numerical bundle demonstrates lateral expansion, similar to what is seen experimentally. The experimental contour is adapted from the study detailed in [40]).

outward as the bundle is loaded uniaxially; this freedom likely contributes to the lateral expansion demonstrated in the numerical results.

Figure 5.11 shows the comparison of the axial numerical strain response (along the ‘3’ axis, also the direction of loading) to the AM bundle strains measured via DIC.

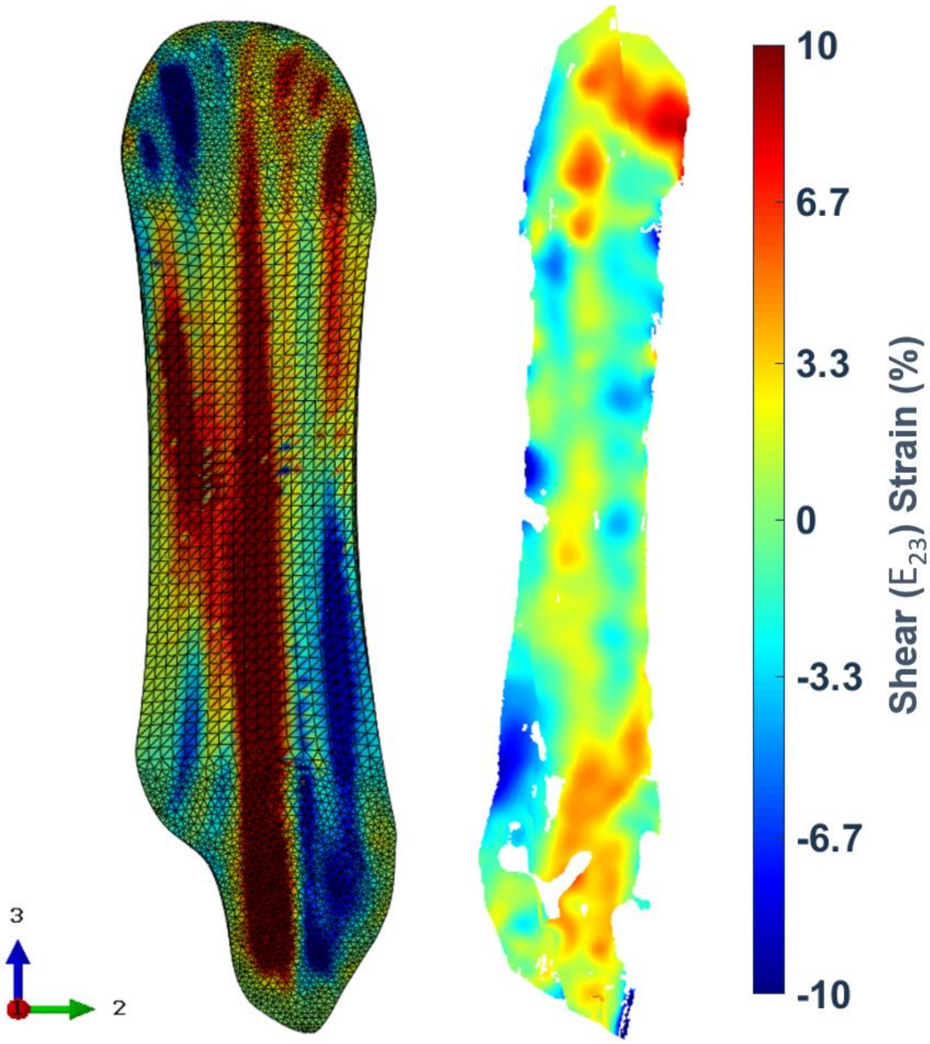

Figure 5.13: Comparison of numerical and experimental in-plane shear true strains (within ‘2-3’ plane). The computational element strains have been averaged within ABAQUS 2016. Both bundles are scaled from -10% to 10% true strain with the same color scheme. The numerical bundle manifests high shear throughout the bundle, as was seen by the experimental bundle shown here, as well as all other bundles tested in the experimental study discussed in **Chapter 3**. The experimental contour is adapted from the study detailed in [40]).

Both contours are scaled from -5% to 20% true strain using the same color scheme, and the computational element strains have been averaged within ABAQUS 2016. The numerical results demonstrate relative homogeneity in the mid-substance as well as strains at the same levels as the seen in the experimental contour. This behavior would be expected in traditional tensile testing of homogenous materials. However, the transverse true strain contours shown in **Figure 5.12** are unexpected for uniaxial tensile loading. As with the horizontal displacement contours, the transverse strain contours demonstrate lateral expansion in both the numerical and experimental data, with the numerical model capturing the localized nature of the experimental transverse expansion. **Figure 5.13** shows the shear contours, and the computational model

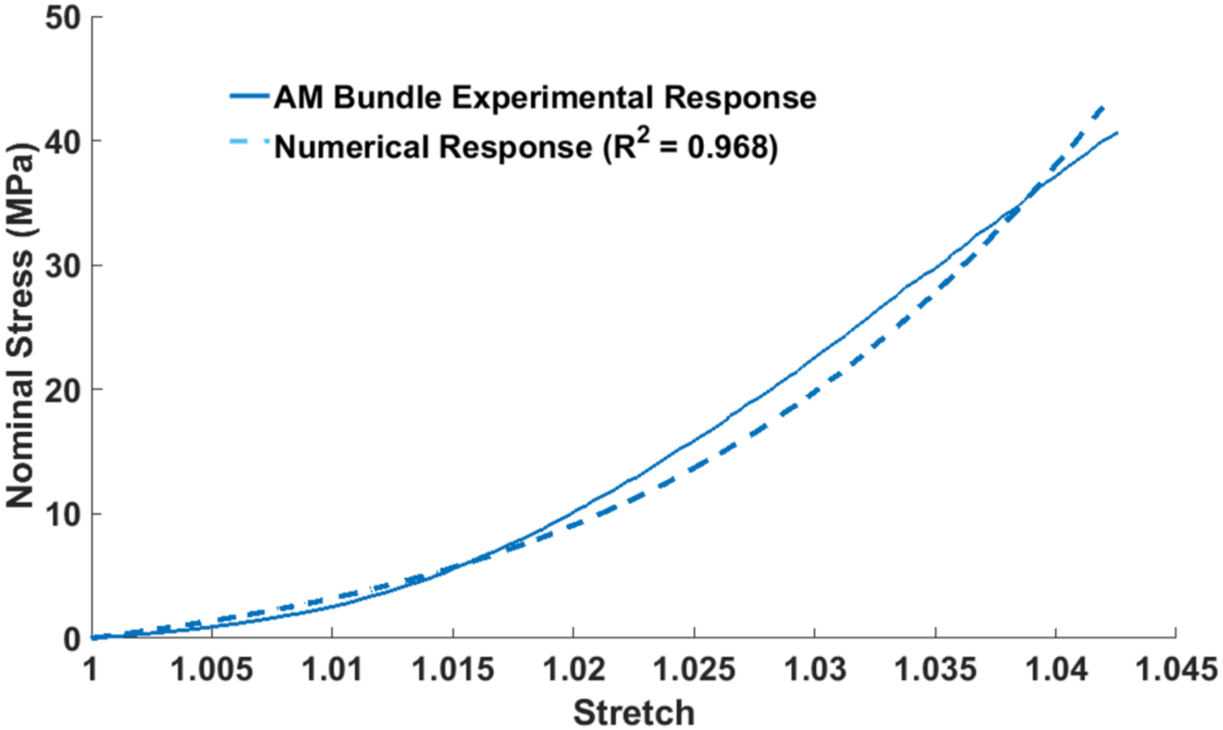

Figure 5.14: Stress vs. stretch comparison of the numerical simulation and experimental stress vs. stretch response. The numerical and experimental results have good agreement. At the peak experimental displacement, the nominal strains are 4.19% and 4.26% for the numerical and experimental results respectively, and nominal stresses of 42.7 MPa and 40.7 MPa for the numerical and experimental results. The R^2 value of 0.968 demonstrates reasonable fit of the overall numerical data to the experimental response.

demonstrates the surprising banded nature and large shear present in the experimental contour.

Figure 5.14 shows the nominal stress vs. stretch response of the AM computational model to the prescribed 1.50 mm displacement. This displacement generated 4.24% nominal strain in the mid-substance of the FE AM bundle, and is compared to the experimental stress vs. stretch data that had nominal strains up to 4.26%. At these strains, the numerical bundle manifested a nominal stress of 42.7 MPa, while the experimental bundle manifested 40.7 MPa. Overall, the numerical response has an R^2 of 0.968, demonstrating reasonable fit between the curves. The tangent moduli for the numerical model were calculated for comparison of the numerical response to the experimental data and are seen in **Figure 5.15**, calculated either at a stress of 20 MPa (1.41 GPa) or at 3% nominal strain (1.44 GPa). These values compare quite well with the tangent moduli of the specific experimental bundle used for the creation of the constitutive model properties (1.35 GPa at 20 MPa and 1.42 GPa at 3% nominal strain). The numerical tanagent moduli are reasonably in line with the range of AM experimental

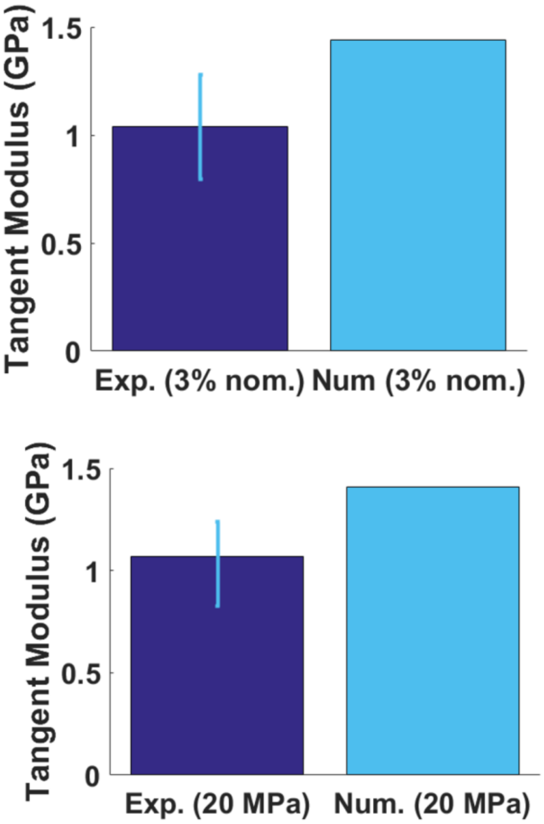

Figure 5.15: Tangent moduli of the experimental and numerical results, demonstrating 1.44 GPa at 3% nominal strain (experimental data 1.04 ± 0.24 GPa, n=8) and 1.41 GPa at 20 MPa (compared with 1.07 ± 0.17 GPa, n=8 for experiments).

tangent moduli of 1.07 ± 0.17 GPa (n=8) at 20 MPa and 1.04 ± 0.24 GPa (n=8) at 3% nominal strain.

5.4 Discussion

As mentioned previously, full-field displacements and strains provide a plethora of information on the behavior of complex materials, and there is a paucity of full-field surface-level strains reported for the ACL and its bundles. This model demonstrates expected axial strains, as well as the unexpected shear and transverse strains. In addition, the tangent moduli from the numerical model, measured at constant strain and stress, are in line with the experimental results (discussed in detail in **Chapter 3** [40]). The tangent moduli computed via DIC and demonstrated numerically are significantly higher than tangent moduli calculated using grip-to-grip measurements and reported in the literature. Butler et al. 1992 found tangent moduli of 283 ± 114 MPa and 286 ± 141 MPa for the anteromedial and anterolateral bundles investigated in this study. It is now widely accepted that the ACL is comprised of an anteromedial bundle and a posterolateral bundle. The anteromedial and anterolateral bundles in the Butler et al. 1992 study are likely a division of the anteromedial bundle now widely accepted [45]. In this study, tangent moduli were calculated from displacement data measured using an Instron LVDT (obtaining grip-to-grip displacement measurements). Other works by Butler et al. ([36,37]) are frequently used in the computational biomechanics community as a basis for the mechanical properties of the ACL in FE modeling [6,7,9,10,12,14,18,19]. However, without surface-level experimental properties for characterization, it is difficult to predict the tissue-level response numerically.

At least three levels of collagen and extracellular matrix exist in the ACL: the highest level consists of collagen fascicles, each separated by inter-fascicle matrix components, as is included in this model. The next hierarchical levels consist of fibrils (also present in this model) and subsequently fibers. Collections of fibers make up

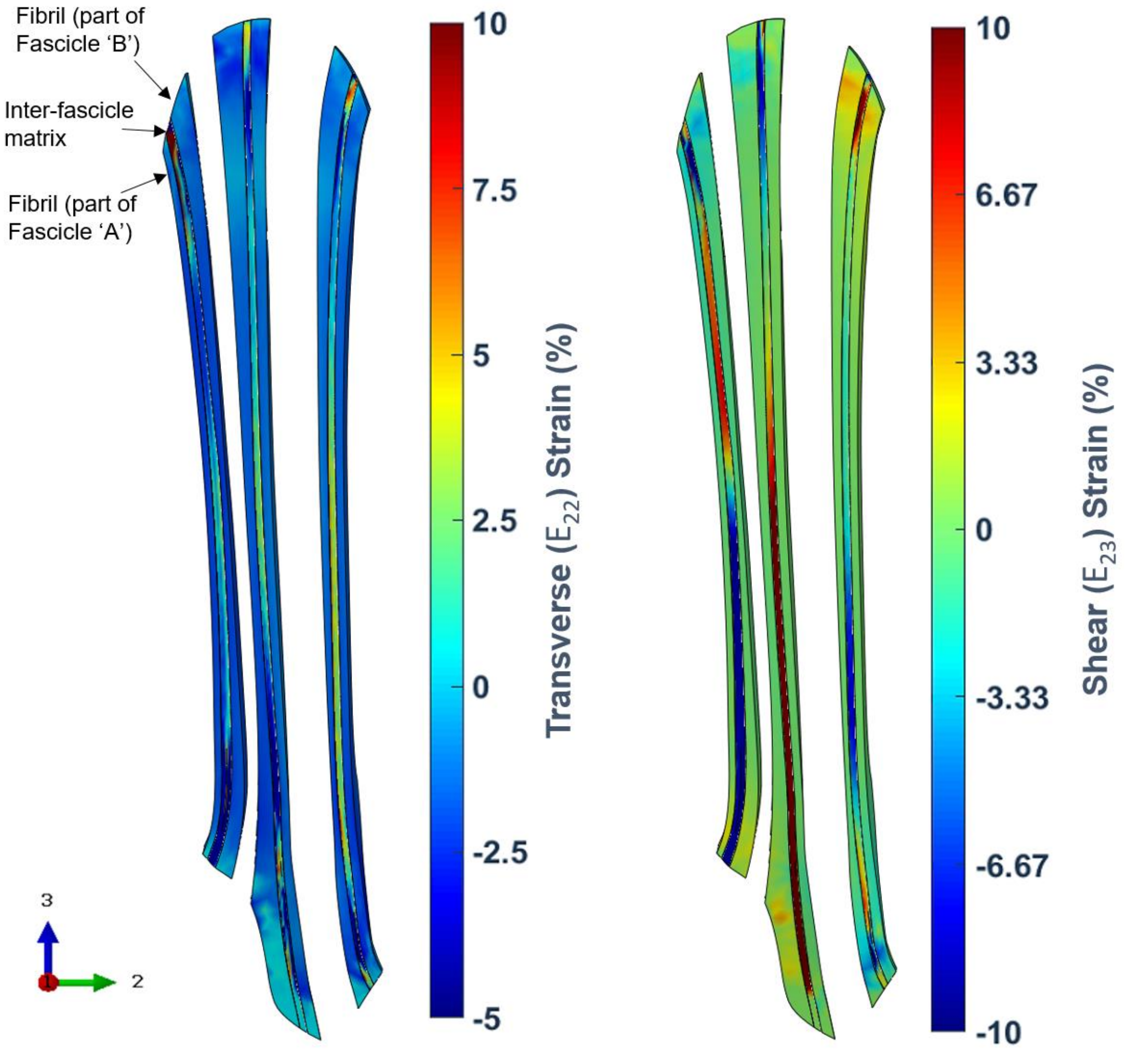

Figure 5.16: Transverse (left) and shear strains (right) in the inter-fascicle matrix components. It is evident that the inter-fascicle matrix components experience positive lateral strains in the bundle mid-substance while the neighboring fibril components manifest negative lateral strains. The inter-fascicle matrix also exhibit high in-plane shear during loading,this shear is not evident in the fibril components.

fibrils, and collections of fibrils make up fascicles, with matrix alternating between collagen components at all levels. It was computationally prohibitive to include the collagen fibers as well the matrix at the fibril and fiber levels (as well as difficult to ascertain these structures from the resolution of the digital images). However, within the current model (containing fascicle, fiber, and inter-fascicle matrix components), the inter-fascicle matrix exhibits both positive transverse strains and large in-plane shear strains. **Figure 5.16** shows both the transverse (**Figure 5.16, left**) and in-plane shear (**Figure 5.16, right**) strains of the inter-fascicle matrix at peak loading. The fibril components directly adjacent to the inter-fascicle matrix components are also shown for comparison of the strain responses, each fibril is part of a larger fascicle (**Figure 5.16, right** shows the fibrils belonging to Fascicle ‘A’ and Fascicle ‘B’ as an illustration). It is evident from the manifested positive transverse strains in the inter-fascicle matrix (**Figure 5.16, left**) that this model captures the more compliant matrix response in the transverse direction. The large shear response is also evident in the matrix component only (**Figure 5.16, right**), and is not present in the fibril components. While the fibril components do not manifest positive lateral strains, they do demonstrate translation away from the bundle axial mid-line during loading. The overall lateral expansion is thus captured through both the outward translation of the fibrils as well as the expansion of the matrix components.

The unexpected lateral strains can be further discussed by investigating the effect of ‘form-factor’ (the hourglass shape of the AM bundle away from the bones). For the computationally constructed bundle, the width dimension ranges from 5.5 mm at the mid-substance to 7.6 ± 0.2 mm at the femoral and tibial entheses. This form-factor would theoretically allow a maximum transverse strain of 38.1% at the mid-substance. This aligns well with transverse strains seen experimentally, where along a line in the mid-substance the transverse strain was measured to be 36 ± 1.6% using ImageJ (National Institutes of Health, Bethesda, MD). DIC provides more detail on the local response of the tissue, with experimental transverse strains ranging from 7.4% to 56% locally along the same line of the tissue, likely an indication of matrix shear. It is possible the matrix shear contributes to the resulting transverse strains in the computational model, as transversely directed forces are needed to maintain the dimensions of materials undergoing shear loading. However, these transversely directed forces are on the order of the square of the shear strain, and would be close to 1% for the experimentally-seen shear strains on the order of 10%. Thus, the contribution of transversely directed strains arising from the matrix shear is likely to be small compared to the strains possible due to the hourglass form of the tissue in its aligned state.

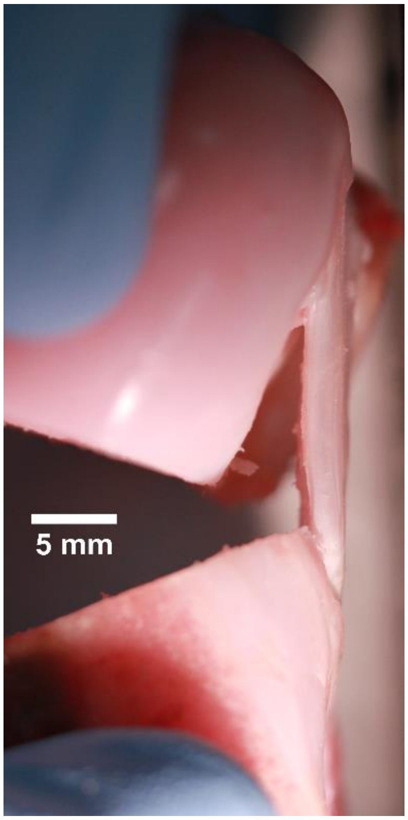

Figure 5.17: Profile view of an AM BLB specimen. The fascicles can be seen extending from femur to tibia, but the through-thickness profile of the femoral and tibial insertions is difficult to ascertain via surface images alone.

Notwithstanding the ability of this model to demonstrate the full-field strain and constitutive AM bundle responses under uniaxial loading, there are several limitations with this work. Regarding contact at the femoral and tibial insertions, an assumption was made on the amount of tissue contacting the femur and tibia. Portions of the femur and tibia were trimmed away (this can be seen in on the tibia in **Figure 5.3, right**). The outline shown in **Figure 5.4** was selected to mimic the outer upper and lower edges of the bundle at the tibia and femur. It is possible that this choice of femoral insertion causes the region of lower strain seen in the axial strain contour (**Figure 5.11, left**). The femoral and tibial insertions of the AM bundle are complex, and the specimen has been oriented to optimize the alignment of the tissue along the axis of loading (**Figure 5.1**). As seen in the profile view of the AM bundle femoral insertion (**Figure 5.17**), while all the fascicles insert into the tissue, the insertion profile through the thickness of the bundle is not straightforward to determine from digital images of the surface alone. It was computationally prohibitive to include matrix between the smaller hierarchical structures in the simulations; in addition, the mechanical properties of the matrix at these length scales are unknown. Due to these constraints, it was hypothesized that the matrix was more compliant than the surrounding fascicles at the macroscale, and modelled as a very compliant matrix by allowing the fibrils on either side to deform independently. That is, in this simulation, gaps were enabled to open up, by assuming that in order to capture the lateral expansion; a very compliant material is needed at the smaller length scales. While good agreement exists between the experimental and numerical contours in this model, these constraints are a limitation of the model. It is possible that the addition of springs between fibrils could be used as a matrix alternative; this would provide controllability of the level of compliance between fibrils. Another alternative method is to tune the compliance of the matrix stiffness—in essence modifying the initial matrix Poisson’s ratio. Smaller Poisson’s ratios could allow lateral expansion without allowing independent fibril expansion. In addition, further insight on the through thickness and through width insertion profiles and fibril behavior response would be useful for FE models.

5.5 Summary

The properties of the individual bundles of the ACL in their native state have been afforded little attention in the literature, and those studies that discuss the AM and PL bundles often focus on graft mechanics. In addition, there is a paucity of full-field strain data reported on the ACL or its bundles. As previously demonstrated in Mallett et al. 2017, the AM bundle has a complex full-field strain response to tensile loading, and unexpected transverse and shear strain responses [40]. Through the inclusion of individual fascicles, fibrils, and matrix, as well as an enveloping matrix sheath, this work demonstrates a similar numerical response as the full-field experimental response, especially the large transverse and shear responses of the bundle in the mid-substance. The MacKintosh model utilized has advantages through the implementation of a microstructurally-based strain energy density function for the fibril constitutive model. The fibrils dominate the longitudinal response of the tissue, and the numerical response provides tangent moduli well in line with experimental data. Models that capture the actual response of soft tissue are crucial to the prediction of the ACL mechanical response within the biomechanics community, and this work serves as an aid in understanding the response of the ACL to diverse loading and injury situations.

5.6 References

[1] J. Yao, J. Snibbe, M. Maloney, A.L. Lerner, Stresses and Strains in the Medial Meniscus of an ACL Deficient Knee under Anterior Loading: A Finite Element Analysis with Image-Based Experimental Validation, J. Biomech. Eng. 128 (2006) 135. doi:10.1115/1.2132373.

[2] D. D D'Lima, P. C Chen, C. W Colwell, Osteochondral grafting: effect of graft alignment, material properties, and articular geometry., Open Orthop. J. 3 (2009) 61–8. doi:10.2174/1874325000903010061.

[3] B. Jones, C.T. Hung, G. Ateshian, Biphasic Analysis of Cartilage Stresses in the Patellofemoral Joint, J. Knee Surg. (2015) 92–98. doi:10.1055/s-0035-1568989.

[4] J.C. Gardiner, J.A. Weiss, Subject-specific finite element analysis of the human medial collateral ligament during valgus knee loading., J. Orthop. Res. 21 (2003) 1098–1106. doi:10.1016/S0736-0266(03)00113-X.

[5] M.A. Baldwin, J.E. Langenderfer, P.J. Rullkoetter, P.J. Laz, Development of subject-specific and statistical shape models of the knee using an efficient segmentation and mesh-morphing approach, Comput. Methods Programs Biomed. 97 (2010) 232–240. doi:10.1016/j.cmpb.2009.07.005.

[6] M.Z. Bendjaballah, A. Shirazi-Adl, D.J. Zukor, Biomechanics of the human knee joint in compression: reconstruction, mesh generation and finite element analysis., Knee. 2 (1995) 69–79.

[7] M.Z. Bendjaballah, A. Shirazi-Adl, D.J. Zukor, Finite element in varus-valgus analysis of human knee joint, Clin. Biomech. 12 (1997) 139–148.

[8] A. Homyk, A.D. Orsi, S. Wibby, N. Yang, H. Nayeb-Hashemi, P.K. Canavan, Failure locus of the anterior cruciate ligament: 3D finite element analysis., Comput. Methods Biomech. Biomed. Engin. 15 (2012) 865–74. doi:10.1080/10255842.2011.565412.

[9] A.M. Kiapour, V. Kaul, A. Kiapour, C.E. Quatman, C. Samuel, T.E. Hewett, C.K. Demetropoulos, V.K. Goel, The Effect of Ligament Modeling Technique on Knee Joint Kinematics: A Finite Element Study, Appl. Math. 4 (2014) 91–97. doi:10.4236/am.2013.45A011.The.

[10] A. Kiapour, A.M. Kiapour, V. Kaul, C.E. Quatman, S.C. Wordeman, T.E. Hewett, C.K. Demetropoulos, F. Grati, Finite element model of the knee for investigation of injury mechanisms: development and validation., J. Biomech. Eng. 136 (2014) 011002. doi:10.1115/1.4025692.

[11] K.E. Moglo, A. Shirazi-Adl, Biomechanics of passive knee joint in drawer: Load transmission in intact and ACL-deficient joints, Knee. 10 (2003) 265–276. doi:10.1016/S0968-0160(02)00135-7.

[12] Y. Wang, Y. Fan, M. Zhang, Comparison of stress on knee cartilage during kneeling and standing using finite element models, Med. Eng. Phys. 36 (2014) 439–447. doi:10.1016/j.medengphy.2014.01.004.

[13] K.-T. Kang, S.-H. Kim, J. Son, Y.H. Lee, H.-J. Chun, In vivo evaluation of the subject-specific finite element model for knee joint cartilage contact area, Int. J. Precis. Eng. Manuf. 16 (2015) 1171–1177. doi:10.1007/s12541-015-0151-9.

[14] G. Li, J. Suggs, T. Gill, The effect of anterior cruciate ligament injury on knee joint function under a simulated muscle load: a three-dimensional computational simulation, Ann. Biomed. Eng. 30 (2002) 713–720. doi:10.1114/1.1484219.

[15] G. Li, J. Gil, A. Kanamori, S.-Y.S.L.-Y.Y. Woo, A validated three-dimensional computational model of a human knee joint., J. Biomech. Eng. 121 (1999) 657–62. doi:10.1115/1.2800871.

[16] A. Vairis, G. Stefanoudakis, M. Petousis, Evaluation of an intact, an ACL-deficient, and a reconstructed human knee joint finite element model, Comput. Methods Biomech. Biomed. Engin. 5842 (2015) 1–8. doi:10.1080/10255842.2015.1015526.

[17] N.A. Ramaniraka, P. Saunier, O. Siegrist, D.P. Pioletti, Biomechanical evaluation of intra-articular and extra-articular procedures in anterior cruciate ligament reconstruction: A finite element analysis, Clin. Biomech. 22 (2007) 336–343. doi:10.1016/j.clinbiomech.2006.10.006.

[18] R. Huang, H. Zheng, Q. Xu, Biomechanical evaluation of different techniques in double bundle anterior cruciate ligament reconstruction using finite element analysis, J. Biomimetics, Biomater. Tissue Eng. 13 (2012) 55–68. doi:10.4028/www.scientific.net/JBBTE.13.55.

[19] E. Peña, B. Calvo, M.A. Martínez, M. Doblaré, A three-dimensional finite element analysis of the combined behavior of ligaments and menisci in the healthy human knee joint, J. Biomech. 39 (2006) 1686–1701. doi:10.1016/j.jbiomech.2005.04.030.

[20] J.Y. Bae, G.H. Kim, J.K. Seon, I. Jeon, Finite element study on the anatomic transtibial technique for single-bundle anterior cruciate ligament reconstruction, Med. Biol. Eng. Comput. 54 (2016) 811–820. doi:10.1007/s11517-015-1372-x.

[21] H.Y. Kim, Y.J. Seo, H.J. Kim, T. Nguyenn, N.S. Shetty, Y.S. Yoo, Tension changes within the bundles of anatomic double-bundle anterior cruciate ligament reconstruction at different knee flexion angles: A study using a 3-dimensional finite element model, Arthrosc. - J. Arthrosc. Relat. Surg. 27 (2011) 1400–1408. doi:10.1016/j.arthro.2011.05.012.

[22] R.W. Westermann, B.R. Wolf, J. Elkins, Optimizing Graft Placement in Anterior Cruciate Ligament Reconstruction: A Finite Element Analysis., J. Knee Surg. (2016). doi:10.1055/s-0036-1581137.

[23] Y. Song, R.E. Debski, V. Musahl, M. Thomas, S.L.Y. Woo, A three-dimensional finite element model of the human anterior cruciate ligament: A computational analysis with experimental validation, J. Biomech. 37 (2004) 383–390. doi:10.1016/S0021-9290(03)00261-6.

[24] R.S. Marlow, A general first-invariant hyperelastic constitutive model, in: Const. Model. Rubber III, 2003: pp. 157–160.

[25] A.C. Abraham, J.T. Moyer, D.F. Villegas, G.M. Odegard, T.L. Haut Donahue, Hyperelastic properties of human meniscal attachments, J. Biomech. 44 (2011) 413–418. doi:10.1016/j.jbiomech.2010.10.001.

[26] J.A. Weiss, J.C. Gardiner, B.J. Ellis, T.J. Lujan, N.S. Phatak, Three-dimensional finite element modeling of ligaments: Technical aspects, Med. Eng. Phys. 27 (2005) 845–861. doi:10.1016/j.medengphy.2005.05.006.

[27] D.R. Nolan, A.L. Gower, M. Destrade, R.W. Ogden, J.P. McGarry, A robust anisotropic hyperelastic formulation for the modelling of soft tissue, J. Mech. Behav. Biomed. Mater. 39 (2014) 48–60. doi:10.1016/j.jmbbm.2014.06.016.

[28] S.A. Maas, B.J. Ellis, D.S. Rawlins, J.A. Weiss, Finite element simulation of

articular contact mechanics with quadratic tetrahedral elements, J. Biomech. 49 (2016) 659–667. doi:10.1016/j.jbiomech.2016.01.024.

[29] D. Ren, Y. Liu, X. Zhang, Z. Song, J. Lu, P. Wang, The evaluation of the role of medial collateral ligament maintaining knee stability by a finite element analysis, J. Orthop. Surg. Res. 12 (2017) 64. doi:10.1186/s13018-017-0566-3.

[30] C. Wan, Z. Hao, S. Wen, A review on research on development of ligament constitutive relations on macro, meso, and micro levels, Acta Mech. Solida Sin. 26 (2013) 331–343. doi:10.1016/S0894-9166(13)60030-0.

[31] G. Limbert, J. Middleton, M. Taylor, Finite element analysis of the human ACL subjected to passive anterior tibial loads, Comput. Methods Biomech. Biomed. Engin. 7 (2004) 1–8. http://www.ncbi.nlm.nih.gov/entrez/query.fcgi?cmd=Retrieve&db=PubMed&dopt=Citation&list_uids=14965874.

[32] S. Hirokawa, R. Tsuruno, Three-dimensional deformation and stress distribution in an analytical/computational model of the anterior cruciate ligament, J. Biomech. 33 (2000) 1069–1077. http://www.sciencedirect.com/science/article/B6T82-40GHY88-4/2/8faf6c6a33fd77ff12a73e02387abd80.

[33] X. Zhang, G. Jiang, C. Wu, S.-Y.S.L.-Y.Y. Woo, A subject-specific finite element model of the anterior cruciate ligament., Conf. Proc. IEEE Eng. Med. Biol. Soc. 2008 (2008) 891–894. doi:10.1109/IEMBS.2008.4649297.

[34] A.D. Orsi, S. Chakravarthy, P.K. Canavan, E. Peña, R. Goebel, A. Vaziri, H. Nayeb-Hashemi, The effects of knee joint kinematics on anterior cruciate ligament injury and articular cartilage damage., Comput. Methods Biomech. Biomed. Engin. 5842 (2015) 1–14. doi:10.1080/10255842.2015.1043626.

[35] G. Limbert, M. Taylor, J. Middleton, Three-dimensional finite element modelling of the human ACL: simulation of passive knee flexion with a stressed and stress-free ACL., J. Biomech. 37 (2004) 1723–31. doi:10.1016/j.jbiomech.2004.01.030.

[36] D.L. Butler, M.Y. Sheh, D.C. Stouffer, V. a Samaranayake, M.S. Levy, Surface strain variation in human patellar tendon and knee cruciate ligaments., J. Biomech. Eng. 112 (1990) 38–45. http://www.ncbi.nlm.nih.gov/pubmed/2308302.

[37] D.L. Butler, M.D. Kay, D.C. Stouffer, Comparison of Material Properties in Fascicle-Bone Units from Human Patellar Tendon and Knee Ligaments, J. Biomech. 19 (1986) 435–432.

[38] K.M. Quapp, J.A. Weiss, Material Characterization of Human Medial Collateral Ligament, 120 (1998) 757–763.

[39] C. Bonifasi-Lista, S.P. Lake, M.S. Small, J.A. Weiss, Viscoelastic properties of the human medial collateral ligament under longitudinal, transverse and shear loading., J. Orthop. Res. 23 (2005) 67–76. doi:10.1016/j.orthres.2004.06.002.

[40] K.F. Mallett, E.M. Arruda, Digital image correlation-aided mechanical characterization of the anteromedial and posterolateral bundles of the anterior cruciate ligament, Acta Biomater. (2017). doi:10.1016/j.actbio.2017.03.045.

[41] J.S. Palmer, M.C. Boyce, Constitutive modeling of the stress-strain behavior of F-actin filament networks., Acta Biomater. 4 (2008) 597–612. doi:10.1016/j.actbio.2007.12.007.

[42] J.E. Bischoff, E.M. Arruda, K. Grosh, Orthotropic hyperelasticity in terms of an arbitrary molecular chain model, J. Appl. Mech. 69 (2002) 198–201.

[43] E. Kuhl, K. Garikipati, E.M. Arruda, K. Grosh, Remodeling of biological tissue: Mechanically induced reorientation of a transversely isotropic chain network, J. Mech. Phys. Solids. 53 (2005) 1552–1573. doi:10.1016/j.jmps.2005.03.002.

[44] E.M. Arruda, M.C. Boyce, A three-dimensional constitutive model for the large stretch behavior of rubber elastic materials, J. Mech. Phys. Solids. 41 (1993) 389–412. doi:10.1016/0022-5096(93)90013-6.

[45] D.L. Butler, Y. Guan, M.D. Kay, J.F. Cummings, S.M. Feder, M.S. Levy, Location-dependent variations in the material properties of the anterior cruciate ligament, J. Biomech. 25 (1992) 511–8. http://www.ncbi.nlm.nih.gov/pubmed/1592856.

Chapter 6: Conclusions and Future Work

6.1 Conclusions

The ACL is the most commonly injured soft tissue in the knee, and there is a pressing need to understand its intrinsic mechanical properties to provide insight into tissue failure mechanisms. **Chapter 1** provided an outline of the challenges facing ACL research, including the role of the ACL in various knee motions, ACL mechanics and comparisons with common replacement grafts, the use of animal models for ACL research, and ACL computational models. The ACL is an extremely complex soft tissue, and challenges have faced researchers in quantifying the mechanical properties of the ACL as a whole in well-understood loading states. In addition, there is a dearth of information on the full-field response of the ACL, leading to lack of understanding on its complete response, even in well-understood loading states. **Chapter 2** of this work developed a method for patterning soft biological tissue to aid in applying DIC to testing of soft biological tissue. This pattern technique utilizes a biologically friendly, removable patterning medium that allows for tissue hydration without loss of pattern integrity, and the patterning method produces patterns with controlled density and individual speckle size. This pattern design and fabrication technique provides enhanced DIC patterns for correlation of soft tissue surface strains.

The experimental characterization was achieved by studying the two ACL bundles independently in a well-known loading state, and the ACL as a whole under physiologically relevant loading conditions. **Chapters 3** and **4** quantified the material response of the individual and aligned AM and PL bundles using DIC. The tissue-level surface strains demonstrate that both bundles are stiffer than previously reported grip-to-grip methods. In addition, the AM bundle is stiffer than the PL bundle manifesting tangent moduli of 1.04±0.24 GPa for DIC compared to 284.0±80.1 MPa for the PL bundle (at 3% nominal strain) (AM data from [1]). Both bundles demonstrated unexpected transverse behavior to longitudinal loading, with the AM bundle demonstrating up to 55% lateral strain and the PL demonstrating undulation, as individual fascicles moved into or out of the camera’s plane of view during loading. Few if any previous studies have discussed the full-field strain response of the AM and PL bundles of the ACL; this dissertation provides insight into the complexity of the ACL response. Finally, computational finite element frameworks are valuable tools to investigate the response of soft biological tissue under diverse loading conditions, especially those difficult to achieve in a laboratory. However these models depend on accurate constitutive laws, and must be able to capture the full response of the material. The computational model of the AM bundle developed in **Chapter 5** has the geometric complexity to capture the off-axis response of the bundle in uniaxial tension as well as the appropriate constitutive model to capture the longitudinal material response.

While this dissertation addresses several gaps in the field regarding experimental characterization and computational modeling of the ACL, there are several remaining questions of note for future work. The rest of this chapter is dedicated to discussing areas of study that would provide useful information to the biomechanics community.

6.2 Relative strain for *in vivo* investigations

The definition of a reference state for strain measurements is of importance in the performance and analysis of materials tests. This is especially true for *in vivo* tests of biological specimens, where the orientation of the tissue under investigation as well as the presence of other biological structures and muscle forces all contribute to a complex strain state. A distinction should be made between tensile testing of bone-ligament-bone (BLB) specimens and in *in vivo* experiments; for tensile loading the

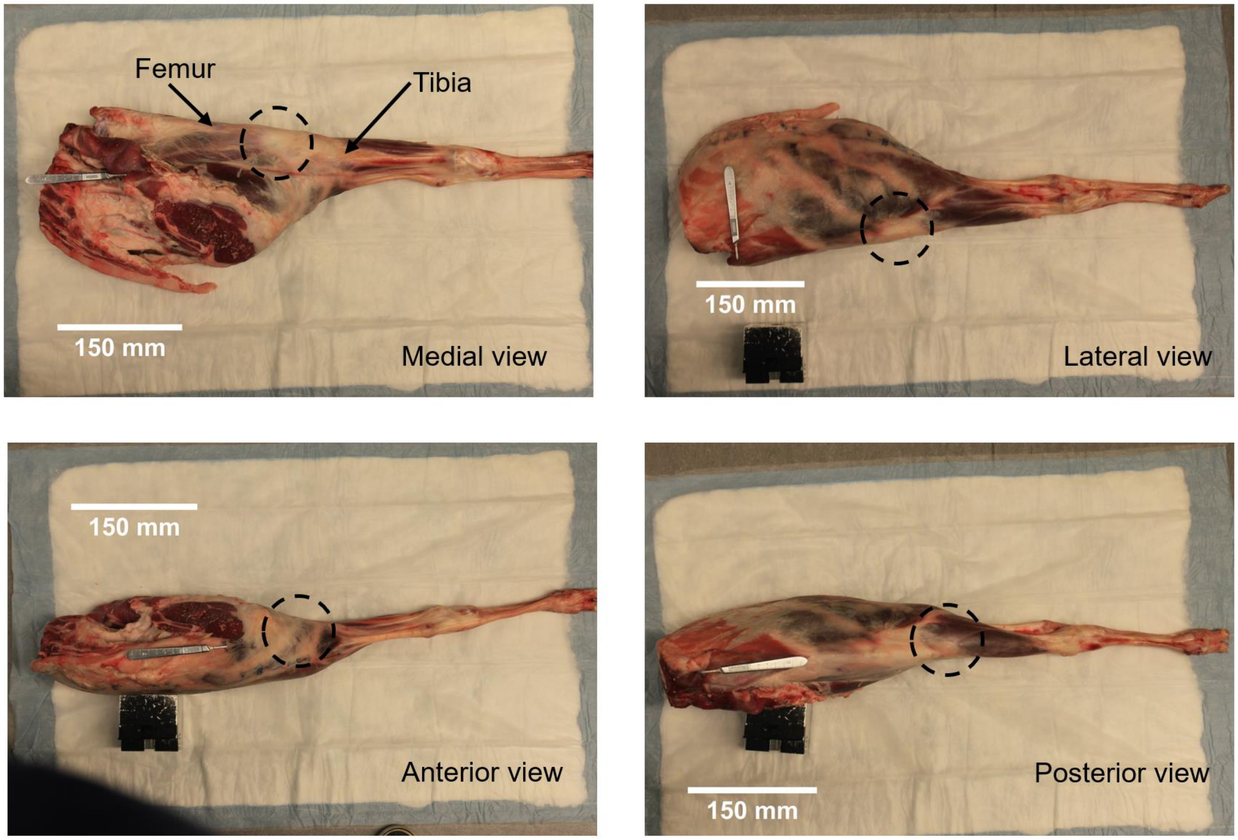

Figure 6.1: Medial, lateral, anterior and posterior views of the ovine knee as-received from a local butcher. The dashed line indicates the location of the knee joint.

location of zero strain is commonly determined to be the point at which the specimen registers load (often after the application of a minimal tare load) [2]. However, the complex *in vivo* state, especially the twist of the ACL in its native state, makes clear determination of a reference state difficult [2–4].

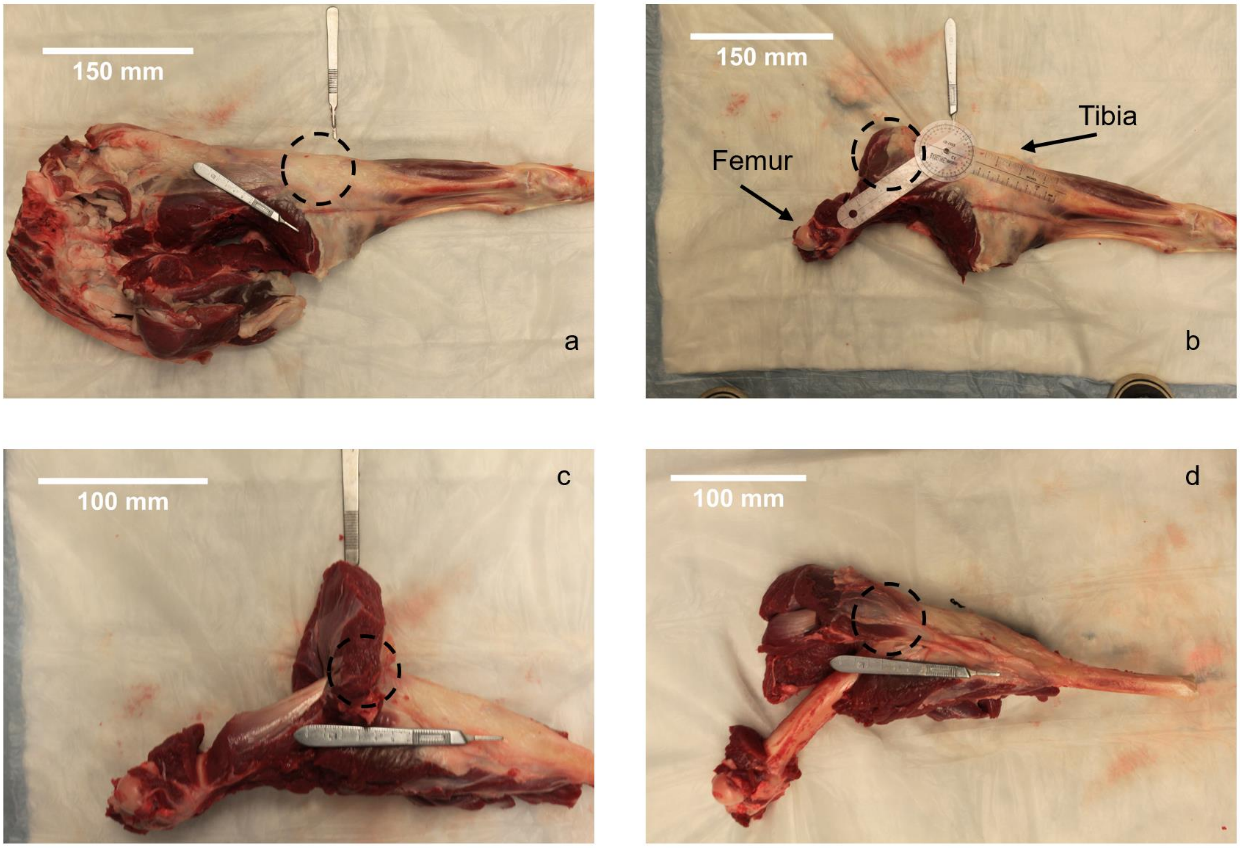

Figure 6.2: Dissection of knee to visualize ACL. a) Transection of the muscle groups on the posterior aspect of the femur. b) Removal of hip joint and transection of femoral anterior muscle groups. c) Removal of quadriceps connected to patellar tendon. d) Complete removal of anterior and posterior muscle groups at the femur. This is required for flexion of the knee joint (prior to this the knee is relatively rigid at 10° of flexion.

Often, studies have sought to clearly indicate the choice of a relative strain state for ACL testing. [5–14]. This relative strain state can be defined as the change in length of the displacement transducer applied to the surface of the material [5]. An

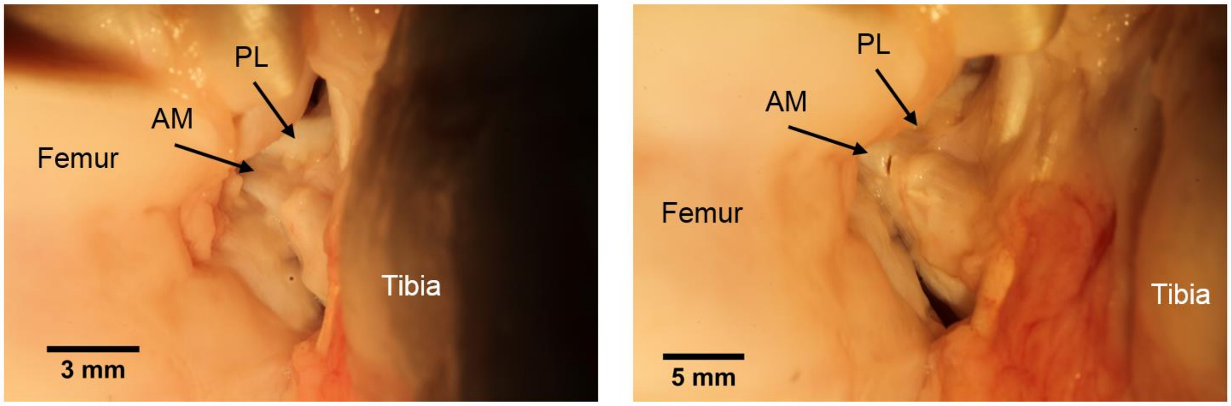

Figure 6.3: Intact ACL rigidly fixed in the gravity-free plane. The distal portions of the AM and PL are visible near the tibial insertion. Right: After incising the AM with blade of rectangular geometry, a cavity develops, with dimensions 1.246 ± 0.034 mm x 0.048 ± 0.030 mm.

investigation was made into a method for determining the relative strain state of the *in vivo* ACL. Tests were conducted on as-received knees (**Figure 6.1**) that initially contained the hip, knee and ankle joints (dashed black line indicates the location of the knee). In the as-received state, knees had a flexion angle of 10°. Dissection was performed by first transecting the muscle groups on the posterior aspect of the femur, with care taken not to sever the connections close to the knee joint (**Figure 6.2a**). The muscle groups on the anterior aspect of the femur were then removed, with care again taken to preserve the muscles directly connected to the knee joint capsule (**Figure 6.2b**). The quadriceps was then removed (**Figure 6.2c**). In one knee, it was observed that at this point of the dissection process, the knee manifested an inability to flex, and remained stiffly at 10°. It was necessary to completely sever both the anterior and posterior muscle groups from the femur, as shown in **Figure 6.2d**, in order to permit the knee to flex beyond 10°. After removal of these muscle groups, the knee was easily maneuverable. In order to visualize the ACL, further dissection was required. The joint capsule was transected from the proximal aspect femoral head to the tibia. As seen in **Figure 6.3 (left)**, the femoral condyles and patella are visible after transection of the

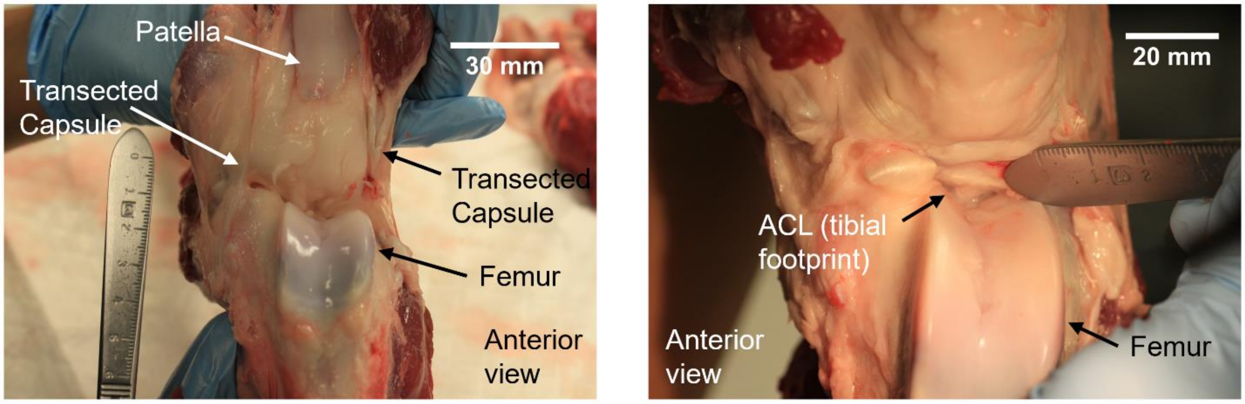

Figure 6.4: Anterior view of the knee joint after transection of the joint capsule. The anterior aspect of the joint capsule, containing the patella (**left**) must be pulled back in order to visualize the ACL (**right**).

joint capsule. Further dissection was required to remove the fatty tissue present in the joint, and after this tissue removal the tibial footprint of the ACL can be visualized in **Figure 6.3 (right)**. After all dissection, only the tibial portion of the ACL was visible, and of that, mostly the AM bundle, and all tests were performed on the visible portion of the tissue.

Two tests were performed, one on a knee fixed in the gravity-free plane (held on a flat surface), and the other in a custom load frame designed for testing of intact whole knee specimens. Both knees were arranged at 30° of knee flexion. Both knees were incised with a blade of rectangular geometry and dimensions 2.11 ± 0.01 mm x 0.50 ± 0.01 mm (gravity-free plane knee) and 2.58 ± 0.01 mm x 0.58 ± 0.01 mm (load frame knee). In the gravity-free plane knee, it was possible to incise both the AM and PL independently, and a cavity was seen to develop in the AM bundle, with dimensions 1.246 ± 0.034 mm x 0.048 ± 0.030 mm (**Figure 6.4, right**). The PL bundle did not demonstrate any visible cavity after incision in the gravity-free plane knee. For the load-frame knee, only the AM bundle was visible, and it was marked with a marker as far as

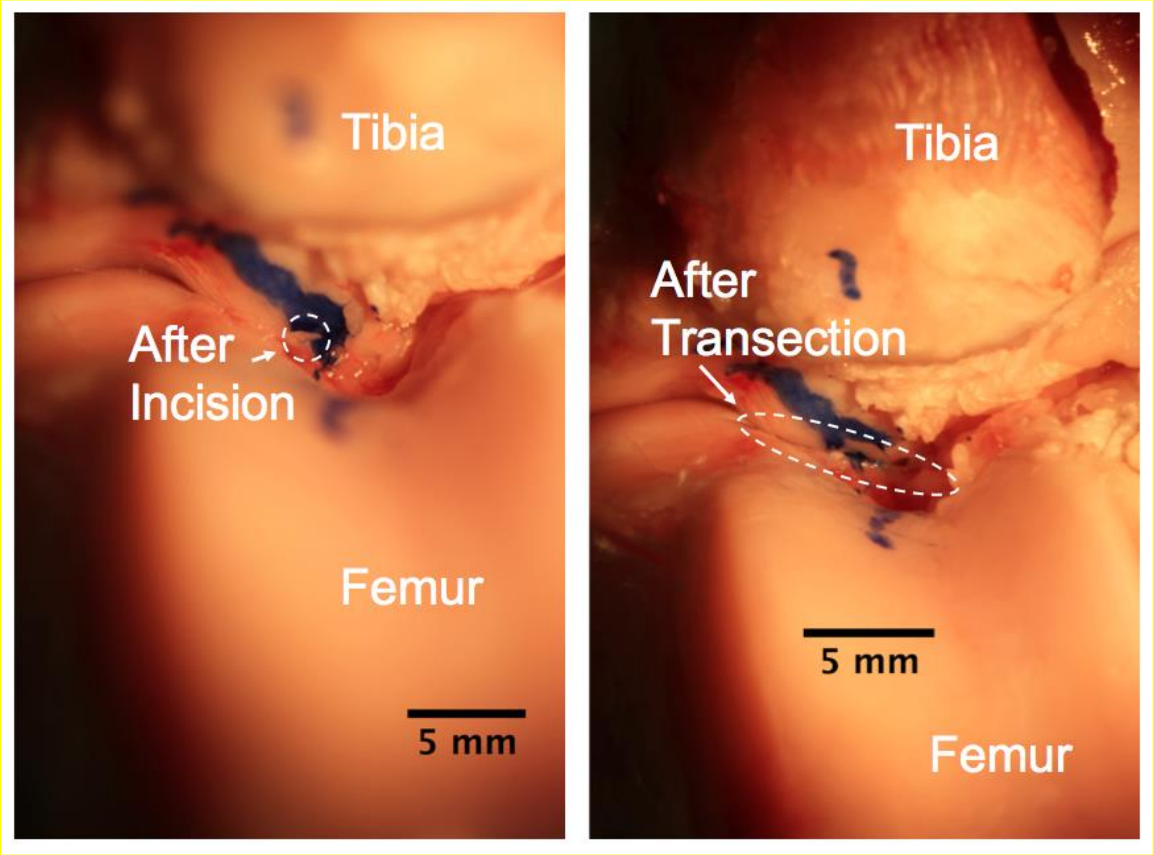

Figure 6.5: Left: ACL rigidly fixed at **30° within a custom load frame.** The distal portion of the AM is visible near the tibial insertion. After incising the AM with blade of rectangular geometry, no cavity was seen to develop, although some of the marker ink came off with the removal of the scalpel blade after incision. Right: After transection, no visible movement of the ACL was detected.

was accessible. The AM bundle was incised with the rectangular blade; the PL was not incised, as it could not be seen. After incision of the AM bundle, the entire ligament was transected completely, as the distinction between the AM and PL could not be visualized. **Figure 6.5** shows the tissue after incision and transection. After incising the AM bundle, no cavity was seen to develop, although some of the marker ink came off after removing the scalpel blade, indicating the location of the incision. After transection, no motion was seen in the tissue.

Several complications existed for this study, rendering conclusions difficult to ascertain. There was a need to remove the anterior portion of the knee capsule in order to visualize the ACL. Although the custom load-frame utilized for testing was capable of applying muscle forces and body weights for human knee studies, it was not possible to arrange the knee at 30° of knee flexion with the application of those muscle forces and body weights. Initially, it was attempted to apply the quadriceps force at an alternate location at the tibia through a split nylon strap. However, during the dissection process, the strap prevented access to the anterior portion of the capsule had to be removed in order to continue dissection. It was not possible to apply the quadriceps muscle forces or body weight and maintain access to the anterior portion of the joint capsule. In addition, without the muscle forces and body weight, the knee was able to move during dissection. It was observed that after removal of the medial meniscus, the femur and tibia were impinging on each other. Further removal of the bones (i.e. to visualize the entire length of the ACL) would likely detrimentally allow changes in the orientation of the ACL. The lack of muscle forces and body weight and possible unavoidable motion of the knee joint during dissection renders the results for the load frame knee inconclusive.

This experimental investigation points to the challenges facing researchers in biomechanically testing the ACL, especially in visualizing such an embedded structure while maintaining simulated muscle forces and body weights. However, *in vivo* tests of living patients offer a solution in the determination of the existence of a reference location of the ACL. Howe et al. 1990 [4] investigated the determination of a zero ACL strain state *in vivo* while preserving the ligament, other joint structures and muscle activity. In this study, several clinically relevant motions, including anterior and posterior tibial translation, were prescribed for 5 patients (aged 18-40). A displacement transducer was implanted on the intact ACL *in vivo*, and a force plate was attached to the tibia to measure the loads generated during motion. With this method, the authors were able to identify a reference length at which the ACL became initially load-bearing. Below this reference length the ACL was palpably and visually slack, and above this reference length the tissue was taut or load-bearing. This study develops a methodology to provide a reference length for *in vivo* strain calculations. Future studies should endeavor to clearly indicate the state of loading and the distinctions between loading states tested under laboratory conditions and those that occur *in vivo*.

6.3 Computational reorientation of ACL bundles

There is a gap in the biomechanics community between mechanical tests and clinically relevant tests. Mechanical tests are required to obtain material properties and as foundations for computational

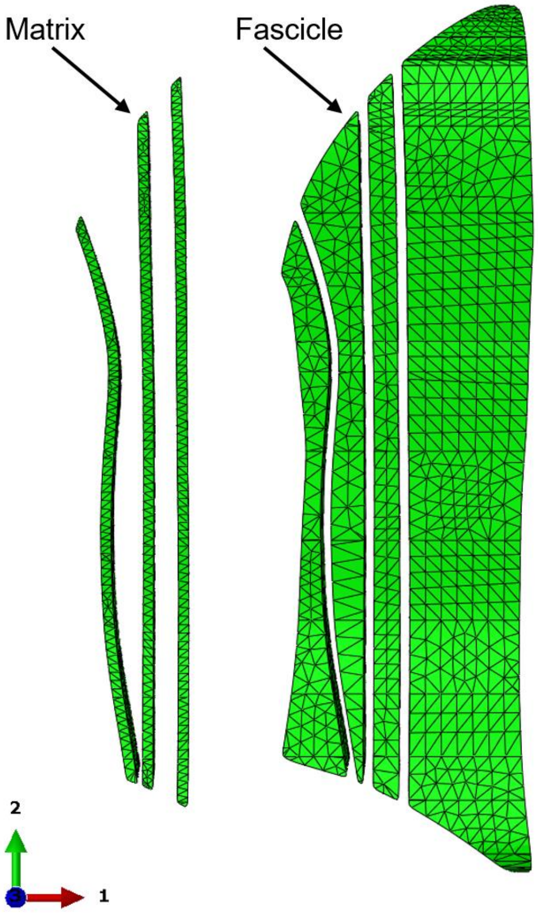

Figure 6.6: Matrix and fascicle components of PL FE bundle.

models. However, the direct applicability of mechanically motivated experiments is difficult to determine, with load and displacement data from whole knee tests more amenable to many physiologically-relevant situations. In this work, tests in well-understood loading states were performed on both the AM and PL bundles, and these tests have given insight into the material properties needed for experimental characterization and computational modeling. ATT tests have also been performed in this work, providing insight into the full-field strain response of the ACL in a complex loading state familiar to clinicians. A next step is to tie the information in these two states together, by computationally twisting the AM bundle discussed in **Chapter 5** to the configuration it would have in the native knee. This would require a FE model of the PL bundle that is able to capture the complexity of the tissue response. **Figure 6.6** shows the components of a representative PL bundle. This bundle has been sectioned in the same manner as the AM FE model discussed in **Chapter 5**, with matrix separated fascicles. The full PL BLB assembly is shown in **Figure 6.7**. These components were made from front and profile digital images of the PL bundle. However, the PL

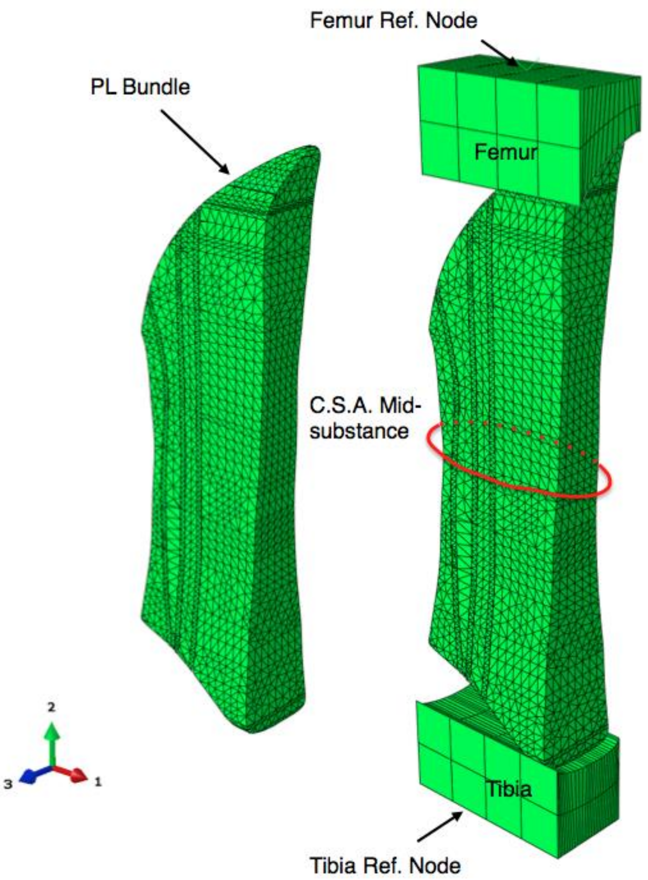

Figure 6.7: FE assembly of PL BLB specimen.

demonstrates a large variation in it surface profile (as seen in **Figure 4.1**) with fibrils appearing and disappearing from view along the bundle's length. It is difficult to identify the 3D positions of individual fibrils from images of the surface only. However, through-volume visualizations and measurements of the aligned bundle are an option that can offer the insight to create FE soft-tissue models with the necessary complexity to capture experimental behavior. The reorientation of the FE bundles in a whole knee model would require knowledge of the rotations and translations undergone by the bundles of the ACL in order to align them for tensile testing. This is not simple to achieve, as both bundles exhibit twist and extend from the posterolateral aspect of the femur to the anteromedial aspect of the femur, requiring translations of the bones to achieve alignment.

In the process of this dissertation, the author mentored an undergraduate who designed and built an apparatus to hold the knee in its anatomic state for baseline measurements, and then methodically translate and rotate the femur and tibia to achieve alignment of the AM and PL bundles. Preliminary analysis of the results has shown that, in addition to translation of the femur and tibia to align both bundle insertions, the PL requires an untwist of the femur in external rotation of 81 ± 23° (n=5). This twist is about its own longitudinal axis. The AM bundle also requires translations to align its femoral and tibial insertion. However, an added complexity for the AM is that it twists around the PL, and requires an external rotation (86 ± 8°, n=4) of the femur, as well as flexion of the tibia and rotations of the femur and tibia in their respective coronal planes to remove the twist and align the bundle. This information is critical for computationally twisting and aligning the AM bundle in its native state. Once this transformation is performed in a computational model, the experimentally characterized AM bundle can be used as a tool to simulate a variety of loading conditions, especially those prohibitive due to cost and/or time in a laboratory setting. As a final validation, the ATT experimental data performed in this work will be useful to validate the twisted bundle and provide insight to clinicians on the strain response and failure mechanisms of the ACL.

6.4 References

[1] K.F. Mallett, E.M. Arruda, Digital Image Correlation-Aided Mechanical Characterization of the Anteromedial and Posterolateral Bundles of the Anterior Cruciate Ligament, Acta Biomater. (2017).

[2] B.C. Fleming, B.D. Beynnon, H. Tohyama, R.J. Johnson, C.E. Nichols, P.A. Renstrom, M.H. Pope, Determination of a zero strain reference for the anteromedial band of the anterior cruciate ligament, J. Orthop. Res. 12 (1994) 789–795.

[3] B.D. Beynnon, J.G. Howe, M.H. Pope, R.J. Johnson, B.C. Fleming, The measurement of anterior cruciate ligament strain in vivo, Int Orthop. 16 (1992) 1–12.

[4] J.G. Howe, C. Wertheimer, R.J. Johnson, C.E. Nichols, M.H. Pope, B.D. Beynnon, Arthroscopic strain gauge measurement of the normal anterior cruciate ligament, Arthroscopy. 6 (1990) 198–204.

[5] T.J. Withrow, L.J. Huston, E.M. Wojtys, J.A. Ashton-Miller, The effect of an impulsive knee valgus moment on in vitro relative ACL strain during a simulated jump landing., Clin. Biomech. (Bristol, Avon). 21 (2006) 977–83. doi:10.1016/j.clinbiomech.2006.05.001.

[6] T.J. Withrow, L.J. Huston, E.M. Wojtys, J.A. Ashton-Miller, The relationship between quadriceps muscle force, knee flexion, and anterior cruciate ligament strain in an in vitro simulated jump landing, Am. J. Sports Med. 34 (2006) 269–274. doi:0363546505280906 [pii]10.1177/0363546505280906.

[7] T.J. Withrow, L.J. Huston, E.M. Wojtys, J.A. Ashton-Miller, Effect of varying hamstring tension on anterior cruciate ligament strain during in vitro impulsive knee flexion and compression loading, J. Bone Joint Surg. Am. 90 (2008) 815–823. doi:90/4/815 [pii]10.2106/JBJS.F.01352.

[8] Y.K. Oh, J.L. Kreinbrink, J.A. Ashton-Miller, E.M. Wojtys, Effect of ACL transection on internal tibial rotation in an in vitro simulated pivot landing, J. Bone Joint Surg. Am. 93 (2011) 372–380. doi:93/4/372 [pii] 10.2106/JBJS.J.00262.

[9] S.G. McLean, Y.K. Oh, M.L. Palmer, S.M. Lucey, D.G. Lucarelli, J.A. Ashton-Miller, E.M. Wojtys, The relationship between anterior tibial acceleration, tibial slope, and ACL strain during a simulated jump landing task, J. Bone Joint Surg. Am. 93 (2011) 1310–1317. doi:10.2106/JBJS.J.00259.

[10] Y.K. Oh, J.L. Kreinbrink, E.M. Wojtys, J.A. Ashton-Miller, Effect of axial tibial torque direction on ACL relative strain and strain rate in an in vitro simulated pivot landing, J. Orthop. Res. 30 (2012) 528–534. doi:10.1002/jor.21572.

[11] D.B. Lipps, Y.K. Oh, J.A. Ashton-Miller, E.M. Wojtys, Morphologic characteristics help explain the gender difference in peak anterior cruciate ligament strain during a simulated pivot landing., Am. J. Sports Med. 40 (2012) 32–40. doi:10.1177/0363546511422325.

[12] Y.K. Oh, D.B. Lipps, J.A. Ashton-Miller, E.M. Wojtys, What strains the anterior cruciate ligament during a pivot landing?, Am. J. Sports Med. 40 (2012) 574–83. doi:10.1177/0363546511432544.

[13] D.B. Lipps, E.M. Wojtys, J.A. Ashton-Miller, Anterior cruciate ligament fatigue failures in knees subjected to repeated simulated pivot landings., Am. J. Sports Med. 41 (2013) 1058–66. doi:10.1177/0363546513477836.

[14] M.L. Beaulieu, Y.K. Oh, a. Bedi, J. a. Ashton-Miller, E.M. Wojtys, Does Limited Internal Femoral Rotation Increase Peak Anterior Cruciate Ligament Strain During a Simulated Pivot Landing?, Am. J. Sports Med. 42 (2014) 2955–2963. doi:10.1177/0363546514549446.

Appendix A: Supplementary Information

A volumetric analysis was performed on bundles from the experimental study described in **Chapter 3** and **Chapter 4**. Eleven bundles (6 AM, 5 PL) were selected for the volume analysis, and ten image pairs of the front and profile images were selected for analysis of the bundle volume change during loading. Digital images of the front and profile views of the bundles were acquired with Fastcam SA1.1 cameras (resolution 0.049 ± 0.003 mm, n=11, Photron USA, Inc., San Diego, CA) and a Grasshopper Gras-50SM-C camera (resolution 0.034 ± 0.004 mm, n=11, Point Grey Research Inc., Richmond, BC, Canada).

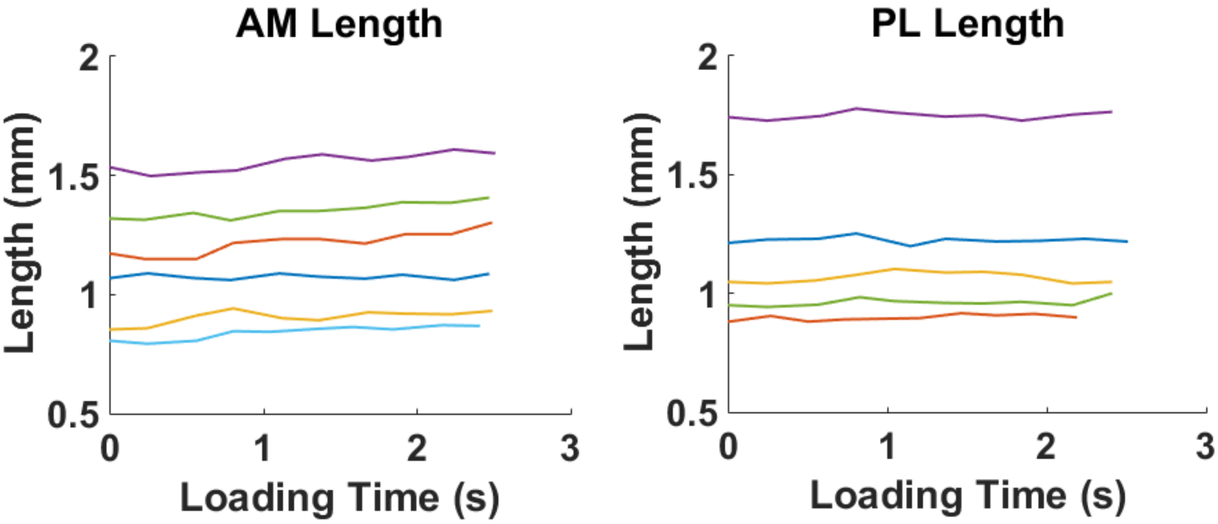

Figure A.1: AM and PL measured length during loading (to ~12% grip-to-grip nominal strain). The length dimension is aligned with the direction of loading.

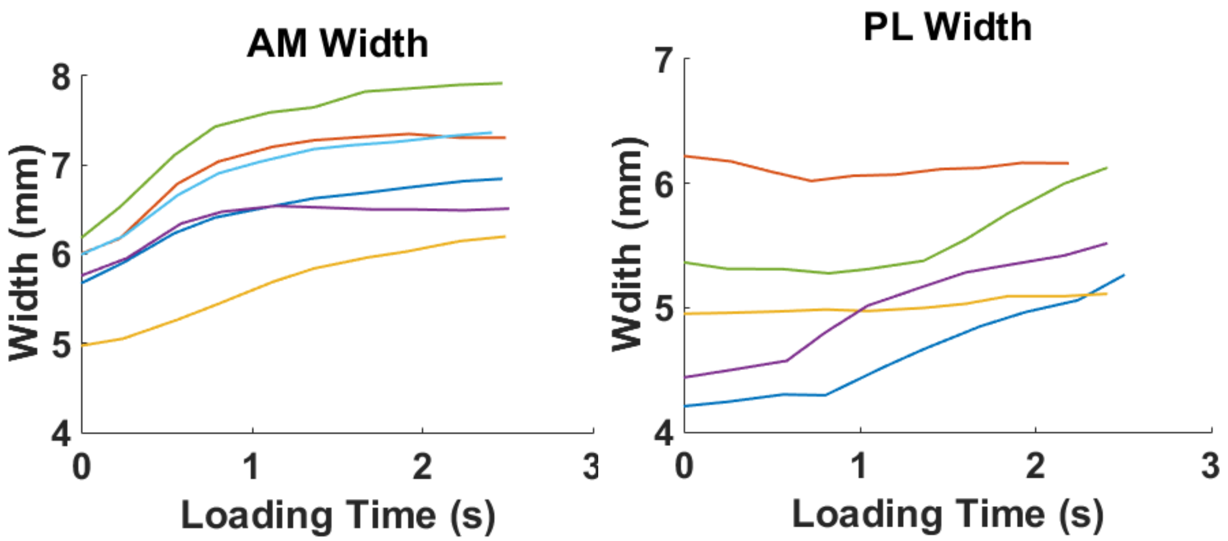

Figure A.2: AM and PL measured width during loading (to ~12% grip-to-grip nominal strain). The width dimension is transverse to the direction of loading.

Within ImageJ (National Institutes of Health, Bethesda, MD), the same region of the tissue visible in both front and profile views was selected for measurement of the length, width, and thickness. The length is the dimension along the direction of loading, the width is the dimension transverse to the direction of loading (and in the plane of view of the Fastcam cameras). The thickness is transverse to the direction of loading,

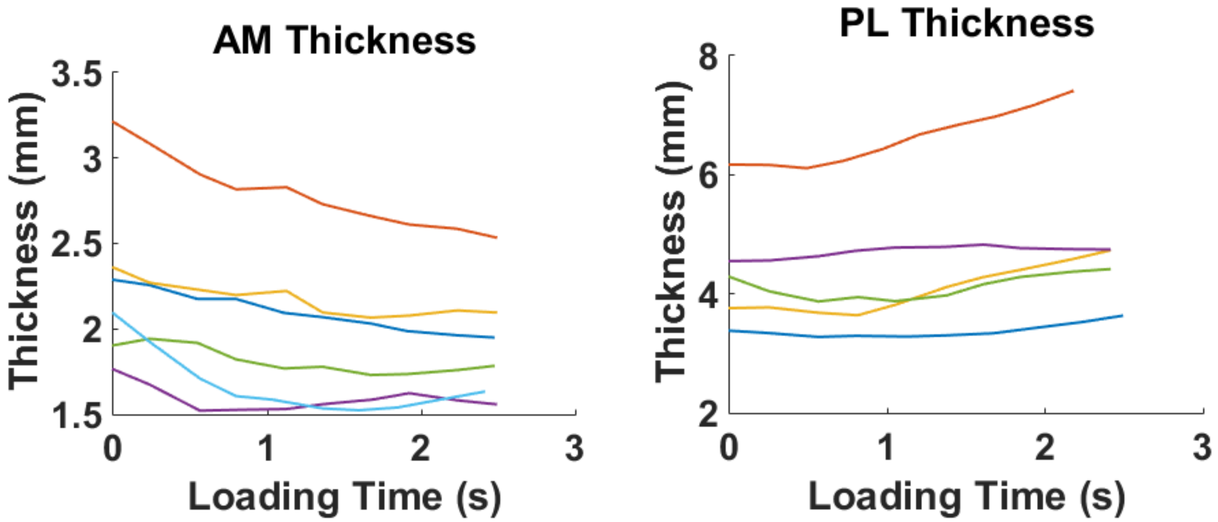

Figure A.3: AM and PL measured thickness during loading (to ~12% grip-to-grip nominal strain). The thickness dimension is transverse to the direction of loading.

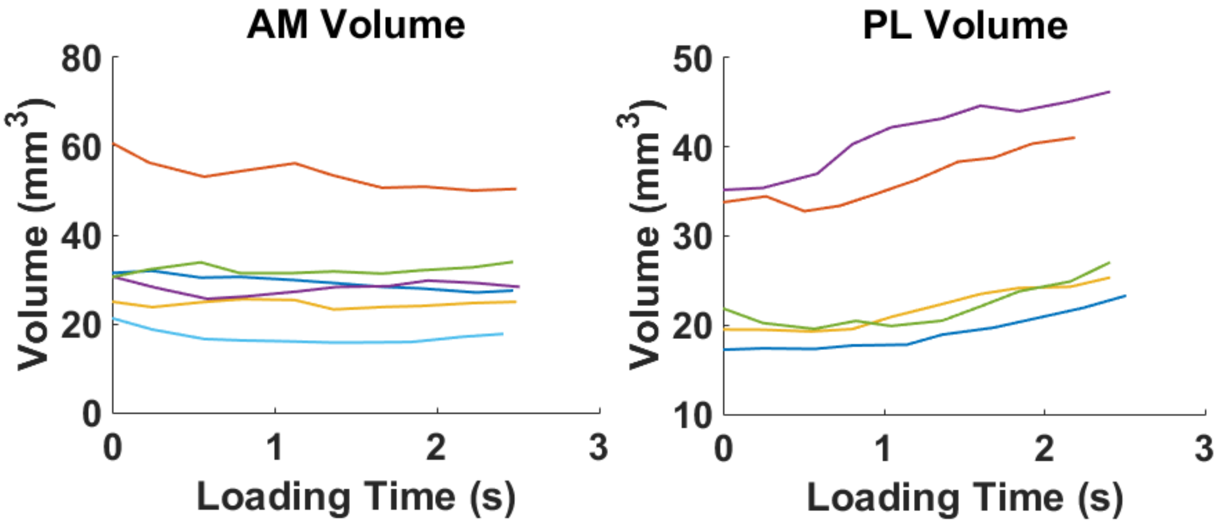

Figure A.4: Volume of AM and PL bundles during loading

and into the page from the Fastcam camera's point of view and in the page from the perspective of the Grasshopper camera (see **Figure 3.2 b, c** and **d** for representative front and profile views). 10 image pairs were selected at evenly spaced points during the loading time, and the length, width and thickness of the bundles measured in these image pairs. Each length, width and thickness measurement was made three times to account for operator error. The length and width were measured from the front image, and the thickness from the profile image.

Figures A.1, **A.2** and **A.3** show the dimensional data of the AM and PL bundles during loading. Both bundles demonstrate and increase in length, however the AM width markedly increases, while the PL does not demonstrate a consistent pattern of expansion or contraction in the width dimension. The AM data demonstrate a reduction in thickness for the majority of the bundles, while the PL demonstrates an increase in thickness for most bundles.

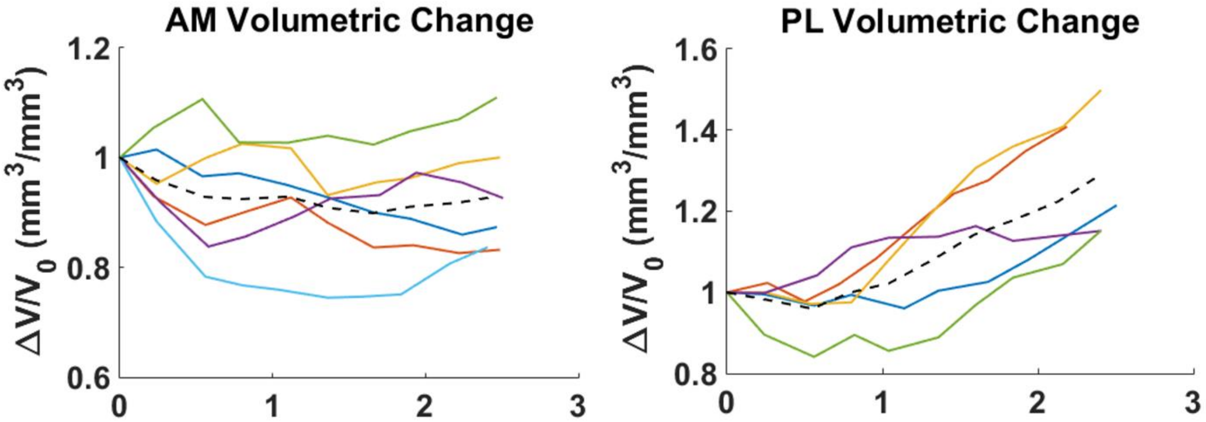

Figure A.5: Volumetric change of AM and PL bundles.

The volume for the AM was calculated by multiplying the measured tissue length by the assumed cross-sectional area (CSA) of the mid-substance (as discussed in **Chapter 3**). The AM was assumed to have a rectangular cross-section with rounded semi-circular edges, and the PL CSA was assumed to be rectangular. The bundle volume during loading is shown in **Figure A.4**, and volumetric change shown in **Figure A.5**. The AM demonstrated a slight reduction in volume, demonstrating a peak volumetric change of 0.99 ± 0.06 mm^3/mm^3. This indicates that while the bundles see large lateral expansion, the overall bundle volume does not expand. A reduction in volume is not expected for materials with positive Poisson’s ratios undergoing uniaxial tension. However, the measured amount of volumetric decrease lies within the uncertainty of the experimental measurement, thus it is not possible to ascertain for certain if the bundle is manifesting a decrease in volume.

The PL demonstrates marked increase in volume and volumetric change for all bundles, with a mean peak volumetric change of 1.28 ± 0.00 mm^3/mm^3. One reason for this marked increase could be due to the assumption of a rectangular cross-section for the PL bundle. The PL demonstrates a significant variation in its surface throughout the bundle, making determination of its cross-sectional area profile difficult. It is possible that this lack of initial fibril alignment contributes to the manifested volume expansion. It is also possible that the lateral expansion of individual fibrils (see **Figure 4.1**) away from each other contributes to this volume expansion. **Table A.1** summarizes the peak dimension measurements, and volume and volumetric change calculations for the AM and PL bundles investigated.

Table A.1: Peak AM and PL dimension measurements, volume, and volumetric change.

Bundle	**Average Peak Length (mm)**	**Average Peak Width (mm)**	**Average Peak Thickness (mm)**	**Average Peak Volume (mm^3)**	**Average Peak Volumetric Change (mm^3/mm^3)**	**Average Peak Axial Strain (mm/mm)**
AM (n=6)	1.20 ± 0.69	7.02 ± 2.41	0.86 ± 0.37	30.45 ± 1.25	0.99 ± 0.06	0.07 ± 0.00
PL (n=5)	1.19 ± 0.67	5.63 ± 1.75	4.98 ± 1.673	32.55 ± 0.06	1.28 ± 0.00	0.02 ± 0.00

Table A.2: Dissertation Project Repository

Project Location	Project Filename	Project Description
Google Drive\Mallett_Kaitlyn_Repository\Stencil_Generation_Patterning_Project	Stencil_Generation_Patterning_Project	Data files of measurements of individual, paired and pattern speckle files (digital images from Olympus microscope) as discussed in **Chapter 2**
Google Drive\Mallett_Kaitlyn_Repository\AM_PL_Experimental_Data	AM_PL_Experimental_Data	Experimental data (digital images, MTS load/displacement .txt files) and analysis files (Matlab .m (codes) and .fig files (figures), Excel .xlsx spreadsheets for the data discused in **Chapters 3** and **4**
Google Drive\Mallett_Kaitlyn_Repository\FE_Bundle_Simulation_Project	FE_Bundle_Simulation_Project	Geometry files for the AM and PL bundles. ABAQUS CAE and JNL files of final simulations for AM bundle in uniaxial tension discussed in **Chapter 5**
Google Drive\Mallett_Kaitlyn_Repository\Relative_Strain_Images	Relative_Strain_Images	Raw images from relative strain test (with So Young Baek) in May 2017. Video files of AM and PL 'nick' with well-defined blade.
Google Drive\Mallett_Kaitlyn_Repository\Shock_Tube_Assembly_Project	Shock_Tube_Assembly_Project	Autodesk Inventor files (.iam, .ipt) of shock tube assembly (with Kip Schimmoeller, Keith Brodek, Fabian Venegas, Antonia Crews). Final assembly files and updated parts order list.
Google Drive\Mallett_Kaitlyn_Repository\Bundle_Untwist_Project	Bundle_Untwist_Project	All images from January 2017 experiments (with Rebecca Pavlock). Also included are bundle untwist calculations and Rebecca's experimental reports, tables and presentations.
Google Drive\Mallett_Kaitlyn_Repository\Volumetric_AM_PL_Data	Volumetric_AM_PL_Data	Excel spreadsheet of all ImageJ measurements (length, width, thickness) of AM and PL bundles undergoing loading (from AM_PL_Experimental_Data tests). Matlab .fig files of final dimension, stretch, volume, and volumetric change data)